International Committee for Future Accelerators

Sponsored by the Particles and Fields Commission of IUPAP

Beam Dynamics Newsletter

No. 45

Issue Editor:
R. Wanzenberg

Editor in Chief:
W. Chou

April 2008

Contents

4

6

1   Foreword

1.1   From the Chair

Weiren Chou, Fermilab
Mail to: chou@fnal.gov

The International Committee for Future Accelerators (ICFA) met on February 11-12, 2008 at DESY, Germany. There was considerable discussion about the present status and future of the International Linear Collider (ILC) in view of recent budget cuts for this project in both the U.K. and the U.S., which will inevitably lead to a slowdown of ILC activities. However, it was noted that there has been no subsequent "domino effect." ILC support remains strong in Europe and Asia. Spain recently made a commitment to the ILC GDE Common Fund, and India will do so also. Despite the cuts the U.S. will continue to support the Common Fund this year. A revised GDE work schedule will be stretched from 2010 to 2012. The positive side of this new GDE plan is that it is more focused, with strict prioritization and strengthens collaboration with other related international projects such as XFEL and CLIC. ICFA issued a statement on ILC funding. This statement is a message to the particle physics community that there is still a desire to continue the ILC, and to politicians that being a reliable international partner is important in science. The text of the statement can be found in Rolf-Dieter Heuer's "Letter to the Editor" (Section 2 of this issue). It is also published on the ICFA website: http://www.fnal.gov/directorate/icfa/index.html.

ICFA approved the 43rd ICFA Advanced Beam Dynamics Workshop: *Nanobeam2008*, a continuation of the Nanobeam workshop series. This workshop will take place from May 25 to 30, 2008 in Novosibirsk, Russia, and will be hosted by the Budker Institute of Nuclear Physics (BINP).

The ICFA Seminar takes place once every three years. The next one will be from Tuesday October 28 to Friday October 31, 2008 and will be hosted by SLAC. The meeting place (Kavli Auditorium) has 154 seats. Attendance will be by invitation only. Among topics of the program will be a discussion of the future of the field, and other topics of community-wide importance, such as the sociology of the field and the challenges to the laboratories.

The Third International Accelerator School for Linear Colliders will be held from October 19 to 29, 2008 at the Oak Brook Hills Marriott Hotel near Chicago, U.S.A. Fermilab will be the host institution. The deadline for registration is May 1, 2008. A maximum of 70 students will be accepted from around the world. Financial aid including travel (full or partial) will be provided. More information can be found in Section 3.1 of this issue as well as on the school web site: http://www.linearcollider.org/school/2008/.

The editor of this issue is Dr. Rainer Wanzenberg, a panel member and a scientist from DESY, Germany. Dr. Wanzenberg collected a number of fine articles for this issue. Among them, the ten articles under the theme of "wakefields and instabilities" are

well-prepared and valuable contributions to our field. I want to express my sincere thanks to him for producing a high-quality Newsletter.

1.2   From the Editor

Rainer Wanzenberg
Deutsches Elektronen-Synchrotron, A Research Centre of Helmholtz Association
Notkestr. 85, 22603 Hamburg, Germany
Mail to: rainer.wanzenberg@desy.de

First and foremost I would like to thank all the authors who have contributed to this issue of the ICFA Beam Dynamics Newsletter. The theme is Wakefields and Instabilities, with an emphasis on synchrotron light sources. I really appreciate the positive response of my colleagues to my proposal to focus on this subject. I received ten contributions for the theme section. In addition contributions to the ILC section and a report on an ICFA mini-workshop are closely related to the subject of the theme section, demonstrating the recent interest in wakefields and instabilities.

This newsletter begins with a letter to the editor by R. Heuer on the future of the ILC, outlining the perspectives for the ILC after the recent budget cuts in the U.K. and the U.S. The original "Engineering Design Phase" was quickly replaced by a two-phase programme (Technical Design Phase I and II), which will, in phase I, concentrate on the project's most critical risk-mitigating areas of R&D. The ILC community is looking forward to their next meeting, which will be held in Dubna, Russia, in June 2008. The Third International Accelerator School for Linear Colliders is announced in the ILC section of this newsletter and will take place at Oak Brook near Chicago, Illinois, U.S.A from Oct 19-29, 2008, continuing the series of schools started two years ago.

 Ion effect studies and, in particular, fast ion instabilities in the damping ring of the linear collider are the subjects of a contribution to the ILC section of the newsletter. "Wakefields from Start to End in Linear Colliders" is one of the major interests of the Cockcroft Institute Wakefield Interest Group. This is followed by a contribution from the University of Darmstadt with an emphasis on the computational aspects of wake fields. Wakefields, impedance models and instabilities in synchrotron light sources are presented in the following eight contributions of the theme section.

The contributions from ELETTRA, APS, and SOLEIL also report on their operational experience with respect to current limitations and accelerator studies on beam instabilities. The well-written and interesting report by R. Nagoaka et al. on the activities at the French third generation synchrotron light source SOLEIL gives detailed and valuable insights to the theoretical impedance model of SOLEIL and a comparison with observations. The third generation synchrotron light sources ALBA and PETRA III are currently under construction. The contribution from CELLS, the consortium which constructs ALBA, reports on the computation of the longitudinal and transverse impedance of the ring as well as the study of higher order modes in the cavities. The impedance of PETRA III has been studied in a collaboration between DESY, the University of Darmstadt (Germany), the Otto-von-Guericke University of Magdeburg (Germany), CANDLE (Yerevan University, Armenia), and the Budker Institute of Nuclear Physics (BINP in Novosibirsk, Russia). All institutes have contributed to the theme section of this newsletter.

The contribution to the section on workshop and conference reports, namely a "Summary of WAKE Fest 07", is closely related to the ILC and theme sections of this newsletter. The workshop focused on the wakefield effects of RF and HOM couplers as well as RF kicks due to these couplers, which is important for the ILC and also for the European X-ray Laser Project (http://www.xfel.eu/en/index.php). A short report on a mini workshop on the microbunching instability, held in September 2007 at ELETTRA, Trieste, Italy, can be found in the ELETTRA contribution in the theme section 4.3.2.5.

The abstracts of two recently finished doctorial theses are in section 6 of the newsletter.

Future beam dynamics events can be found in section 7 including a meeting on X-Band structures, the EPAC'08, the 15th Workshop on Beam Dynamics and Optimization, and the Workshop on High-Intensity High-Brightness Hadron Beams, HB2008. Reports from these conferences and workshops are expected for the forthcoming issues of the Beam Dynamics Newsletter.

2 Letters to the Editor

2.1 The Future of the ILC

Rolf-Dieter Heuer
Deutsches Elektronen-Synchrotron, A Research Centre of Helmholtz Association
Notkestr. 85, 22603 Hamburg, Germany
Mail to: rolf-dieter.heuer@desy.de

Just as the 500 or so scientists involved in planning the International Linear Collider (ILC) were gearing up for the next phase of their project – a three-year period at the end of which they had hoped to approach governments with a sound and cost-effective design to ask for construction approval – two sets of bad news hit the community. In December, the UK's Science and Technology Facilities Council (SFTC) suddenly announced that they would pull out of a number of international science projects, including the ILC. A report stated that the STFC "will cease investment in the International Linear Collider. We do not see a practicable path towards the realisation of this facility as currently conceived on a reasonable timescale."

Just two weeks later, a few days before Christmas, another blow came from another major contributor to the ILC: the United States. The US Congress passed the so-called omnibus bill, a budget plan for the fiscal year 2008. It contained severe cuts in science funding, bringing the ILC down from an expected 60 million dollars to a mere 15 million. Because the bill was passed in December, a quarter of the expected funds had already been spent, meaning that all work on the ILC had to stop immediately. Both major particle physics labs in the US, SLAC and Fermilab, have to lay off staff, and the long-term effects of these cuts are still unclear.

What does all this mean for the project? Obviously it is still very early to say. The community has lost many key people and rearrangements within groups and for the overall planning are being made. What is clear, however, is that it has brought the ILC community both closer together and has opened it even further to projects with similar

goals and technologies, like CLIC or the European XFEL. A sense of 'now, more than ever' prevails and manifests itself in even more determination and hard work, and in small gestures like financial support for team members whose funds were cut. At the first community-wide meeting in Japan in March, for example, Japan and France paid for a number of American colleagues to fly over and attend the meeting.

Director Barry Barish and his Executive Committee, consisting of regional directors, project managers and a few key experts, were able to draw up a new plan very quickly after meeting at DESY in Hamburg early in 2008. What was formerly known as 'Engineering Design Phase' and was supposed to be final by the year 2010 has effectively been delayed by two-years, and replaced by a two-phase programme (now referred to as the Technical Design Phase I and II). The first phase will last until 2010 and concentrates on the project's most critical risk-mitigating areas of R&D. These are high-gradient SCRF aiming at consistent yields at 35 MV/m and international cryomodule design, electron cloud mitigation techniques in the positron damping ring, cost effective RF power sources and the demonstration of final-focus optics. In parallel to these R&D activities, a somewhat reduced effort on the collider design and cost optimisation will focus primarily on the main linacs and the machine-detector interface, the latter giving a strong link the emerging detector communities. The second phase (2010-2012) will focus on the more global engineering aspects and cost optimisation of the entire collider, together with an updated value estimate for the cost. An important additional deliverable for the TDP-II will be a project implementation plan, including construction schedules and a model for in-kind contributions and cross-regional mass production of components such as the cryomodules. As with the original ED phase, the goal is to be ready for project approval in 2012, if the results from LHC indeed support the physics case for a 200-500 GeV centre-of-mass collider.

Thus, the community interprets the cuts not as a criticism of the ILC's physics case – the US Department of Energy has stated several times that a next-generation linear collider is a very high priority, albeit with a possibly too optimistic timescale – but as the result of a series of complicated political and far-reaching events beyond science policy. Europe, though shocked at and shaken by the news, agrees with this interpretation. The ILC and its labs in the US received a lot of support from key media (including Science, Nature, Scientific American and many more). Appeals have been and are being made to delegates and representatives to reinstate funding both in the US and the UK. ICFA also issued a statement (link to http://www.interactions.org/cms/?pid=1025970) calling for more stability in science funding that I could not agree with more. To quote the statement: "*Carrying out frontier science relies increasingly on stable international partnerships, since the scientific and technical challenges can only be met by enabling outstanding men and women of science from around the world to collaborate, and by joining forces to provide the resources they need to succeed.   A good example is the proposed International Linear Collider. In order to advance the understanding of the innermost structure of matter and the early development of the universe, several thousand particle physicists and accelerator scientists around the world, during the past 15 years, have coordinated their work on developing the technologies necessary to make a Linear Collider feasible. In view of these tightly interlinked efforts, inspired and driven by the scientific potential of the Linear Collider, the sudden cuts implemented by two partner countries have devastating effects. ICFA feels an obligation to make policy makers aware of the need for stability in the support of major international science efforts. It is important for all*

governments to find ways to maintain the trust needed to move forward international scientific endeavours."

The community is working even harder now on key technologies, gradients and cost saving options, and will come together in Dubna, Russia, in June for a meeting dedicated to site considerations. It will certainly be an interesting and intense meeting.

3 International Linear Collider (ILC)

3.1 Third International Accelerator School for Linear Colliders

Barry Barish, Director, ILC GDE,
Enzo Iarocci, Chair, ILCSC,
Shin-ichi Kurokawa, KEK
Weiren Chou, Chair, ICFA BD Panel
http://www.linearcollider.org/school/2008/

We are pleased to announce the Third International Accelerator School for Linear Colliders. This school is a continuation of the series of schools started two years ago. The first school was held in 2006 at Sokendai, Hayama, Japan and the second one in 2007 at Erice, Sicily, Italy. The school is organized by the International Linear Collider (ILC) Global Design Effort (GDE), ILC Steering Committee (ILCSC) and the International Committee for Future Accelerators (ICFA) Beam Dynamics Panel. The school this year will take place at the Oak Brook Hills Marriott Hotel near Chicago, Illinois, U.S.A. from October 19 – 29, 2008. It is hosted by Fermilab and sponsored by a number of funding agencies and institutions around the world including the U.S. Department of Energy (DOE), the U.S. National Science Foundation (NSF), SLAC, CERN, DESY, INFN, IN2P3, CARE/ELAN, KEK, KNU, PAL and IHEP.

We will offer a 9-day program, with 8 days of lectures on accelerators at the Marriott Hotel and a one-day site visit to Fermilab, where hands-on training in a control room will be given. The program also includes a half-day field trip to downtown Chicago. There will be a total of 12 lectures covering both basic accelerator topics (e.g. synchrotrons, linacs, superconductivity, beam-beam interactions) and advanced topics. The advanced topics will be focused on the ILC as well as the Compact Linear Collider (CLIC). While these two types of linear colliders share a number of similarities (e.g., sources, damping rings, beam delivery, instrumentation, feedback, conventional facilities and detectors), each applies a different technology for acceleration (superconducting rf vs. room temperature rf, klystron vs. beam driven). There will also be a lecture on muon collider, a new type of lepton colliders. All lectures will run in sequence. (There will be no parallel sessions.) A complete description of the program is attached below and can also be found on the school web site. There will be homework assignments and a final examination but no university credits.

We encourage young physicists (graduate students, post doctoral fellows, junior researchers) to apply. In particular we welcome those physicists who are considering changing to a career in accelerator physics. The school will accept a maximum of 70 students from around the world. Students will receive financial aid covering their

expenses for attending the school including travel (full or partial). There will be no registration fee. Each applicant should complete the online registration form (which can be found at www.linearcollider.org/school/2008/) and submit a curriculum vita as well as a letter of recommendation from his/her supervisor (in electronic form, either PDF or MS WORD). The deadline for application is May 1, 2008. For more information, please contact: Cynthia M. Sazama, Fermilab, P.O. Box 500, Batavia, Illinois 60510, U.S.A., fax: +1-630-840-8589, e-mail: sazama@fnal.gov

Organizing Committee:

Barry Barish (GDE/Caltech, Co-Chair)
Shin-ichi Kurokawa (KEK, Co-Chair)
Weiren Chou (ICFA BD Panel/Fermilab)
Jean-Pierre Delahaye (CERN)
Rolf-Dieter Heuer (DESY)
In Soo Ko (PAL)
Kaoru Yokoya (KEK)
Alex Chao (SLAC)
Paul Grannis (Stony Brook Univ.)

Curriculum Committee:

Weiren Chou (Fermilab, Chair)
William Barletta (USPAS)
Daniel Brandt (CERN)
Alex Chao (SLAC)
Jie Gao (IHEP/China)
Shin-ichi Kurokawa (KEK)
Carlo Pagani (INFN/Milano)
Junji Urakawa (KEK)
Andrzej Wolski (Univ. of Liverpool)

Third International Accelerator School for Linear Colliders – Curriculum
(v.3, 03/18/2008)

October 19-29, 2008, Oak Brook Hills Marriott Hotel, Oak Brook, Illinois, U.S.A.

<u>Daily Schedule</u>

Breakfast	08:00 – 09:00
Morning	09:00 – 12:30, including ½-hour break
Lunch	12:30 – 14:00
Afternoon	14:00 – 17:30, including ½-hour break
Dinner	17:30 – 19:00
Tutorial & homework	19:00 – 22:00

<u>List of Courses</u>

	Morning	Afternoon	Evening
October 19		*Arrival, registration*	*Reception*
October 20	Introduction	Sources & bunch compressors	Tutorial & homework
October 21	Damping ring I	Linac I	Tutorial & homework
October 22	Damping ring II	Linac II	Tutorial & homework
October 23	LLRF & high power RF	Beam delivery & beam-beam	Tutorial & homework
October 24	*Site visit to Fermilab*	*Site visit to Fermilab*	*Free time*
October 25	Superconducting RF & ILC I	*Excursion*	Tutorial & homework
October 26	Superconducting RF & ILC II Room temperature RF & CLIC I	Room temperature RF & CLIC II	Tutorial & homework
October 27	Instrumentation & control	Muon collider	Tutorial & homework
October 28	*Final exam*	Operations; Physics & detectors	*Banquet; Student Award Ceremony*
October 29	*Departure*		

Program

	Monday, October 20	Tuesday, October 21	Wednesday, October 22	Thursday, October 23

Morning 09:00 – 12:30	**Opening remarks** (10)
	Lecture 1 – Introduction (180)
	Barry Barish (Caltech)
	• Why LC
	• What's ILC
	• Layout of ILC
	• Parameter choices & optimization
	• Overview of accelerator issues
	• Other future lepton colliders: CLIC and muon collider
		Lecture 3a – Damping ring I (180)
		• Role of damping rings
		• High-level overview of structure, and principles of operation
		• Review of basic linear beam dynamics
		• Damping ring lattice
		• Radiation damping (derivation of damping times, and the need for a damping wiggler in LC damping rings)
		• Quantum excitation and equilibrium beam emittances
			Lecture 3b – Damping ring II (180)
			• Brief overview of technical systems
			• R&D challenges for selected technical components
			  ➢ injection/extraction kickers
			  ➢ damping wiggler
			• Brief overview of beam dynamics issues
			• Selected beam dynamics issues
			  ➢ impedance effects
			  ➢ electron cloud effects
				Lecture 5 – LLRF & high power RF (180)
				Stefan Simrock (DESY)
				• RF system overview
				• LLRF
				• Timing and synchronization
				• Modulators
				• Klystrons
				• RF distribution

Afternoon 14:00 – 17:30	**Lecture 2 – Sources & bunch compressors** (180) • e- gun • e+ sources • Polarized sources • Bunch compressors • Spin rotator	**Lecture 4a – Linac I** (180) • Phases & superposition • Basics of RF cavities • Lumped circuit analogy, metrics • RF Pillbox cavity • Coupled rf-cavities, mode structure • Shunt impedance, transit-time factor • Standing wave linacs and structures • Beam loading and power coupling • Slow wave structures	**Lecture 4b – Linac II** (180) • Traveling wave linacs • Structure parameters • Scaling relationships for TW linacs • Power flow & beam loading • Multi-bunch energy gain • Wakefields & impedances • Linac lattice • Emittance preservation & instabilities • Beam based alignment	**Lecture 6 – Beam delivery & beam-beam** (180) • Overview • Beam-beam interaction and crossing angle • Collimation • Accelerator-detector interface, shielding and beam dump • Background and detector protection • Beam monitoring and control at final focus • Luminosity optimization
Evening 19:00 – 22:00	Tutorial & homework	Tutorial & homework	Tutorial & homework	Tutorial & homework

<u>Program</u> (cont'd)

	Saturday, October 25	Sunday, October 26	Monday, October 27	Tuesday, October 28
Morning 09:00 – 12:30	**Lecture 7a – Superconducting RF & ILC I** (180) • Superconductivity basics • Cavity design & SRF constraints • Lorentz force detuning in SCRF • Microphonics & vibration issues • Cavity fabrication and tuning • Surface preparation • Gradient limit and spread • Cryogenics • ILC cryomodules • Alignment issues	**Lecture 7b – Superconducting RF & ILC II** (90) • Power Coupler • HOMs & HOM Couplers • Slow and fast tuner • ILC design & challenges **Lecture 8a – Room temperature RF & CLIC I** (90) • Gradient limits at X-band • Breakdown mechanism • Pulse heating • Pulse train formats • Klystron *vs.* beam driven • RF power manipulation options	**Lecture 9 – Instrumentation & control** (180) • Beam monitoring • Precision instrumentation • Feedback systems • Energy stability • Orbit control • Electronics • Data processing	**08:00 – 12:30 Final exam** (270)
Afternoon 14:00 – 17:30	**Excursion to Downtown Chicago**	**Lecture 8b – Room temperature RF & CLIC II** (180) • CLIC layout • Cavity fabrication and tuning • HOM out-coupling • Thermal stability • Driver beam stability • Power coupling • Alignment issues • CLIC design & technical challenges	**Lecture 10 – Muon collider** (120) • Muon collider basics • Machine layout • Major sub-systems • Challenges **Study time** (60)	**Lecture 11 – Operations** (90) • Reliability • Availability • Remote control and global network **Lecture 12 – Physics & detectors** (90) **Rolf-Dieter Heuer (DESY/CERN)** • Tera scale physics • Physics beyond 1 TeV • ILC *vs.* LHC • Detectors
Evening 19:00 – 22:00	Tutorial & homework	Tutorial & homework	Tutorial & homework	Banquet; Student Award Ceremony

Notes to the Program:

1. There will be 12 lectures, each taught by one lecturer.
2. The curriculum covers both the ILC and CLIC. Those lectures in which the two machines share similarities (e.g. sources, damping rings, beam delivery & beam-beam, instrumentation & control, operations, physics & detectors) should cover both machines.
3. There is also a 90-minute lecture on muon collider, which is another type of future lepton collider. But we will not lecture on plasma/laser acceleration.
4. There are a total of 8 lecture days: Oct 20 – Oct 23 and Oct 25 – Oct 28, with one afternoon excursion/free. October 24 is set for a site visit to Fermilab, where hands-on training in a control room will be given.
5. There will be homework assignments, but no homework due for grade. There will be a final exam, and some of the exam problems are to be taken from the homework assignments. Lectures 11 and 12 take place after the final exam. So they do not take part in the exam. The exam papers will be graded right after the exam and results announced in the evening of Oct. 28 at the student award ceremony.
6. There is a tutorial and homework period every evening. It is part of the curriculum and students are required to attend. Lecturers will be available in the evening of their lecture day during this period.
7. Lecturers are strongly suggested to cover the basics as well as possible. Their teaching material will be made available online to the students well ahead of time (~ 1 month prior to the school), while students are likewise encouraged to study the material ahead of time as much as possible.
8. Lecturers are responsible for the design of homework and exam problems as well as the answer sheet. They are also responsible for grading the exams.
9. The award ceremony will honor top (~10) students based on their exam scores.

3.2 Ion Effect Studies in the ILC Electron Damping Ring

Guoxing Xia and Eckhard Elsen
Deutsches Elektronen-Synchrotron, A Research Centre of Helmholtz Association
Notkestr. 85, 22603 Hamburg, Germany
Mail to: guoxing.xia@desy.de

3.2.1 Introduction

In electron storage rings, the ions due to collisional ionization between the circulating particles and residual gas molecules in the beam duct may generate adverse effects such as beam lifetime reduction (local gas pressure increases), emittance growth, beam loss through excitation of resonances and coherent beam instabilities. There are two types of ion effects. The first is ion trapping, which denotes the ions trapped in the space charge potential of the beam. These ions repeatedly interact with the beam particles possibly for many turns. This ion trapping effect can be successfully cured by a few means. For example, by applying the cleaning electrodes along the ring, most of the ions will be collected by the clearing electrodes. In addition, a simple way is to leave contiguous RF

buckets empty after the bunch train (a train gap) so as to make the ion trapping unstable. In general, the train gap amounts to a few percentage of the total RF buckets of the ring. If the gap is long enough, the ions may be driven to large amplitude, and hence, form a halo which will not affect the beam motion considerably. Another remedy consists in resonant beam shaking, which proves very effective. The second ion effect is the so-called fast ion instability (FII), which indicates that the ion induced instability occurs during the single passage of the beam [1,2]. It can occur either in linacs or storage rings. This instability can be alleviated by introducing a fast feedback system which may damp the instability before it grows. Recently, simulation shows that the concept of a mini-train is also very promising to overcome this instability [3]. In the mini-train case, the bunches are divided into many small bunch trains followed by gaps (empty RF buckets). The gaps between bunch trains typically reduce the number of ions. Therefore, the FII can be reduced as well. The FII is a concern in low-emittance, high-intensity storage rings with multi-bunch operation.

In this paper, we study the latter, namely, the FII, in the electron damping ring of the International Linear Collider (ILC). The motivation is to see how severe this instability is and which parameter setting will trigger this instability in the ILC damping ring.

In order to obtain the specific luminosity for the ILC, the damping rings have to accommodate about 3000 bunches in the ring with each bunch more than 1×10^{10} particles inside. In addition, the vertical emittance of the ring is extremely low (2pm) which is a factor of 2 less than the achievable lowest-emittance ring to date [4]. Hence the FII is regarded as one of the very high priorities for R&D of the damping rings for the ILC. In order to investigate this instability in detail, we study the gap effects in the fill patterns in the baseline lattice [5]. Meanwhile, the FII in different gas pressures and fill patterns is simulated. The feedback system is also applied in the simulation.

This paper is structured as follows. In section 2, the FII is briefly introduced. Section 3 gives the analytical calculation of ion density near the beam in different fill patterns [6]. Section 4 introduces the simulation process. The simulation results in various fill patterns and gas pressures are also presented. In the end, a short summary is given.

3.2.2   Fast Ion Instability

The FII occurs in many various high-intensity machines such as ALS, PLS, TRISTAN-AR and ATF etc. The beam size blow-up, tune shift and spread and emittance growth due to ions have been observed typically when intentionally leaking gases such as He, N_2 into the vacuum vessel to enhance the ion effects.

The major species of residual gas in vacuum chamber are CO and H_2. In the specific beam energy of 5GeV for the ILC damping ring, the ionization cross section is about 1.86×10^{-22} m^2 and 0.31×10^{-22} m^2 for the CO and H_2, respectively. It can be seen that the ionization cross section of CO is about 6 times higher than that of H_2. Therefore, we consider CO$^+$ ions as the instability source. The line density of the ions created by the electron beam with a population N_0 is given by

$$\lambda_i = \sigma_i N_0 n_b p / kT \tag{1}$$

where σ_i is the ionization cross section of CO$^+$, n_b is the bunch number, p is the gas partial pressure of CO, k is the Boltzmann constant and T is the temperature of the gas. Eq. (1) shows that that the ion density is larger if the bunch intensity and the number of bunch are very large in the ring. For the ILC damping ring, there are about 3000 bunches with each bunch over 1×10^{10} particles inside. Under these conditions, the

number of ions caused by ionization of residual gas will become large for a single passage of beam. The FII potentially gives adverse impact to the ILC damping ring's performance.

3.2.3 Gap Effects in the Fill

If there is one long bunch train in the storage ring, the ions are trapped by the long bunch train. The trapping condition is disturbed when the fill pattern consists of a number of short bunch trains (mini-trains) with gaps in between. In this section, the gap effect will be studies analytically.

The ions inside the beam are defined as those ions within $\sqrt{3}\sigma_{beam}$ of the beam centroid (here, σ_{beam} is the beam dimension). Note that the growth rate of FII is proportional to the ion density. The diffusion of the ions during the gaps increases the volume of the ion cloud and reduces the ion density [3, 7]. Hence, it is expected that the growth rate of FII is reduced for mini-trains.

When a gap is introduced in the bunch train, one can estimate the density of the residual ions in the beam after the clearing gap as [8]

$$\rho_i \approx \frac{\rho_{i0}}{\sqrt{\left(1 + L_{gap}^2 \omega_x^2\right)\left(1 + L_{gap}^2 \omega_y^2\right)}} \qquad (2)$$

where ρ_{i0} denotes the ion density at the end of one bunch train, L_{gap} the gap length between two adjacent bunch trains, $\omega_{x,y}$ the ion oscillation frequency which is given by

$$\omega_{x,y}^2 = \frac{2N_0 r_p}{L_{sep} A \sigma_{x,y} \left(\sigma_x + \sigma_y\right)} \qquad (3)$$

where r_p is the classical radius of proton, L_{sep} is the bunch spacing, A is the atomic mass number of the ion which causes the instability, σ_x and σ_y are the horizontal and vertical beam sizes respectively.

According to the linear theory of FII, the tune shift due to ions is proportional to the number of ions in the ring [3]. In order to make the ion density as low as possible, the mini-train concept is adopted, namely, each bunch train is assumed to consist of tens of bunches following by some empty RF buckets unfilled (gaps). These unfilled gaps cause the ions to drift to large amplitudes. The diffused ions form the ion halo and do not affect the beam motion. Take an example by using the three typical fill patterns *A*, *B* and *C* as shown in Table 1 for the ILC damping ring OCS8 [5], the ion density for one long bunch train case and mini-trains are calculated and compared, as shown in Fig.1, Fig.2 and Fig.3, respectively. The CO partial pressure assumed is 1.0 nTorr. The ion density for a single long bunch train increases linearly with the number of bunches. However, with gaps between bunch trains, the ion density is significantly reduced. The ion density for mini-trains can quickly reach the peak value after a few short bunch trains [7]. For fill patterns *A, B* and *C* the ion density diminishes by about two orders of magnitudes compared to a single long bunch train case. The FII growth time for mini-train increases by two orders of magnitude compared to a single long train. The tune-shift is also significantly reduced. With mini-trains the FII can hence be damped by a fast bunch-by-bunch feedback system [9].

Table 1: Typical fill patterns in the ILC damping ring.

Fill patterns	A	B	C
Bunch spacing, [bucket]	2	2	4
Number of trains, p	117	78	58
Bunches per even-numbered minitrain, f_2	0	0	23
Gaps per even-numbered minitrain, g_2	0	0	30
Bunches per odd-numbered minitrain, f_1	45	45	22
Gaps per odd-numbered minitrain, g_1	30	90	30
DR average current, mA	405	405	401
Total number of bunches	5265	3510	2610
Bunch population [$\times 10^{10}$]	1.04	1.56	2.07
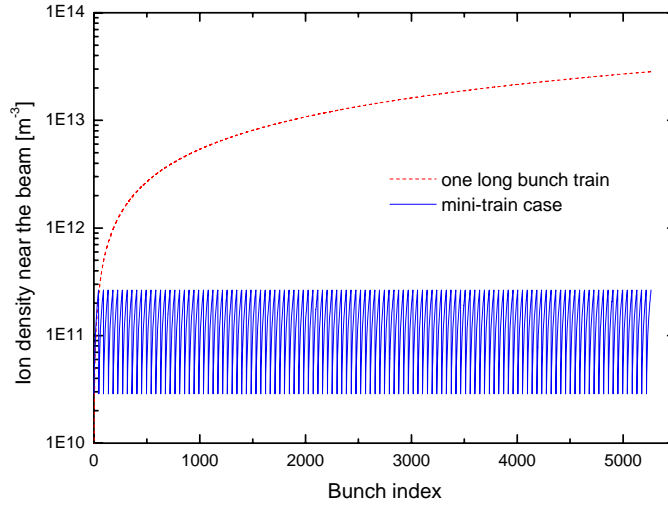
Figure 1: Ion density near the beam for one long bunch train case (dash) and for fill pattern *A* in the mini train case (solid) in ILC damping ring OCS8.
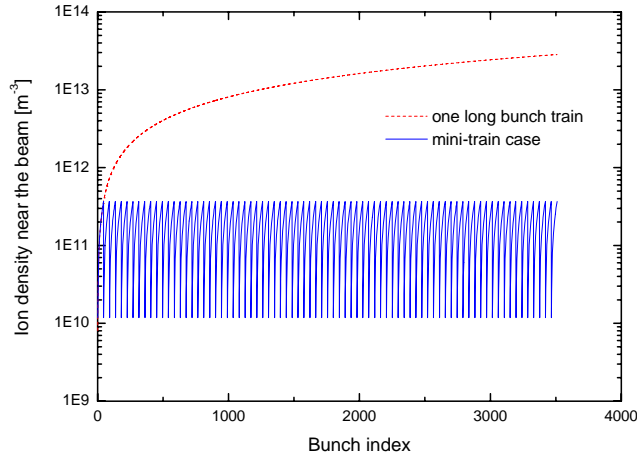
**Figure 2:** Ion density near the beam for one long bunch train case (dash) and for fill pattern *B* in the mini train case (solid) in ILC damping ring OCS8.
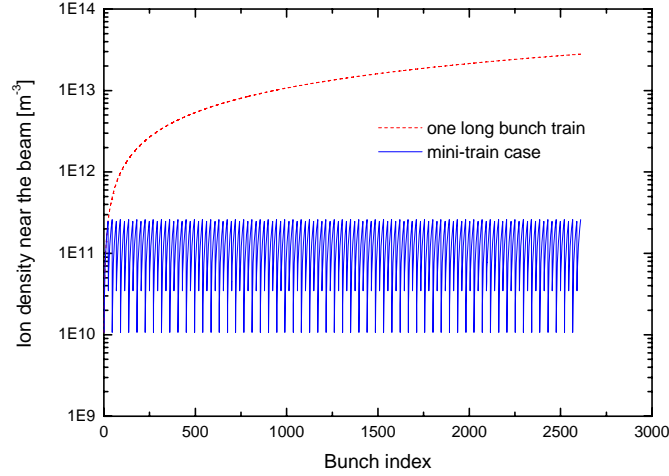
Figure 3: Ion density near the beam for one long bunch train case (dash) and for fill pattern C in the mini train case (solid) in ILC damping ring OCS8.

3.2.4 Simulation of FII in ILC Electron Damping Ring

In order to investigate the FII in details for the ILC electron damping ring, a weak-strong simulation code is employed [10]. The ions are regarded as macro particles and the electron beam is treated as rigid Gaussian beam. The motion of the beam centroid is taken into account. The number of ions is increased with respect to the bunch index in the train. In the simulation model, the first bunch will only produce the ions and it does not interact with the ions, while the trailing bunches in the train will produce the ions and interact with the ions created by the preceding bunches. The interaction between ions and electron beam is based on the Bassetti-Erskine formula which is similar to the beam-beam interaction of two Gaussian beams [11]. To relate adjacent interaction points a linear transfer matrix is used. In this code, the beam size variation due to beta function and dispersion function change is taken into account.

The number of ions that are generated by an electron beam with the population of N_0 is given by $n_i[m^{-1}] = 0.045 N_0 p$ [Pa]. For the CO partial pressure of 1 nTorr, the ion line density are 62m^{-1}, 93m^{-1} and 124m^{-1}, for fill pattern cases A, B and C, respectively.

Since the vertical beam emittance is smaller than the horizontal one, the FII affects predominantly the vertical plane. In our simulations, the time evolution of the growth of dipole amplitude of the beam is simulated and recorded turn by turn. The vertical amplitude of bunch centroid is half of the Courant-Synder invariant which is given by

$$J_y = \frac{1}{2}\left[\frac{(1+\alpha^2)}{\beta} y^2 + 2\alpha y y' + \beta y'^2 \right] \quad (4)$$

where α and β are the Twiss parameters of the ring. We compare $\sqrt{J_y}$ with the vertical beam size which is represented by the value of $\sqrt{\varepsilon_y}$ (here, ε_y is the vertical emittance of the beam). These quantities are measured in units of m$^{1/2}$.

Table 2 lists the basic parameters of the OCS8 damping ring. In the simulation, we use the parameters of three typical fill patterns listed in Table 1. In order to save CPU time, the optical functions of only one of the octants of the ring are used. For each fill pattern, 10 bunch trains are chosen in our simulation.

Figure 4 shows the evolution of maximum amplitude with respect to number of turns for fill pattern case *A* without and with active feedback damping. The feedback damping time is 50 turns (~ 1ms) in the simulation (this is rather conservative considering the current technology). In this Figure, N_0 denotes the number of particles per bunch, n_b the bunch number per train, n_{train} the train number, L_{sep} the bunch spacing in units of RF bucket, LtrainGap the gap length between two bunch trains in units of RF bucket. It can be seen that for the CO pressure of 1 nTorr, the growth of vertical amplitude is beyond the beam size. By employing the feedback system, the growth of vertical amplitude can be almost damped to the value of the initial beam size. Figure 5 gives the growth of maximum amplitude with respect to the number of turns for fill pattern case *B* without and with feedback damping. The growth of vertical amplitude is again beyond the beam size in CO pressure of 1 nTorr. Feedback can suppress the growth of instability to a certain amount. Figure 6 shows the case in fill pattern *C*, in which we modified the number of bunches per train in order to simplify the simulation. The conclusion is nearly the same as the fill pattern case *A* and *B*. Figures 7 and 8 show the beam oscillation due to ions in different turns for fill pattern case *B* without and with feedback system, respectively. It can be seen clearly that the beam oscillation grows with respect to the time (number of turns). In addition, the tail bunch oscillates with larger amplitude than that of the preceding bunches. If the feedback system is applied, the amplitude of beam oscillation can be suppressed by nearly one order of magnitude.

Mini-trains help to remedy: Figure 9 shows the evolution of the maximum amplitude with respect to the number of turns for fill pattern *C* for short and long bunch train cases without feedback damping. We take 5 trains with 46 bunches per train and 10 trains with 23 bunches per train respectively (the total number of bunches is the same in both cases). It shows that the growth of vertical amplitude for long bunch train is faster than that of the short bunch train. This is because the gaps between bunch trains reduce the ion density near the beam and therefore weaken the growth of FII.

The evolution of the vertical amplitude in different gas pressures is shown in Figure 10 for the fill pattern case *A*. It indicates the trend: the higher the gas pressure, the higher the growth of vertical amplitude. The vertical amplitude grows quickly in the beginning and then slows and finally saturates. This is also the characteristics of FII in linear theory [1]. The growth time of FII can also be estimated from the simulation results in different gas pressures and shown in Figure 11. It indicates that the growth time of FII becomes faster if the gas pressure is larger.

Table 2: The basic parameters of OCS8 damping ring.

Energy	5 GeV
Circumference	6476.4395 m
Harmonic number	14042
Betatron tunes	49.23, 53.34
Chromaticity	-63.7, -63.3
Momentum compaction	3.96×10^{-4}
Natural emittance	4.95 μm
Damping time	25 ms
RF voltage	21.2 MeV
Energy loss per turn	8.7 MeV
Momentum acceptance	1.48%
Synchrotron tune	0.06
Equilibrium bunch length	9 mm
Equilibrium energy spread	0.128%
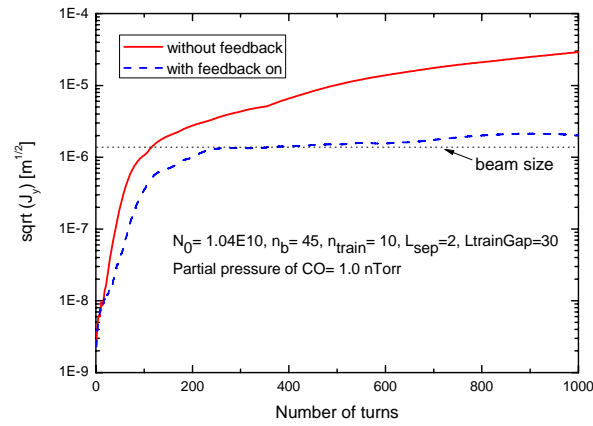
Figure 4: Evolution of maximum amplitude with respect to number of turns for fill pattern *A* without and with feedback damping.
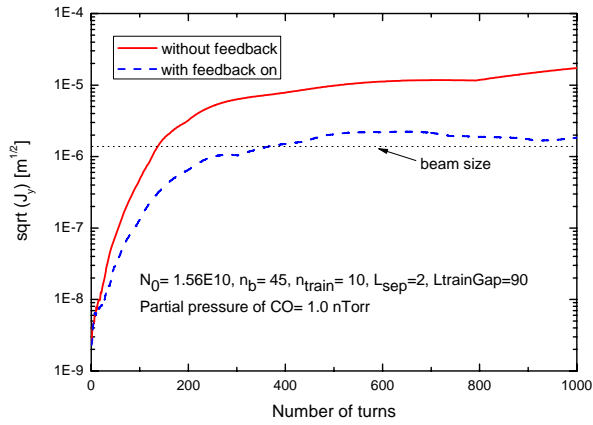
Figure 5: Evolution of maximum amplitude with respect to number of turns for fill pattern *B* without and with feedback damping.
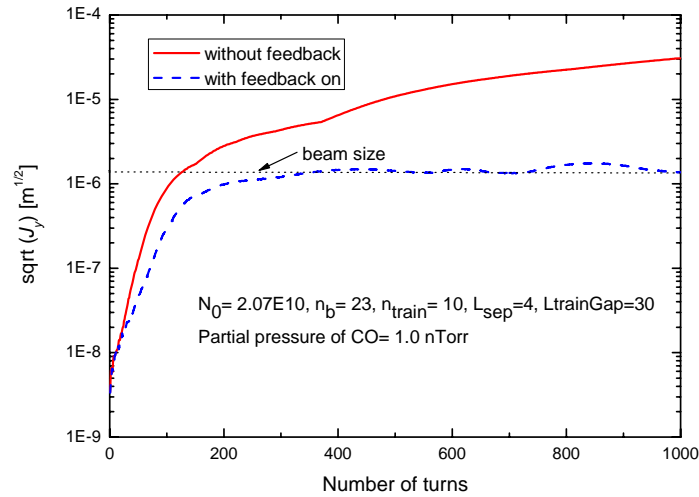
Figure 6: Evolution of maximum amplitude with respect to number of turns for fill pattern *C* without and with feedback damping.
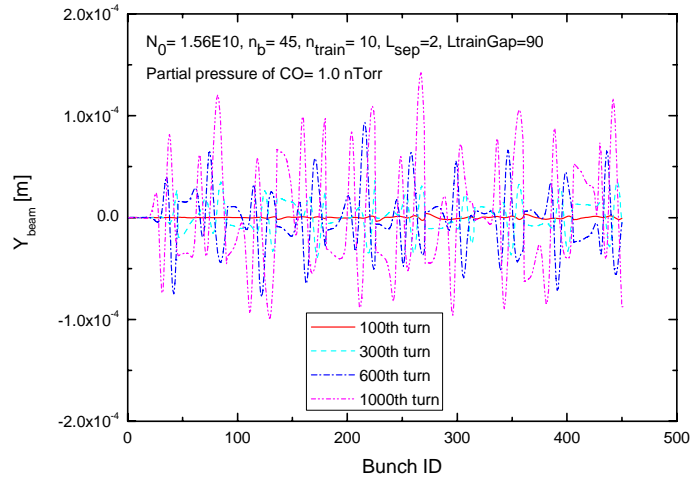
Figure 7: Beam oscillation pattern in different turns for fill pattern *B* without feedback.
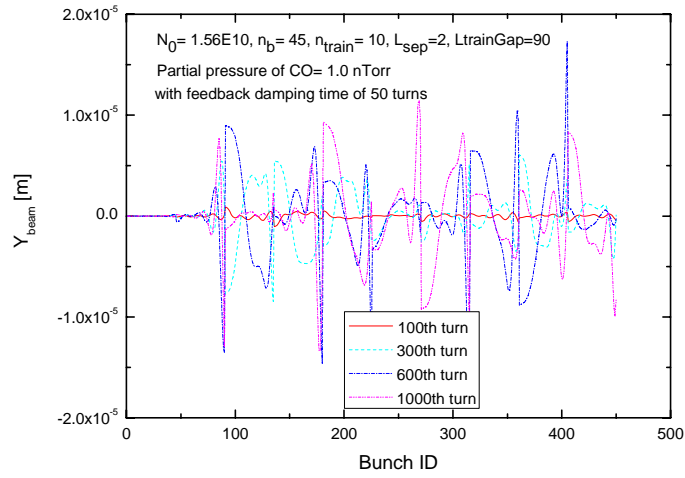
Figure 8: Beam oscillation pattern in different turns for fill pattern *B* with feedback.
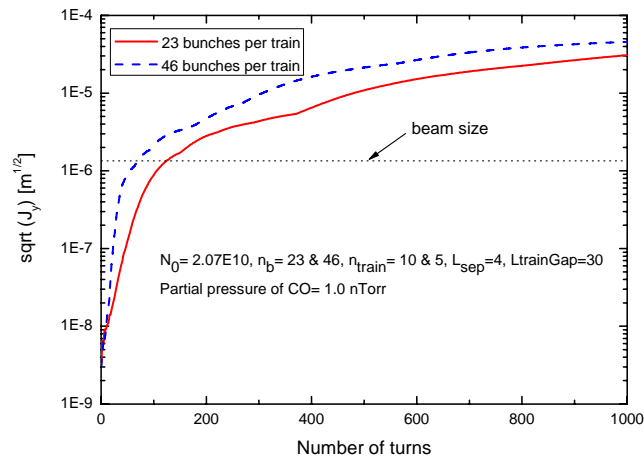
Figure 9: Evolution of maximum amplitude with respect to number of turns for fill pattern *E* for short bunch and long bunch case without feedback damping.
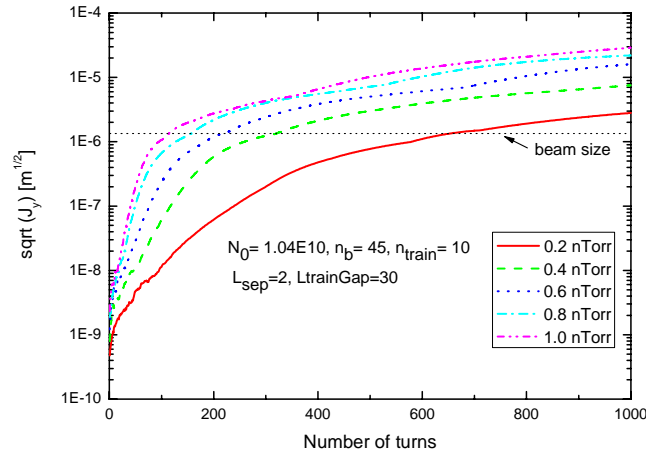
Figure 10: Evolution of maximum amplitude with respect to number of turns for fill pattern *A* in various gas pressure of CO.
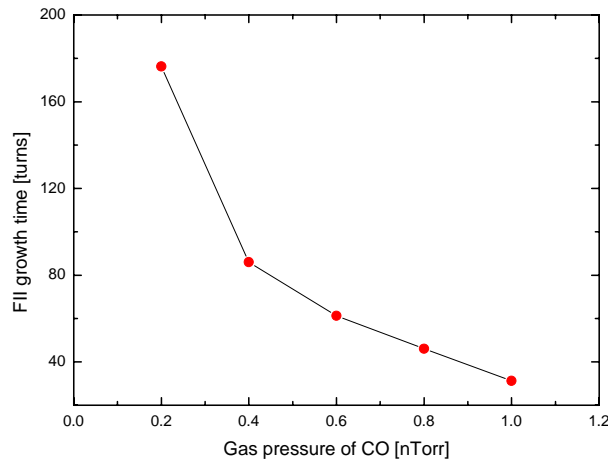
Figure 11: FII growth time *vs.* gas pressures of CO for fill pattern *A* without feedback.

3.2.5 Conclusions

The study in this report reveals that with the introduction of mini-trains the ion density near the beam can effectively be reduced. For the three typical fill patterns of the ILC damping ring, the ion density in the mini-train case is about a factor of 100 less than that of the single long bunch train case. The simulation results show for three fill patterns *A*, *B* and *C*, the fast ion instability can not be totally damped by a fast feedback system with the damping time of 50 turns if the gas pressure of CO is larger than 1nTorr. Therefore, a better vacuum pressure (< 1nTorr) and a more advanced feedback system with damping time less than 50 turns are crucial to overcome FII. Comparing to one long bunch train case, the mini-train can reduce the growth of FII significantly.

3.2.6 Acknowledgement

3.2.7 References

1. T.Raubenheimer and F.Zimmermann, Phys. Rev. E52, no.**5**, p.5487 (1995).
2. G.V.Stupakov, T.Raubenheimer *et al*., Phys.Rev.E52, no.**5**, p. 5499 (1995).
3. L.Wang, T.Raubenheimer and A.Wolski, SLAC-PUB-11932, (2006).
4. K.Kubo, M. Akemoto *et al*., Phys. Rev.Lett. 88 194801(2002).
5. L.Emery and A.Xiao, ILC Damping Ring Mini Workshop at KEK, (2007).
6. A.Wolski, https://wiki.lepp.cornell.edu/ilc/bin/view/Public/DampingRings/.
7. G.Xia, E.Elsen et al., Proceedings of PAC07, Albuquerque, NM, USA (2007).
8. J.M.Byrd, A.W.Chao, S.Heifets et al., SLAC-PUB-7389, (1996).
9. A.Drago, talks at ILCDR07 Workshop in Frascati, (2007).
10. K.Ohmi, Phys. Rev. E55, no.**6**, p.7550 (1997).
11. M.Bassetti and G.A.Erskine, CERN-ISR-TH/80-06.

4   Theme Section: Wakefields and Instabilities

4.1   The Cockcroft Institute Wakefields Interest Group

D. Angal-Kalinin, R. Appleby, R. Barlow, C. Beard, A. Bungau, G. Burt, D. A. Burton, R. Carter, S. Chattopadhyay, J. Clarke, D. C. Christie, J. Dainton, A. C. Dexter, J. L. Fernandez-Hernando, S. Goto, P. Goudket, J. Gratus, K. Hock, F. Jackson, S. Jamison, R. M. Jones, P. A. McIntosh, B. Muratori, A. Noble, H. Owen, V. Perlick, M. Poole, F. Roncarolo, D. Scott, I. Shinton, J. Smith, S. Smith, A. Toader, R. W. Tucker, T. Walton, A. Wolski, E. Wooldridge
Cockcroft Institute, Keckwick Lane, Daresbury, Cheshire, UK, WA4 4AD
Mail to: g.burt@dl.ac.uk

4.1.1   Introduction

The Cockcroft Institute is a newly created international centre for Accelerator Science and Technology in the UK. It is a joint venture between the Universities of Lancaster, Liverpool and Manchester, and the Science and Technology Facilities Council. The Cockcroft Institute has a large expertise base in Wakefields and Impedances which is linked through the Cockcroft Institute Wakefields Interest Group. Members of this group have experience in wakefields in linear colliders, ring colliders, light sources as well as generic fundamental research and focus on a wide range of specialist areas. In this article we summarize the work performed in this important field of research at the Cockcroft Institute.

4.1.2 Wakefields from Start to End in Linear Colliders

The Cockcroft institute has a large amount of expertise in wakefields and impedances and their effects in e+/e- linear colliders. Work has been performed on wakefields from start to end on the proposed ILC and CLIC colliders, including positron sources, damping rings, main linac and the collimators and crab cavities of the beam delivery system. In the following sub-sections we will look at the work performed in each of these key areas.

4.1.2.1   Wakefields in the ILC Positron Source Undulator Line

The ILC positron source relies on a long (~200 m) helical undulator producing ~MeV photons when the main electron beam, at 150 GeV, passes through it. To achieve the high on-axis magnetic fields the magnet has a cylindrical bore with a diameter of ~6 mm. The magnet is superconducting and operates at ~ 4 K [1]. The undulator is built in ~4 m long modules. In the current design, the undulator module has tapered transitions between the cold bore and room temperature connections. These are necessary to accommodate the bellows and sliding joints needed to handle contractions during cool-down of the magnet. The undulator line consists of a FODO lattice with three undulator modules, ~4 m in length, between quadrupoles. In order to achieve the required vacuum their must be photon collimators [2]. These are placed in the gaps between undulator modules where there are no quads. They are axially symmetric, have a minimum (full) aperture of 4.4 mm and taper angle of 100 mrad.

The effects of resistive wall and geometric wakefields of the undulator beam-tube, cold to warm transitions and the photon collimators on the beam have been assessed for the undulator line [3,4,5,6]. As the main electron beam passes through the undulator line before reaching the interaction point it is important to ensure that any disruptions are acceptable.

For the resistive wall wakefields, DC, AC, and ASE conductivity models of different materials were considered for Gaussian and non-Gaussian charge distributions. The studies indicated that a stainless steel tube should not be used, unless it was coated with a suitable material. Aluminium, gold or copper would all be suitable. It was found that the total energy lost and increase in energy spread of the beam for a copper tube at 77 K was ~ 0.15 MeV m^{-1} and 10^{-5} m^{-1}, respectively. For this tube a transverse momentum kick of ~0.26 eV μm^{-1} m^{-1} was calculated and the increase in emittance associated with such a kick is negligible. Further studies by the ILC-Low Emittance Transport working group have confirmed the emittance increase is currently acceptable [7]. The heating of the undulator due to image currents is expected to be 0.081 W m^{-1}, in the worst case.

The effects of the surface roughness on the energy spread indicated that an extremely smooth vessel, with surface roughness features <300 nm should be used to keep the induced energy spread below 10% of the nominal ILC value. A smooth copper vessel, with surface roughness ~100 nm and the required dimensions is available from industry today [8].

The geometric wakefields of the undulator transitions and photon collimators were assessed using ECHO2-D [9] and analytic formula [10]. For the cylindrically symmetric tapered elements a good agreement between the two methods was found. ECHO was used to assess the wakefields of the bellows. The emittance increase due to misalignments of these elements was calculated. The misalignment of each element was

randomly chosen from a Gaussian distribution for different rms values, truncated at ±300 μm (to reflect accurate surveying of the components). For an rms value of 300 μm the average vertical emittance increase of 1 000 different undulator lines was 2.7%.

All calculations, so far performed, on the wakefield affects on the electron beam of the ILC positron source undulator system have been demonstrated to be acceptable. It is planned that further work will continue to update the calculations with better conductivity models of 4 K vessels, and account for the latest ILC beam parameters and component designs. There is also plenty of opportunity to optimise the design. For example, the taper angles, number of photon collimators and their aperture all have potential to be changed if further studies indicate a need.

4.1.2.2   *Effect of Beta Function Variation on Multi-Bunch Instability in Damping Rings*

Instability of bunches that are coupled by resistive wall wake fields in a storage ring is a well-known phenomenon.   The instability is generally understood in terms of a model that has been widely used for many years [11].   In order to obtain a solution analytically, this model has to assume that the beta function is a constant around the ring.   The resulting solution of the equations of motion gives the growth rates of the bunch amplitudes. During the design of a storage ring, this information can be used to specify the feedback system needed to control the growth.

In linear collider damping rings [1], the large number of bunches and narrow beam pipe (for example, in the damping wiggler) lead to coupled-bunch growth rates that approach the limits of modern feedback systems. A highly accurate estimate of the growth rates is needed to provide sufficient confidence in the specifications for the feedback system, and this motivates a re-examination of some of the underlying assumptions in the conventional model. Assumptions that may need to be addressed include: use of constant beta function; uniformity of the fill pattern; uniformity of the beam pipe; and linearity of the dynamics.
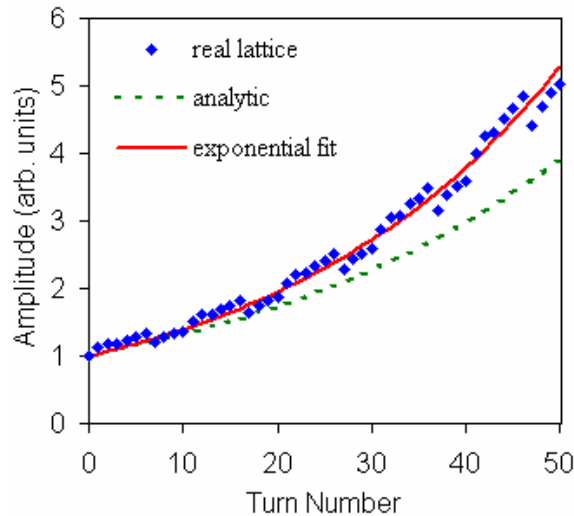

Figure 1: Time domain simulation in a design for the ILC damping ring, for bunches arranged in the mode with maximum growth rate. The blue points show the amplitude of one of the bunches.

Here, we consider the impact of variation of the beta function on coupled-bunch growth rates in the damping rings of the International Linear Collider. As it is no longer possible to find an analytic solution to the equations of motion when variations in the beta function are included in the model, time domain simulations have to be performed to find the transverse motion of the bunches. Figure 1 shows how the amplitude of one of the bunches stored in the ring grows with the number of turns around the ring. Details of the method used are given in [12]. With beta function assumed constant, the growth time is calculated to be around 37 turns; the time-domain simulations, using the real beta function in the lattice, predict a growth time of 30 turns. Given that a state-of-the-art feedback system would be able to provide a damping time of around 20 turns, the more accurate model (using the real beta function) indicates a much narrower margin; however, it should still be possible to control the instability using a feedback system.

Further topics likely to be important for the study of long range wake fields in linear collider damping rings include: the effects of thin coatings (that may be used to improve vacuum and suppress electron cloud); and the effects of uneven fill patterns. Related to uneven fill patterns are effects associated with transients that may arise during the extraction and injection process. For example, typically undamped bunches would be injected into the damping rings before all the damped bunches are extracted. Long-range wake fields may couple jitter on the injected bunches to the damped bunches, leading to unpredictable bunch-to-bunch jitter on the extracted beam. Given the sensitivity of a linear collider to beam stability, a thorough and detailed understanding of such effects is necessary, in order to optimise the design.

4.1.2.3   *Wakefields in the ILC and X-FEL Main Linacs*

The modes excited by the accelerated beam in the main linacs of the XFEL facility in DESY and the proposed ILC [1] will give rise to wake-fields which disturb the progress of the bunches and in the worst case scenario can give cause a BBU (Beam Break Up) instability. We are studying these wake-fields with a view to characterising their influence on beam dynamics with realistic fabrication errors included. In order to facilitate an understanding of modes trapped in accelerating cavities within multiple modules in particular, we have applied a global scattering matrix technique [13] which enables the modes of the structure to be rapidly determined. This methodology is being applied to both understand the electromagnetic field in the modules at FLASH and those in the ILC. Indeed, as part of a collaboration between four laboratories (SLAC, DESY, FNAL, and Cockcroft) and two Universities (Manchester and Rostock) we are also actively involved in an experimental accelerator beam studies program at FLASH with a view to developing beam position monitors from the signal generated from the higher order dipole modes (HOM) radiated to the HOM couplers. To date the HOM beam position monitors developed for this purpose have indicated a beam alignment of better than 5μm [14]. Further studies are ongoing developing methods to characterise the cavity and sub-cavity misalignment from similar measurements of the dipole radiation. In addition to the work on the TESLA-style cavities, we are also engaged in studying the mode properties of the new high gradient designs proposed by KEK in the form of a low loss Ichiro cavity and by Cornell University as a re-entrant shape. The modes in these cavities have been analysed for up to 6 bands using several computer codes in which we take advantage of parallel processing and their impact on the beam dynamics has been ascertained by tracking the beam through the complete linac [15,

16]. Detailed simulations have been conducted on the damping requirement of the HOM couplers and modes with particularly damaging transverse kick factors have been found.

We note that this research has resulted in two students graduating at the University of Manchester with MSc theses in the area of HOM wake-fields in both the main linacs [17] and crab cavities [18] of the ILC.

4.1.2.4 *Collimator Wakefields*

The collimator wakefield work at the Cockcroft Institute is centred on advancing the state of the art in design procedures through comparison of 3D EM simulations, experimental measurements produced in collaboration with partners in the UK and at SLAC, and analytical theory, and to enable higher order modes to be incorporated into tracking codes such as MERLIN and PLACET.

The collimator apertures in the ILC beam delivery system are required to be small, with the betatron spoiler apertures expected to be of the order of 1 mm [1]. This tight collimation of the beam halo allows synchrotron radiation emitted in the strongly focussing final quadrupoles to pass cleanly through the interaction region, thus minimising the detector background. This constraint combined with the low emittance of the ILC beam means that the physical aperture of the collimators is very narrow, giving rise to large wakefield effects. These may perturb the beam, distort the bunch shape, increase the emittance and thus decrease the luminosity. It is important to study such effects to ascertain whether they pose a problem.

Collimator wakefields differ from cavity wakefields as a collimator is not naturally resonant, and the expansion of wakefields in frequency space is therefore less simple. This lack of high Q resonances also means that wakes will not persist and we can concentrate on the study of short range intra-bunch wake effects rather than the long range inter-bunch ones. Also we study only transverse wakes, ignoring any potentially disruptive effects of longitudinal wakes on the particle energies.

The kick factor κ is generally defined [11] by the relation between the displacement and deflection

$$\Delta y' = \frac{N r_e \kappa \Delta y}{\gamma} \tag{1}$$

This is a simplification in two respects: firstly it assumes that the wakefield is a dipole, and that higher terms can be ignored, secondly it refers to the displacement and deflection of the bunch as a whole and does not describe the different fields experienced by different particles.

Initially MAFIA was used, and through comparison we were able to prove the validity of fields calculated with GdfidL [19]. This provides a platform on which we are able to run simulations on a much larger scale, principally due to features such as a moving mesh solver and parallel architecture [20]. Our principal concern was the transverse geometric kick, and prototype collimators were simulated that were tested on the 28.5 GeV beam at SLAC, results are in good agreement. [21]

In addition to the transverse geometric kick, we also developed prototypes to investigate resistive wall wake, and surface roughness.

The measurements for all of these have been compared with analytical estimates of their values.

The MERLIN C++ library provides a way of simulating effects on individual particles. In its standard form it only provides dipole transverse wakes, and it furthermore assumes that any transverse deflection is radial. We have adapted this to more general transverse fields and angular modes of arbitrary order [22]. We are still restricted to cases of axial symmetry, and represent a rectangular collimator by a circular one of diameter equal to the smaller rectangular dimension: this is inexact but enables us to consider order of magnitude effects.

In these simulations we use the formula for the geometric wake of a collimator tapering from radius a to radius b given in [23]

$$W_m(z) = 2\left(\frac{1}{a^{2m}} - \frac{1}{b^{2m}}\right)\exp\left(-\frac{mz}{a}\right)\Theta(z) \qquad (2)$$

But any other formula can readily be implemented in the code.

Simulation studies of a single collimator confirm that if the beam displacement is small compared to the gap size, the dipole mode is adequate. However larger offsets need more modes for a full description [24]. The bunch also shows considerable distortion: the head is unaffected, but the effect increases down the bunch length, and then lessens again in the far tail.

Studies were then performed on the ILC BDS [25], looking at the loss in luminosity as a function of the beam offset at the exit of the Linac.

Luminosity was taken from the emittance and bunch-bunch interactions were not considered. Effects are small for reasonable displacements, and the effect of higher order modes only becomes significant at unrealistically large displacements. Studies were performed for resistive wake effects and give reassuringly similar results. Further studies with different collimator shapes and materials are planned to confirm them. A similar study using the PLACET program [26] was conducted revealing qualitatively similar results. This does consider rectangular cavities and the beam-beam effect on luminosity, but does not include higher angular modes.

4.1.2.5   *Calculations of Impedances and Wakefields in Crab Cavities*

The current ILC [1] design requires a crab cavity [27] in order to rotate the beams prior to collision. It is necessary for these cavities to be close to the final focus in a region with a high beta function. Due to this, the crab cavity wakefields (particularly in the transverse plane) can have very large detrimental effects on machine luminosity. For dipole-mode cavities in general, the fundamental monopole mode is an unwanted mode and due to the relatively small beam pipe diameter, this mode becomes trapped in the cavity. This mode, referred to as the lower order mode (LOM) requires damping (QL typically $<10^4$ for ILC) to avoid excessive fields in the cavity and couplers.

The ILC crab cavity is a 9-cell superconducting RF (SRF) cavity with the fundamental dipole mode being resonant at 3.9 GHz [28]. The finite difference code MAFIA was used to calculate all the dipole modes up to 18 GHz and monopole higher order modes (HOM) up to 16 GHz. The results of these simulations have been used to specify the required damping in order to stop collective effects deflecting the beam by more than σ/4 at the IP [29]. The MAFIA simulations have also been used in conjunction with a diffractive technique to calculate the single bunch wakefields. These calculations were verified by simulating the cavity using the code ECHO2D, and are shown in Figure 2.
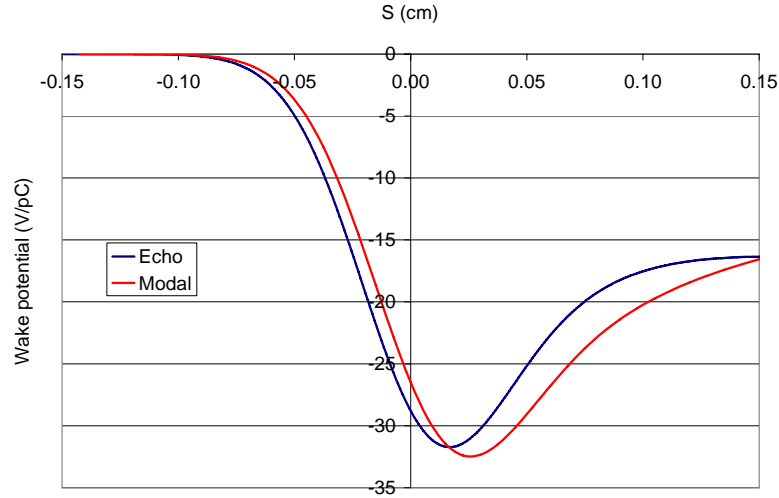
Figure 2: Longitudinal short range wakefields, comparing ECHO 2D and modal/diffractive calculation.

Having calculated the higher and lower modes of the cavity and the delta wake at short range, the effect of the wakefields were calculated in the particle tracking code PLACET as well as using analytical techniques. The output from PLACET was also used with GUINEA-PIG to calculate the loss in luminosity due to the wakefields.

After verifying the design in simulations, a prototype of the crab cavity with its couplers was constructed out of aluminium and copper. This prototype has been used to verify the simulation results by measuring the loss factors, kick factors and external Q factors of the dominant cavity modes. The field structure of the first monopole and dipole passbands were studied using bead-pull techniques, utilising metal beads, dielectric beads and metal needles. The dipole modes up to 13 GHz were studied using a frequency domain reflectrometry technique [30], shown in Figure 3, where a wire is stretched along the beam pipe and the wire transmission is measured as a function of frequency. This method provides a measurement of the transverse impedance and hence the kick factor and resonant frequency of the modes can be evaluated. Finally the external Q factors of the most dominant modes were measured using a series of reflection and transmission measurements at the couplers.
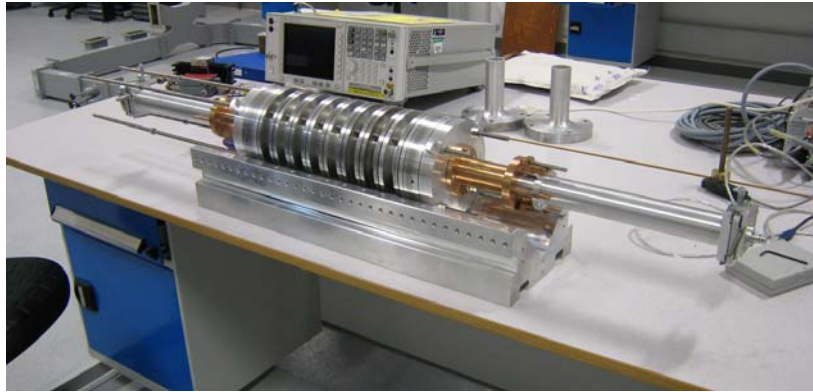
Figure 3: Wire test experimental set-up

The Cockcroft Institute has now commenced a program of research looking into the design of a crab cavity system for CLIC, and also on the development of a crab cavity system as an upgrade option for LHC in collaboration with CERN and US-LARP.

4.1.3 The Mathematical Physics Group

The Mathematical Physics Group at Lancaster University is applying methods of differential geometry and the electrodynamics of continuous media to fundamental problems in laser-plasma interactions and electron beam dynamics in the vacuum. The research is motivated by contemporary challenges that arise in the control of beam stability in the presence of coherent electromagnetic radiation in intense light-sources and future laser wake-field accelerators.

A principle aim of their work is to explore the motion of large collections of rapidly accelerating charged particles in small bunches moving at ultra-relativistic energies in the laboratory (see, for example, [31] on the behaviour of relativistic spinning particles in electromagnetic fields). They have developed a covariant perturbation theory [32] that offers a new mathematical approach in regimes where a charged fluid description provides insights to collective effects analogous to turbulent mixing in fluid dynamics [33]. This work is being developed in a number of directions including the influence on the bunches of boundary effects of various kinds, the influence of radiation reaction and the inclusion of statistical fluctuations via a new formulation of the relativistic Maxwell-Vlasov equation.

Wake-fields arise in many of their studies. Particular programs include radiation properties in straight guides with slowly varying cross-sections and guides with fixed cross sections but slowly varying curvature.

4.1.4 Large Hadron Collider

We maintain a significant involvement with activities at CERN in research on the RF properties of various components of the LHC and in participating in beam commissioning. In particular, we have conducted research in areas related to impedance measurement and calculation.

In the first area, the FP420 collaboration is assessing the feasibility of detecting protons outgoing from the LHC beams collision, that have lost less than 2% of their longitudinal momentum [34]. We launched a campaign of studies to verify the different

aspects of the FP420 impedance. Analytical calculations and numerical simulations assess the longitudinal and transverse impedance values. Laboratory measurements on the available FP420 station prototypes have been used to benchmark the simulations. The relevant upper frequency limit is assessed by the nominal LHC rms beam bunch length, $\sigma_z = 0.25$ ns. This permits us to limit our study up to a frequency of 3 GHz. The majority of the studies are based on the stretched wire method for evaluating the longitudinal coupling impedance through the measurement of the scattering parameters of the device under test [35]. The laboratory setup at the Cockcroft Institute comprises a sophisticated mechanical system equipped with micrometers, to stretch, move and monitor the relative position of the wire. The impact of the impedance on the overall impedance budget of the LHC has been verified to be acceptably small.

The second area of research is on the LHC ATLAS, Roman Pot-like detectors [36]. The impact of the insertion of these detectors on the LHC beam coupling impedance is under investigation. In the laboratory, the stretched wire method has been applied to an ATLAS Roman Pot prototype while setting the pots at different locations from the nominal operation positions. A second set of measurements has been taken after mounting on the pots walls ferrite tiles with the aim of absorbing the electromagnetic power at the observed resonances. Results are shown in Fig. 4 in terms real part of the longitudinal impedance with and without damping. This research is ongoing with an aim to add further ferrite dampers in the roman pots to minimize the impact on the beam dynamics.
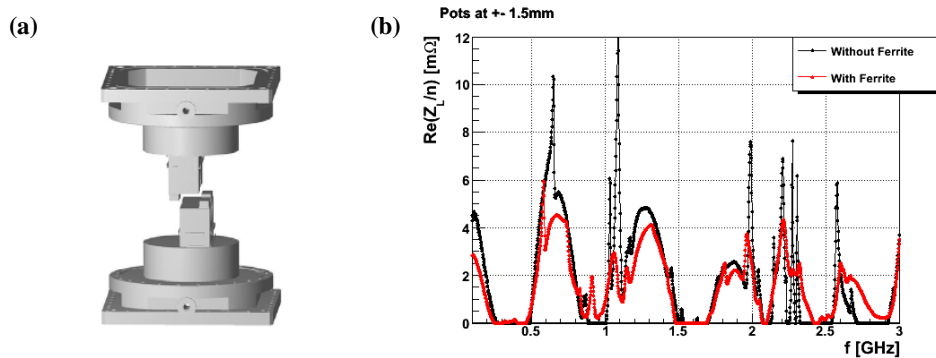
Figure 4: (a) Roman pot detector and (b) the real part of longitudinal impedance of as measured before and after inserting absorbing ferrite tiles into the pot.

Finally, the third area of research is concerned with verifying the prediction of the resistive wall transverse beam impedance down to frequencies around the first unstable betatron line (8 kHz) of the LHC. The Cockcroft Institute are participating in a series of laboratory measurements at CERN with the aim of benchmarking analytical predictions and numerical simulations of the resistive wall transverse impedance. At such low frequencies, in the presence of resistive materials with thickness larger than the distance between the beam and the material itself, and below a critical frequency that is related also to the material skin depth, recent theories [37,38] diverge from classical models. The aim of the experiment at CERN is to validate the predicted divergence with a method based on the measurement of the variation of a probe coil inductance [39] in the presence of three set-ups: sample graphite plates, stand-alone LHC collimator jaws and a full LHC collimator assembly. Preliminary results validate the theory in all the

relevant frequency range and will be presented at the forthcoming EPAC08 conference [40].

4.1.5 Light Sources

Light sources driven by electron accelerators utilise either undulators or wigglers, and there is usually a demand to minimise the magnet (and therefore vacuum) gap in these devices both to maximise the magnetic field that is technologically available, and thereby to minimise the electron beam energy required for a particular wavelength output. This is particularly true for linacs driving free-electron lasers (FELs), where a reduction in magnet gap from, say, 10 mm to 5 mm can save up to 30% of the linac [41]. Whether this is practicable or not is often down to the resistive-wall wakes that drive energy spread growth in the short bunches and heating of the enclosing vacuum vessel, problems that are exacerbated if those bunches are very short (e.g. sub-picosecond), as is demanded for FEL and short-pulse photon output. The EuroFEL collaboration for future light sources [42] has been examining wakefield limitations for such sources, in which the Cockcroft Institute has been involved.

Some wiggler sources desire very high fields that are more conveniently created using superconducting magnets, and a cold beam vessel allows the magnet gap to be minimised. The anomalous skin effect (ASE) however changes the conductivity at these low temperatures [43], and the image current heating of these cold vessels can be markedly larger; in high-repetition-rate systems such as an energy recovery linac this heating can dominate the total heat load and make cooling difficult, so it is important to estimate the effect of the ASE to determine the choice of vacuum vessel material and cooling. For example, the 4GLS proposal [44] has a target of 1.3 GHz, 77 pC bunches in the ERL section with a length down to 100 fs. Figure 5 shows the relative heat loads of the ERL compared to the lower repetition rate XUV line, calculated using an image-current heating approach; the resistive wakefield loss approach gives comparable results [45].
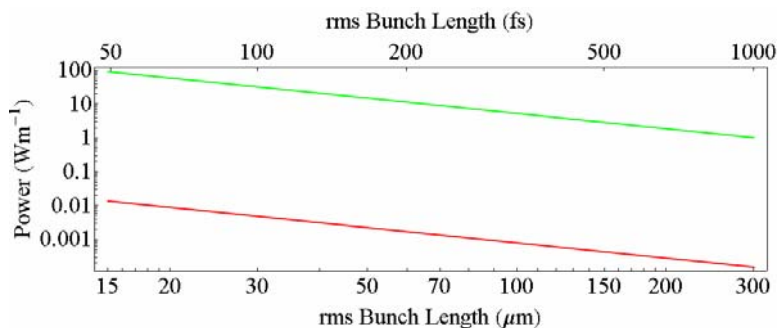
Figure 5: Power deposited per meter in a 7 mm copper vessel with an RRR of 60 operating in a 3.5T magnetic field and at 4K for the 4GLS ERL (green – 1.3 GHz, 77 pC, 100 fs) and 4GLS XUV-FEL line (red – 1 kHz, 1 nC, 250 fs).

As well as vessel heating, the energy spread growth from the c.200m 4GLS ERL transport system – which is driven mainly by the undulator vessels and the collimation system - must be limited by trading the vacuum aperture and conductivity against the local bunch length; the energy spread growth must be constrained within 0.1% to limit the spontaneous undulator output linewidth and to allow efficient driving of the included VUV-FEL [44]. This has led to the use of a progressive compression scheme

[46] which gradually reduces the bunch length through the five undulator straights. Collimators are needed in the design to localise parasitic losses from beam halo, which could be considerable (c. 600 W) from the overall 4GLS average beam power of 60 MW. Wakefield estimates have been made in collaboration with TEMF Darmstadt using ECHO3D to help determine the minimum possible aperture of these collimators, and to determine how long the taper sections should be – 200 mm each end of a Cu collimator with overall length 600 mm.

Beam Break-Up is a particular issue for ERLs whereby the higher-order modes of the accelerating cavities can drive a feedback-based instability of the recirculating beam.

4GLS have produced an optimised HOM-damped 7-cell cavity design [47] and explored the role of cavity deformations and beam optics in optimising the beam break-up threshold - the latter studied with Arc-en-Ciel, where both optics utilise graded-gradient focusing through the linac [48].

The wakefield work undertaken within the Cockcroft Institute has contributed to an understanding of the appropriate design choices for future light sources, and the expertise that has been developed with the Institute will be useful for many future light source projects.

4.1.6   References

1. International Linear Collider Reference Design Report, (2007).
2. O. B. Malyshev, D. J. Scott *et al,* J. Vac. Sci. Technology A, **25,** 4**,** pp 791-801, (2007).
3. D. J. Scott, EUROTeV-Report-2006-084, (2006)
4. D. J. Scott, EUROTeV-Report-2006-085, (2006)
5. D. J. Scott and J. Jones, EUROTeV-Report-2007-007, (2007)
6. D. J. Scott , EUROTeV-Report-2007-015, (2007)
7. D. Shulte and K.Kubo, 'Workshop on Low Emittance Transport for the ILC,' Daresbury Laboratory, (2007)
8. Swagelok Ltd, 29500 Solon Road, Solon, OH 44139,USA, http://www.swagelok.com
9. I. Zagorodnov and T. Weiland, Phys. Rev. ST Accel. Beams, **8**, 4, 042001, (2005).
10. P. Tenenbaum, K.L.F. Bane *et al*, Phys. Rev. ST Accel. Beams, **10,** 3, 034401, (2007)
11. A.W. Chao, *Physics of Collective Beam Instabilities* (John Wiley & Sons, New York, 1993), pp. 38–117 and 203–211.
12. K. M. Hock and A. Wolski, Phys. Rev. ST Accel. Beams **10**, 084401 (2007).
13. I. Shinton and R.M. Jones, Scattering matrix calculation of higher order modes and sensitivity to cavity fabrication errors for the ilc superconducting cavities, Proceedings of SRF07 (2007).
14. S.Molloy et al, High precision superconducting cavity diagnostics with higher order mode measurements, Physical Review Special Topics - Accelerators and Beams 9, 112802, (2006).
15. C.J. Glasman, R.M. Jones, I. Shinton, G. Burt, Simulations of Transverse higher order deflecting modes in the main linacs of ILC, Proceedings of SRF07 (2007).
16. R.M. Jones and C.J. Glasman, Simulation of HOM wakefields in the main linacs of the ILC, Proceedings of PAC07 (2007).
17. C. Glasman, Higher order mode wake-fields in the main linacs of the international linear collider, MSc thesis, University of Manchester, 2006.
18. N. Chanlek, Theoretical and experimental study of higher order modes in deflecting mode crab cavities, MSc thesis, University of Manchester, 2007.
19. C.D Beard and J.D.A.Smith, MOPLS070, Proc EPAC2006, Edinburgh 2006
20. J.D.A. Smith, TUPMS092, Proc PAC2007, Albuquerque, 2007

21. S. Molloy et al., FRPMS074, Proc PAC2007, Albuquerque, 2007
22. A. Bungau and R. Barlow, Implemenmting wake fields in Tracking Codes, WEPCH123, Proc EPAC2006, Edinburgh, 2006
23. P. Raimondi et al. "Closed Form Expression for the Geometric Effect of a Beam Scraper on the Transverse Beam Distribution, SLAC-PUB-8552 (2000)
24. A. Bungau and R. Barlow, Emittance Growth Due to High Order Angular Multipole Mode Wakefields in the ILC-BDS Collimators, THPAN079, Proc PAC2007, Albuquerque, 2007
25. R. Barlow, A. Bungau, J.D.A. Smith et al, Wakefield Models for Particle Tracking Codes, THPAN068, Proc PAC2007, Albuquerque, 2007
26. R. Barlow and A. Bungau, Collimator Wakefields: Formulae and Simulation, THPAN081, Proc PAC2007, Albuquerque, 2007
27. R. B. Palmer, Energy scaling, crab crossing and the pair problem, SLAC-PUB-4707, 1988
28. C. Adolphsen, et al, Design of the ILC Crab Cavity System, EuroTeV Report_2007_010
29. G. Burt, R. M. Jones, A. C. Dexter, Analysis of Damping Requirements for Dipole Wake-Fields in RF Crab Cavities, IEEE Trans. Nuc. Sci. 54 (5) 2007
30. P. Goudket, Impedance Measurements on a Test Bench Model of the ILC Crab Cavity, WEPMN 077, PAC 2007
31. D.A. Burton, R.W. Tucker, Cockcroft-05-05
32. D.A. Burton, J. Gratus, R.W. Tucker, Ann. Phys. 322 (3), 599, 2007
33. D.A. Burton, J. Gratus, R.W. Tucker, JPhysA, 40 (4), 811, 2007
34. FP-420, M. Albrow et al., CERN-LHCC-2005-025, LHCC-I-015.
35. F. Roncarolo, R.M. Jones, R. Appleby, Beam coupling impedance simulations and laboratory measurements for the LHC FP420 detector, Proceedings of Particle Accelerator Conference (PAC 07), Albuquerque, New Mexico, 25-29 Jun 2007, pp 4294.
36. ATLAS collaboration, ATLAS forward detectors for luminosity measurement and monitoring, CERN-LHCC/2004-010, LHCC I-014 (2004).
37. A. Burov and V. Lebedev, Transverse resistive wall impedance for multi-layer round chambers, Proceedings of EPAC02 (2002).
38. E. Métral et al., "Resistive-wall impedance on an infinitely long multi-layer cylindrical beam pipe," LHC Project Report 1014 , CERN (2007)
39. Bench Measurements of Low Frequency Transverse Impedance, F. Caspers,U. Iriso-Ariz, and A. Mostacci, CERN-AB-2003-051-RF.
40. F. Roncarolo et al, Comparison between laboratory measurements simulations and analytical predictions of the resistive wall transverse beam impedance, to be presented at EPAC08.
41. SCSS Design Report, available from http://www-xfel.spring8.or.jp/
42. EuroFEL collaboration, www.eurofel.org.
43. W.Chou and F. Ruggiero, "Anomalous Skin Effect and Resistive Wall Heating," LHC Project Note 2 (SL/AP), 1995.
44. H.Owen, "The 4th Generation Light Source at Daresbury", Proceedings of LINAC 2006, (Knoxville, TN). www.jacow.org.
45. D. Scott, "Image Current Heating of the 4GLS Narrow Gap Vessels and Collimators", EuroFEL report 2007-DS2-084.
46. P.H. Williams et al., "Electron Beam Dynamics in 4GLS", Proceedings of PAC 2007 (Albuquerque, NM), www.jacow.org.
47. E. Wooldridge, 'Alternate Cavity Designs to Reduce BBU', Proceedings of EPAC 2006, www.jacow.org.
48. E. Wooldridge and B. Muratori, 'Linac Focusing and Beam Break Up for 4GLS', Proceedings of EPAC 2006, www.jacow.org.

4.2   Computation of Short Range Wake Fields with PBCI

Erion Gjonaj, Thomas Lau, Thomas Weiland
TUD, TEMF, Schlossgartenstr. 8, 64283 Darmstadt, Germany
Rainer Wanzenberg
Deutsches Elektronen-Synchrotron, A Research Centre of Helmholtz Association
Notkestr. 85, 22603 Hamburg, Germany
Mail to: gjonaj@temf.de

4.2.1   Introduction

4.2.1.1   Wake Fields and Wake Field Instabilities

An ultra-relativistic electron beam passing through an accelerator cavity generates electromagnetic wake fields. Wake fields act back on the beam and, thus, influence its dynamics. The beam-cavity interaction via wake fields may lead to degradation of beam quality (emittance growth, energy spread) or even to collective instabilities [1-3]. Such instabilities pose the main limitation on the maximum achievable current per bunch or on the total beam current or on both of them.

The integral quantity which describes the total wake field force on an electron bunch traveling in the *z*-direction is the wake potential,

$$\vec{W}(s) = \frac{1}{Q} \int\limits_{-\infty}^{+\infty} dz'(\vec{E} + c\,\vec{e}_z \times \vec{B})_{t=(z'+s)/c} \ , \tag{1}$$

where Q is the bunch charge, $\vec{E}$ and $\vec{B}$ are the electromagnetic fields evaluated at the retarded time with respect to the relative position *s* within the bunch [4]. The effect of wake fields on the beam dynamics can be roughly estimated from the analysis of the wake potential (1). Electromagnetic fields associated with short electron bunches are high frequency fields. They propagate within the cavity with nearly the speed of light in vacuum, almost synchronously with the bunch. The corresponding wake potential (1) is a short range function which is restricted to small values of *s*. Thus, the wake field of a short electron bunch represents, in the first place, a source for single-bunch instabilities. Contrary, the low frequency wake fields generated by long bunches tend to dwell in the cavity for a very long time. Such wakes are often referred to as captured modes. They are responsible for multi-bunch instabilities which arise from the interaction between consecutive bunches passing through the cavity.

Apart from the wake potential (1), other quantities of interest are the loss parameter, $k_{\parallel}$, and the kick parameter, $k_{\perp}$. These are defined as:

$$k_{\parallel} = \int\limits_{-\infty}^{+\infty} ds\, \rho(s) \cdot W_{\parallel}(s) \ , \qquad k_{\perp} = \int\limits_{-\infty}^{+\infty} ds\, \rho(s) \cdot W_{\perp}(s) \quad , \tag{2}$$

where $W_{\parallel}$ and $W_{\perp}$ are the longitudinal and transversal components of the wake potential (1), respectively, and ρ is the normalized bunch charge density. The loss parameter can be considered as a measure for the energy spread experienced by the bunch due to wake

field interaction. The kick factor is useful for the estimation of emittance growth within the cavity. Another parameter related to the beam-wake interaction is,

$$k_\parallel(1) = \int_{-\infty}^{+\infty} ds \; \rho(s) \cdot \frac{d}{ds} W_\parallel(s) \, . \tag{3}$$

This parameter is often used in the calculation of the synchrotron tune shift for the longitudinally coupled mode instabilities in storage rings such as PETRA III [5, 6].

The present paper is concerned with the numerical calculation of the wake field related quantities (1)-(3) in the context of the X-FEL and the ILC projects. These projects require high luminosity beams with ultra-short electron bunches. The rms bunch length for the ILC is 150μm [7]; for the X-FEL as low as 25μm [8]. The main focus is, therefore, on the computation of short range wake fields. From the numerical point of view, wake field simulations are very challenging. This is mainly related to the large computational resources which are needed for an appropriate discretization of the extremely high-frequency fields (in the X-FEL case, with frequencies of up to 5THz [8]). Furthermore, fully 3D simulations are required in order to account for the often complex geometries of the accelerator structures involved.

4.2.1.2   *Numerical Solutions in Wake Field Computation*

In the course of the past 20 years, several wake field simulation codes have been used with considerable success in accelerator design. Table 1 gives a brief overview on the available wake field codes and their properties. There exists an extensive literature on each of these codes. Of particular importance, however, are the numerical algorithms which have been developed in the context of wake field simulations.

The *moving window* technique for ultra-relativistic bunches (Bane et al [9]) and the *indirect path* wake potential integration (Weiland [10], Napoly et al [11]) represent two important milestones in this development. In the moving window technique, discretization is applied only on a comparatively small computational grid which encloses the ultra-relativistic bunch while moving along the accelerator with the speed of light in vacuum. This approach allows for a very efficient calculation of short range wake fields. The indirect path wake potential integration allows for the computation of wake field contributions in outgoing beam pipes using a semi-analytical approach. The indirect integration technique was originally introduced for rotationally symmetric structures. Recently, a number of generalizations of this approach for arbitrary 3D geometries have been proposed [12, 13].

In a pioneering work of Zagorodnov et al [14], a novel 3D discretization technique for Maxwell equations with *no longitudinal dispersion* was introduced. This property of the numerical scheme is prerequisite for a moving window implementation, since in this case, the numerical phase velocity of longitudinal waves must exactly match the speed of light in vacuum. An important extension of this work was the Uniformly Stable Conformal (USC) scheme [15] for the Finite Integration Technique (FIT). This scheme allows for the application of a *boundary conformal* approximation in a moving window implementation.

Code *parallelization* is another key issue in wake field simulation. The huge computational resources required by the simulation of short electron bunches in 3D geometry can only be handled in a parallel computing environment. Hereby, as the

bunch lengths become shorter, the accurate but computationally expensive conformal approximation of geometrical boundaries appears to be of less importance for the overall simulation quality. In many cases, the spatial resolution required by the short wave lengths involved in the simulations is by far sufficient for an appropriate geometry approximation even when a simple stair-step geometry representation is used.

Recent developments have seen the implementation of high order Finite Element Methods (FEM) in wake field computations [16, 17]. These methods allow for highly accurate electromagnetic field solutions. At the current stage, however, the use of unstructured or boundary fitted grids associated with the application of these methods requires a static computational window. This is an important limitation on efficiency, since the computational costs associated with the spatial discretization increase linearly with the length of the cavity to be simulated.

Table 1: Attempted listing of the available wake field codes.

Code	Dispersionless	Moving Window	Conformal	Parallel
TBCI / URMEL	–	+	–	–
NOVO	+	–	–	–
MAFIA	–	+	–	–
ABCI	–	+	–	–
GDFIDL	–	–	+	+
ECHO	+	+	+	–
TAU3P	–	–	+	+
CST Particle Studio	–	–	+	–
PBCI	+	+	–	+
NEKCEM	–	–	+	+

In the following, the Parallel Beam Cavity Interaction (PBCI) code is discussed. PBCI is designed for massively parallel wake field simulations in arbitrary 3D geometry. The algorithms use a dispersionless split-operator scheme as well as a domain decomposition approach for balanced parallel computations. A description of these algorithms is given in Section 1.1.2. The rest of the paper is dedicated to a number of wake field applications in the context of the X-FEL and ILC projects.

4.2.2 The PBCI Code

4.2.2.1 *Finite Integration Technique*

The discretization of electromagnetic fields in PBCI is based on the Finite Integration Technique (FIT) [18]. The semi discrete equations of FIT are

$$\frac{d}{dt}\begin{pmatrix} \widehat{\mathbf{e}} \\ \widehat{\mathbf{h}} \end{pmatrix} = \begin{pmatrix} \mathbf{0} & \mathbf{M}_\varepsilon^{-1}\mathbf{C}^T \\ -\mathbf{M}_\mu^{-1}\mathbf{C} & \mathbf{0} \end{pmatrix}\begin{pmatrix} \widehat{\mathbf{e}} \\ \widehat{\mathbf{h}} \end{pmatrix} - \begin{pmatrix} \mathbf{M}_\varepsilon^{-1}\widehat{\widehat{\mathbf{j}}} \\ \mathbf{0} \end{pmatrix}, \qquad (4)$$

where the unknowns, $\widehat{\mathbf{e}}$ and $\widehat{\mathbf{h}}$, are interpreted as electric and magnetic voltages along the edges of a dual-orthogonal pair of staggered grids and $\widehat{\widehat{\mathbf{j}}}$ is the excitation current.

The operator $\mathbf{C}$ denotes the topological curl: $\mathbf{M}_\varepsilon$ and $\mathbf{M}_\mu$ are the positive definite and diagonal material operators of FIT.

The integration of (4) in time is typically performed by applying an explicit time-marching scheme of the form

$$\begin{pmatrix} \widehat{\mathbf{e}} \\ \widehat{\mathbf{h}} \end{pmatrix}^{n+1} = \mathbf{G}(\Delta t) \begin{pmatrix} \widehat{\mathbf{e}} \\ \widehat{\mathbf{h}} \end{pmatrix}^{n} - \begin{pmatrix} \Delta t \mathbf{M}_\varepsilon^{-1} \widehat{\mathbf{j}} \\ \mathbf{0} \end{pmatrix}^{n}.$$ (5)

In (5), $\mathbf{G}(\Delta t)$ represents the specific evolution operator of the time integration scheme, and Δt is the integration time step. For the commonly used leapfrog integrator this operator is explicitly given by

$$\mathbf{G}(\Delta t) = \begin{pmatrix} \mathbf{1} & \Delta t \mathbf{M}_\varepsilon^{-1} \mathbf{C}^T \\ -\Delta t \mathbf{M}_\mu^{-1} \mathbf{C} & \mathbf{1} - \Delta t^2 \mathbf{M}_\mu^{-1} \mathbf{C} \mathbf{M}_\varepsilon^{-1} \mathbf{C}^T \end{pmatrix}.$$ (6)

The leapfrog-FIT scheme has been thoroughly investigated in terms of stability and dispersion properties. In particular, for Cartesian grids it can be shown that the dispersion error is largest for waves propagating in the direction of coordinate axes (see below). This property of the scheme is responsible for the large dispersion error (numerical noise) which is often observed in particle beam simulations. This is because the longitudinal waves associated with the bunch motion dominate the high-frequency electromagnetic field spectrum.

Yet another drawback of the leapfrog scheme is that no moving computational window can be used in wake field simulations with ultra-relativistic bunches. Since the longitudinal phase velocity of the numerical field solution does not exactly match the speed of light in vacuum, unphysical reflections are produced at the boundaries of the moving computational window. These errors increase systematically with simulation time, thus, deteriorating numerical accuracy.

4.2.2.2 *Dispersionless Split-Operator Scheme*

The idea of split-operator methods is based on the modification of the evolution operator $\mathbf{G}(\Delta t)$ such that no numerical dispersion occurs in the longitudinal, bunch propagation direction. The split-operator scheme used in PBCI was originally developed for the purpose of suppressing numerical noise in self-consistent Particle-In-Cell (PIC) simulations [19]. It is obtained by decomposing $\mathbf{G}(\Delta t)$ into longitudinal and transversal parts using the second order accurate, *Strang splitting* procedure [20]. The resulting Longitudinal-Transversal (LT) splitting scheme reads

$$\begin{pmatrix} \widehat{\mathbf{e}} \\ \widehat{\mathbf{h}} \end{pmatrix}^{n+1} = \mathbf{G}_t\left(\frac{\Delta t}{2}\right) \mathbf{G}_l(\Delta t) \, \mathbf{G}_t\left(\frac{\Delta t}{2}\right) \left[\begin{pmatrix} \widehat{\mathbf{e}} \\ \widehat{\mathbf{h}} \end{pmatrix}^{n} - \begin{pmatrix} \Delta t \mathbf{M}_\varepsilon^{-1} \widehat{\mathbf{j}} \\ \mathbf{0} \end{pmatrix} \right].$$ (7)

The propagators, $\mathbf{G}_l(\Delta t)$ and $\mathbf{G}_t(\Delta t)$, contain only spatial derivatives in the longitudinal and transversal directions, respectively. Thus, the two transversal updates

in (7) will not affect plane wave solutions propagating in the longitudinal direction, whereas the longitudinal update, $\mathbf{G}_l(\Delta t)$, represents the time evolution of a simple one dimensional system.

The LT scheme is completed by replacing each of the time evolution operators in (7) with second order accurate *Verlet-leapfrog* propagators. In matrix operator form they can be written as

$$\mathbf{G}_{l;t}\left(\Delta t\right)=\begin{pmatrix} \mathbf{1}-\dfrac{\Delta t^{2}}{2}\mathbf{M}_{\varepsilon}^{-1}\mathbf{C}_{l;t}^{T}\mathbf{M}_{\mu}^{-1}\mathbf{C}_{l;t} & \Delta t\mathbf{M}_{\varepsilon}^{-1}\mathbf{C}_{l;t}^{T}-\dfrac{\Delta t^{3}}{4}\mathbf{M}_{\varepsilon}^{-1}\mathbf{C}_{l;t}^{T}\mathbf{M}_{\mu}^{-1}\mathbf{C}_{l;t}\mathbf{M}_{\varepsilon}^{-1}\mathbf{C}_{l;t}^{T} \\ -\Delta t\mathbf{M}_{\mu}^{-1}\mathbf{C}_{l;t} & \mathbf{1}-\dfrac{\Delta t^{2}}{2}\mathbf{M}_{\mu}^{-1}\mathbf{C}_{l;t}\mathbf{M}_{\varepsilon}^{-1}\mathbf{C}_{l;t}^{T} \end{pmatrix}. \quad (8)$$

Exact numerical dispersion relations for the LT scheme using von Neumann analysis have been derived in [19]. Here, we only show the behavior of the numerical phase velocity as compared to the standard leapfrog scheme. Figure 1 shows normalized numerical phase velocities in the *xz*-plane, which are computed from the dispersion relations as, $v=\omega/\left(ck\right)$, where ω and k are the numerical frequency and wave number, respectively, and c is the speed of light in vacuum. In each of the two graphs, two different grid resolutions have been used.
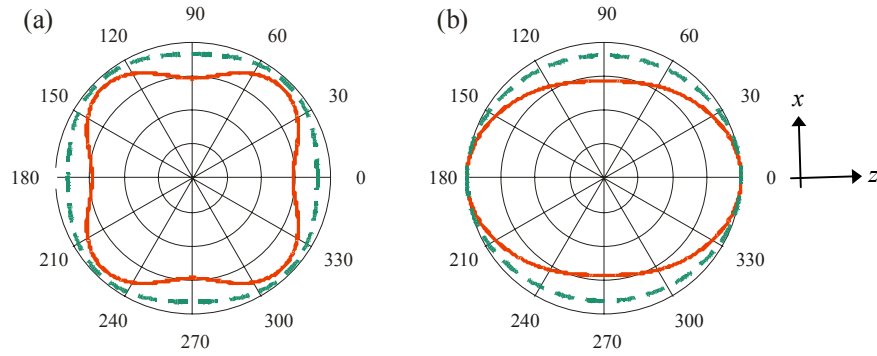
Figure 1: Normalized numerical phase velocities for the (a) leapfrog and (b) LT schemes in the *xz*-plane. The solid and dashed lines show the normalized phase velocities for a grid resolution of 5 and 10 grid points / wave length, respectively. In (b), the "magic time step" is used.

The dispersion error of the leapfrog scheme becomes largest in the directions of coordinate axes. Contrary, the LT scheme (Fig. 1b) minimizes the dispersion error in the longitudinal, *z*-direction. Thus, the effect of operator splitting consists in rotating the optimum dispersion direction in the longitudinal direction. In particular, at the so called "magic time step", $\Delta t=\Delta z/c$, the LT scheme has no numerical dispersion along this direction (see Fig. 1b). The exact propagation of longitudinal waves allows for a moving window implementation. Additionally, the integration scheme (4) is purely explicit in time which makes the time stepping algorithm easily parallelizable.

4.2.2.3   *Termination Conditions for Long Beam Pipes*

Wake fields generated by a geometrical discontinuity on the accelerator walls may *catch-up* the bunch at a very large distance (time) behind the discontinuity. For any

fixed traveling distance, z, within the structure, a longitudinal wake potential can be defined as

$$W_z(s,z) = \frac{1}{Q} \int\limits_{-\infty}^{z} dz' E_z\left(x,y,z',t=\frac{z'+s}{c}\right).$$ (9)

The total longitudinal wake potential is, then, $W_z(s,\infty)$. The numerical integration of $W_z(s,\infty)$ in the time domain, however, is often impossible. The distance where the bunch is caught by the wake fields is inversely proportional to the bunch length. Thus, in particular, for short electron bunches, the integration time becomes prohibitively large for a full time domain simulation.

The simple approach used in PBCI for overcoming this difficulty is schematically shown in Fig. 2. The total wake potential is separated into a "direct part", $W_z(s,0)$, containing the incoming beam pipe and the discontinuity, and a "transient part" which accounts for the wake field force in the outgoing pipe. The direct wake potential is integrated according to (9) using the time domain simulation data. For the computation of the transient wake potential a modal expansion of the electromagnetic field solution in a transversal plane within the outgoing pipe is performed. Assuming the location of the plane at $z = 0$, the general form of such an expansion is

$$E_z(x,y,0,t) = \int\limits_{-\infty}^{\infty} d\omega \sum_n c_n(\omega) e_z^n(x,y) \exp(i\omega t)$$ (10)

where $e_z^n(x,y)$, is the n-th (TM) eigenmode solution in the pipe and $c_n(\omega)$ is the frequency domain spectral coefficient of the mode extracted by Fourier analysis. Using (10) and the vanishing of wake fields at infinity, the wake potential contribution of a single wave guide mode within the pipe,

$$W_n(s) = \int\limits_{0}^{\infty} dz' \int\limits_{-\infty}^{\infty} d\omega c_n(\omega) \exp\left[ik_n(\omega)z' - i\omega\frac{z'+s}{c}\right],$$ (11)

is readily found to

$$W_n(s) = \int\limits_{-\infty}^{\infty} d\omega \frac{c_n(\omega)}{i[\omega/c - k_n(\omega)]} \exp\left(-i\omega\frac{s}{c}\right),$$ (12)

where $k_n(\omega)$ is the wave number of the mode. The total longitudinal wake potential is, then, given by

$$W_z(s,\infty) = W_z(s,0) + \frac{1}{Q} \sum_n e_z^n(x,y) W_n(s).$$ (13)

From the point of view of numerical implementation, the above procedure includes the solution of a 2D eigenmode problem in the outgoing pipe, the Fourier analysis of the modal coefficients and the inverse Fourier transforms (12). Hereby, the number of wave guide modes considered in the analysis may be critical to the validity of numerical

results. However, since only a 2D eigenmode problem needs to be solved, the calculation of a large number (several hundred) of modes can be typically performed with a comparably small computational effort.
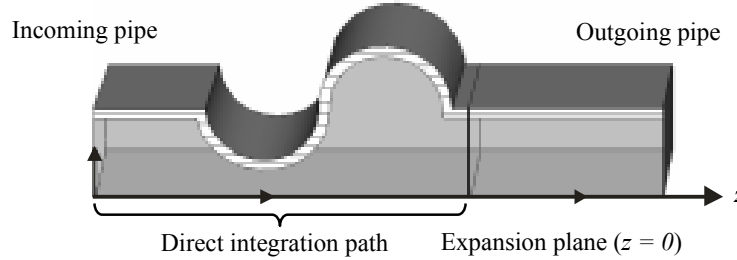
Figure 2: Separation of the wake potential computation into a direct part and a transient part in the outgoing beam pipe.

Apart from the explicit frequency domain representation of the modal coefficients, the procedure used in PBCI is equivalent to the approach proposed in [13, 21]. In [13], the inverse Fourier transform (12) is avoided by introducing centered differences in time and space for the time dependent modal coefficients. Maintaining the explicit frequency domain representation, however, is of advantage for purposes other than the calculation of wake potentials. In particular, this representation allows for the reconstruction of the full time domain simulation data at any downstream position in the outgoing pipe.
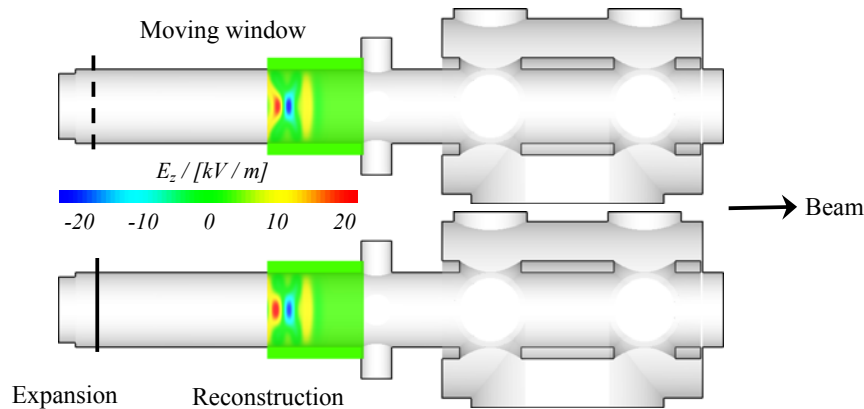
Figure 3: Time domain simulation (top) vs. frequency domain reconstruction within the moving window (bottom) in the separating pipe of PITZ. For illustration, only 15 waveguide modes were used in the reconstruction.

Such a situation is illustrated in Fig. 3. Exemplarily, the PITZ diagnostics section [22] (see also Section 4.2.3.2) is considered. About one third of the structure consists of a homogeneous pipe separating a small step at the entrance from the rest of the structure. The modal expansion is performed shortly behind the step. Using the frequency domain representation, the full electromagnetic field solution is reconstructed within the moving window at the end of the pipe. There, the time domain wake field simulation for the rest of the structure is resumed. This procedure results in considerable

computational savings when the cavity consists of a number of inhomogeneous sections separated by long beam pipes.

4.2.2.4   Code Parallelization

In 3D simulations involving short electron bunches, huge computational resources in terms of both memory and CPU time are needed. Such simulations can only be handled in a parallel computing environment (cluster). The parallelization model used in PBCI is based on a geometrical decomposition of the computational domain (partitioning) between the single processes in the cluster. Each processing node is responsible for performing computational tasks on the field data contained within the respective subdomain.

In Fig. 4, the partitioning approach is shown schematically for a three-node cluster. Starting with the global computational domain, an orthogonal bisection procedure is recursively applied. The procedure results in a binary tree, whose internal nodes are intermediate subdomains whereas the leaf nodes correspond to active (computational) subdomains. Because of the local nature of the FIT operators, only field values residing on the subdomain boundaries need to be exchanged in the computation. For Cartesian grids, the orthogonal bisection approach minimizes the number of such boundary values and, thus, the communication overhead in the field update equations.
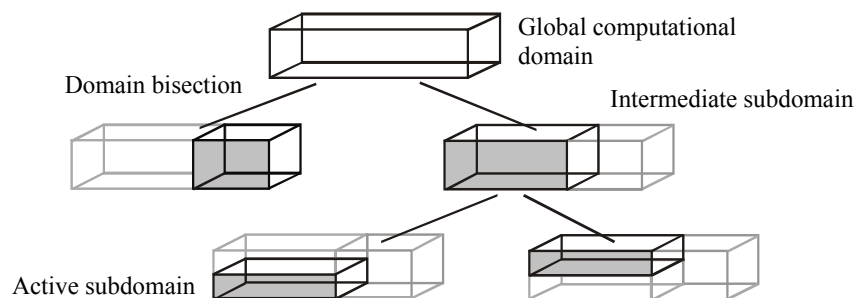
Figure 4: Example decomposition of the computational domain on a three-node cluster.

In order to determine the optimum partitioning which results in equally balanced workloads among the processing nodes, PBCI implements the load balancing scheme proposed in [23] for Particle-In-Cell simulations. The bisection procedure is performed on the basis of computational weights W_i which are assigned to each grid point. The total computational load associated with a given intermediate subdomain is, $W = \sum W_i$, where the summation includes only grid points within the subdomain. If the subdomain has to be partitioned between N processes, the bisection is such that

$$\frac{W_{\text{left}}}{W_{\text{right}}} = \frac{N_{\text{left}}}{N_{\text{right}}}, \quad \text{with} \quad N_{\text{left}} = \left\lceil \frac{N}{2} \right\rceil, \ N_{\text{right}} = \left\lfloor \frac{N}{2} \right\rfloor \tag{14}$$

where W_{left}, W_{right} and $N_{\text{left}}, N_{\text{right}}$ are the computational weights and the number of processes, respectively, assigned to the two subdomains created by subdivision. This algorithm allows for an almost ideally balanced distribution of computational

workloads. In addition, it can be applied to simulations involving an arbitrary number of processors on heterogeneous clusters.

4.2.3   Applications

4.2.3.1   Tapered Transition for PETRA III

PETRA III [6] will serve as a dedicated 3rd generation synchrotron radiation facility at DESY. The impedance model presented in [24, 29] shows that an important contribution to the total impedance budget of PETRA III comes from the tapered transitions which are installed between the "standard" vacuum chamber and the undulator vacuum chamber. A total of 16 such transitions will be used in the ring. The basic geometry of the tapered transition including the vacuum pumping ports is shown in Fig. 5. The detailed geometrical dimensions for two slightly different geometrical configurations (referred to as Variant 1 and 2) can be found in [25].
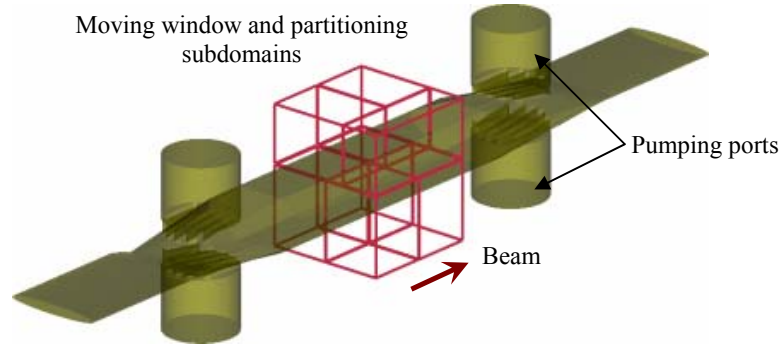
Figure 5: Geometry of the tapered transition together with a schematic view of the moving computational window. The subdomain bounds of the resulting parallel partitioning are shown as red lines for an exemplary computation on 7 processors.

The wake potentials of the tapered transition have been calculated with MAFIA [26] and PBCI for different mesh resolutions. Although the electron bunch considered in the simulations is comparably long ($\sigma = 10$mm), the geometrical complexity of the structure with a total length of $L \approx 1$m, necessarily leads to a large computational mesh. Figure 5 illustrates the moving window approach used in PBCI. Also shown are the resulting subdomains for an exemplary parallel partitioning on 7 processors.

In Fig. 6, the longitudinal wake potential for Variant 1 of the taper geometry is shown. The MAFIA result corresponds to a step size of $\Delta z = 0.1$mm, $\Delta x = 1$mm and $\Delta y = 0.5$mm. Due to computer memory limitations it was not possible to use a finer mesh in MAFIA. It can be seen that MAFIA does not give sufficiently accurate results for this smoothly tapered structure although the step sizes in all directions are much smaller than the bunch length. A convergent result was obtained in PBCI using a discretization with $\Delta x = \Delta y = \Delta z = 0.25$mm. PBCI converges to a wake potential which is about 30% lower than the MAFIA result. The loss and kick parameters obtained with the two codes are summarized in Table 2.
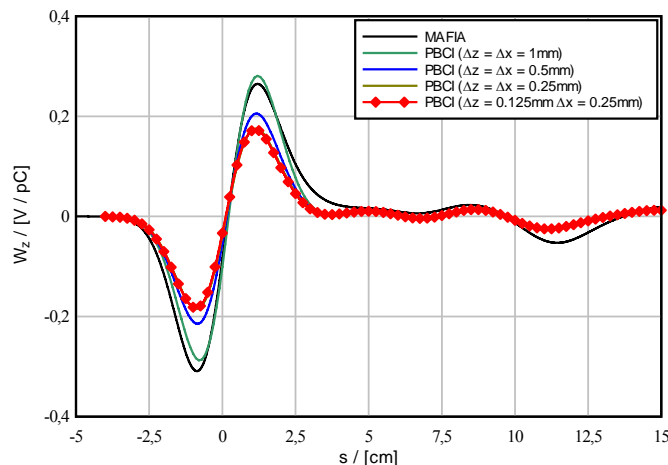
Figure 6: Longitudinal wake potential for Variant 1 of the tapered transition. The curves obtained for different mesh resolutions are shown.

Table 2: Comparison of the loss and kick parameters of the tapered transition obtained with MAFIA and PBCI.

Code	$k_\parallel$ / (V/nC)	$k_\parallel(1)$ / (V/pC m)	$k_\perp$ / (V/pC)
Variant 1 / MAFIA	-7.4	-6.8	138.6
Variant 1 / PBCI	-7.1	-4.8	75.6
Variant 2 / PBCI	-5.2	-4.6	62.8

4.2.3.2   *Analysis of the PITZ Diagnostics Section*

In this application, the wake fields induced by the different components within the diagnostics double cross of the PITZ injector [22] are estimated. This section is the first in the X-FEL beam line which breaks axial symmetry. Thus, a 3D simulation of the structure is necessary. The geometrical layout of the ten-port vacuum device is shown in Fig. 7. The investigation includes three separate simulations for comparing the influence of the wake fields induced by the different geometrical obstacles within the structure. In the first simulation, the geometry was simplified to the beam tube including only the small step at the entrance of the section. The second simulation included the vacuum vessel without shielding tube. The third simulation considered the full geometry as shown in Fig. 7.

The simulation results for an electron bunch of rms-length 2.5mm are summarized in Fig. 8. For resolving the small details of the geometry, a total of 250 million grid points were needed in the discretization. It was found, in particular, that the small step of 1mm height is responsible for 10-15% of the induced wake fields. The effect of the vacuum vessel inside the cross is about six times higher. The wake field effects are reduced, as expected, when the tube shielding is included.
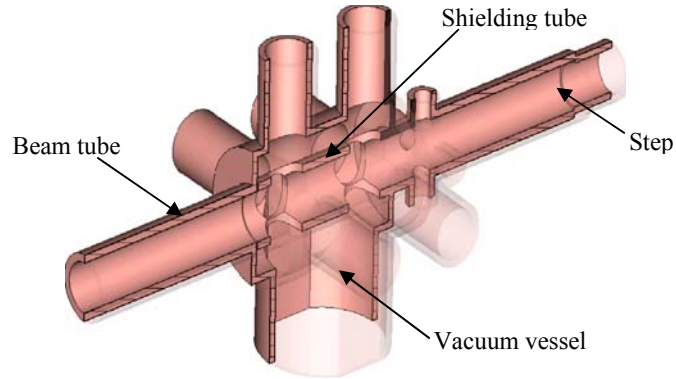
Figure 7: Geometrical view of the diagnostics double cross in the PITZ injector.
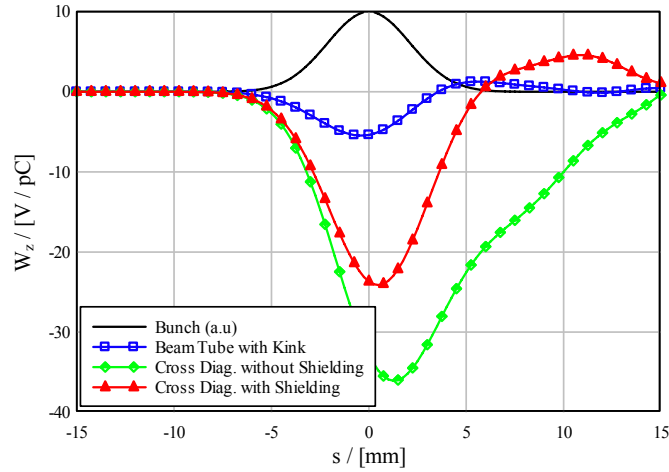
Figure 8: Longitudinal wake potentials induced by the different obstacles within the PITZ diagnostics section.

4.2.3.3   ILC-ESA Collimators

The collimator considered is part of the ILC-ESA test beam program [27]. A schematic view and the dimensions of the structure are shown in Fig. 9. Due to the extremely short bunch length ($\sigma = 300\mu$m) a discretization with $\Delta x = \Delta y = \Delta z = 20\mu$m is used. This results in a computational model with $\sim 4.5 \cdot 10^8$ grid points.

Figure 10 shows the convergence behavior of the longitudinal wake potential with grid resolution. It is interesting to note that convergence is obtained for 10-15 grid points / sigma. This figure corresponds to the standard resolution imposed by wave length in typical FIT simulations. Thus, in this case, the simple stair-step geometry approximation used in the current implementation of PBCI does not seem to influence simulation accuracy.

Figure 11 shows the directly computed part of the wake potential vs. the wake potential transition in the outgoing pipe. The catch-up distance of the wake fields behind the collimator can be estimated to 2.4m. Due to this large distance, the transition potential is expected to dominate the solution. This is clearly seen in Fig. 11.
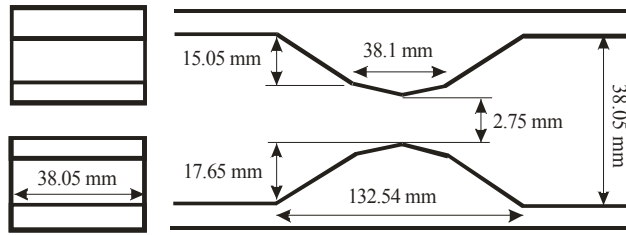
Figure 9: Beam and side views of the collimator #8 for the ILC-ESA test beam experiments.
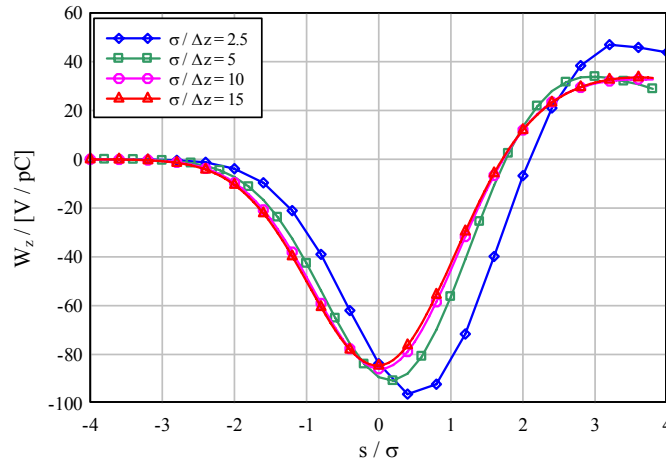
Figure 10: Convergence of the wake potential vs. grid resolution for the ILC collimator #8.
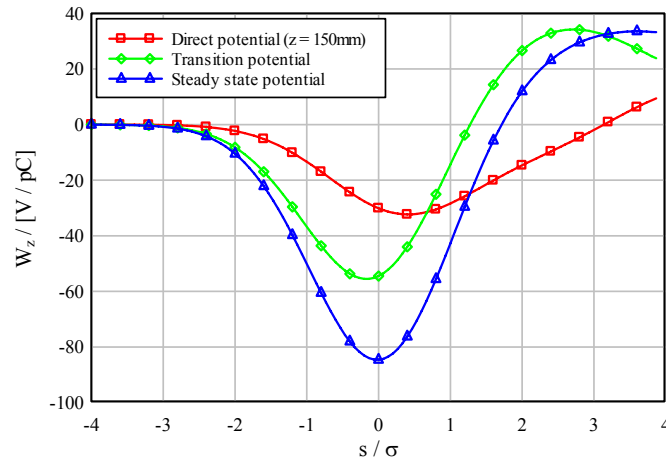
Figure 11: Direct vs. transition wake potential. 150 waveguide modes were used in the computation of the transition wake potential.

4.2.3.4   TESLA HOM-Couplers

Both, the X-FEL and the ILC use accelerating cavities, based on the TESLA superconducting technology. The ~1m long cavities consist of 9 resonating cells which support an accelerating mode at 1.3GHz. At each side of the TESLA cavities two Higher Order Mode (HOM) couplers are mounted on the upstream and downstream beam pipes, respectively. HOM couplers are designed primarily for absorbing the

higher order modes which are exited by the bunch within the cavity. Figure 12 shows the beam view of the X-FEL HOM couplers which will be installed at DESY. Each of them contains a notch filter which reduces the coupling to the accelerating mode. Furthermore, they are rotated with respect to each other by 115º in order to maximize the total coupling to the dipole modes [28].

Figure 13 and 14 show the PBCI results for the transverse wake fields induced by a 1mm bunch passing through the upstream coupler. The curves are shown for different grid resolutions in order to demonstrate the convergence behavior of the solution. In the simulations, a computational window of dimensions 100x100x10mm was used. Thus, a moderate discretization with 10 grid points / sigma in each direction already leads to a computational mesh with 10^8 grid points. This figure illustrates the need for parallelization in wake field simulations with short electron bunches. In the present case, a computer cluster with 384 processor cores was used. The computation time on this platform amounts to ~12 hours for the largest mesh used (20 points / sigma).
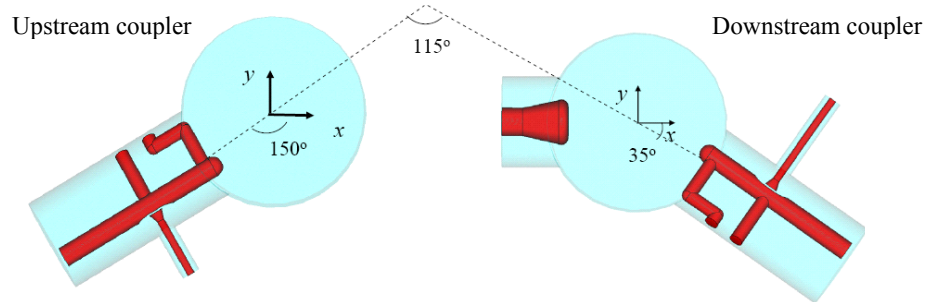
Figure 12: Beam view of the X-FEL upstream and downstream HOM couplers.
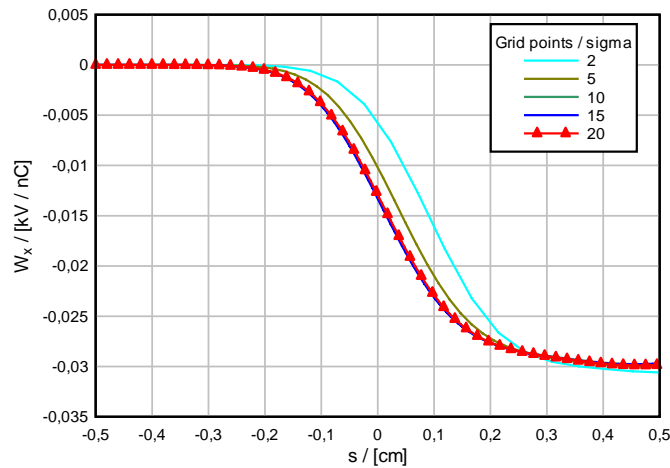
Figure 13: Convergence of W_x vs. grid resolution for the X-FEL upstream coupler.

As in the case of the ICL collimator #8 (Section 4.2.3.3), numerical convergence is obtained for a mesh resolution with 10-15 grid points / sigma. This behavior is typical for difference schemes such as FIT. It indicates that, for short bunches, the mesh size condition imposed by the dominant wave length tends to be more restrictive than the one related to the geometry approximation. This is an important observation knowing the high computational costs which are required by the meshing procedure in the boundary conformal approximation [15].
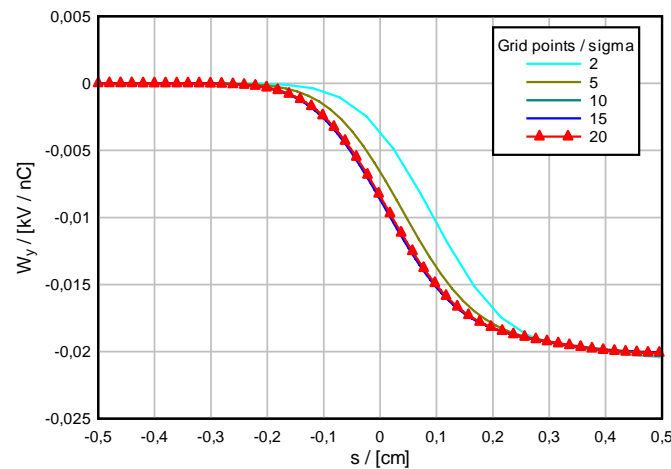
Figure 14: Convergence of W_y vs. grid resolution for the X-FEL upstream coupler.

4.2.4   References

1. A. Chao, B. Richter, C.Y. Yao, "Beam emittance growth caused by transverse deflecting fields in a linear accelerator", Nucl. Instr. Meth., 178 (1980), p. 1.
2. M. Dohlus, R. Lorentz, T. Kemps, H. Schlarb, R. Wanzenberg, "Estimation of the longitudinal wakefield effects in the TESLA-TTF FEL undulator beam pipe and diagnostic section", TESLA-FEL 98-02 (1998).
3. A. Chao, "Physics of Collective Beam Instabilities in High Energy Accelerators", John Wiley & Sons, New York, USA. (1993).
4. T. Weiland, R. Wanzenberg, "Wakefields and Impedances", Proc. of the CAT-CERN Accelerator School (1993), p. 140.
5. K. Balewski, R. Wanzenberg, "Beam Current Limitations in the Synchrotron Light Source PETRA III", Proc. of EPAC'04, Lucerne (2004), p. 2308.
6. PETRA III: A low Emittance Synchrotron Radiation Source, Technical Design Report, DESY 2004-035 (2004).
7. International Linear Collider - Reference Design Report, ILC-REPORT-2007-001 (2007).
8. The European X-Ray Free-Electron Laser - Technical Report, DESY 2006-097 (2006).
9. K. Bane, T. Weiland, "Wake Force Computation in the Time Domain for Long Structures", Proc. of 12th Int. Conf. on High Energy Accelerators, Chicago, IL, USA (1983), p. 314.
10. T. Weiland, "Comment on wake field computation in time domain", Nucl. Instrum. Methods 216, 31 (1983).
11. O. Napoly, Y.H. Chin, B. Zotter, "A Generalized Method for Calculating Wake Potentials", NIM-A, Vol. 334 (1993), p. 255.
12. A. Henke, W. Bruns, "Calculation of Wake Potentials in General 3D Structures", Proc. of EPAC'06, Edinburgh, UK (2006), WEPCH110.
13. I. Zagorodnov, "Indirect Methods for Wake Potential Integration", Phys. Rev. ST Accel. Beams 9, (2006).
14. I. Zagorodnov, T. Weiland, "TE/TM Scheme for Computation of Electromagnetic Fields in Accelerators", J. Comp. Phys., Vol. 207 (2005), p. 69.
15. I. Zagorodnov, R. Schuhmann, T. Weiland, "A uniformly stable conformal FDTD-method in cartesian grids", Int. J. Numer. Model. 16 (2003), p. 127.
16. C. Ng et al, "State of the Art in EM Field Computation", SLAC-PUB-12020 (2006).

17. M. Min, Y.-C. Chae, P.F. Fisher, "Spectral-Element Discontinuous Galerkin Simulations for Wake Potential Calculations: NEKCEM", Proc. of PAC'07, Albuquerque, NM, USA (2007).
18. T. Weiland, "A Discretization Method for the Solution of Maxwell's Equations for Six-Component Fields", Int. J. Elect. Comm., Vol. 31 (1977), p. 116.
19. T. Lau, E. Gjonaj and T. Weiland, "Time Integration Methods for Particle Beam Simulations with the Finite Integration Technique", FREQUENZ, Vol. 59 (2005), p. 210.
20. G. Strang, "On the Construction and Comparison of Difference Schemes", SIAM J. Num. Anal., 5 (1968), p. 506.
21. G. Aharonian, R. Meller, R.H. Siemann, "Transverse wake field calculations", CLNS Report, CLNS 82/535 (1982).
22. A. Oppelt et al, "Status and first results from the upgraded PITZ facility", Proc. of FEL'05, Stanford, CA (2005), p. 564.
23. F. Wolfheimer, E. Gjonaj, T. Weiland, "A Parallel 3D Particle-In-Cell (PIC) with Dynamic Load Balancing", Nucl. Inst. Meth. in Phys. Res. A, Vol. 558 (2006), p. 202
24. K. Balewski, R. Wanzenberg, "The Impedance of Selected Components of the Synchrotron Light Source PETRA III", Proc. of PAC'05, Knoxville, (2005), p. 1752.
25. R. Wanzenberg, K. Balewski, E. Gjonaj, "Wake Computations for Undulator Vacuum Chambers of PETRA III", Proc. of PAC'07, Albuquerque, NM, USA (2007), FRPMN01.
26. MAFIA Version 4.106, CST GmbH, Büdingerstr. 2a, D-64289 Darmstadt, Germany (2002).
27. N. Watson et al, "Direct Measurement of Geometric and Resistive Wakefields in Tapered Collimators for the International Linear Collider", Proc. of EPAC'06, Edinburgh, UK (2006), MOPLS06.
28. I. Zagorodnov, M. Dohlus, "Coupler Kicks", Proc. of ILC'07, Hamburg, Germany (2007).
29. K. Balewski, R. Wanzenberg, O. Zagarodnova, "The Impedance Model of PETRA III", this ICFA Beam Dynamics Newsletter.

4.3 Wakefields and Impedances at Elettra and FERMI@Elettra

E. Karantzoulis, C. Bontoiu, P. Craievich
Sincrotrone Trieste S.C.p.A.
Strada Statale 14 - km 163,5 in AREA Science Park
34012 Basovizza, Trieste ITALY
Mail to: Emanuel.karantzoulis@elettra.trieste.it

4.3.1 Introduction

Understanding wake fields and impedances is of great importance for the performance of accelerators. Instabilities driven by the wakes of the beams can very much limit the perforce of accelerators in both beam intensity and quality. At Elettra there has always been a strong activity concerning wake fields, including also many measurements and observation on the storage ring like the impedance evolution with the addition of many low vertical gap vacuum chambers or the impedance increase due NEG coated chambers [6]. With the advent of the modern free-electron lasers in the last decade, the wakefield/impedance problem has significantly grown up since the beam quality may be seriously degraded, limiting thus the lasing process itself or even worse,

rendering it uncertain. The analytical and numerical approaches in computing wakefields have also known an unprecedented evolution, with the stress on short-range monopole or dipole effects. Below there is a brief review of the most recent activities concerning impedances and wakefields for Elettra and the FERMI@Elettra Project.

4.3.2 Wakefields and Impedances

4.3.2.1 *Longitudinal Loss Factor Measurements at ELETTRA Storage Ring*

An electron beam passing through any irregularity of a vacuum chamber loses energy proportionally to the beam charge Q_b and to the induced voltage in the structure $V_{ind} = -Z_{\parallel} I_b$, where $Z_{\parallel}$ is the longitudinal impedance and I_b is the beam current. Since I_b is proportional to Q_b, the total energy loss of the beam (E_{loss}) is proportional to the square of its charge [5], as:

$$E_{loss} = -k_{\parallel} Q_b^2 \tag{1}$$

The proportionality factor $k_{\parallel}$ is the total longitudinal loss factor and it depends on the real part of $Z_{\parallel}$ and on the Fourier transform $\tilde{\rho}(\omega)$ of the particle distribution $\rho(t)$:

$$k_{\parallel} = \frac{1}{\pi} \int_0^{\infty} \Re Z_{\parallel} |\tilde{\rho}(\varpi)|^2 \, d\varpi \tag{2}$$

Since the energy loss of equation (1) changes by varying the beam charge, an indirect method to measure $k_{\parallel}$ is to take the closed orbit at a reference beam current I_0 and measuring the horizontal BPMs readings deviation in the dispersive region of the storage ring versus the beam current [6]:

$$\Delta x(z) \cong \eta(z) \frac{\Delta E}{E_b} \quad , \tag{3}$$

Where $\eta(z)$ is the dispersion, E_b the total beam energy at the beam current I_b and ΔE is the energy loss difference when the beam current changes from I_0 to I_b.

In reference [6] impedance budget measurements on the ELETTRA storage ring is extensively handled. Recently the Libera electron [7] device was used to upgrade the original Beam Position Monitor (BPM) detectors. These new detectors provide micrometric accuracy and fast data rate of the beam position measurements and thus the previous impedance budget has been updated. Preliminary measurements of the longitudinal loss factor were presented in [8].

4.3.2.2 *Resistive-Wall Wakefields*

Arising through the excitation of conduction electrons in the wall skin depth, resistive wakefields are of first concern even with good electric conduction metals like aluminum or copper. The resistive wall wakefield magnitude increases as the pipe

radius decreases and for a circular cross-section pipe there is roughly an exponential decay of the wake function peak with increasing pipe radius.
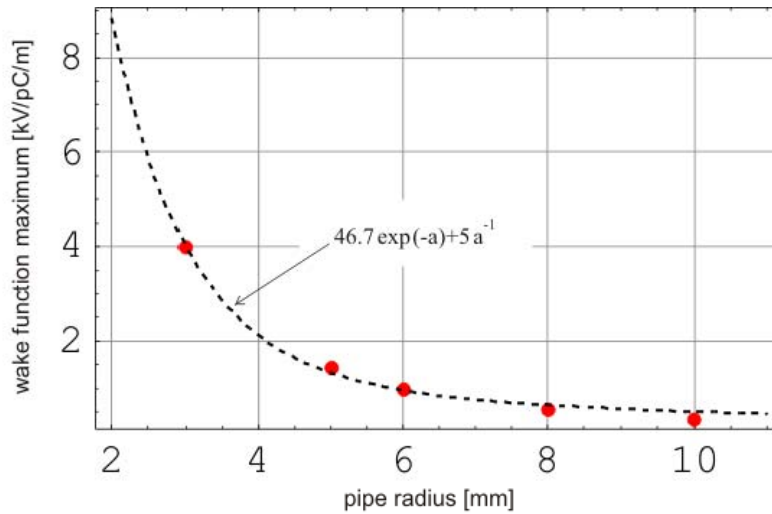
Figure 1: Dependence of the maximum wake function on the pipe radius. The red spots indicate computed values while the dashed line is their fit.

The resistive wakefields can be modeled by a damped oscillator whose quality factor is related to the material relaxation time and this makes aluminum be preferred to copper. Of course there is dependence on the shape of the pipe as well and for example at FERMI, calculations [1, 2] have shown that upon using aluminum the energy spread induced at the core of the medium bunch is: 16.5 keV/m for the circular cross-section and 11.71 keV/m for the rectangular and elliptic cross-section.

4.3.2.3   *Geometric Wakefields*

These kinds of wakes appear due to field scattering and reconfiguration of the equipotential lines as the beam passes along interruptions of the vacuum chamber or variations of the cross-section. There are many points where this happens along an accelerator and the difficulty in calculating them resides in accurate numerical modeling, since analytical tools are rather scarce compared with the complexity of the objects that need to be evaluated. In general analytic formulae with well defined range of validity have been used in the past to evaluate the impedance budget of Elettra [9]. Although the agreement with measurements has been very good, those formulae brake down at "extreme" condition (e.g. very small chambers or beams). Since the FERMI beam and chamber dimensions are in that range, there is currently an ongoing program to compute geometric wakes for various structures using existing numerical codes. For the time being a 3D code benchmarking test is ongoing [3]. Computations of simpler structures, like the RF beam deflectors, are also in progress using the 2D ABCI code.

4.3.2.4   *Surface Roughness Wakefields*

Surface roughness wakes are known since long as a source of impedance but they have come into attention lately due to the FELs high peak currents (kA) passing in the

proximity of the chamber walls, this kind of wake can be considered as a serious danger increasing the energy spread of the beam a very important and sensitive factor in lasing. Physical concepts at the base of the beam-roughness interaction are enormously complex involving dielectric excitation and relaxation, inductance of small objects fixed on the pipe etc. and one can only regard it as scattering on a corrugated surface. Thus, based on in-house measurements and modeling them with a sinusoidal, the energy spread at the core of the medium bunch was found to be 1.73 keV/m, which is an order of magnitude less than in the case of resistivity [4].

4.3.2.5 Micro-Bunching Instability

In September 2007 a mini workshop on microbunching instability was organized by the Accelerator Physics Team (ref. Simone.Dimitri@elettra.trieste.it) at Elettra, with about 25 participants from Europe and USA. The meeting was focused on FERMI@Elettra and mainly discussed analytic theory limitations, 1-D vs. 3-D impedance models (CSR , LSC) and code bench marking. The outcome of the meeting concluded that if one trusts the CSR and LSC impedance models then one must trust the microbunching instability predicting very large growths (>100) and also that there is a satisfactory convergence of predictions (codes, theory) providing thus a reasonable basis for the project design on the laser heater(s) and overall FEL performance.

4.3.3 References

1. C. Bontoiu, P. Craievich, "Longitudinal Resistive Wall Wakefields in the Vacuum Chamber of the FERMI FEL1 Undulator", ST/F-TN-06/17, Oct. 2006;
2. A. Lutman, M. Castronovo, R. Vescovo, C. Bontoiu, P. Craievich, L. Rumiz., "Wakefield Induced Energy Spread in the FERMI Undulator", FEL 2007;
3. C. Bontoiu, P. Craievich, "Numerical Code Evaluation for the Impedance Budget of FERMI", to be registered as internal note;
4. C.Bontoiu, P.Craievich, L.Casalis, M.Castronovo, L.Rumiz − "Surface Roughness Wakefield. An Account for FERMI Undulators";
5. B.W. Zotter and S.A. Kheifets , " Impedances and Wakes in High-Energy Particle Accelerators", World Scientific, 2000;
6. E.Karantzoulis, V. Smaluk and L.Tosi,"Broadband Impedance measurements on the electron storage ring ELETTRA", Phys. Rev. ST-AB, Vol. 6, 030703 (2003);
7. M. Lonza et al., "BPM Detectors Upgrade for the Elettra FastOrbit Feedback", DIPAC '07, Venice, May 2007;
8. G.Penco, C.Bontoiu, P.Craievich, E. Karantzoulis, V. Forchì, "Review of the longitudinal impedance budget of the ELETTRA storage ring", PAC 2007.
9. E. Karantzoulis, "The Coupling Impedance of the Elettra Storage Ring", Sincrotrone Trieste internal report, ST/M-TN-90/14, 1990

4.4 Study of Impedance and Its Effect on Single-Bunch Instability at the Advanced Photon Source

Yong-Chul Chae

Advanced Photon Source, Argonne National Laboratory

9700 S. Cass Avenue, Argonne, IL 60439, USA

Mail to: chae@aps.anl.gov

4.4.1 Introduction

One of the main challenges at the Advanced Photon Source (APS) in maintaining high single-bunch intensity in either the 24-bunch or the hybrid operating mode [1] is characterizing and mitigating intensity-dependent collective instabilities in the storage ring. Such collective effects can arise when the electron beam excites electromagnetic fields as it traverses the vacuum chamber, and these fields act back on and perturb the beam. The integral of the field behind the beam is the wake potential, which represents the impact of structure on the beam; its Fourier transform is called the coupling impedance, which can be used as a versatile tool for instability analysis.

The first impedance database (DB1) was completed in 2003 [2]. DB1 was a collection of wake potentials excited by the beam passing through all the mechanical components in the storage ring. Because of the reciprocity between duration and bandwidth, the shorter the electron bunch, the broader the impedance. Broadband impedance is needed to investigate fine density modulation in the beam, but limited computer resources available at the time restricted DB1 to computations based on a 5-mm-long electron bunch. Despite this limitation, modeling the storage ring with DB1 and the particle tracking code **elegant** [3] reproduced various instabilities observed in the ring, including anomalous bunch lengthening and energy spread growth with single-bunch current, horizontal bunch centroid relaxation oscillations, and vertical beam size blow up [4,5,6].

Importantly and for the first time in the APS, the single-bunch injection accumulation limit was reproduced by DB1, and stored beam loss during injection was found to significantly contribute to this limit. However, the prediction accuracy was only about 60%; the transverse impedance had to be scaled by about +35% together with a 0.1 Ω increase to the longitudinal impedance to achieve good agreement between modeling and experiment [7]. The ad hoc scaling was necessary, as it turned out, in order to make up for the missing high-frequency and resistive-wall impedance. Until the broader impedance model was available, the scaled DB1 was used as a working impedance model for practical application to the storage ring. One example was predicting the single-bunch current limit in the future ring. The result in Fig. 1 shows that a 30% increase in the impedance will reduce the single-bunch limit by a factor of two, from 20 mA to10 mA. We also found that one 5-mm-gap insertion device (ID) chamber is equivalent to four 8-mm-gap chambers and increases the ring impedance by 6%. These results guide the plans for the design and installation of new ID chambers or radio-frequency cavities [8].
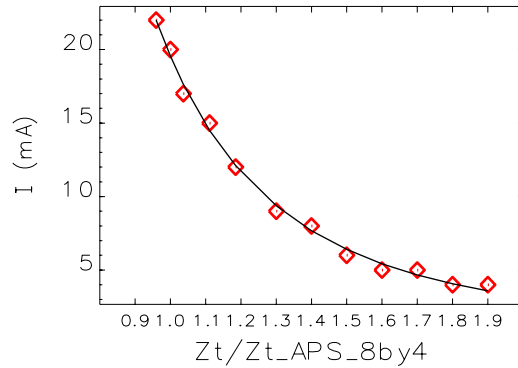
Figure 1: The current limit of a single bunch (vertical axis) can be reduced as the transverse impedance of the ring increases. The horizontal axis is the transverse impedance normalized to the transverse impedance of the present APS storage ring. The symbols give the simulation results and the line is a polynomial fit.

Improved accuracy for state-of-the-art modeling of the APS storage ring required impedance computation up to 100 GHz or greater, which could be obtained by computing the wake potential excited by the 1-mm or shorter bunched beam. The computational requirements were estimated to be 300 GB of memory and a speed of 10 Gflop. A new APEX Linux cluster was purchased, equipped with 60 cores of processing units and 240 GB of memory. Efficient use of the cluster also prompted the purchase of the parallelized software GdfidL [9], a state-of-art, three-dimensional electromagnetic code. The second impedance database (DB2) was thereby completed in 2007 [10, 11], and its resulting wake potential is compared with the old one by DB1 in Fig. 2. The resistive wake is not included in this figure, but it was computed separately by using analytical formulas, and its effect was considered in the modeling.
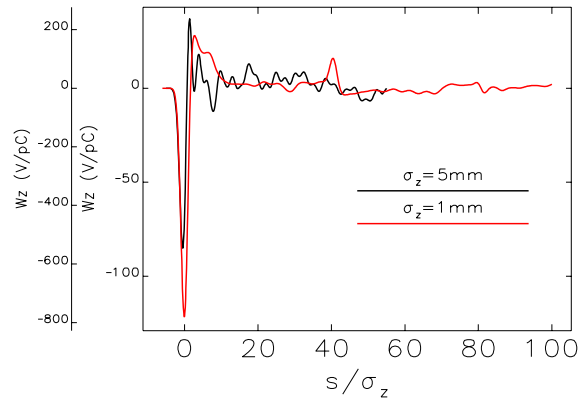
Figure 2: The total longitudinal wake potential of the APS storage ring computed by a 5-mm-long bunch (black curve) and a 1-mm-long bunch (red curve). The horizontal axis is normalized by the rms bunch length, and the vertical axis represents the magnitude in two different scales. The maximum wake potential of the bunch is about 800 V/pC and 80 V/pC for 1-mm and 5-mm bunches, respectively.

   With the broader impedance available from DB2, simulation tracking sub-million particles by the parallelized **elegant** program resulted in excellent agreement between accelerator modeling and actual operation without introducing any ad hoc modification to the impedance. One example is the prediction accuracy of DB2 on microwave instability. The horizontal beam size at the undulator with non-zero dispersion was measured by using an x-ray pin-hole camera for comparison with the simulation. The data were obtained by varying the bunch current twice, and their results are shown in Fig. 3. The systematic difference between the modeling and measurements is about 10 μm, corresponding to 97% accuracy.
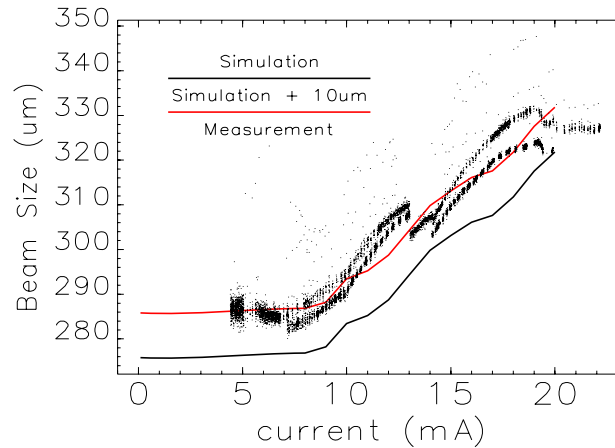
Figure 3: The dots represent the horizontal beam size measured at the undulator, where the non-zero dispersion of 17 cm contribute to the beam size owing to energy spread of the beam. Two sets of data were measured in the same shift within a one-hour interval. The black curve is the simulation results by using DB2 without any modification. The red curve is shifted by 10 μm for a better comparison with the experiment. Note that the resolution limit of the camera is 40 μm, which also contributed to the beam size data.

   The second example showing the prediction accuracy of DB2 for the dependence of collective effects on the ring lattice is shown in Fig. 4, where the singe-bunch limit is modeled as a function of the chromaticity set by the sextupole magnets.
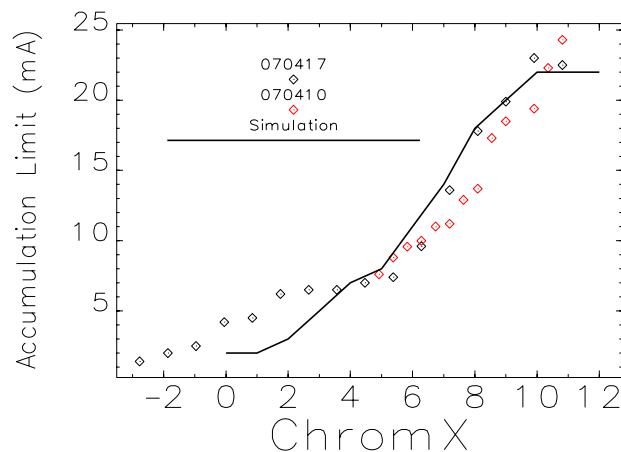
Figure 4: Modeling of the single-bunch accumulation limit in the APS storage ring as a function of chromaticity agrees very well with measurements. The wake potentials were computed for a 1-mm bunch with the code GdifdL on the APEX cluster.

The experimental data were obtained during two machine studies separated by one week, where we first measured the chromaticity prior to determining the accumulation limit by stacking the beam. The simulation results agree very well with observations. Furthermore, analysis of the phase-space data of Fig. 4 showed that the resistivity of the ID chamber was a critical horizontal impedance source limiting injection efficiency. This was not clearly understood using DB1. Thus, the broadband impedance from DB2 not only reproduced the ring performance accurately, but also enhanced understanding of the intricate role of each impedance source.

The impedance database project started with the modest goal of providing accelerator scientists with a simulation tool that could be used to analyze data acquired during machine studies. Over the last four years, the improvements made in wake potential computation, particle tracking, and parallelization of software, as well as the purchase of a powerful computer with large memory, pushed the capability to model the accelerator in operation as close as possible to actual performance. This has greatly enhanced confidence in predicting future machine performance.

4.4.2   Acknowledgements

Experimental data were acquired with much help from C. Yao, B. Yang, L. Emery, V. Sajaev, and the operating staff. We thank B. Soliday, Y. Wang, M. Borland, and W. Bruns for their computer and software support including **elegant** and GdfidL. We acknowledge K.-J. Kim for his coordination efforts in purchasing the APEX cluster. We also appreciate K. Harkay for her continuous interest and encouragement for this work.

4.4.3   References

1. http://www.aps.anl.gov/Accelerator_Systems_Division/Operations_Analysis/SRparameters/SRparameters.html
2. Y.-C. Chae, "Impedance database and its application to the APS storage ring," Proc. of PAC2003 (Portland, OR, 2003), 3017.

3. M. Borland, "elegant: A flexible SDDS-compliant for accelerator simulation," Advanced Photon Source Light Source Note LS-287, 2000.
4. Y.-C. Chae, K. Harkay, and X. Sun, "Horizontal coupling impedance of the APS storage ring," Proc. of PAC2003 (Portland, OR, 2003), 3008.
5. Y.-C. Chae, K. Harkay, and X. Sun, "Vertical coupling impedance of the APS storage ring," Proc. of PAC2003 (Portland, OR, 2003), 3011.
6. Y.-C. Chae, K. Harkay, and X. Sun, "Longitudinal coupling impedance of the APS storage ring," Proc. of PAC2003 (Portland, OR, 2003), 3014.
7. Y. Chae, Y. Wang, A. Xiao, "Single-Bunch Instability Estimates for the 1-nm APS Storage Ring Upgrade with a Smaller Vacuum Chamber," Proc. of PAC2007, (Albuquerque, NM, 2007), 4330.
8. Y. Chae, G. Waldschmidt, V. Dolgashev, "The Wakefield Effects of Pulsed Crab Cavity at the Advanced Photon Source for Short X-ray Pulse Generation," Proc. of PAC2007, (Albuquerque, NM, 2007), 4339.
9. http://www.gdfidl.de
10. Y. Chae, "The Impedance Database Computation and Prediction of Single Bunch Instabilities," invited talk presented at PAC2007, (Albuquerque, NM, 2007), 1996.
11. Y. Chae, Y. Wang, "Impedance Database II for the Advanced Photon Source Storage Ring," Proc. of PAC2007, (Albuquerque, NM, 2007), 4336.

4.5 Activities Related to Collective Beam Instability at SOLEIL

R. Nagaoka, P. Marchand, M.P. Level, L. Cassinari, M.E. Couprie, J.C. Denard,
J.M. Filhol, M. Labat, C. Mariette, R. Sreedharan
Synchrotron SOLEIL, BP 48, F-91192 Gif-sur-Yvette, France
Mail to: nagaoka@synchrotron-soleil.fr

4.5.1 Introduction

SOLEIL is the 2.75 GeV French third generation light source ring commissioned in 2006 and starting the user operation since the following year [1-3]. Its main goal is to store high intensity and low emittance electron beam with excellent stability for synchrotron radiation users. The storage ring has successfully been operated in the multibunch mode achieving a total current of 300 mA so far and aiming 500 mA when a second RF unit shall be installed, as well as in the time structure mode where more than 20 mA of bunch current has been stored, already doubling the designed value. Being a synchrotron radiation dedicated machine, the ring consists of a large number of low gap straight sections for insertion devices and has a relatively small vertical half gap of 12.5 mm for the standard chambers to avoid large vacuum chamber transitions. All straight vacuum vessels are made of aluminium, the surface of which is coated with Non Evaporable Getter (NEG) material to reduce photo-desorption. Since the design stage efforts have been made to overcome the known current-dependent collective beam instabilities. HOM free superconducting cavities were developed to eliminate cavity-induced coupled-bunch instabilities. 3D numerical calculations of coupling impedance were launched, not only to evaluate the impedance budget, but to optimise various vacuum components geometry exposed to beam, such as bellows, flanges and tapers. Resistive-wall impedance was systematically evaluated taking into account metallic layers and non-circular cross sections. The obtained impedance was then directly used

in simulations to predict instability thresholds and to examine the necessity of a feedback system to control beam instability.

The present article reviews the collective instability studies made above and comparisons between the observed instabilities and expectations, as well as a unique HOM free RF system and a bunch-by-bunch digital transverse feedback system developed at SOLEIL.

4.5.2   Impedance Calculations

4.5.2.1   Geometric Impedance

4.5.2.1.1 Numerical Code Used

Prior to commencing the work, some time was spent in finding the best suited 3D code. Upon comparison, the program GdfidL [4] was chosen, principally for its superiority in performing parallel processed computations with a cluster of processors, gaining a significant factor in terms of speed over mono-processed computations, as well as in its reduced required memory. With GdfidL, the core memory is computer resource limited. As seen below, these two features were critically helpful in treating 3D objects having a fine structure of the order of tenths of millimetres, and in performing long integrations of the wake potential. On the other hand, for a large axis symmetric object such as the SOLEIL cavity, the 2D code ABCI [5] was used. At SOLEIL, the computer cluster initially composed of 12 AMD Athlon MP 2000+ at 1.7 GHz, and 4 AMD Opteron at 2.0 GHz, with 20 Gbyte of RAM in 2004, has evolved to comprising presently 232 core AMD Opteron of 2.2 to 2.6 GHz with 500 Gbyte of distributed memory.

4.5.2.1.2 Impact of Monopole Fields

The absence of axis symmetry of the vacuum chamber brings about excitation of wake fields even with passage of the beam on axis. The field is thus monopole in terms of the driving beam, and is known to be quadrupolar in terms of the trailing beam. Namely, a trailing particle is linearly focused transversely. The incoherent tune shift due to the resistive-wall (RW) is evaluated in Section 4.5.4.2.3. The monopole component is disturbing, as it is contained in the usual wakes excited by a dipolar beam. For the SOLEIL chambers, they may amount to as large as 30~40% of the dipole impedance. Without removal of which, the vertical impedance tends to be overestimated and vice versa horizontally. The smallness of the horizontal dipole impedance may even lead to a sign error without correction (i.e. capacitive instead of inductive). The dipole impedance was evaluated by placing the trailing particle on axis in post-processing. The quadrupolar wake due to the geometric taper impedance was compared with the RW contribution in a typical stainless steel low-gap chamber (Fig. 1). The former was found to be non-negligible, and its relative importance is expected to rise for aluminium chambers.
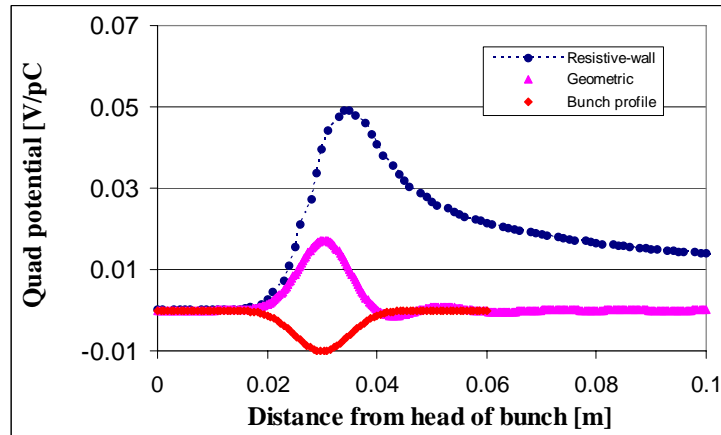
Figure 1: Quadrupole wake in a 5 m long stainless steel chamber with 16 mm vertical gap.

4.5.2.1.3 Dipole Chamber Slot

The work was motivated in particular following requests to increase the vertical slot size from its initial value of 9 mm. Numerical results obtained were in agreement with the theory [6] in the following respects: - No dependence of the impedance on slot length. - Steep increase of magnitude with increasing slot opening. - Presence of narrow bands related to the beam pipe cut-offs. By increasing the slot size, the slot impedance exceeded the remaining contributions at around 18 mm slot size (an example shown in Fig. 2). The slot affects predominantly the horizontal impedance, the magnitude of which is however sufficiently small compared to contributions of other machine components. The latter was also confirmed to be in agreement with studies made elsewhere.
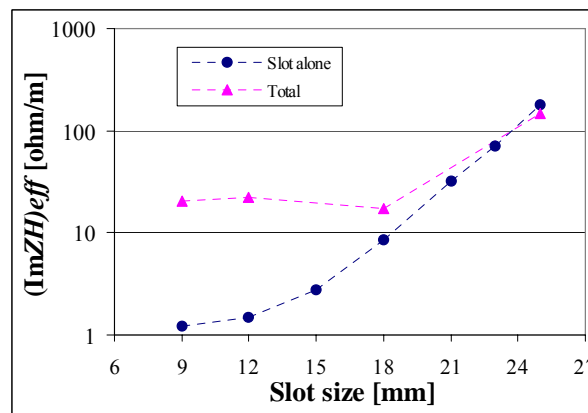
Figure 2: Horizontal impedance versus slot size.

4.5.2.1.4 Flange

A model having a slit of 0.4 mm long and 50 mm deep with no shielding was initially considered. The impedance calculated exhibited strongly trapped modes in all planes from low frequencies, on top of large broadband (BB) impedance (Fig. 3).
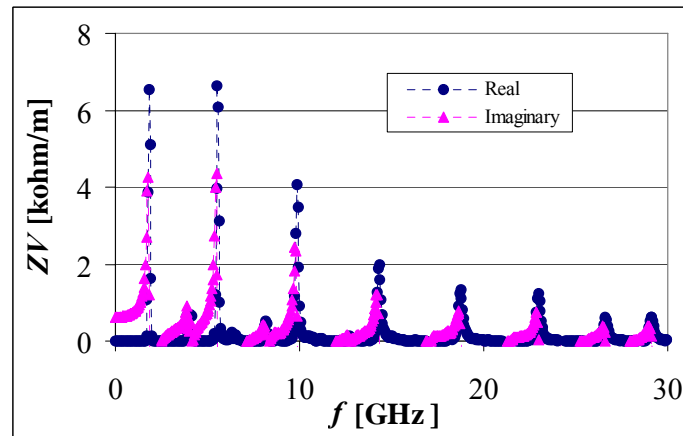
Figure 3: Vertical impedance of the initial flange model.

As the former caused unacceptably low multibunch instability thresholds, a detailed study was launched. Wake potentials were integrated over a long distance (~6 m) to assure good convergence of *R*/*Q*'s of the trapped modes. Since *Q*'s are infinite in wake computations, eigenvalue computations were carried out to verify the possible overestimation of the effect. By identifying the modes, the surface energy loss due to the resistivity of stainless steel was taken into account to compute the more realistic finite *Q* values. Shunt impedance *R*'s were then rescaled according to *R*/*Q*'s previously found. The latter, however, did not much alter the low instability thresholds obtained earlier. Both the frequency and amplitude of the narrow bands turned out to depend much on the slit depth, especially at small values. Introduction of short circuiting [7], as shown in Fig. 4, then led to a dramatic reduction of both the narrow and broadband impedance.
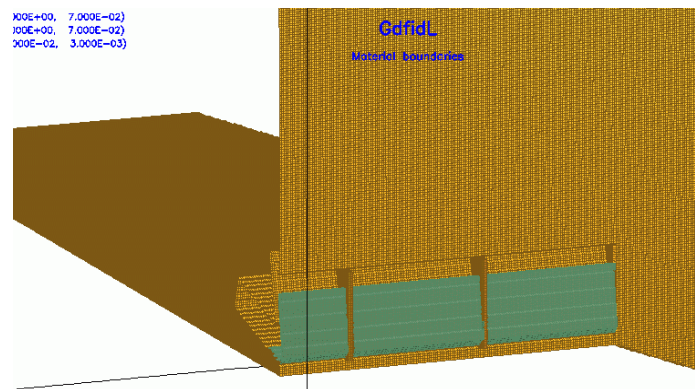
Figure 4: Short circuited flange. The metallic sheet (green) inserted between the two plates effectively shields a cavity-like structure.

4.5.2.1.5 BPM
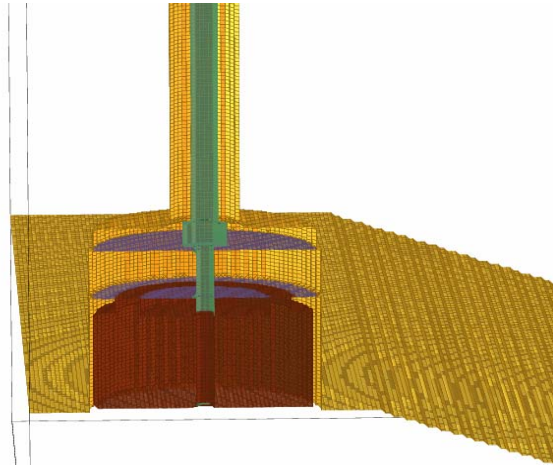
Figure 5: Part of the BPM structure used in GdfidL.

The impedance of a SOLEIL BPM was studied with GdfidL [4] by including the entire feed through structure under the waveguide boundary condition, with which the reflection in the former was optimised simultaneously (Fig. 5). The sensitivity of the impedance to the gap and thickness of an electrode was investigated in detail, finding opposing effects between a narrower gap that lowers the impedance and a thinner thickness. The gap was fixed to 0.25 mm [8]. The main problem encountered was a mode strongly trapped between the button and the BPM block around 8 GHz, which is expected to be TE_{110} (Fig. 6).
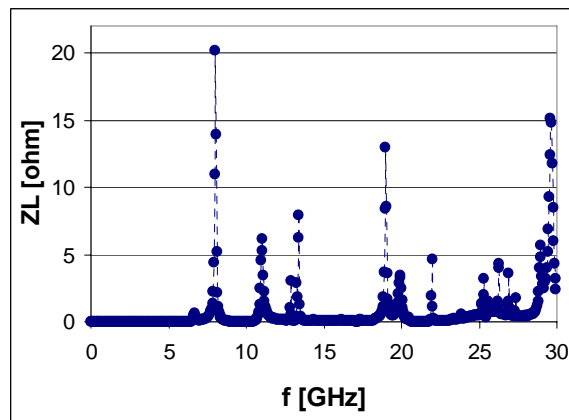
Figure 6: The real part of the longitudinal impedance.

Trapped modes are troublesome since on top of their enhanced sensitivity due to the reduced vertical aperture, short bunches interact with them, as mentioned previously. The dependence of the loss factor on the gap between a button and a BPM block, the button diameter as well as the thickness was followed. A simple solution of reducing the button diameter to raise the trapped mode frequency was not adopted as it is in conflict with the button sensitivity which scales as the square of the diameter. The button

thickness was therefore sought to increase, finding that a change from 2 to 5 millimetres reduces the loss factor by as much as a factor of 2 (Fig. 7).
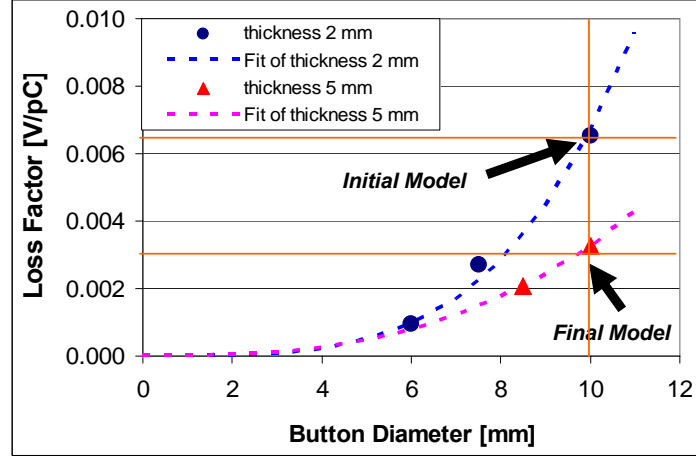
Figure 7: Calculated loss factor versus button diameter for different button thickness.

In view of the risk of spoiling the BPM reading accuracy due to dilation of the button, the heat that goes into the button was evaluated with the surface integral

$$\iint \frac{H_{//}^2}{2\kappa\delta}\, dF \quad [\text{W}] \tag{1}$$

where $H_{//}$ is the tangential magnetic field obtained in the wake potential calculation, κ is the conductivity and δ is the skin depth at the trapped mode frequency. By assuming in one case that the BPM block is superconducting, a half of the Joule loss was concluded to arise from the button, signifying the power on the button to be around 0.6 W at 500 mA. The study was extended to include a coupled-bunch effect on the loss factor, which may increase the net beam power experienced by an electrode. The effective damping time of the trapped mode was estimated by equating the wall energy loss (Eq. 1) integrated over time to the single bunch energy loss, finding it to be roughly three RF periods. The generalised loss factor was then evaluated by taking into account the passage of subsequent bunches, with a formula

$$k_{loss} = \frac{1}{\pi}\sum_{m=0}^{\infty}\int_0^{\infty} \operatorname{Re} Z_{//}(\omega)\cdot e^{-\sigma_\tau^2 \omega^2}\cos(m\Delta T\omega)\, d\omega \tag{2}$$

in which ΔT denotes the RF period and the trapped mode impedance is fitted with a resonator with its Q-value adjusted to the damping time found. The latter resulted in an enhanced power per electrode of 2.1 W against the original 0.6 W, in the worst case when the trapped mode is in resonance with the RF. To prevent this, gold coating the electrode was pursued, where the power would be reduced down to 0.9 W despite an increased damping time. The idea was however abandoned due to technical complications in realisation, as well as to low probability estimated for the resonance to

occur, under the assumption that the trapped mode frequency (fractional part) is random. On the contrary, the probability that the coupled bunch effect reduces the original loss factor was estimated to be higher than 70%.

Table 1: Beam induced heating with a coupled bunch effect, in comparison with the single bunch case. The last column indicates the current dependence of the reading.

Material Block/ button	Q	k_{loss} ratio	P_{tot} [W]	P_{button} [W]	T_{button} [°C]	Curr. dep. [μm]
S.S/S.S	211	3.43	4.18	2.09	180	4.1
S.S/Gold	366	5.45	6.65	0.89	88	1.7
S.S/S.S	Low	1.00	1.22	0.61	68	1.2

4.5.2.1.6 Vertical Scraper

The geometric impedance of the ESRF type vertical scraper adjusted to SOLEIL was estimated with GdfidL with a major concern on heating. The impedance was expectedly dominated by the cavity-like structure created at the open position at both ends of the blades (full gap = 25 mm), and by the taper of the blades at the working position (full gap = 8 mm) (Fig. 8).
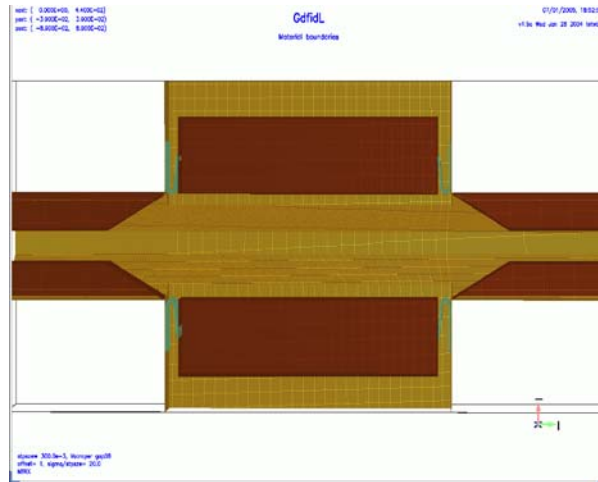
Figure 8: Inverted scraper structure at gap = 8 mm used for the wake potential computation.

The beam power turned out to be larger in 500 mA multibunch (σ=14 ps) than in 8×10 mA single bunches (σ=20 ps), which were respectively 530 and 400 W at the open and working positions. These values being excessive above all at the open position, it was decided to reinforce the cooling as well as to inhibit the gap opening beyond 15 mm with high current beam. With the constraint of fixing the total length, doubling of the taper length was attempted with no success, as a significant reduction only occurred around the working position. Reflecting the optimised geometry, the impedance showed a minimum around the working position, where the power changes by less than 5% against ±1 mm gap variations (Fig. 9).
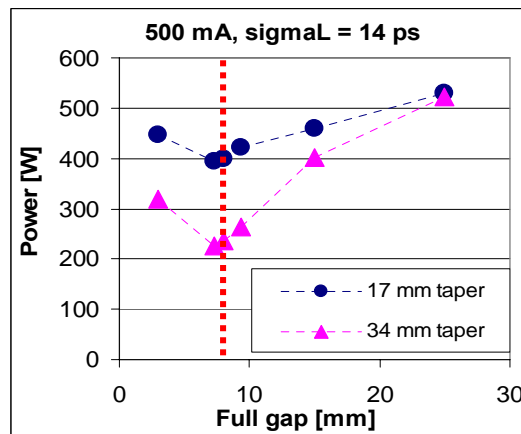
Figure 9: Beam-induced power versus scraper gap.

4.5.2.1.7 Stripline
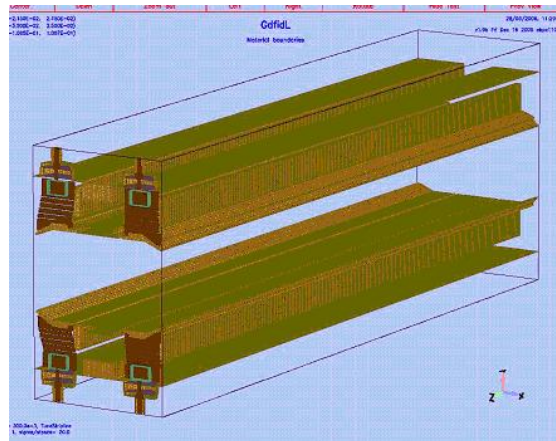
Figure 10: Structure of the stripline for tune measurement.

The impedance of a stripline having four electrodes with transmission lines in one end and short circuited in the other end (Fig. 10) developed for the tune measurement in the two transverse planes was investigated. The stripline has a thin slit (0.3 mm) azimuthally along the chamber perimeter, perpendicular to the beam direction at the transmission line position. The impedance consequently exhibits narrow band resonances at relatively low frequencies up to about 5 GHz (Fig. 11). The overall magnitude of the impedance remains however in the tolerated range ($|Z_{//}/n|_{eff}$ = 0.27 mΩ and the loss factor = 6.7×10^{-3} V/pC).

68
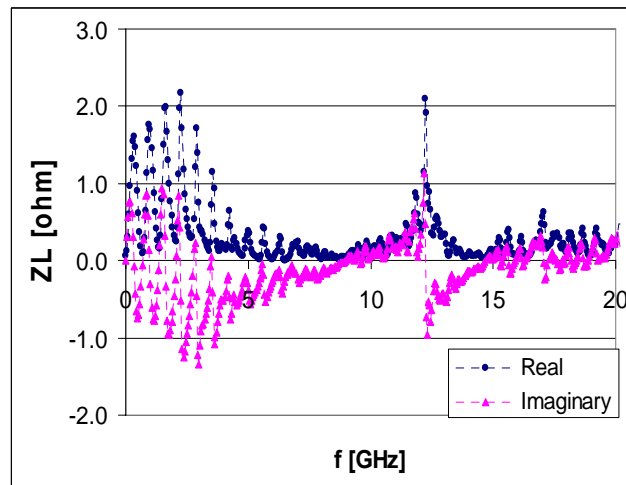
Figure 11: Calculated longitudinal impedance.

4.5.2.2 Resistive-Wall Impedance

4.5.2.2.1 Machine Data Organisation

Although the resistive-wall (RW) impedance is generally known analytically, accurate evaluation of its magnitude, as well as its product with the beta function over the entire machine, may not be simple when both the vacuum chamber and the optics are varying rapidly around the ring. To be able to trace as well the evolution of the machine impedance associated with chamber replacements, a systematic approach was adopted to evaluate RW effects in a consistent manner. A large machine file was prepared containing all the basic information related to the RW, piecewise for each chamber component around the ring. Data include cross section form, length, wall thickness, electric resistivity and average beta values over the component length. In addition, coating information as well as parameters specific to the incoherent tune shift, such as form factor and effective focusing strength, are entered (Fig. 12). These machine files are commonly used by codes developed to study different RW effects.

69

```
C----------------------------------------------------------------------------------------------------
C  Name        s1      s2      a0      b0      d0      rho     shape surface dW/dy    r     keffs    <betaH> <betaV>
C              [m]     [m]     [mm]    [mm]    [mm]    [ohm*m]                         [m-2]    [m]     [m]
C----------------------------------------------------------------------------------------------------
   IDLD_S1     0.000   5.434  35.000  12.500   2.000  2.80e-08  elli  Coat  3.63e-02  1.00  4.18e-07  11.06    9.23
   STND_S1.1   5.434   5.864  35.000  12.500   2.000  2.80e-08  elli  Coat  3.63e-02  1.00  4.18e-07  13.25   11.99
   BPM_S1.1    5.864   6.064  42.000  12.500  17.000  1.00e-06  elli  NoCo  2.17e-01  1.00  1.00e-06  13.55   12.38
   STND_S1.2   6.064   7.234  35.000  12.500   2.000  2.80e-08  elli  Coat  3.63e-02  1.00  4.18e-07  20.18    9.38
   BPM_S1.2    7.234   7.434  42.000  12.500  17.000  1.00e-06  elli  NoCo  2.17e-01  1.00  1.00e-06  23.10    7.33
   STND_S1.3   7.434   8.948  35.000  12.500   2.000  2.80e-08  elli  Coat  3.63e-02  1.00  4.18e-07   9.79   11.85
   SOUF_S1.1   8.948   9.089  42.000  12.500  17.000  1.00e-06  elli  NoCo  2.17e-01  1.00  1.00e-06   2.58   14.30
   BEND_S1.1   9.089  10.677  35.000  12.500   2.000  1.00e-06  elli  NoCo  2.17e-01  1.00  1.00e-06   0.94   15.90
   STND_S1.4  10.677  11.147  35.000  12.500   2.000  2.80e-08  elli  Coat  3.63e-02  1.00  4.18e-07   3.17   16.55
   BPM_S1.3   11.147  11.347  42.000  12.500  17.000  1.00e-06  elli  NoCo  2.17e-01  1.00  1.00e-06   6.22   13.35
   STND_S1.5  11.347  12.413  35.000  12.500   2.000  2.80e-08  elli  Coat  3.63e-02  1.00  4.18e-07  13.91    7.91
   BPM_S1.4   12.413  12.613  42.000  12.500  17.000  1.00e-06  elli  NoCo  2.17e-01  1.00  1.00e-06  16.71    6.44
   STND_S1.6  12.613  13.679  35.000  12.500   2.000  2.80e-08  elli  Coat  3.63e-02  1.00  4.18e-07  14.48    7.55
   BPM_S1.5   13.679  13.879  42.000  12.500  17.000  1.00e-06  elli  NoCo  2.17e-01  1.00  1.00e-06   7.05   12.49
   STND_S1.7  13.879  14.453  35.000  12.500   2.000  2.80e-08  elli  Coat  3.63e-02  1.00  4.18e-07   3.35   16.29
   SOUF_S1.2  14.453  14.594  42.000  12.500  17.000  1.00e-06  elli  NoCo  2.17e-01  1.00  1.00e-06   1.45   17.03
   BEND_S1.2  14.594  16.182  35.000  12.500   2.000  1.00e-06  elli  NoCo  2.17e-01  1.00  1.00e-06   1.08   15.60
   STND_S1.8  16.182  17.042  35.000  12.500   2.000  2.80e-08  elli  Coat  3.63e-02  1.00  4.18e-07   7.26   11.29
   BPM_S1.6   17.042  17.242  42.000  12.500  17.000  1.00e-06  elli  NoCo  2.17e-01  1.00  1.00e-06  15.00    6.61
   STND_S1.9  17.242  18.412  35.000  12.500   2.000  2.80e-08  elli  Coat  3.63e-02  1.00  4.18e-07  13.67    6.70
   BPM_S1.7   18.412  18.693  42.000  12.500  17.000  1.00e-06  elli  NoCo  2.17e-01  1.00  1.00e-06   7.06    8.58
   STND_S1.10 18.693  19.406  35.000  12.500   2.000  2.80e-08  elli  Coat  3.63e-02  1.00  4.18e-07   6.23    6.82
   CVTP2U_S2  19.406  19.634  42.500  31.250   1.000  1.00e-06  elli  NoCo  1.00e-02  1.00  5.00e-08   5.55    5.32
   CVTB2U_S2  19.634  19.892  50.000  50.000   1.000  1.00e-06  circ  NoCo  0.00e+00  1.00  0.00e+00   5.28    4.68
   CVTP1U_S2  19.892  20.217  90.000  90.000   1.000  1.00e-06  circ  NoCo  0.00e+00  1.00  0.00e+00   4.97    3.98
   CVTB1U_S2  20.217  20.570 130.000 130.000   1.000  1.00e-06  circ  Coat  0.00e+00  1.00  0.00e+00   4.65    3.28
   SCCVU_S2   20.570  22.030 130.000 130.000   1.000  0.00e+00  circ  NoCo  0.00e+00  1.00  0.00e+00   4.17    2.17
   SCCVD_S2   22.030  23.490 130.000 130.000   1.000  0.00e+00  circ  NoCo  0.00e+00  1.00  0.00e+00   4.17    2.17
   CVTB1D_S2  23.490  23.843 130.000 130.000   1.000  1.00e-06  circ  Coat  0.00e+00  1.00  0.00e+00   4.65    3.28
```

Figure 12: A file containing the machine data.

4.5.2.2.2 Impact of Metallic Coating

The standard RW impedance formula assumes a circular beam pipe with infinite wall thickness. To take into account metallic coating on the wall surface, we have employed A. Chao's formalism [9] to derive extended formulae longitudinally and transversely. They were found to agree numerically with those obtained by Burov and Lebedev in a different approach. They also derived expressions for flat chambers [10], which differ from the former by form factors of $\pi^2/12$ vertical and $\pi^2/24$ horizontal. Elliptical and rectangular chambers lie between the two extremities.

The formula was applied to in-vacuum undulators that have 50 µm thick Cu coating on the surface with 10 µm Ni in between Cu and NdFeB magnet blocks. While the Cu coating is found to well suppress the energy loss, its thickness is insufficient at the lowest betatron frequency that most strongly induces the RW instability (Fig. 13).
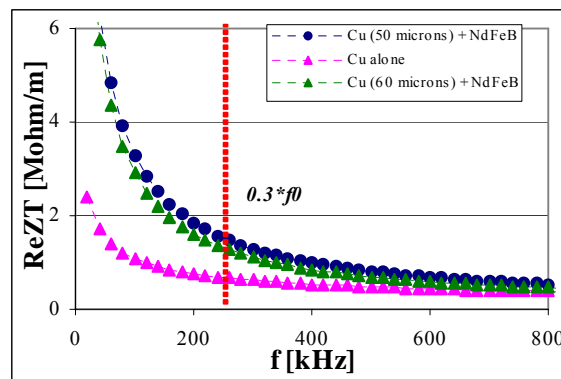
Figure 13: Transverse RW impedance for an in-vacuum undulator with Cu coating. The true case with Ni is expected to lie between the blue and green curves.

Triggered by the observation of an anomalous increase of the single bunch dipole mode detuning associated with installation of NEG coated aluminium chambers at

Elettra [11], its impact was studied with the above two metallic layer model. The use of NEG coated Al chambers was envisaged for SOLEIL in all straight sections. Assuming the thickness of 1 μm and the resistivity of 25×10^{-8} Ωm, which is of Vanadium, the constituent material with the lowest resistivity, we find that the reactive part is nearly doubled, while the resistive part is roughly unchanged, in the frequency range up to ~10 GHz (Fig. 14). This feature is common transversely and longitudinally. The increase of the reactive part is in qualitative agreement with the observation.
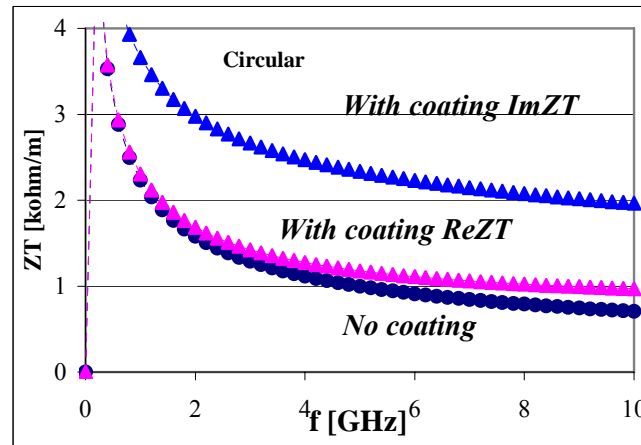
Figure 14: Transverse impedance with and without NEG coating.

Though the effective resistivity of NEG is not known, the impedance is found to saturate fast with increasing resistivity (Figs. 15a). This, along with the measurement of E. Plouviez finding ~ 1600×10^{-8} Ωm for NEG [12], would indicate that the result in Fig. 13 represents the plausible cases. The impedance also saturates fast with increasing thickness, correctly to the value determined by the coating material (Figs. 15b).
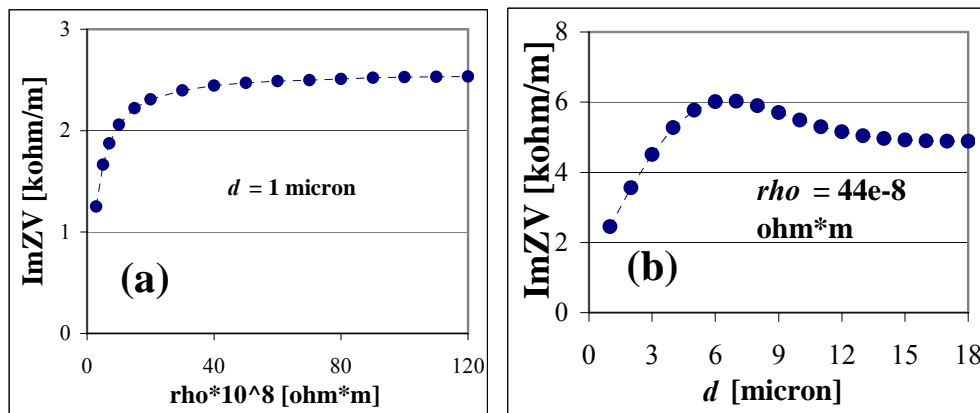
Figure 15: Dependence of the vertical impedance (calculated at 2 GHz) on the resistivity ρ (left) and the coating thickness d (right).

With all straight section coated with NEG, it follows that for SOLEIL, the NEG nearly doubles the total imaginary impedance as well, though the increased value is still roughly half of what it would have been had all the chambers been made in stainless

steel. As long as the increase occurs only on the imaginary part, the resistive-wall instability is supposed to be unaffected. On the other hand, the threshold of the transverse mode coupling instability (TMCI) in single bunch may be seriously reduced. The latter is quantified in a later section.

Despite the qualitative agreement, the present model fails to reproduce the Elettra observation quantitatively by as much as an order of magnitude. Staying within the model, one is obliged to assume unreasonably large values for both the thickness and the resistivity. This discrepancy, along with an additional observation at ELETTRA suggesting a simultaneous increase of the real part of the impedance, may indicate that the origin may well be other than the model considered here. One good candidate would be the surface roughness, which is already known for NEG coated aluminium chambers. Collaboration was made with ELETTRA and the ESRF to analyse the ELETTRA observations [13].

4.5.2.2.3 Titanium Coated Ceramic Chambers

To evaluate the heating of titanium coated ceramic chambers used for kickers and shakers, their longitudinal impedance was studied analytically. The EM field matching made earlier to chambers having different metallic layers was extended to include dielectric materials in the MKSA unit, working with (E, H). The obtained impedance per unit length for a circular chamber of radius b reads

$$\frac{Z_{//}(\omega)}{L} = \frac{-i}{2\pi\varepsilon_0 cb}\left\{\left(\frac{a}{k}-\frac{k}{a}\right)\cdot\frac{[1+A\tanh(ad)]}{[A+\tanh(ad)]}-\frac{kb}{2}\right\}^{-1} \tag{3}$$

where $k=\omega/c$, $a=[1-i\cdot\text{sgn}(\omega)]/d_s$ (d_s: skin depth), d the titanium coating thickness, A is equal to $A_0 \equiv i(a/k - k/a)\sqrt{\mu_r\varepsilon_r - 1}/\varepsilon_r$ for infinitely thick ceramic, or to $-iA_0\tan(vd_c)$ when the thickness is d_c, with $v = k\sqrt{\mu_r\varepsilon_r - 1}$. Other symbols have their usual meanings. The derived impedance formula comprises that of Piwinski found in Ref. 14. As compared to the impedance of a chamber made of titanium alone, that given by Eq. 3 is characterised by an enhanced real part and a reduced imaginary part. The beam induced power for the case considered (b=12.5 mm and d = 2 µm) turns out to be 46 W for 500 mA uniformly filled beam (σ_L=14 ps) and 43 W for 80 mA beam composed of 8 bunches (σ_L=20 ps), respectively per unit length. These values are found to agree well in the range d=1~5 µm with those obtained from the scheme by S. Milton et al. in Ref. 15, which evaluates the Joule energy of the image charge flowing uniformly across the titanium cross section. The picture assumed in the latter was assessed with the derived EM fields inside the chamber wall. Firstly with the resistivity 50×10^{-8} Ωm of titanium, the skin depth is found to exceed 2 µm up to 30 GHz. This however is only a necessary condition for the image charge to flow uniformly. Since the image current is proportional to the longitudinal electric field E_z in the metal, its radial dependence was followed as a function of frequency, in comparison with when the titanium thickness is infinite or ceramic is replaced by air. We clearly observe that the longer will be the skin depth as compared to the coating thickness, the more will ceramic render the image current to flow uniformly across titanium (Figs. 16). Such compression of the EM field in the coating due to the presence of ceramic was already pointed out by Piwinski in Ref. 16.
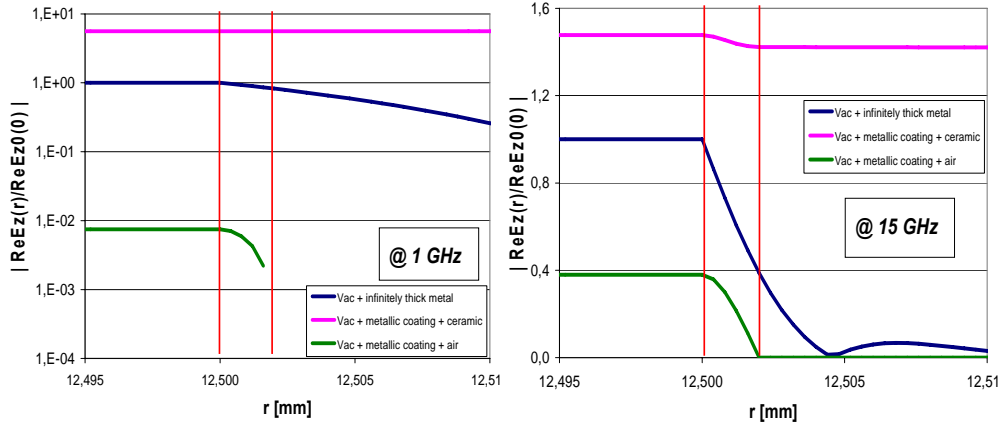
Figure 16: Amplitude of $E_z(r)$ at 1 GHz (left) and 15 GHz (right). Magenta: Ti+ceramic. Blue: Infinite Ti. Green: Ti+air. Red lines: Location of the titanium coating.

We have evaluated the total power for the racetrack shaped SOLEIL ceramic chamber starting from a circular chamber having the radius equal to the vertical half gap of b=12.5 mm, whose equality is justified by Yokoya [17] and Piwinski [18]. The surface power density, which is more directly related to the temperature distribution, however, shall clearly vary along the perimeter. To derive the latter, Piwinski's study on a flat chamber was utilised, where EM fields are solved analytically in the transverse plane [18]. Although the study assumes an infinitely thick wall, we consider that the geometric effect, such as the dependence of the surface power density on the horizontal position, will not be different for our ceramic chamber with a metallic coating. Justification of applying the flat chamber result to our racetrack chamber will be made later. Integrating E_z over its momentum and frequency variables in the metal and taking its square, the surface power density $P_s(x)$ reads

$$P_s(x) = \frac{\pi^2}{4\cosh^2(\dfrac{\pi}{2b}x)} \cdot (P_s)_{circle} \tag{4}$$

where $(P_s)_{circle}$ denotes the surface power density of a circular chamber of radius b. The obtained relation indicates that with the vertical half gap of 12.5 mm, the surface density is peaked above and below the beam position (x=0) at nearly 2.5 times the circular chamber value, which decays to zero before $x=\pm20$ mm. Since the flat section of the SOLEIL chamber extends to $x=\pm27.5$ mm, the use of the flat chamber model may be justified. The derived surface density was used to compute the temperature distribution of the ceramic chambers with a 3D code, by simulating the actual air cooled structure [19]. First results indicated that while with 0.5 µm thick coating, the hottest point is limited to ~90° C at 500 mA, the temperature rises up to ~195° C for 0.2 µm thickness, rendering the latter to be unacceptable [20].
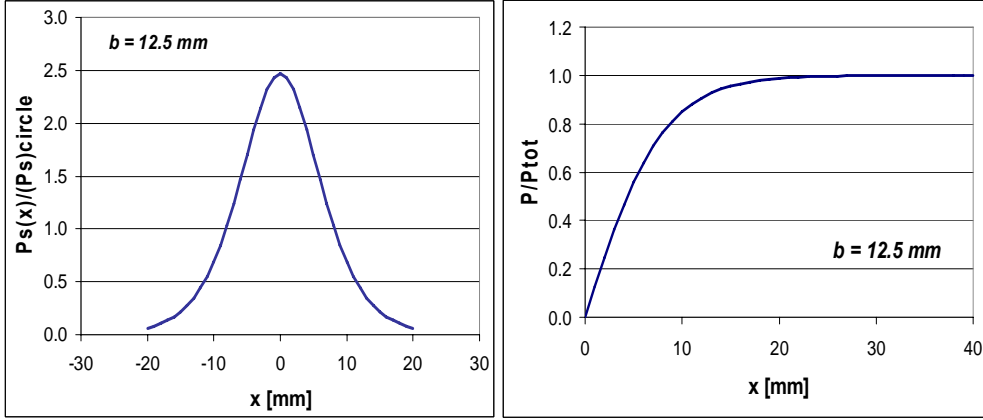
Figure 17: Local surface power density (left) and its integral as a function of the horizontal position x (right).

4.5.2.3   *Impedance Budget*

Table 2 summarises the contribution of the machine components evaluated so far in all three planes. Besides the loss factor and the beam power loss at 500 mA in multibunch, the effective impedances are listed, convoluted with the spectrum of a 6 mm long bunch. Real parts of the transverse impedance are evaluated by shifting the bunch spectrum with the chromaticity (normalised value of 0.3 vertically and 0.1 horizontally), since they vanish otherwise. Also listed in the transverse planes are the sum of the product of the local beta values and the impedance, the quantity that counts for collective effects. Figures 18 display the frequency content of the impedance.

Table 2: Impedance budget for SOLEIL obtained so far.

Object	Number	Loss factor [V/pC]	$(P)_{500\,mA}$ [kW]	$\Sigma \|Z_L/n\|_{eff}$ [mΩ]	$(Z_V)_{eff}$ [kΩ/m]	$\Sigma \beta_V \times (Z_V)_{eff}$ [kΩ]	$(Z_H)_{eff}$ [kΩ/m]	$\Sigma \beta_H \times (Z_H)_{eff}$ [kΩ]
Shielded bellows	176	8.72×10^{-3}	**1.17**	**48.30**	(0.03, 0.14)	**(52.8, 246.4)**	(0.01, 0.06)	**(15.8, 112.6)**
Flange[1]	332	4.67×10^{-4}	0.12	11.65	(0.00, 0.01)	(0.7, 42.3)	(0.00, 0.01)	(9.1, 46.8)
Dipole chamber	32	1.64×10^{-4}	2.63×10^{-3}	0.48	(0.00, 0.00)	(0.2, 0.7)	(0.00, 0.03)	(0.1, 0.8)
Soleil cavity	1	2.20	**1.55**	9.30	(0.29, 0.44)	(0.8, 1.3)	(0.17, 0.44)	(0.8, 2.0)
BPM	120	6.10×10^{-3}	0.56	**19.20**	(0.03, 0.05)	(20.5, 41.1)	(0.01, 0.05)	**(14.7, 44.14)**
Medium section tapers	10	1.76×10^{-3}	1.24×10^{-2}	9.31	(1.35, 3.41)	**(85.5, 215.9)**	(0.01, 0.56)	(0.4, 33.7)
Long section tapers	3	7.32×10^{-4}	1.55×10^{-3}	1.52	(0.43, 1.13)	(14.9, 39.2)	(0.00, 0.24)	(0.1, 9.2)
In-vacuum ID tapers[2]	4	0.25	0.76	18.92	(0.50, 1.42)	(6.0, 17.0)	(0.13, 0.50)	(9.4, 36.0)
Soleil cavity outer tapers	1	0.17	0.13	6.70	(0.49, 1.56)	(2.6, 8.3)	(0.01, 0.29)	(0.0, 1.6)
Resistive-wall	-	7.31	**5.17**	**85.50**	(21.8, 101.5)	**(135.2, 743.5)**	(7.10, 51.7)	**(34.8, 376.3)**
Injection zone[3]	1	1.86×10^{-3}	1.42×10^{-3}	0.09	(0.00, 0.01)	(0.0, 0.1)	(0.10, 0.72)	(1.2, 8.7)
Pumping holes (@quads)	128	$< 1.0\times10^{-7}$	$< 1.0\times10^{-7}$	0.01	(0.00, 0.00)	(0.0, 0.0)	(0.00, 0.00)	(0.0, 0.5)
Vertical scraper[2]	1	4.48×10^{-1}	0.32	9.42	(2.00, 3.41)	(20.0, 34.1)	(0.31, 0.94)	(3.1, 9.4)
Short circuited stripline	1	6.72×10^{-3}	4.75×10^{-3}	0.20	(0.01, 0.02)	(0.10, 0.20)	(0.03, 0.07)	(0.30, 0.69)
Total	-	-	**9.52**	**214.2**	-	**(339.3, 1390.1)**	-	**(89.8, 682.4)**

1. The shielded flange as described in the main text
2. At open-gap position
3. At nominal position

We confirm first of all the domination of the resistive-wall for SOLEIL, which accounts for nearly half or more of the total. Its imaginary part is further enhanced by almost a factor of two due to the NEG layer (Sec. 4.5.2.2.2). Other main contributors found are bellows, BPMs, SOLEIL cavity and tapers (medium straight section). A large

peak appearing at around 10 GHz (Figs. 18) comes from BPMs. The impedance is found mostly inductive in all three planes. The horizontal impedance is roughly half of the vertical, which is even larger than the linear ratio of the two apertures (~0.3). Among others, $|Z_{//}/n|_{eff}$ for SOLEIL turned out to be around 0.2 Ω, of which roughly half comes from the resistive-wall.
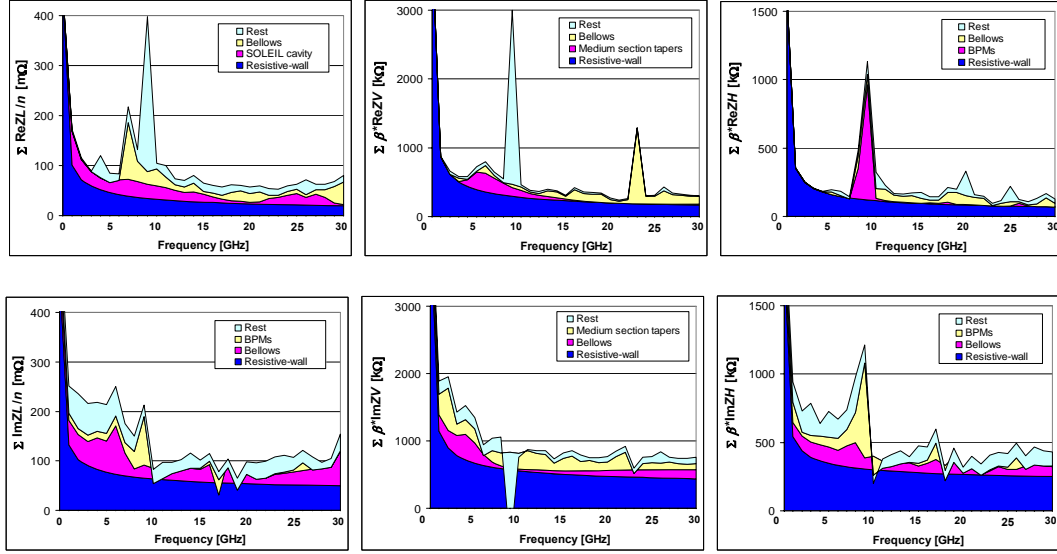

Figure 18: Frequency content of the total impedance in all planes. The three largest contributors are distinguished. Upper: Real part. Lower: Imaginary part. Left: Longitudinal. Centre: Vertical. Right: Horizontal.

4.5.3 Simulation of Beam Instabilities

4.5.3.1 *Codes developed and used*

Since obviously the dynamics involved is totally different, simulations of beam instability were done using different codes for single and multibunch, respectively. In both cases calculations were done basically in two ways in time and frequency domains, and the results were compared with each other. As usual, time domain calculations consist in tracking, while frequency domain calculations solve Sacherer type equations to obtain complex frequencies of different eigenmodes. Tracking codes were developed in house, creating *sbtrack* for single bunch and *mbtrack* for multibunch, respectively. Both codes track macroparticles in the full 6-dimensional phase space. For frequency domain calculations of single bunch, the code *MOSES* [21], or a code developed in house that calculates complex frequencies without modal decomposition, were used. As known, the time and frequency domain methods are complementary; Bunch lengthening and Landau damping effects are difficult to treat in the frequency domain approach, while modal identification is cumbersome with tracking.

The frequency domain code *rwmbi* developed in house solves the Sacherer equation for given head-tail and coupled-bunch modes in a multibunch system. Since the model employed is only valid for cases in which bunches are uniformly filled, however, the

code is incapable of describing the filling pattern dependence that one often observes in reality. This motivated us to develop *mbtrack*, a code that tracks multi-bunches, where each bunch consists of macroparticles, thereby treating both intra and inter bunch wake fields. Details of this development are further described in Sec. 4.5.3.3. All of the internally developed codes are capable of using the impedance data (geometric and resistive-wall) described in the previous chapter. Its procedure is explained in the next section.

4.5.3.2   *Use of numerically obtained wake fields*

Although instability studies for the SOLEIL storage ring date back to as far as the R&D times, some simplified models had to be assumed for the broadband impedance, leaving some ambiguity in the results obtained due to the introduced uncertainty. Having obtained the impedance budget through component-wise numerical calculation with GdfidL and analytical methods (Chap. 4.5.2), we are in the position to re-carry out the instability study with more realistic impedance models. Comparison of the numerically obtained total impedance with the assumed models indicates, commonly in the longitudinal and transverse planes, that the resonant structure assumed around 20 GHz in the models is not present, while the magnitude of inductive components is in good agreement (Figs. 19).
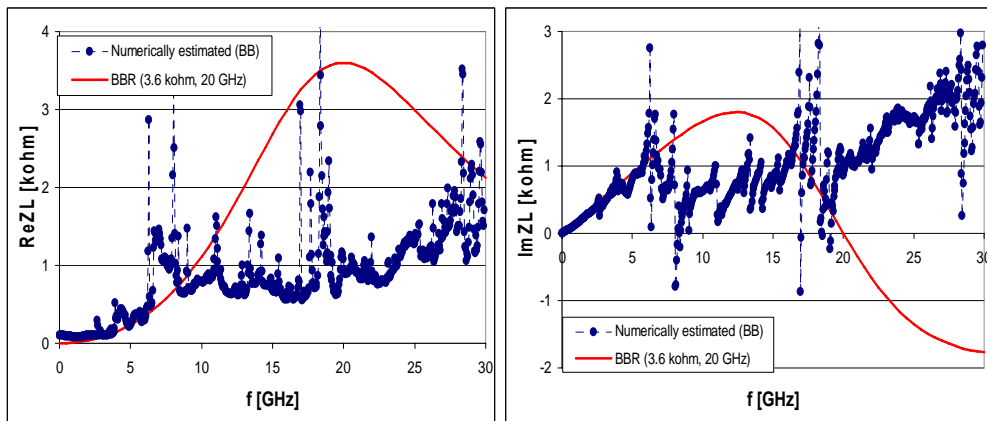
Figure 19: Numerically calculated longitudinal broadband impedance in comparison with the model employed.

The absence of the resistive component is expected to change the instability aspect in both single and multibunch. We may note that a broadband resonance at around 20 GHz was assumed in the vertical plane at the ESRF upon observing the defocusing of *m*=-1 head-tail mode in single bunch, which was later identified as an incoherent tune shift. Unlike the previous models the calculated impedance exhibits a series of narrow band peaks that originate from components such as BPMs, bellows and flanges.

To make use of numerically obtained impedance in the instability simulation, they must be further processed, since, as known, what calculated with impedance codes such as GdfidL are wake potentials. Instead of aiming to deduce the Green's function by reducing the bunch length, we have chosen to fit the obtained impedance in terms of broadband resonators, purely inductive and resistive components, whose Fourier transforms in the time domain are analytically known. Despite being cumbersome, the

76

procedure was carried out for every component longitudinally, considering the fact that the number of components (such as flanges) may vary with time, as well as to have a better insight into the content of the impedance budget. In the transverse planes, however, the decomposition was made on the total impedance due to the lack of time. An example of such fit is shown below for a BPM, which required 15 resonators and a purely inductive term (Figs. 20 upper). The wake potential re-constructed from the fit consistently reproduces the original one to the extent shown (Figs. 20 lower).

The use of purely inductive components was avoided in the transverse planes, as they would represent space charge fields which should not be seen by relativistic particles. Satisfactory results could in fact be achieved using only broadband resonators. The decomposed broadband impedance data, as well as the resistive-wall impedance data taking into account the chamber cross section form factors, local conductivity and metallic layers, are uploaded systematically by the instability simulation codes. For time domain codes, wake functions are firstly constructed.
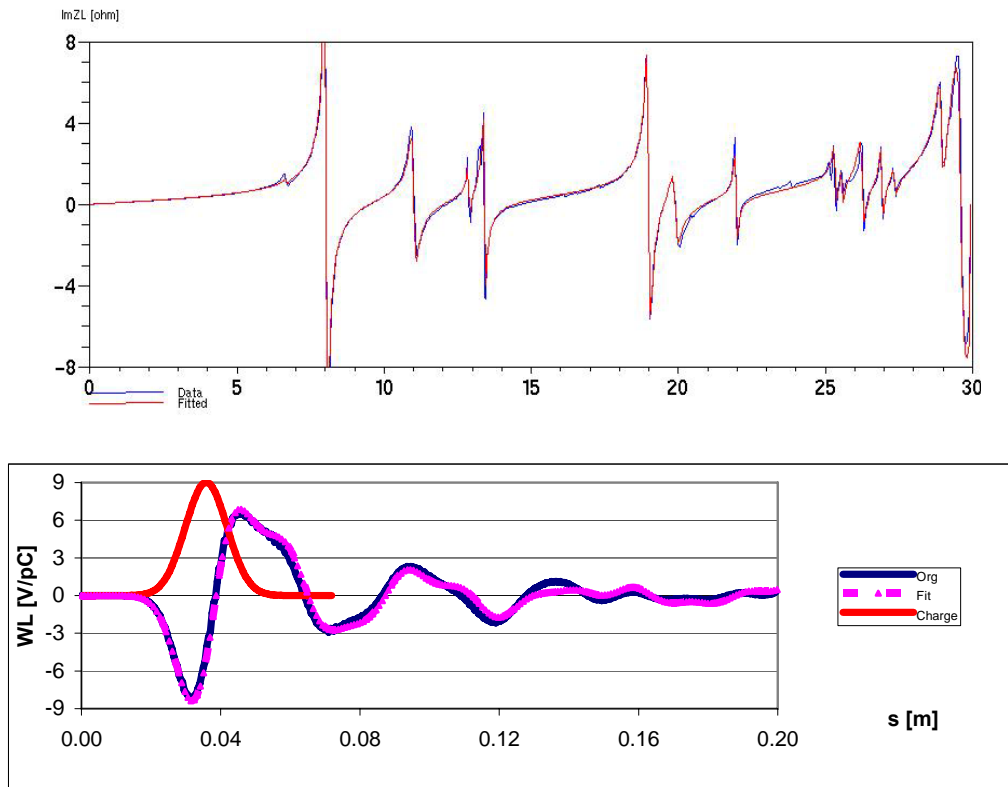
Figure 20: BPM impedance decomposition (upper) and reconstruction of a wake potential (lower).

4.5.3.3   *Development of a Multibunch Tracking Code*

Anticipating low transverse instability thresholds, especially in the vertical plane, as compared to the nominal current of 500 mA in the multibunch mode, it is important to investigate in detail the underlying beam dynamics, especially for different bunch fillings as a function of chromaticity, as already mentioned. The threshold current has

been observed to depend notably on these quantities in several similar machines [22]. Another important element to consider is the betatron tune spread due to the optics nonlinearity that may brings stabilisation. These features being difficult to deal with in the frequency domain approach, a multibunch tracking code had previously been considered and developed, with preliminary results [22]. As the critical issue here being the required computational time, the algorithm has recently been improved to make the computation parallel among tracked bunches using a cluster of processors.

The scheme developed thus consists of a master and slave structure using *pvm* [23], in which each slave in the first step transforms thousands of particles within a bunch with intra bunch forces in the conventional one turn approximation (Fig. 21a). Centre of mass motions, such as dipole moment, are then deduced and sent to the master, which collects the information over all bunches and stores over multiple turns. In the second step each slave adds kicks to particles in a bunch due to the long range resistive-wall forces, by respecting the distance between bunches over multi turns (Fig. 21b). In view of both the distribution of the RW impedance and the short time scale of the betatron motion, the transformation is divided in several steps around the ring with the use of transfer matrices.

The cpu time required to track the uniformly filled 416 bunches containing 5000 particles per bunch over 2000 turns is merely a couple of hours with less than 10 processors.
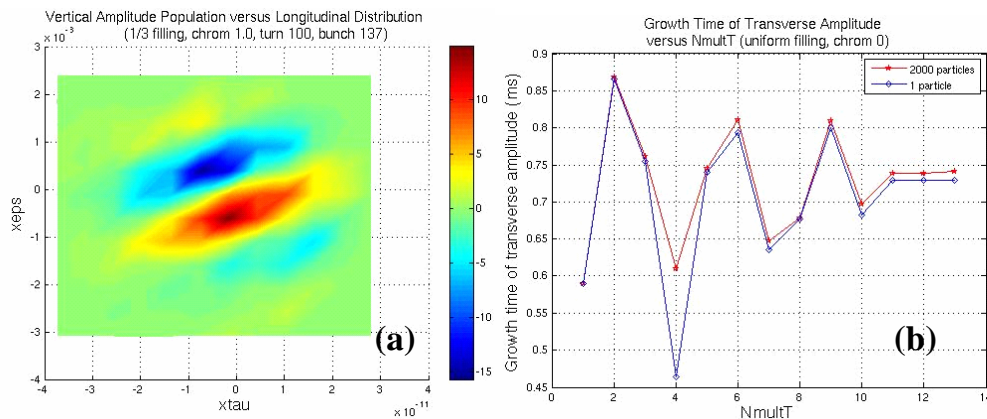
Figure 21: Impact of multi-turn effect on the instability growth rate (left) and bunch internal motion (right).
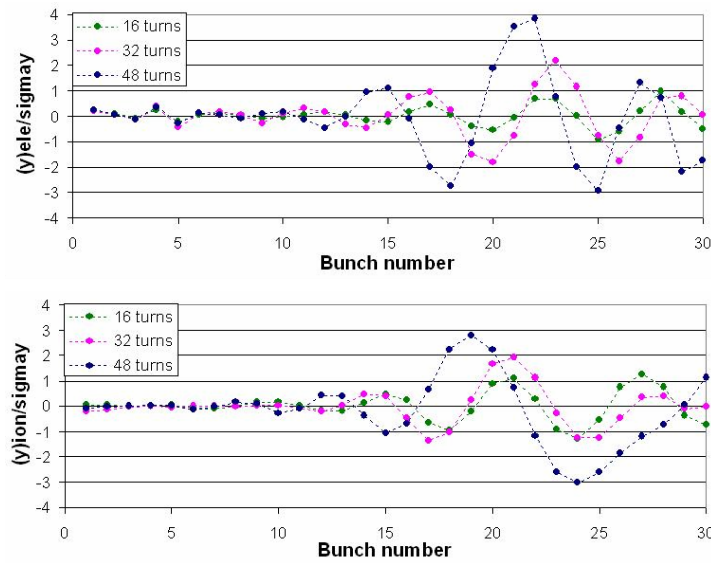
Figure 22: Preliminary result obtained with 30 consecutive bunches and A=28 ions created from 10^{-7} mbar level vacuum (1000 macro electrons/bunch).

In the summer 2007, the code was extended to include fast beam-ion interactions, following the scheme of Raubenheimer and Zimmermann [24]. To conserve the parallel-processed structure, in the first step, each child simulates the ionisation and interaction of ions with a single bunch (parallel-process). In the second step, the sequential passage of electron bunches is simulated and the growing ion distribution interacts with the electron beam. (sequential-process). The code is nearly debugged and ready to produce results.

4.5.4 Observed Beam Instabilities and Comparison with Expectations

4.5.4.1 *Multibunch*

4.5.4.1.1 General Observations

Since the beginning of the commissioning, the transverse multibunch threshold was followed, vertically and horizontally, as a function of the beam filling and the chromaticity (Fig. 23).
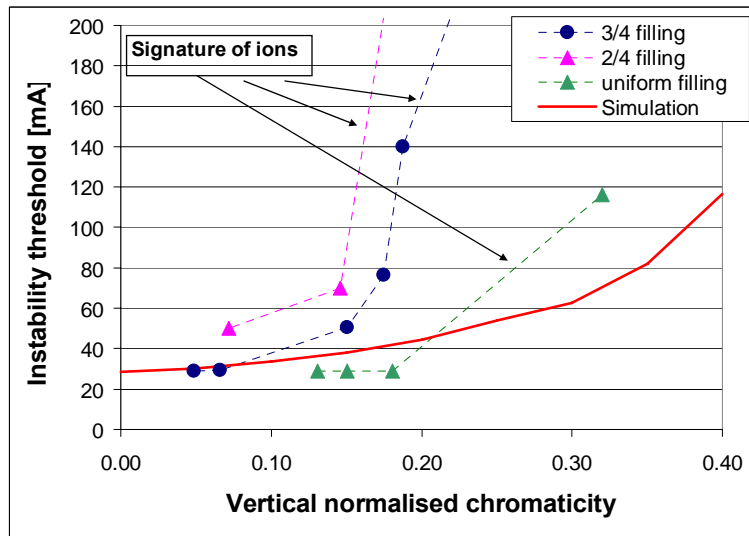
Figure 23: Measured vertical multibunch instability threshold versus chromaticity.

Longitudinally, no coupled-bunch instability has been observed, as anticipated from the use of HOM-free superconducting SOLEIL cavities (see also Chap. 4.5.5). The characteristics of the beam spectrum seen on a spectrum analyzer is that it exhibits transverse oscillation spectra with shapes typical to RW (Fig. 24 left) and beam-ion interactions (Fig. 24 right), the degree of which depending upon beam conditions. With chromaticities close to zero, thresholds appeared at around 30 mA for different fillings vertically, in good agreement with the calculated RW threshold, where indeed RW spectra tended to show up.
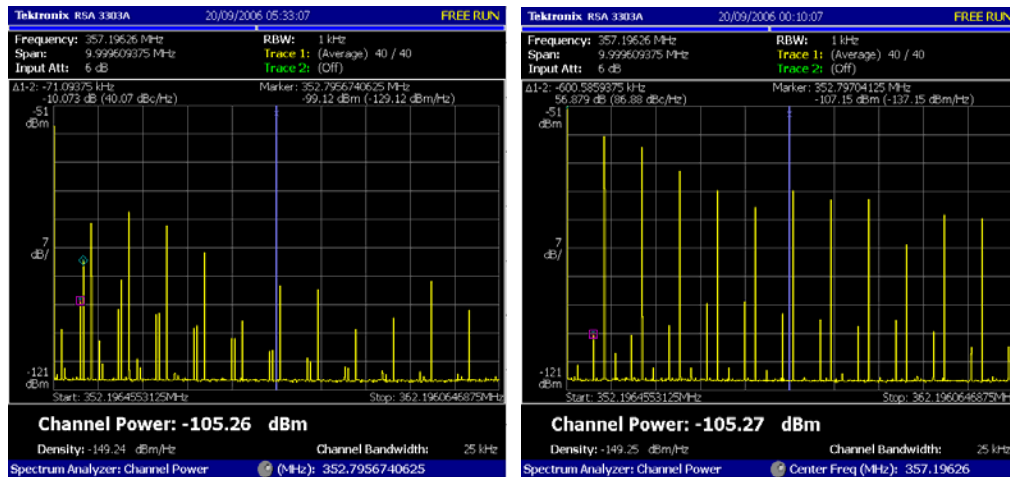
Figure 24: Spectra of vertically unstable beam in 3/4th filling. Left: RW dominated. Right: Ion dominated.
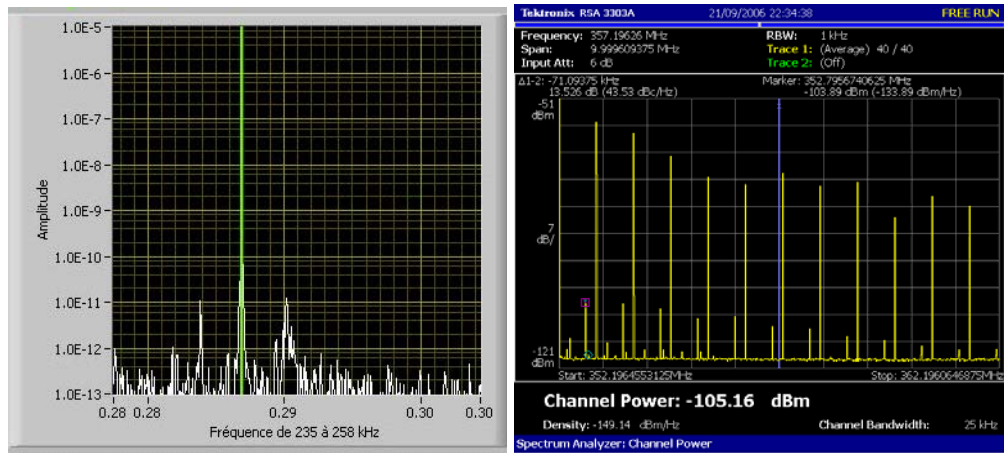
Figure 25: Observation of vertical m=-1 mode excitation in 3/4th filling. Left: Display of relative head-tail modes. Right: Global spectrum.

The rise of the threshold with increasing chromaticity was more pronounced for partial fillings (Fig. 23), where the spectra tended to be more beam-ion dominated. Although the stabilization of m=0 mode seemed to occur with chromaticity values smaller than expected, we could identify the excitation of m=-1 mode that takes over m=0, in accordance with the expectation (Fig. 25 left). Indeed, as anticipated, many sidebands appeared in such cases, due presumably to the latter being excited by the broadband (BB) impedance (Fig. 25 right). The unstable higher-order modes signify that for SOLEIL an alternative means such as feedback must be used to stabilize the beam. Although the observed trend was similar horizontally, with zero chromaticity the beam was unstable at a current much lower than expected.

4.5.4.1.2 Predicted Resistive-Wall Instabilities

Instability thresholds were calculated in the frequency domain, by solving the Sacherer equation and equating the growth rate with that of the radiation damping. As already said, only the case of uniform filling was considered. At zero chromaticity, the preferred value for the operation, unstable modes appear at around 30 mA vertically and 80 mA horizontally, whose numbers grow up to around 90 and 30, respectively (Fig. 26). The computation assumed no broadband (BB) impedance, which anyway has little effect at zero chromaticity.
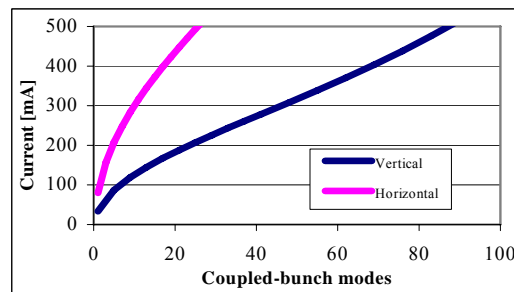
Figure 26: Number of unstable modes versus current at zero chromaticity.

To follow the dependence of the instability on the chromaticity ξ, the knowledge of BB impedance is important. Here, a set of broadband resonator (BBR) impedance, deduced from the ESRF case [22], was initially employed to investigate the more stringent vertical stability: $R_V \cdot \beta = 1.43$ MΩ, $f_{res} = 22$ GHz, $Q=1$. We note that the value of $R_V \cdot \beta$ is close to the estimated budget (Subsec. 4.5.2.3).

It turns out that the current threshold does not rise favourably by increasing ξ (Fig. 27a). Namely, where the higher-order head-tails ($m>0$) are involved, the threshold current remains low. Interestingly, the number of unstable modes shows a minimum around $\xi =0.1$, where $m=0$ gets stabilised while $m=1$ is not yet unstable (Fig. 27b). Above this point, all coupled-bunch modes become unstable once $m > 0$ modes are excited by the BB impedance. Clearly there is an advantage to work at this minimum for the transverse feedback. The behaviour of $m > 0$ modes at $\xi > 0$, as well as the minimum described here were also observed in a study made earlier [25].
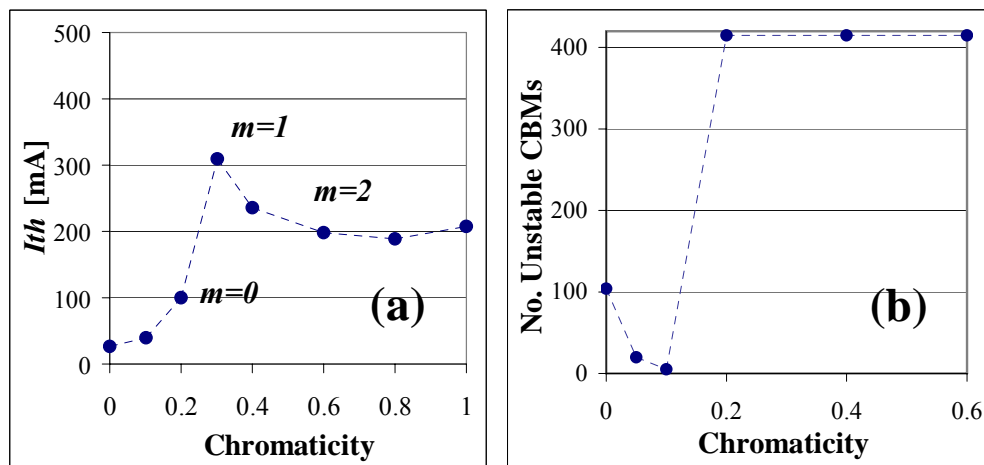
Figure 27: Dependence on the chromaticity (normalised). Left: Vertical current threshold. Right: Number of unstable modes. The computation includes the BBR described in the main text.

Once the procedure was established to utilise the numerically evaluated impedance in the simulation codes as described in Subsec. 4.5.3.2, the instability thresholds were recalculated with the obtained impedance data. The main point of interest here is to see the behaviour of the instability at non zero chromaticity where the broadband impedance plays an important role, namely, to compare with the previous result obtained with the model impedance above.
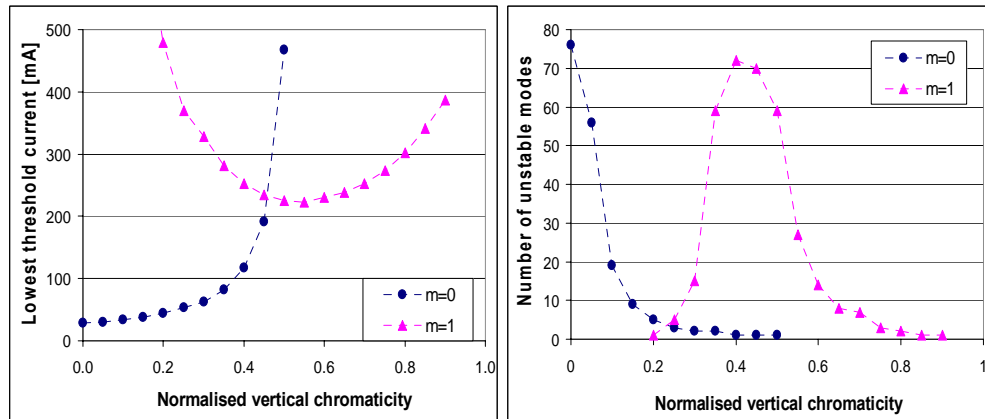
Figure 28: Vertical multi bunch instability. Threshold (left) and the number of unstable modes (right) versus chromaticity.

Reflecting the smaller resistive impedance of the numerically obtained impedance at higher frequencies as compared to the model employed, as stated earlier, the stabilisation of the mode zero with a larger positive chromaticity is found to be much weaker than previously, resulting in requiring as much as the chromaticity of 0.5 to stabilise the instability due to $m=0$ (Figs. 28 left). On the other hand, the instability driven by $m=-1$ mode, which takes over at higher chromaticities, is found to be less harmful. The result indicates that the shifting of chromaticity will not raise the threshold current up to the nominal current of 500 mA, but optical nonlinearity that generates the betatron tune spread could make it possible. There are as many as eighty coupled-bunch modes excited at zero chromaticity and at 0.4, and in between there is a minimum at around 0.2 where the transition of the driving mode occurs between $m=0$ and -1. In the horizontal plane, although the instability is more relaxed as in the single bunch case, the threshold at zero chromaticity is as low as 65 mA. Reflecting the reduced broadband impedance, no $m=-1$ mode instability appears at a positive chromaticity, but it requires the chromaticity of 0.3 to stabilise $m=0$ driven couple-bunch modes.

4.5.4.1.3 Analysis of Digital Transverse Feedback Data

The digital feedback system developed to combat the instability (see Chap. 4.5.6) later provided us with extremely useful diagnosis of the observed instabilities, with its bunch by bunch and turn by turn bunch position data. The instability was followed by switching off the feedback over typically a few milliseconds depending upon the growth rate, to follow the instability (Figs. 29). The evolution of vertical instability was followed in the standard $3/4^{th}$ filling mode with zero chromaticity (Figs. 29-31) at different beam current. At 50 mA, the oscillation amplitude is observed to grow from the head to the tail of the bunch train in a way that reflects the beam current distribution (Fig. 30b).
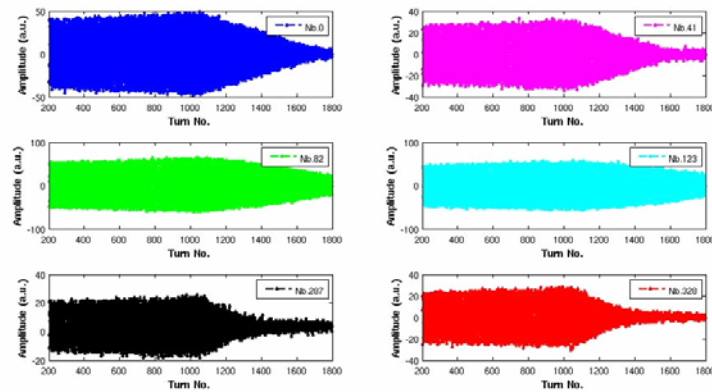
Figure 29: Observed envelops of centre of mass bunch oscillations via transverse feedback.

The oscillation phase evolves smoothly across the bunch train, with the phase shift between adjacent bunches being ~0.9 deg, which is nearly what expected from the strongest RW mode (Fig. 31a, dark blue). At 100 mA, a significant change appears in the bunch oscillation amplitude, with a rapid quasi-periodic variation along the train (Fig. 30c). A similar structure appears on the phase evolution, while the overall slope is still not much different from 50 mA (Fig. 31a, pink). At 250 mA, a dramatic change occurs on the phase where the phase shift per bunch jumps to ~40 deg (Fig. 31a, light blue), constantly across the entire bunch train, while the distribution of the oscillation amplitude remains similar to 100 mA (Fig. 30d).
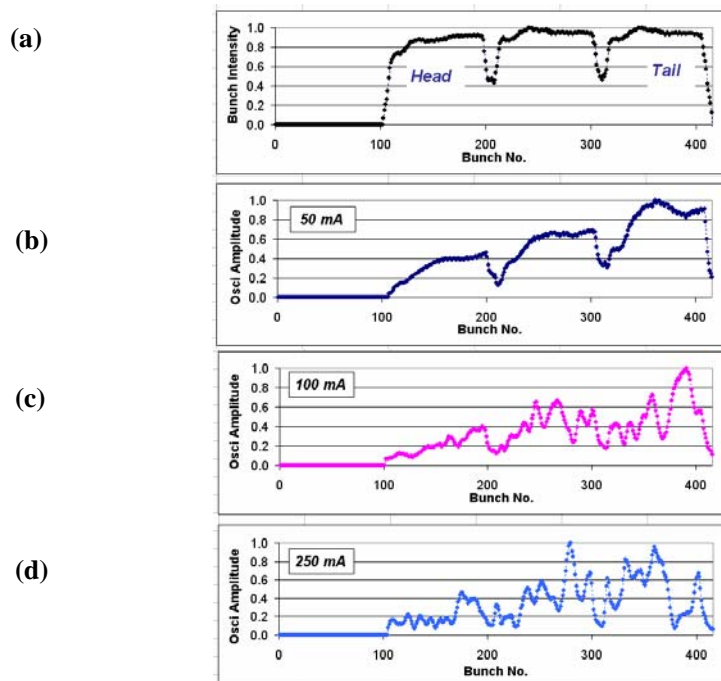
Figure 30: Measured vertical instability in 3/4th filling. Top: Current along a bunch train. Lower three: Oscillation amplitude versus bunch train at 50, 100 and 250 mA.

On the instability growth rate, a large bunch dependent variation appears from 100 mA onwards, although on the average, it increases quasi linearly with beam current, with a slope not far from what expected from the RW instability (Fig. 31b). These observations furthermore support the idea of the mixture of RW and beam-ion instabilities. In all cases, the instability seems to be initialized by the 1/4th of the beam gap. Measurement made in 1/4th filling finds these aspects to be more pronounced for a given beam current, indicating the bunch current dependence of the phenomena, which in turn suggests the presence of fast beam-ion instability.

It may be worth noting that with the gradual improvement of the vacuum in the machine, it became apparently more difficult to encounter RW dominated instability. Namely, it appears as if the threshold of the fast beam-ion instability in the tail of a bunch train became lower than that of the RW instability. Whether worse vacuum could trigger the RW instability via enhanced beam-ion interactions is a point that needs to be verified with full numerical studies.
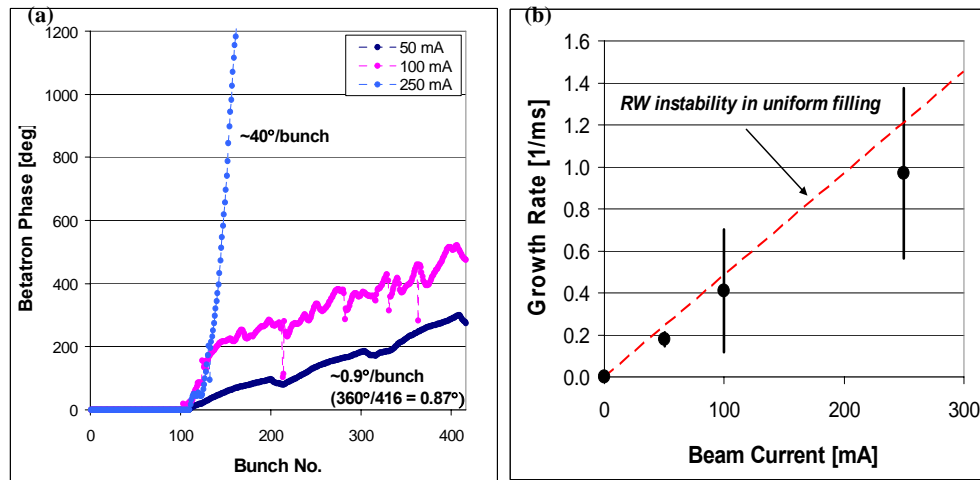
Figure 31: Left: Phase of vertical bunch oscillations measured at 50, 100 and 250 mA in 3/4th filling. Right: Measured average vertical growth rate versus beam current and that expected from RW instability.

Analysing the data acquired by the bunch-by-bunch feedback system, some of them revealed beam oscillation spectra as shown in Fig. 32, where interestingly, the peak of the spectrum matches well the oscillation frequency of ions with the mass 28, which equals that of CO, which in turn is considered to be one of the major components of the residual gas in the vacuum chamber. Along with other observations as seen in Figs. 29-30, the deduced beam spectra constitute a strong support of the idea that the concerned instability is caused by beam-ion interactions.
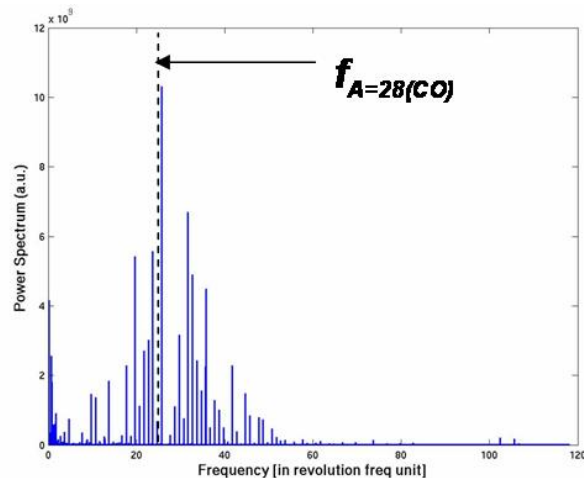
Figure 32: Beam spectrum at 250 mA in 3/4th filling reconstructed with ADC data.

4.5.4.2   Single bunch

4.5.4.2.1 General Observations

The measured transverse mode coupling instability (TMCI) threshold turned out to be lower than the expected by nearly a factor of two both vertically and horizontally (Fig. 33). It signifies underestimation of the effective imaginary impedance, composed of RW and BB impedance, by the same factor. In the horizontal plane, the coherent detuning is seen to be largely cancelled by the incoherent tune shift arising from the chamber cross section asymmetry. In deducing the coherent detuning, the incoherent tune shift is subtracted in both planes.
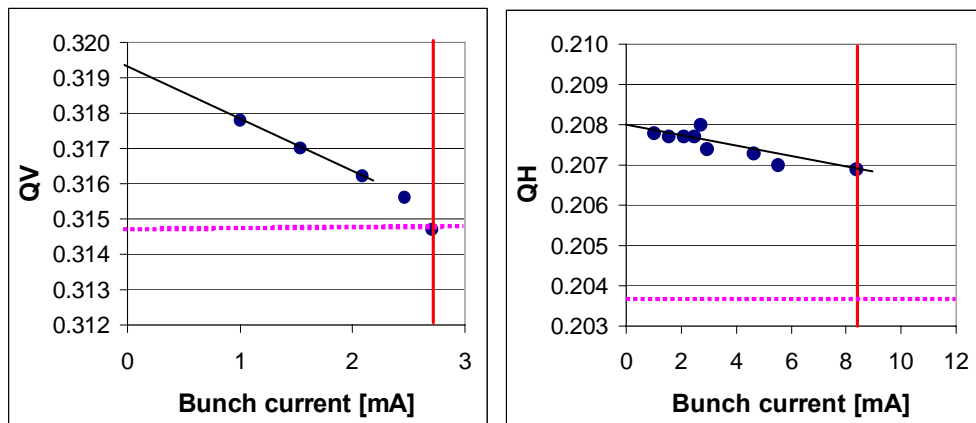
Figure 33: Measured dipole detuning. Left: Vertical. Right: Horizontal. Red line: TMCI threshold. Pink line: One synchrotron tune separation from the zero current tune.
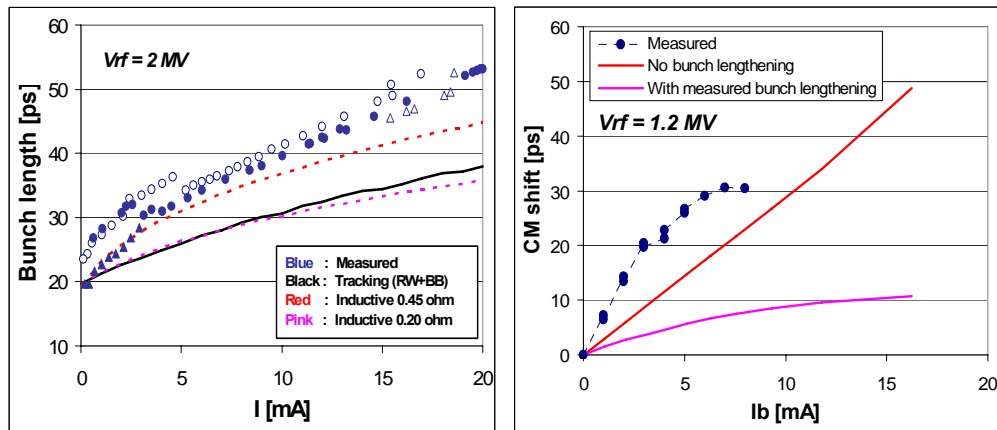
Figure 34: Bunch lengthening (left) and synchronous phase shift (right) measured with a streak camera.

The bunch lengthening and the synchronous phase shift were measured with a streak camera as a function of single bunch current (Fig. 34). Again, the measured values are larger than the expectation. In particular, the fit of the measured bunch lengthening with a purely inductive model requires the impedance of ~0.45 Ω, which is roughly a factor of two above $|Z/n|_{eff} = 0.2\ \Omega$ of the impedance budget. Note that the lengthening due to the purely inductive impedance of 0.2 Ω agrees well with the tracking result using the impedance budget (Fig. 34). On the other hand, the discrepancy on the synchronous phase shift may well be due imprecise evaluation of resistive impedance at high frequencies.

There are reports showing that NEG coating on Al chambers creates granular surface. Besides, an anomalous increase of the reactive impedance was measured in Elettra when NEG coated Al chambers were installed [11]. In fact, if we assume 1 μm of granular variations on the surface of our NEG coated Al chambers, as measured at the ESRF on one of their chambers [13] (Fig. 35a), the observed discrepancy on the imaginary impedance could be explained using the model proposed by K. Bane et al [26]. On the other hand, analysis of SOLEIL Al chamber indicated that, the surface roughness is ~0.3 μm in rms azimuthally and much less in the direction of beam circulation, reflecting the extrusion (Fig. 35b). Moreover, at SOLEIL, the coating thickness was reduced to 0.5 μm for precaution. The electron microscope on sample coupons found no degradation of the roughness after coating (Fig. 35c). To evaluate the roughness impedance the model proposed by G. Stupakov that employs the small angle approximation [27] is suited for such surface instead of the above model. Taking into account directivity of the roughness, the model predicts that the roughness impedance is totally negligible.
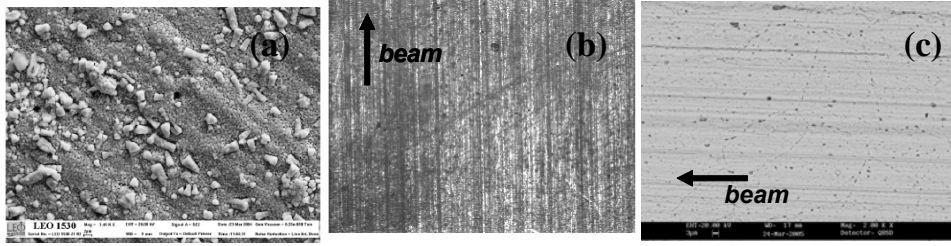
Figure 35: Surface of a NEG coated Al chamber (left) measured at the ESRF [13]. Surface of a SOLEIL Al chamber before (middle) and after (right) NEG coating.

4.5.4.2.2 Predictions from Single Bunch Tracking

The single bunch tracking code *sbtrack* mentioned in Sec. 1.1.3.1 was used to follow the collective effects. As the high bunch current mode of operation envisaged for SOLEIL consists of eight bunches of 10 mA each, studies focused in this current range.
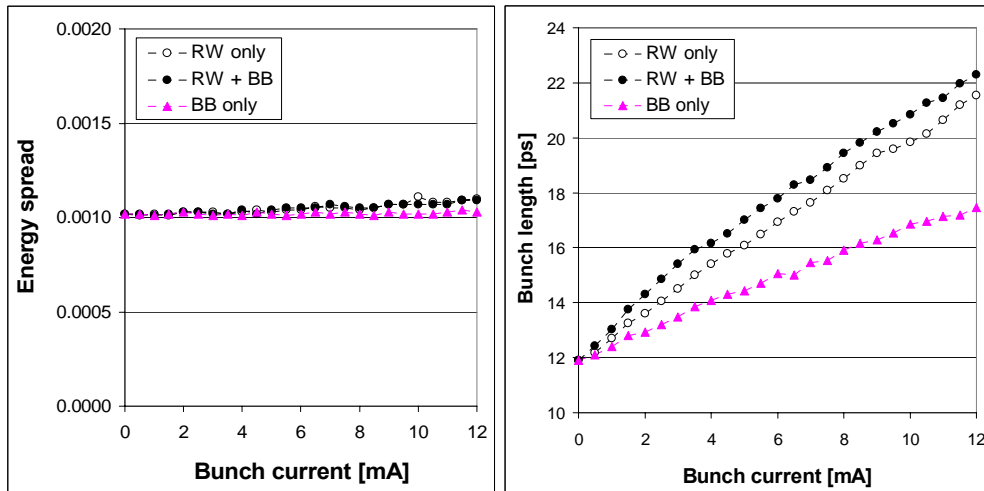
Figure 36: Bunch lengthening (left) and energy spread widening (right).

It may be noted that in treating the RW field in the longitudinal plane, its $|t|^{-3/2}$ dependence on the time variable t as obtained by Fourier transforming the standard impedance formula was found generate wrong wake potentials due to its diverging behaviour at short range. This mathematical problem was overcome by following the work of Henry and Napoly [28], who investigated the correct short range behaviour of the RW Green's function. The bunch length and the energy spread versus bunch current obtained from the tracking show that; -The bunch length is less than the double of its zero current value at 10 mA. -No energy spread widening is observed up to 10 mA. The large tapers in the cavity section however bring the microwave threshold down to approximately 20 mA. -The RW impedance is contributing more to the bunch lengthening than the broadband impedance. To complete the longitudinal evaluation, the effect of NEG coating must be included, which is expected to enhance further the RW contribution (Subsec. 4.5.2.2.2).
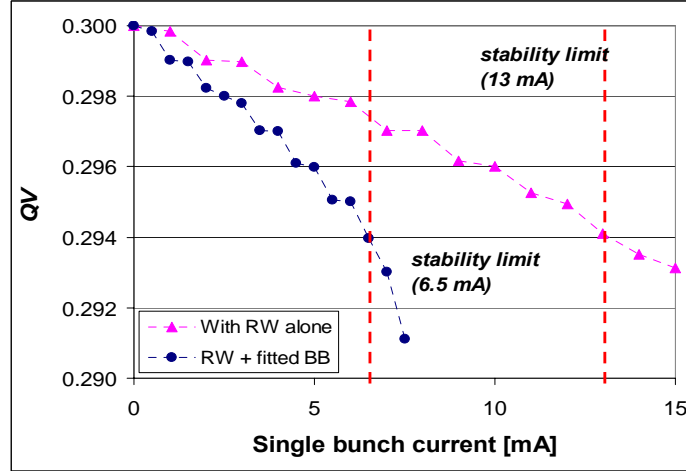
Figure 37: Vertical single bunch instability

In the vertical plane at zero chromaticity, the current ramp is blocked around 6 mA due to the mode coupling (TMCI) between m=0 and -1. Distinguishing the relative contributions, the RW is found to contribute comparably to the broadband impedance to the mode zero detuning. Again, inclusion of the effect of NEG coating is expected to enhance the contribution of the former. Increasing the chromaticity to positive values, the threshold remained unchanged, with instability taken over by the head-tail instability of m=-1, -2, … Inclusion of bunch lengthening however enabled to go above 10 mA with the normalised chromaticity of 0.3. The situation is much more relaxed in the horizontal plane finding the TMCI threshold at around 30 mA.

4.5.4.2.3 Evaluation of Incoherent Tune Shifts

Non-circular chambers with finite resistivity create current-dependent quadrupole fields [29], which generate incoherent betatron tune shifts. The scheme developed earlier by one of the authors (RN) to quantify the effect [30] was improved as follows: On top of evaluating the chambers piecewise around the machine as already described, the focusing strength derived via the formulation of K. Yokoya [29] has now the time dependence according to A. Chao et al. [31]. Namely, the field diffusion is computed as an explicit function of the aperture, wall thickness, resistivity and time, thus eliminating the artificial parameter used earlier. Other details are found in Ref. 30.

Applying it to SOLEIL, tune shifts of as large as ~0.025 are found at 500 mA in uniform filling, horizontally and vertically. Measured tune shifts however appear to be roughly half of the expected values. While the NEG coating is not expected to have any effect in multibunch as the zero frequency field dominates, for single bunch its contribution is taken into account, thanks to the relation in the horizontal impedance $(Z_H)_{incoherent} = -(Z_H)_{coherent}$ for flat chambers. The effective focusing strength felt by a particle in single bunch is then given by

$$< k_{effs} > \ = \ \frac{4\pi}{Q} \cdot \frac{1}{E/e} \int_0^\infty \widetilde{\rho}(\omega)^2 \cdot \mathrm{Im}\, Z_H(\omega)\, d\omega \qquad (5)$$

where Q denotes the total bunch charge, E, the beam energy, $\tilde{\rho}(\omega)$, the Fourier transform of the bunch density, and $Z_H(\omega)$ is the coherent horizontal impedance. The two-metallic layer impedance formula of Ref. 10 is used when considering the NEG coating. Tune shifts in single bunch are again found to be comparable in the two transverse planes. With NEG, they reach nearly 0.0035 at the nominal current of 10 mA.

The impact of resistive-wall on the coherent dipolar tune shift in single bunch is then estimated. Tune shifts are computed as the sum of coherent and incoherent parts, both taking account the NEG effect. The results show that the NEG increases the dipolar detuning in both transverse planes (Figs. 38). With the synchrotron frequency being close to 6 kHz, a naïve estimate of the vertical TMCI threshold gives 14 mA without NEG, which is reduced to 8 mA with NEG. Clearly, the important contribution of numerically calculated BB impedance (Subsec. 4.5.2.3), must be added to make a more realistic estimate.
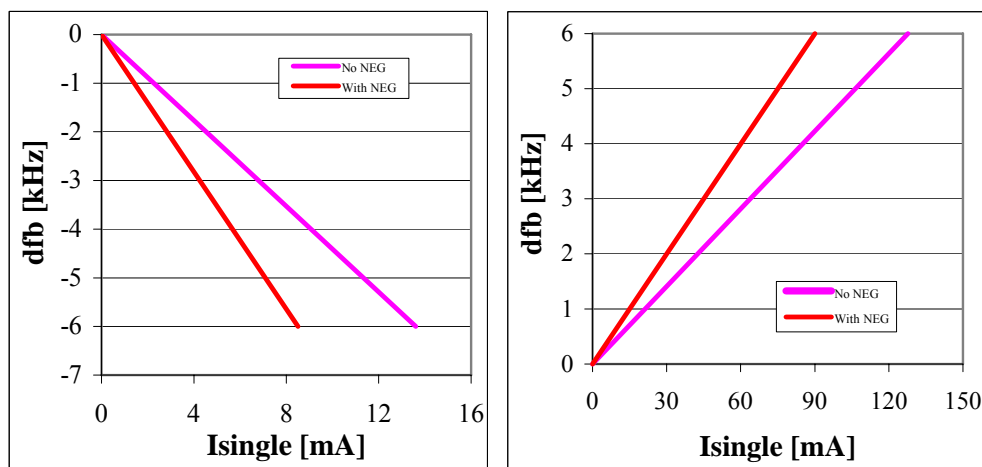
Figure 38: Calculated dipole mode detuning due to resistive-wall, vertical (left) and horizontal (right).

4.5.5   HOM Free RF System Developed at SOLEIL

4.5.5.1   *SOLEIL Cryomodule and HOM Damping System*

In the storage ring of SOLEIL two cryomodules (CMs) will provide the RF power of 600 kW and the accelerating voltage of 4 MV required at 352 MHz with full beam current of 500 mA and all the insertion devices [32]. The SOLEIL CM (Figs. 39 and 40) consists of a cryostat containing two 352 MHz single cell superconducting cavities individually powered with a 190 kW solid state amplifier [33]. The cavities, made of Nb deposited on copper, are enclosed inside Helium tanks where they are immersed in a bath of liquid helium at 4.2 K. Both CMs are supplied in liquid Helium from a single cryogenic source [34]. The cavities were especially designed for SOLEIL with a strong damping of the parasitic High Order Modes (HOMs). This is achieved by means of four HOM couplers, which are located on the central tube connecting the two cavities. Their design is rather similar, of coaxial type terminated by a coupling loop, but two of them (L-type) have their loop oriented parallel to the beam axis, coupling mainly the

longitudinal (or monopole) modes, while the other two (T-type), with their loop perpendicular to the beam axis, are dedicated to the transverse (or dipole) modes. Moreover, for the latter (Figs. 41), which stand closer to the cavities, a notch filter is required to reject the coupling at the fundamental frequency. This filter can be tuned, once the coupler is bolted on the cavity, thanks to an external mechanism which, via a single wave bellow, allows adjusting the gap between the stub and the coupler wall. Both types of HOM couplers are made of bulk niobium (RRR > 200) and are cooled with LHe, derived from the cavity tanks and circulating through their loops. They are connected to external loads through coaxial lines housing a vacuum ceramic window and designed to extract up to 5 kW of power.
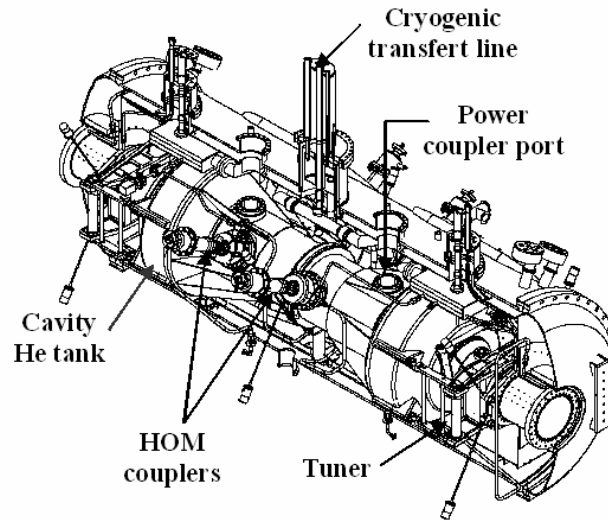
Figure 39: 3D-layout of the cryomodule

Figure 40: Cryomodule in the storage ring
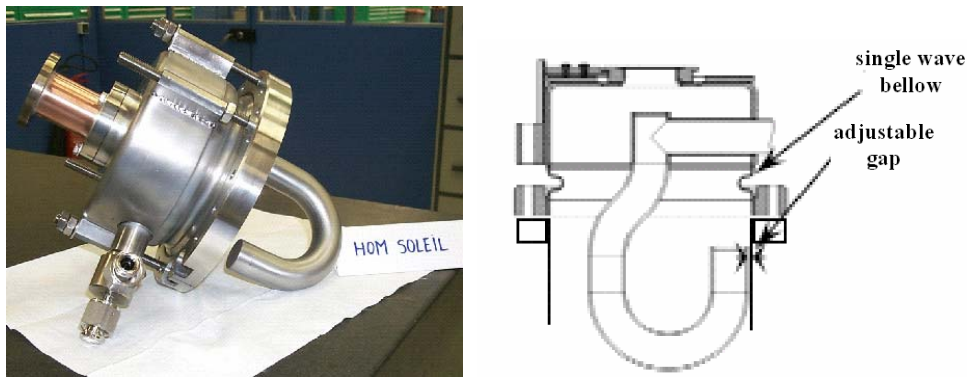
Figure 41: T-type HOM coupler

4.5.5.2   RF System Commissioning and First Operational Experience

During the summer of 2006, one half of the SR RF system (CM1, 2 amplifiers, the associated cryogenic plant, control and LLRF systems) was commissioned, as scheduled for the first year of SOLEIL operation with I_{beam} < 300 mA and a reduced number of insertion devices. The goal of storing up to 300 mA of stable beam, using a single CM, was quickly achieved [35, 3]. At first, without RF feedback, the cavity was slightly detuned in order to cope with the Robinson instability, at the expense of some extra power: at 300 mA, 145 kW incident power, of which 10 kW reflected (1 kW from mismatch + 9 kW from detuning) with 1 MV on each cavity. Figs. 42 shows the effect of detuning on the Robinson stability (ψ is the tuning angle which is automatically set by the tuning loop at any current level): when fully compensating for the reactive beam loading, the beam was lost at a current threshold $\sim$ 230 mA (left graph); by introducing a tuning angle offset of 4° we could insure the stability up to 300 mA (right graph), at the expense of 9 kW extra reflected power, as mentioned before.
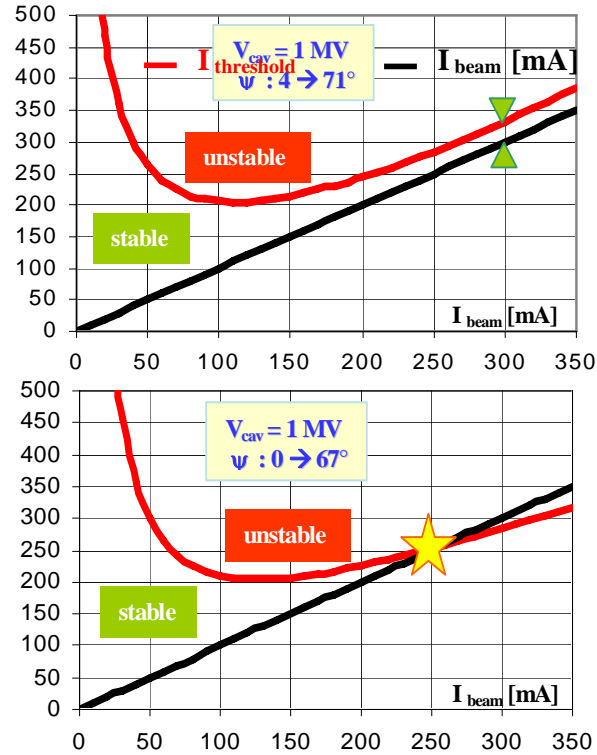
Figures 42: Effect of detuning on Robinson stability

Operating at a larger voltage could also improve the stability but at the expense of an increased reflected power from mismatch. Later on, we have commissioned the RF feedback, which enabled to store up to 300 mA stable beam without any tuning offset, hence saving 9 kW of reflected power.

A diagram of the low level RF (LLRF) system, which is currently in use [36], is shown in Fig. 43. It consists of three fully analogue relatively slow control loops for the frequency, amplitude and phase, complemented with a fast direct RF feedback in order to deal with the Robinson instability at high current as previously discussed. It allows achieving a cavity voltage stability of $\pm$ 0.5% in amplitude and 0.15° in phase without the RF feedback, $\pm$ 0.1 % and 0.05° with the RF feedback, respectively. A fast digital version of the LLRF, based on a FPGA and a I/Q modulator, is presently under development [36]; its tests in real environment should be completed in forthcoming runs dedicated to machine developments.
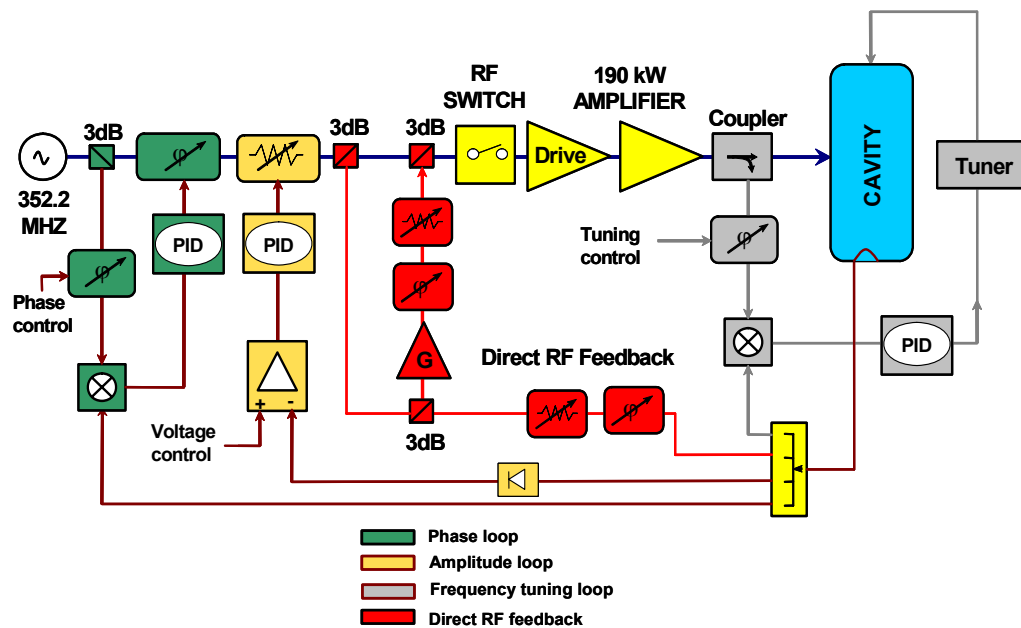
Figure 43: Analogue LLRF system

All results presented up to this point were obtained with the tuning loop continually active, compensating partially (without RF feed-back) or fully (with RF feed-back) for the reactive beam loading. The blue plot of Fig. 44 shows the required RF power versus beam current for the latter case with a cavity voltage of 1 MV : 28 kW, fully reflected (from mismatch) at zero current, up to 135 kW at 300 mA (matched and tuned). Under these conditions, frequency changes of ~ 4 kHz, corresponding to about 10 000 motor steps, are required at each injection.

Injection at constant tuning and variable voltage

Considering some difficulties encountered on the Super-3HC cavities at ELETTRA with a similar tuning system, which happened to get stuck after roughly fifty millions of motor steps [37], it was proposed to operate at constant tuning during the injection, in order to use the tuners more sparingly [38]. Fig. 44 shows that injecting at constant tuning requires a ramping of the voltage; otherwise this would result in too large amount of reflected power at low beam current (red/black plots). Ramping the cavity voltage from 650 kV at 0-current, up to 1.4 MV at 300 mA, with a fixed tuning angle of 60°, allows to maintain the reflected power below 50 kW and the maximum required power at 145 kW (green plot). In return, at voltage as low as 1.3 MV (650 kV / cavity), the energy and phase acceptance are significantly reduced [38]. However, the experience has demonstrated that it is acceptable as the injection efficiency is nearly unaffected when adjusting the injection phase (from BO to SR) with the voltage.
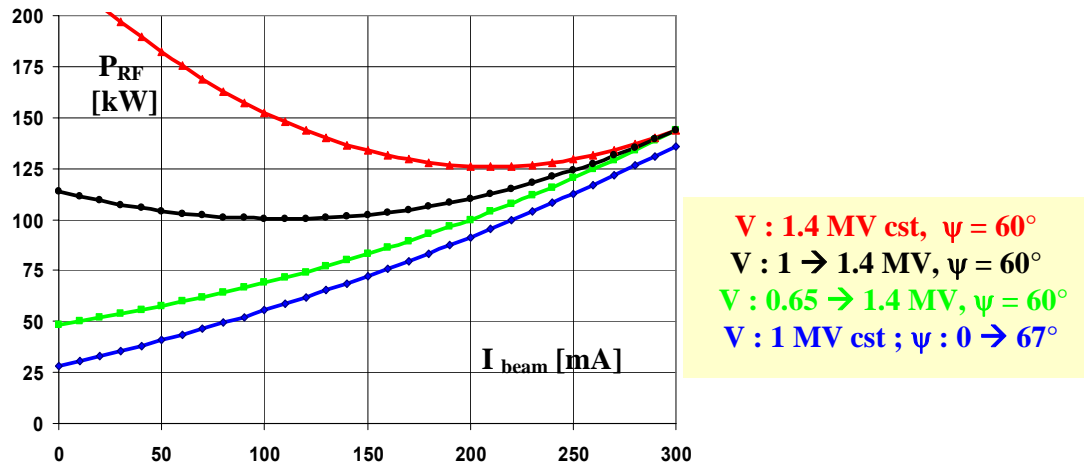
Figure 44: RF power versus I_{beam} for variable (blue) and constant (red, black, green) tuning

Fig. 45 shows that, at constant tuning, the shape of the Robinson stability limit (in red) is completely different than with variable tuning (lower graph of Fig. 43) : it has become quasi linear with the current and the stability margin remains quite comfortable up to 300 mA, even without RF feedback.

The injection at constant tuning and ramped voltage is now routinely used in operation. A software application, programmed in the PLC dedicated to the RF control, set the cavity voltage and phase as a function of the stored beam current ($V = V_0 + k.$ I_{beam} ; $\Phi = Arcsin \Delta U/V$). The switching from the constant to variable tuning modes is fully automated.
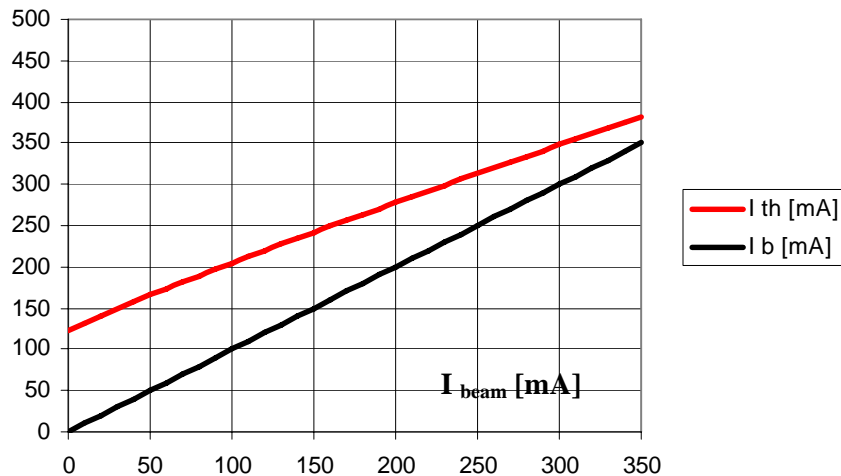
Figure 45: Robinson stability for the constant tuning case

The first operational experience has also confirmed the real efficiency of the HOM damping system: up to 300 mA, there is no evidence of HOM excitation; the power dissipation in the HOM loads remains negligible and the residual beam phase oscillations below 0.1° rms.

More generally, after about 7 000 running hours, all parts of the RF system, CM, cryogenic plant, high power solid state amplifiers, LLRF and control, have demonstrated an outstanding reliability in operation. The construction of the second half of the system is being completed and its implementation, scheduled for September 2008, should allow achieving the full performance (500 mA and 4 MV).

4.5.6 Development of a Transverse Feedback System

4.5.6.1 Introduction

Table 1 summarises the machine parameters related to the transverse feedback. As previously stated, the combination of the high current modes of operation both in terms of total and local intensity, along with small vertical vacuum chamber aperture adopted all around the machine to match low insertion device gaps, results in severe transverse collective beam instabilities, also confirmed with simulation studies. In particular, it was observed in reality that shifting of chromaticity to large positive values, a known remedy against these instabilities, is not effective at SOLEIL, due to excitation of higher order head-tail modes at high current, as predicted. Moreover, the electron beam appears to be driven strongly unstable by ions existing in the chamber. Foreseeing this situation, it had been decided to install a digital bunch by bunch transverse feedback system, with an objective to keep the beam stable at zero chromaticity without spoiling the small emittance (Table 3), as well as to make it operational since the beginning of the user operation.

Table 3: SOLEIL machine parameters related to transverse feedback.

Energy [GeV]	2.75
Nominal current [mA]	500, 8×10
Revolution frequency [kHz]	846.2
RF frequency f_{RF} [MHz]	352.2
Harmonic number	416
Fractional betatron tunes $\Delta Q_H/\Delta Q_V$	0.2/0.3
Synchrotron frequency [kHz]*	2.4
Betatron phase advance between detector and kicker**	0.0
Beta values at detector β_H/β_V [m] **	10/10
Horizontal emittance [nm·rad]	3.7
Vertical emittance [pm·rad]***	5.0

*At RF voltage of 2.0 MV
**In the present configuration
***Measured at low beam current

4.5.6.2 Developed Scheme

Due to the imposed time constraint and the initially limited expertise in the concerned domain of technology at SOLEIL, the strategy adopted was to make use of already existing schemes and devices developed in other labs. We have followed particularly the systems developed at ELETTRA, the ESRF and SPring-8.

4.5.6.2.1 Beam Position Detector

We have started from investigating whether our SOLEIL BPM had enough sensitivity to meet our requirement. Evaluating the signal level induced on an electrode with 500 mA beam current having rms bunch length of 20 ps as a function of frequency, the peak is found around 1.4 GHz, which is roughly four times f_{RF}, the RF frequency (Fig. 46). Signal levels at the end of a 22 m long 50 Ω coaxial cable of several different types are also shown in the figure. Taking the best case (CNT 600) and including the effect of a hybrid operation that creates a sum signal at the end of the cable, the peak difference signal is found to have the sensitivity of Δ_{peak} of 47 µV/mA/µm. The obtained sensitivity is used to evaluate the noise level at the exit of the RF frontend.
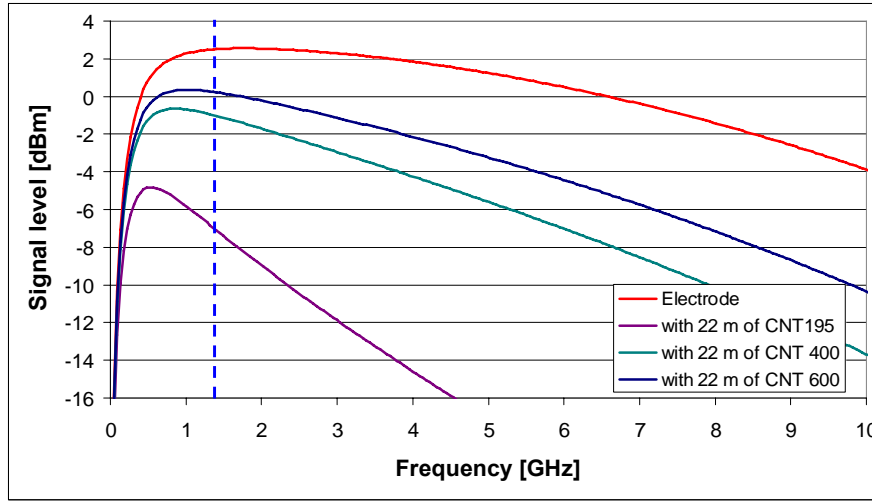
Figure 46: Sensitivity of a SOLEIL BPM against 500 mA beam (1.2 mA/bunch and bunch length of 20 ps).

4.5.6.2.2 RF Front-end

On the basis of the frequency dependence of the BPM sensitivity as found above, the ESRF scheme was followed to extract a band ($f_{RF}/2$) of beam signal at four times f_{RF} and down convert it to the baseband (Fig. 47). Fabrication of such RF frontend was made in house. The measurement precision was evaluated from the thermal noise generated in a 50 Ω cable transporting the 1.4 GHz band of signal, the noise amplification and the baseband conversion in the frontend. By comparing it with the above 47 µV/mA/µm, the resolution σ_δ at the entrance of the ADCs of the digital processor was deduced to be around 1 µm at 1 mA bunch current. On the other hand, Nakamura derived an equation that relates σ_δ to the rms beam size σ_z arising from the feedback, due to its limited resolution, given by $\sigma_z \sim \sqrt{T_0/\tau_{FB}} \cdot \sigma_\delta$, where T_0 is the revolution time and τ_{FB} is the feedback damping time [39]. Assuming $\tau_{FB} = 0.3$ ms, a desired value, which was also confirmed achieved from the measurement (see below), we get $\sigma_z = 0.06$ µm at 1 mA. This means that the feedback induced beam size will not exceed one tenth of the vertical beam size (~10 µm) above the bunch current of 0.06

mA, or equivalently, the total current of 19 mA in the standard ¾ filling mode. We have thus concluded that the sensitivity of a SOLEIL BPM is sufficiently high.
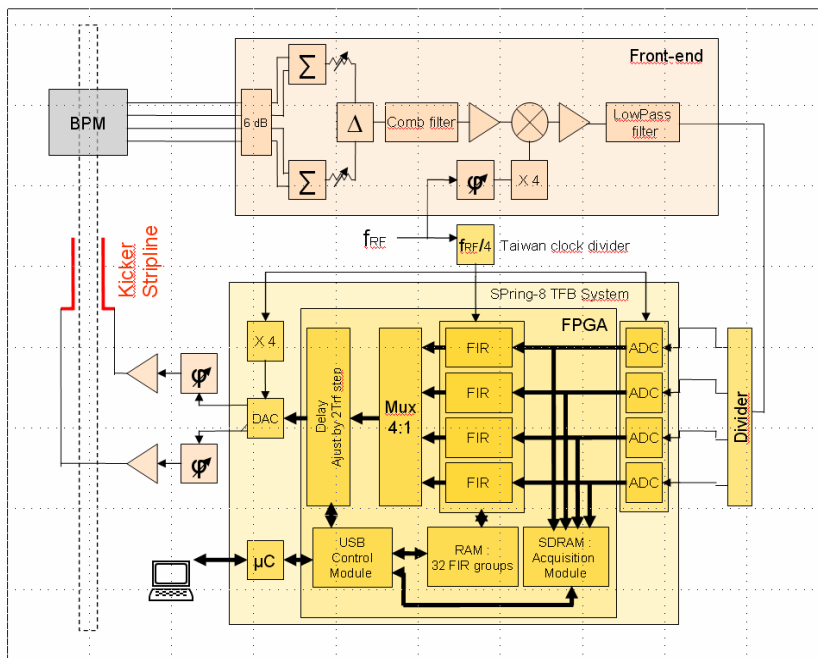
Figure 47: Layout of the SOLEIL feedback chain.

4.5.6.2.3 Digital Signal Processor

Among several solutions that were available, the digital signal processor developed at SPring-8 was chosen primarily for its proven performance in different machines. Details of its characteristics may be found elsewhere [40]. Here we merely note that it consists of 4×12-bit ADCs working at 88 MHz, $1/4^{th}$ of f_{RF}, and having an analog bandwidth of 750 MHz. All FIR filters and multiplexers are integrated into one FPGA board, which allows achieving a latency of less than 1 turn (Fig. 47). The DAC has also 12-bit and works up to 1 GS/s. It must be mentioned that the willingness of the SPring-8 team to collaborate with SOLEIL, along with their expertise, was appreciable aid for the development of the present system.

4.5.6.2.4 Kicker

An extension of the already installed stripline, used for the tune measurement, was made to develop one that has higher shunt impedance, in view of generating a large beam deflection with a reasonable amount of power. In view of the strong vertical single bunch instability, a two-electrode structure (Fig. 48) was adopted for a vertical stripline for its much higher attainable shunt impedance as compared to a four-electrode structure, although the latter works in both transverse planes. The developed stripline achieves the shunt impedance of ~66 kΩ at 50 MHz [41]. It has recently been installed in the ring and commissioned (March 2008), where first tests indicate quite promising results in both single bunch and multibunch. Up to this point, an existing short-circuited stripline, the shunt impedance of which is estimated to be ~0.6 kΩ, has been used for the feedback as a temporary solution.
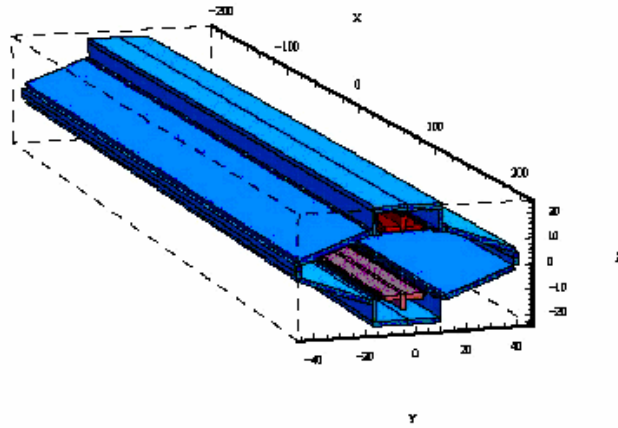
Figure 48: Two electrode type vertical stripline developed at SOLEIL.

4.5.6.2.5 RF Amplifiers

The necessary RF power was evaluated from the instability growth rate calculated with the impedance budget of the machine and the expected shunt impedance of 66 kΩ at 50 MHz attained for the developed vertical stripline. Estimating the maximum betatron amplitude damped by the system upon the condition $\tau_{FB} < \tau_G(I)$, where $\tau_G(I)$ denotes the current dependent instability growth time, we obtain the results as shown in Figs. 49, for the multibunch (left) and single bunch instabilities (right), respectively.
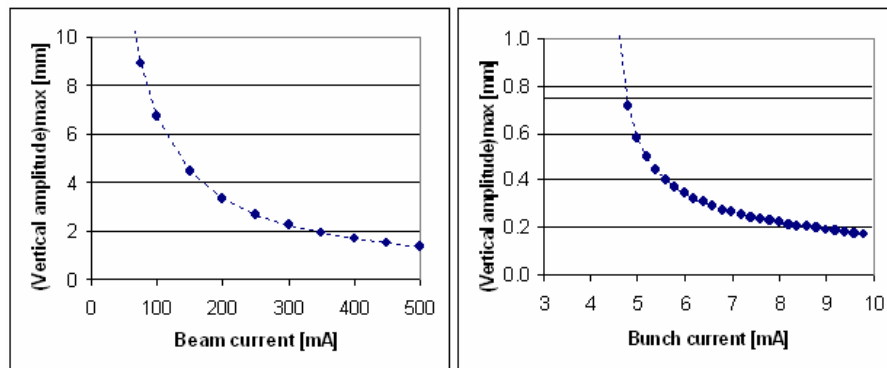
Figures 49: Estimated maximum current-dependent betatron amplitude damped by the feedback system.

A total RF power of 150 W (75 W per electrode) is well suited for the current-dependent resolution in position detection discussed above. Three units of 75 W (10 kHz-250 MHz) amplifiers were purchased.
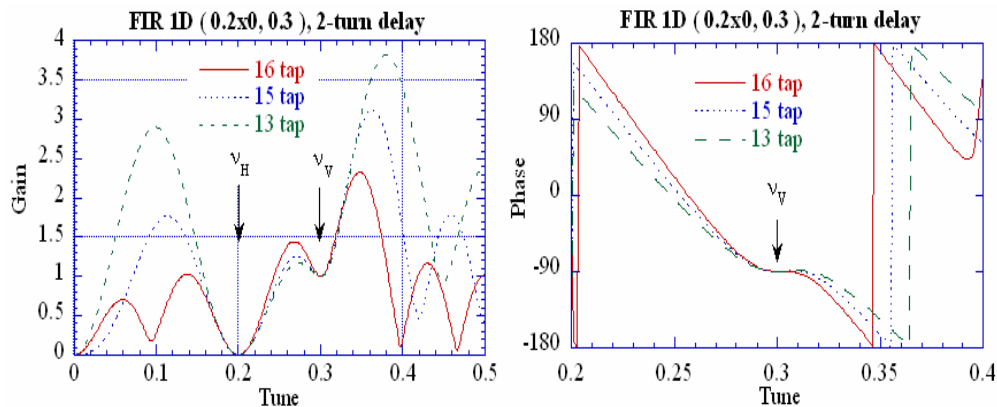
Figure 50: Phase and gain of the FIR filters.

4.5.6.3   *Commissioning of the System*

The entire feedback chain was commissioned with beam during two machine shifts in December 2006, in collaboration with SPring-8. As noted earlier, a shorted type 4-electrode stripline, dedicated to the tune measurement, was used as a provisional kicker, and a BPM in its vicinity as a detector (Table 3). The RF frontend was placed in a nearby rack. For easier operation, the digital processor and its dedicated pc were placed in the control room. The digital filtering was performed using a 16-tap FIR, according to the least-square fit of the betatron oscillation scheme developed by Nakamura [40]. The optimized gain and phase of the filter are shown in Figs. 50 for the vertical case. Taking into account 1.12 µs of delay created due to the distance between the control room and the stripline, the FIR was shifted by 2 turns. Due to the number of RF amplifiers available, only two electrodes were used diagonally to deflect the beam. This, on the other hand, left us the possibility to try the feedback in the horizontal plane as well as in both transverse planes, by tuning the FIR filter. It turned out that the system managed to keep the beam stable up to the maximum allowed current of 300 mA at zero chromaticity in all three cases.

4.5.6.4   *Obtained Performance*

It has been verified that the feedback efficiency is not sensitive to tiny orbit changes. No noted degradation was either observed restarting the system after few weeks of machine shutdown. Using the digital processor's capability to store bunch by bunch data over hundreds of milliseconds, damping and growth times were pursued by triggering the data acquisition in switching off of the feedback over typically a few ms. The obtained data not only allow us to characterize the feedback performance, but also provide useful bunch by bunch information on the collective instability, particularly, on ion induced dynamics (Subsec. 4.5.4.1.3). An example is shown in Figs. 51 where the feedback damping is found notably shorter at the head of the bunch train as compared to the tail, in the standard 3/4th filling. At the maximum allowed current of 250 mA, a

growth time of $\tau_G(I)$ =0.93 ms and a damping time of $\tau(I)$ =0.49 ms were measured at zero chromaticity. The feedback damping time deduced from the former values is τ_{FB} = 0.32 ms.
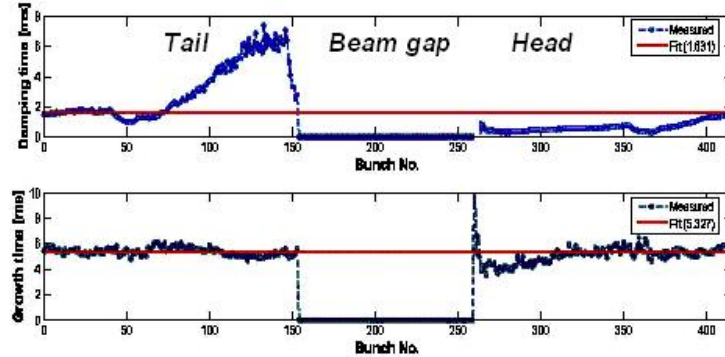
Figure 51: Observed bunch by bunch feedback damping and instability growth times at 50 mA in 3/4th filling.

Regarding the impact of the feedback on the vertical beam size, it has been observed that while the feedback manages to keep the beam size constant against beam current, it generates a slight beam size increase at low current. Starting with the lowest achievable emittance coupling of 0.125%, the vertical emittance increased by ~12%, namely the beam size by ~6% when switching on the feedback at low current. However, there was no further increase up to the maximum current of 200 mA followed [42]. A measurement comparing the beam size with and without feedback with a non-zero chromaticity is shown in Fig. 52. It must be noted that the entire measurement needs be re-carried out with the recently installed dedicated vertical stripline.
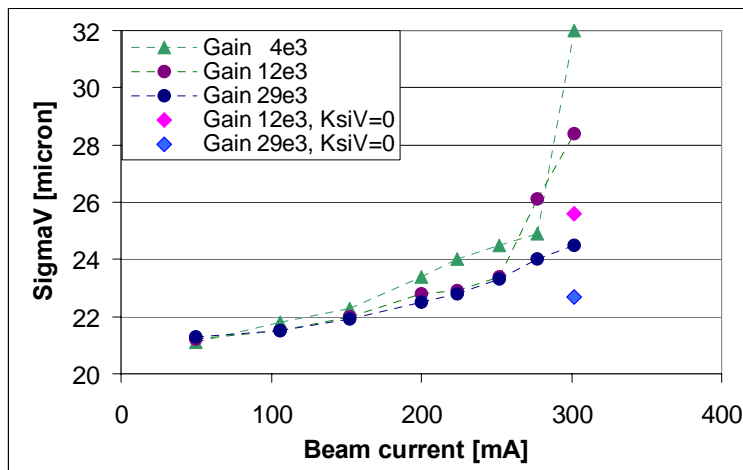
Figure 52: Measured vertical beam size versus current under different feedback gain.

4.5.7 Summary and Conclusion

Anticipating the importance of collective effects at SOLEIL due to the conditions already mentioned, measures were taken from the design stage to fight against them, which consisted primarily of 3D numerical evaluation, analysis of the impedance of each vacuum component and optimisation of their geometry, simulation of beam instability using the obtained impedance data, early development of a bunch-by-bunch transverse feedback system upon the necessity as found from the former, as well as of development of a HOM-free RF system. In particular, the 3D calculations of the geometric impedance brought about a number of modifications on different vacuum components, some of which avoiding critical collective effects. Due to the distinct nature of the wake fields, the two sources of the impedance, namely the geometric and the resistive-wall, were evaluated separately.

Comparing the instabilities measured on the real machine with the expected, relatively good agreement was found on transverse instability thresholds due to the resistive-wall and on the behaviour of higher-order head-tail modes in multibunch, as well as on the absence of microwave threshold up to 20 mA in single bunch. As anticipated, no cavity HOM induced coupled-bunch instability has been observed as well. On the other hand, the measured inductive impedance turned out to be roughly a factor of 2 above expectation in all three planes, as deduced transversely from the mode zero detuning, and longitudinally from the bunch lengthening, the reason of which is yet to be understood. As a feature that was not well investigated in advance, electron beam-ion interactions, both the classical ion-trapping and the fast beam-ion types, turned out to influence the collective beam dynamics significantly in multibunch. Thus, transverse multibunch instabilities are often found to be mixtures of those arising from the former and the impedance, for which a simulation code comprising both effects such as the multibunch tracking code under development at SOLEIL should be necessary to make quantitative studies.

The developed bunch-by-bunch digital transverse feedback system manages to keep the beam stable up to the presently authorised multibunch current of 300 mA with zero chromaticity horizontally and vertically, and allows achieving the designed value of 10 mA per bunch in the time structure mode with acceptably small chromaticities.

4.5.8 Acknowledgement

4.5.9   References

1. M.P. Level et al., "Status of the SOLEIL Project", EPAC 2002, Paris.
2. J.M. Filhol et al., "Overview of the Status of the SOLEIL Project", EPAC 2006, Edinburgh.
3. A. Nadji et al., "Commissioning of the SOLEIL Synchrotron Radiation Source", PAC 2007, Albuquerque.
4. W. Bruns, "The GdfidL Electromagnetic Field Simulator", http://www.gdfidl.de.
5. Y.H. Chin, "User's Guide for ABCI Version 8.7", CERN, SL/94-02 (AP).
6. G. Stupakov, "Coupling Impedance of a Long Slot and an Array of Slots in a Circular Vacuum Chamber", Phys. Rev. E **51**, 3515 (1995).
7. C. Herbeaux, private communication, SOLEIL.
8. J.C. Denard, private communication, SOLEIL.
9. A. Chao, "Physics of Collective Beam Instabilities in High Energy Accelerators", Wiley & Sons, 1993.
10. A. Burov and V. Lebedev "Transverse Resistive Wall Impedance for Multi-Layer Flat Chambers", EPAC 2002, Paris.
11. E. Karantzoulis et al., "Broad band Impedance Measurements on the Electron Storage Ring ELETTRA", Phys. Rev. ST-AB **6**, 030703 (2003).
12. E. Plouviez, ESRF note, Diagnostics 02-03, 2002.
13. T. Perron, "Single Bunch Related Effective Impedance Measurements on the ESRF Ring", dissertation, the ESRF, Grenoble, November 2005.
14. Handbook on Accelerator Physics and Engineering, edited by A.W. Chao and M. Tigner, World Scientific.
15. S. Milton and D. Warner, "The APS Ceramic Chambers", EPAC 1994, London, p. 2494.
16. A. Piwinski, "Penetration of the Field of a Bunched Beam through a Ceramic Chamber with Metallic Coating", PAC 1977, Chicago.
17. K. Yokoya, Part. Acc., **41** (1993) 221.
18. A. Piwinski, "Wake Fields and Ohmic Losses in Flat Vacuum Chambers", DESY HERA 92-04.
19. J.-P. Daguerre, private communication, Synchrotron SOLEIL.
20. P. Lebasque et al., "Optimisation of the Coating Thickness on the Ceramic Vacuum Chambers of SOLEIL Storage Ring", EPAC 2006, Edinburgh.
21. Y.H. Chin, "User's Guide for New MOSES", Technical Report, Center for Beam Physics, Berkeley Laboratory, University of California, USA, 1988.
22. R. Nagaoka, "Study of Resistive-Wall Instabilities with a Multi-Bunch Tracking", EPAC 2002, Paris, p. 1538.
23. PVM, http://www.csm.ornl.gov/pvm/pvm_home.html.
24. T.O. Raubenheimer, F. Zimmermann, "Fast beam-ion instability. I. Linear theory and simulations", Phys. Rev. **E 52**, 5487 - 5498 (1995).
25. A. Mosnier, SOLEIL conceptual design report (APD).
26. K. Bane et al., "Estimate of the Impedance due to Wall Surface Roughness", PAC'97, Vancouver, May 1997, p. 1738.
27. G. Stupakov et al., "Effect of Beam Tube Roughness on X-ray Free Electron Laser Performance" PRST-AB **2**, 060701 (1999).
28. O. Henry and O. Napoly, "The Resistive-Pipe Wake Potentials for Short Bunches",

Part. Accel **35**, p.235 (1991).

29. K. Yokoya, Part. Acc., **41** (1993) 221.
30. R. Nagaoka et al., "Incoherent Transverse Tune Shifts due to Resistive Low-Gap Chambers", EPAC 2002, Paris.
31. A. Chao, S. Heifets, B. Zotter, Phys. Rev. ST-AB **5**, 111001 (2002).
32. P. Marchand et al, Proc. of PAC07, p. 3438.
33. P. Marchand, Ti Ruan, F. Ribeiro and R. Lopes, Physical Review Special Topics - Accelerators and Beams, 10, 11201 (2007).
34. M. Louvet et al, Proc. of SRF2005, ThP42.
35. P. Marchand et al, Proc. of the EPAC06, p. 384.
36. M. Diop et al, Proc. of EPAC06, p. 1447.
37. M. Svandrlik, private communication.
38. P. Marchand et al, Proc. of PAC07, p. 2050.
39. T. Nakamura, "Residual Beam Motion Driven by the Noise at Transverse Feedback", Nanobeam2005, Kyoto University, Japan.
40. T. Nakamura, K. Kobayashi, "FPGA Based Bunch-by-Bunch Feedback Signal Processor", ICALEPCA 2005, Geneva, Switzerland, and references therein.
41. C. Mariette et al., "SOLEIL Vertical Stripline Development", DIPAC, Venice, May 2007.
42. M.A. Tordeux et al., "Ultimate Resolution of SOLEIL X-ray Pinhole Camera ", DIPAC, Venice, May 2007.

4.6   Impedance and Instabilities at the ALBA storage ring

Thomas Günzel, Francis Perez
CELLS, Apartado de Correos 68, 08193 Bellaterra, Spain
Mail to: tguenzel@cells.es

4.6.1   Introduction

ALBA is a Synchrotron Radiation Facility which is currently under construction in Cerdanyola del Vallés near Barcelona, Spain. The responsibility of the construction and operation of ALBA is in the hands of the CELLS consortium which is owned and supported on half each by the Spanish Ministry of Education and Science and the Department of Education and Universities of the Catalan Autonomous Government. As a third generation light source will produce high brilliant photon beams on a maximal number of 33 possible beamlines (under the assumption that synchrotron light from the dipoles is also used). For this purpose the storage ring optics was designed to achieve a horizontal emittance of 4.7nm.rad, on the vertical plane even only 1/100 of this value. The project has started in 2004 and is expected to run in user operation in 2010[1].

4.6.2   Vacuum Chamber Design of the ALBA Storage Ring

The storage ring of ALBA has a very compact design due to relatively small circumference of 268m and due to its large percentage (39%) of straight sections. It is designed to reach ultimately a current of 400mA. Its optics is realized as an expanded DBA lattice with a total of 4 superperiods each covering a quarter of the ring. They are connected to each other by 4 long straight section of 8m length. Each quarter contains 3 middle long straight sections of 4.2m length and 2 short straight sections of 2.6m

length. The large number of straight sections (table 1) allows the installation of many low-gap chambers, RF-cavities and diagnostic devices[2].

   The standard vacuum chamber is of 2a=72mm horizontal and 2b=28mm vertical extension and is connected in most cases to an antechamber by a slot of 10mm (in the dipole chambers it is 15m respectively 22mm in case of the IR-beamline). The vacuum chambers of standard size are made of stainless steel. For some low-gap chambers NEG-coated aluminum chambers are foreseen. In order to cope with the heat of the synchrotron radiation and to minimize the desorption the chambers are equipped with lumped absorbers. The lumped absorbers are crotches which are horizontally inserted in the antechamber and always combined with a vertical pumping port. They are at different horizontal distance to the beam, the closest at 20mm distance. Vertical pumping ports without crotch absorbers also exist. Distributed absorbers are foreseen close to the cavities and the superconducting wiggler chamber, in the NEG-coated low-gap chambers and in the dipole chambers [3].

4.6.3   Computation of the Impedance

   According to the description in the precedent section the ring has large resistive wall impedance and as well as significant geometrical impedance due to the numerous low-gap chambers. In the following these two types of impedance will be distinguished due to the different manner how they are calculated.
Other contributions, as space charge impedance, are sufficiently small or do not drive instabilities so that they will not be considered. First the transverse impedance will be discussed followed by the reduced longitudinal impedance (Z_l/n).

Table 1: Straight section available for low-gap chambers. The figures in parentheses are the number of straight sections which can be equipped with low-gap chambers.

Type of straight section	Quantity	Length[m]	β-function(H/V)
Long straight section	4(3)	8	10.2/5.22
Middle long straight section	12	4.2	1.98/~1.18
Short straight section	8(2)	2.6	8.63/5.79

4.6.3.1   *Transverse Resistive Wall Impedance*

   The computation of the resistive wall impedance is done analytically under the assumption of several simplifying conditions:

- The vacuum chamber wall is infinitely thick
- Only the low-frequency range $\omega \ll c(Z_0\sigma/b^2)^{1/3}$ (σ conductivity, Z_0=376.73Ω) needs to be considered because of the bunch length of σ_τ=15.4ps (4.6mm).
- The vacuum chamber can be considered as parallel plate geometry
- Discussion of two special cases: the *best case* and the *worst case* (explanation below).
- The impedance is weighted by the local β-function

   The first two conditions are usually fulfilled, except for NEG-coated aluminum chambers and chambers equipped with particular thin metal sheets inside of the

chamber. But the latter mainly concerns in-vacuum undulators whose final quantity is not definitively fixed at the actual state of the project so that the computation is done with simplified installation assumptions.

Furthermore the consideration of the vacuum chamber as horizontal parallel plate geometry makes sure that both components of the transverse impedance obtained from the dipolar wake fields[1] only depend on the vertical extension of the vacuum chamber and on the conductivity of the chamber wall (stainless steel). Yokoya [4] developed this theory and also showed that starting from a aspect ratio of the vacuum chamber of $a/b=2.5$ the parallel plate geometry approximation is good. Finally all parts are weighted by the local respectively over the length averaged β-function of the vacuum chamber element. Two configurations will be distinguished: The so-called *best case* describes the status of the storage ring with no low-gap chamber during the commissioning, the so-called *worst case* prospects an occupation of all straight sections with stainless steel 8mm chambers. Certainly this assumption is a simplification of the real situation, but demonstrates very well what will happen if unconsideredly low-gap chambers are installed. For the *best case* the result is:

$$(Z_V\beta_V)_{eff} = 383k\Omega \text{ and } (Z_H\beta_H)_{eff} = 133k\Omega$$

and for the *worst case* the result is:

$$(Z_V\beta_V)_{eff} = 2471k\Omega \text{ and } (Z_H\beta_H)_{eff} = 1836k\Omega.$$

4.6.3.2   *Transverse Geometrical Impedance*

The geometrical impedance is computed numerically by element-wise wakefield evaluation with the 3D-code GdfidL[5]. For a large number of vacuum chamber elements (shown in table 2) the transverse wakefields are calculated and decomposed in their monopolar, dipolar and quadrupolar part. The dipolar part is used to determine the transverse impedance. As already mentioned in the precedent section horizontal and vertical impedance are weighted by the local β-function of the corresponding element. For the time being the impedance of some elements, in particular that of bellows and pump slits are estimated by analytical calculation.

---

[1] Quadrupolar wake fields are also created in these flat chambers, but their effects (incoherent tune shifts) will not be discussed in this report.

Table 2: Breakdown of the transverse impedance budget for the *worst case.* The impedance values of the bellows is based on an analytical calculation of V.Smaluk[6].

Element	Num-ber	Z^V_{eff} [kΩ/m]	$β_V$ [m]	$(Z_{eff}β)_V$ [kΩ]	Z^H_{eff} [kΩ/m]	$β_H$ [m]	$(Z_{eff}β)_H$ [kΩ]
dipole chambers	32	0.138	24.00	106.0	0.055	1.80	3.2
dipole absorbers	64	0.020	12.40	15.7	0.018	6.79	7.7
RF cavity tapers	3	1.170	5.60	19.7	0.410	8.40	10.3
BPMs	123	0.011	9.22	12.5	0.014	6.33	10.9
stripline kickers	1	2.350	5.20	12.2	1.570	8.20	12.9
flanges injection	9	0.076	6.52	4.5	0.040	11.50	4.1
flanges rest	65	0.047	3.56	10.9	0.024	4.73	7.4
Cavity flanges	12	0.033	5.20	2.1	0.033	8.20	3.2
vertical scraper	1	6.630	6.50	43.1	2.910	11.50	33.5
8mm low-gap chamber	15	6.240	5.00	468.0	1.370	7.50	154.1
injection taper	1	0.076	6.70	0.5	0.091	11.60	1.1
Dampy cavities	6	0.647	5.20	20.2	0.647	8.20	31.8
ΣGdfidL calculations:				**715.2**			**280.2**
Pump slits 3mm	5058+916	0.004	3.72	76.4	0.000	8.60	0.27
Bellows(V.Smaluk)	44	0.142	5.19	32.4	0.071	7.64	23.9
Σanalytical calculations:				**108.8**			**24.2**
TOTAL				**824.0**			**304.4**

In fact a detailed study on the transverse (and longitudinal) impedance of the pump slits on the basis of [7] was carried out. Analytical expressions were developed for the impedance of slits in chambers of rectangular and elliptical shape and the resulting figures were compared to those computed by GdfidL which resulted in sufficient agreement. Finally all the analytical figures were summed up to provide the impedance of all slits. It was simpler than to numerically calculate in 3D the different slit arrangements in the vacuum chamber walls.

Furthermore, simplifying assumptions are made for the installation of low-gap chambers in the straight sections. Only one type of low-gap chambers was assumed to be installed in all long and middle long and short straight sections. The spectra of vertical and horizontal impedance were determined and are depicted in the figures 1. For the *best case* in total

$$(Z_V β_V)_{eff} = 307 kΩ \quad \text{and} \quad (Z_H β_H)_{eff} = 150 kΩ.$$

was obtained. For the *worst case* it is

$$(Z_V β_V)_{eff} = 824 kΩ \quad \text{and} \quad (Z_H β_H)_{eff} = 304 kΩ$$

A breakdown of the budget is given in table 2. Under the assumption that the transverse mode m=0 meets after a coherent tune shift of one synchrotron tune the transverse mode m=-1, the impedance values result in the following transverse mode-coupled instability (TMCI)-thresholds for single bunch taking the resistive wall and geometrical impedance into account. It is for the *best case:*

<p style="text-align:center;">28.1mA vertically   and   68.6mA horizontally</p>

And for the *worst case:*

<p style="text-align:center;">5.9mA vertically   and   9.1mA horizontally</p>
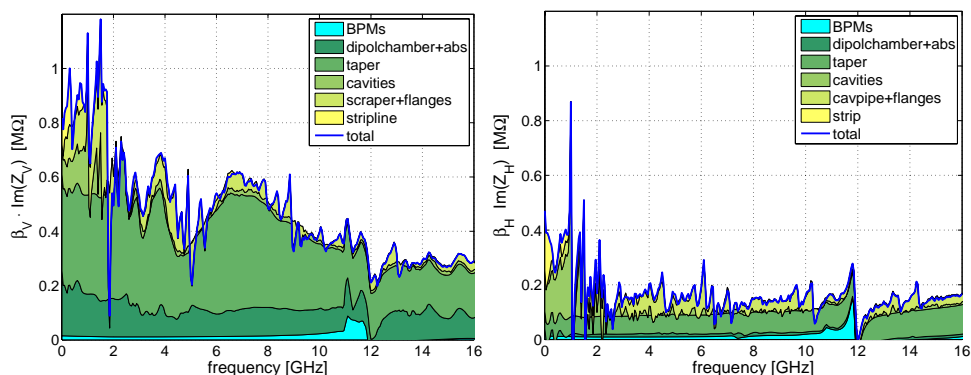
Figure 1: spectra of imaginary part of the β-weighted vertical (left) and horizontal impedance (right) for the *worst case*

4.6.3.3 Longitudinal Impedance

The resistive wall part and geometrical part of the longitudinal impedance are calculated as it has been explained in the preceding subsection. The effective value of the reduced longitudinal impedance Z_l/n ($n=\omega/\omega_0$) of the resistive wall under the *worst case* assumption is $(Z_l/n)_{eff} = 212 m\Omega^2$. This value is too small for the excitation of the longitudinal resistive wall instability at maximal operational current. However, the resistive wall impedance has to be added to the geometrical impedance of the elements around the ring to include its effect on the microwave instability. To this end a sum of several broadband resonator functions are fitted to the spectrum of the geometrical longitudinal impedance. The resulting parameters of the fit are used to calculate the effective impedance by the following expression (with R_{sk} shunt impedance, Q_k quality factor and ω_{rk} resonance frequency of the *k*-th broadband resonator):

$$\left|\frac{Z_l}{n}\right|_{eff} = \sum_k \frac{R_{sk}\omega_0}{Q_k\,\omega_{rk}} \cdot g(\omega_{rk}\,\sigma_\tau) \quad \text{with} \quad g(\omega\sigma_\tau) = \begin{cases} 2(\omega\sigma_\tau)^2 & \text{for} \quad \omega\sigma_\tau \ll 1 \\ 1 & \text{for} \quad \omega\sigma_\tau > 1 \end{cases} \tag{1}$$

The formfactor *g* weights resonators with low resonance frequency only weakly. This meets the fact that only resonators with high frequency can drive the microwave

---

[2] It is pointed out that for resistive wall $|Z_l/n|_{eff} = \sqrt{2}\; Im(Z_l/n)_{eff}$

instability. The total value of $|Z_l/n|_{eff} = 529m\Omega$ is well below the threshold value of $750m\Omega$ provided by the Boussard criterion[3] [8] for a current of 0.9mA, the current of one bunch within 400mA homogeneous filling. However, for 2/3-filling at full current the found value is above the threshold value of $500m\Omega$. This, however, does not automatically imply that the microwave instability is excited because the threshold has been calculated for the zero current bunch length. It will increase with increasing current according to bunch lengthening due to potential well distortion. Additionally the $|Z_l/n|$-value is calculated under the assumption of the *worst case* which might only be realized after the full equipment of all straight sections of the ring with 8mm stainless steel chambers.

4.6.3.4   Two Examples of Optimisation

The design of several vacuum chamber elements had to be improved in order to diminish the impedance. The reduction of the longitudinal impedance budget is particular important in order to avoid the microwave instability. In particular the improvement has been driven by the wish to reduce the heat load of the corresponding vacuum chamber element. This concerns the bottom-based beam loss monitors (BPMs)[9], the slot connecting the dipol chamber with the antechamber, and the tapers for the in-vacuum undulators etc. For this report the stripline kickers and the flanges were selected as examples.

4.6.3.4.1 The Stripline Kickers

In the ALBA ring a horizontal and a vertical stripline kicker will be used necessary for the feedback system. The walls possess several interruptions which make the kickers very prone to act as resonators associated with substantial impedance. They will be mounted in a row (fig. 2). In order to bypass a part of the wall interruptions the installation of connection bars was considered above and below the beam in the horizontal stripline kicker respectively left and right side of the beam in the vertical stripline kicker. GdfidL-simulations showed a significant reduction of the vertical impedance for the horizontal stripline kicker with connection bars. Moreover the real and imaginary part of the longitudinal impedance could be reduced by a factor of 3 (fig. 3). However, the effect of the connection bar on the impedance of the vertical stripline kicker was only very limited. Consequently only the horizontal stripline kicker will be installed with connection bars.

---

[3] The reference [8] applies the strictest form factor in the threshold criterion of possible others mentioned in literature.
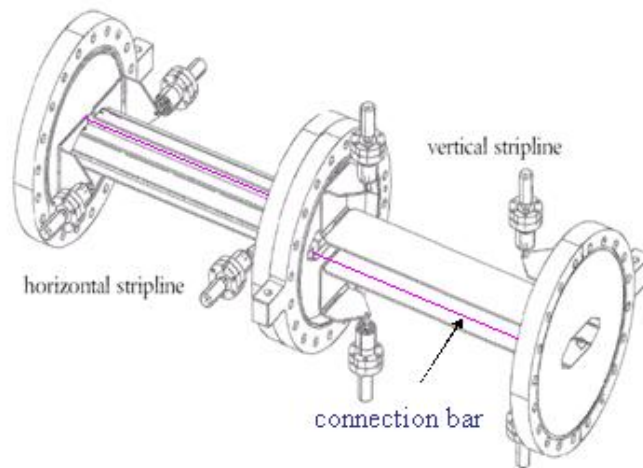
Figure 2: Geometry of the stripline kickers: the horizontal one on the left and the vertical one on the right side. The magenta lines represent the connection bars which are placed in the open space between the strips
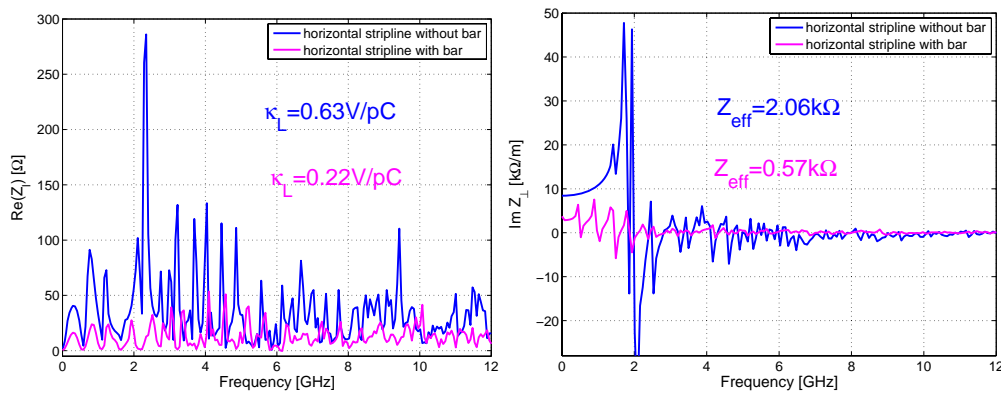
Figure 3: real part of the longitudinal impedance spectrum (left) and imaginary part of the vertical impedance (right) for the horizontal stripline kicker. In blue the spectra of the device without and in magenta the spectra of the device with connection bars.

4.6.3.4.2 Flanges

The ALBA ring contains 74 flanges. Therefore there is a need to optimise the slit size in order to reduce the impedance on all 3 planes. Conflat flanges which only have a slit size of 0.1mm were also considered. But the latter do not fit into the ALBA vacuum system. Finally their benefit (see table 2), in particular for the longitudinal impedance is only small. So Spigot flanges of 0.2mm slit width were chosen.

Table 2: Impedance of flanges

Flange type	Slit size [mm]	$(Z_l/n)_{eff}$ [mΩ]	$Z_\perp$ (V/H)[Ω/m]
Flange of Spigot type	0.4	0.29	151/80
Flange of Spigot type	0.2	0.10	76/40
Flange of Conflat type	0.1	0.09	49/22

4.6.4   Most Important Instabilities

There are several instabilities ALBA could be affected by:
- Transverse Resistive Wall Instability on the vertical and horizontal plane
- Microwave Instability
- Transverse Coupled Mode Instability (TMCI)
- HOMs in the cavities
- Head-Tail Instability

However, we will only concentrate on the two most important instabilities, which are the resistive wall instability and a remaining HOM in the RF-system. The other instabilities are not a limiting factor for the operation of ALBA. By a careful design of the vacuum chamber elements the microwave instability can be avoided in multibunch filling, even in 2/3-filling at 400mA. Furthermore the thresholds of the TMCI are high enough that they do not affect the operation in multibunch filling. If, in case, the head-tail instability is excited, it can probably be easily damped with synchrotron tune spread.

4.6.4.1.1 Transverse Resistive Wall Instability

It is the most menacing instability for ALBA. Although the resistive wall thresholds are still acceptable at commissioning *(best case)*:

41mA vertically   and   171mA horizontally

The threshold currents will decrease steadily with the installation of low-gap chambers. The thresholds reach for the *worst case*

6.4mA vertically   and   12.5mA horizontally.

Unfortunately the use of a higher normalized chromaticity $\xi = (\Delta Q/Q)/(\Delta E/E)$ only has a very limited effect as it can be seen on the figure 4. In comparison to other synchrotron light sources as SOLEIL or the ESRF the ratio of the head-tail phase to the normalized chromaticity at ALBA is quite small. Furthermore, the counteracting effect of a broadband component at higher frequency in the spectrum which is created by the geometrical impedance is very weak. In the vertical plane the set of broadband resonators only can move the RW-threshold of 250mA from $\xi_V = 1$ to $\xi_V = 0.7$. The effect of the broadband component on the horizontal threshold is even smaller. Nevertheless, as only the threshold of the m=0 mode limits the current on the horizontal plane; it might be possible to combat this instable mode with horizontal betatron tune spread via Landau damping. The use of octupoles for the creation of betatron spread was analyzed [10,11], but would require several quite strong magnets. A second order effect of the sextupoles on the tune also creates tune spread as a function of amplitude [12], the analysis is on the way. Otherwise the only solution to avoid the RW-instability is the foreseen installation of a transverse feedback system.
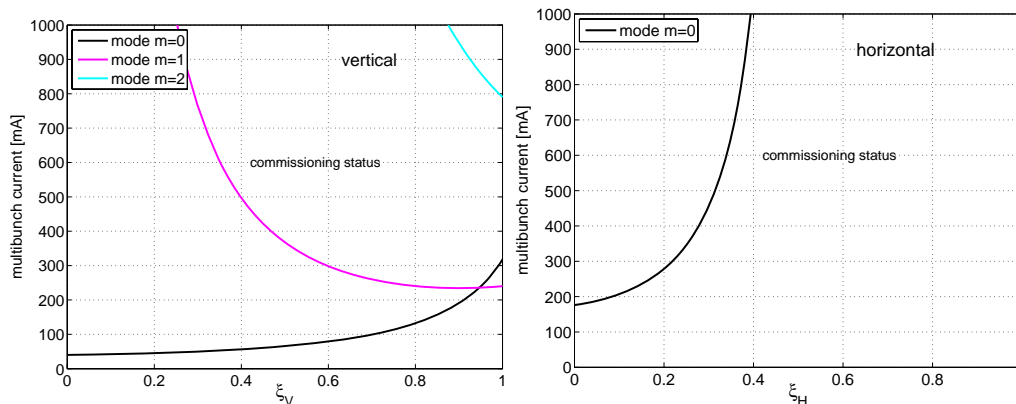
Figure 4: threshold of the resistive wall instability in the vertical (left) and horizontal (right) plane as a function of normalized chromaticity $\xi=(\Delta Q/Q)/(\Delta E/E)$ for homogeni- ous filling and *best case*. On the vertical plane when the threshold of mode m=0 finally increases significantly, the threshold of mode m=1 delimits the maximum stable current.

4.6.4.1.2 The HOM in the DAMPY-cavities

As radio-frequency system a set of 6 warm copper cavities (called DAMPY) with HOM-dampers is foreseen. Recent measurements [13] showed, however, that there exists a HOM in the cavity which is not sufficiently damped. Its threshold is in homogeneous filling at 425mA corresponding to a shunt impedance of R_s=10.8kΩ. Although the found threshold value is above the maximal current at ALBA, there is the concern that it could fall below 400mA in the final version of the cavities according to a slight variation of the shunt impedance. This instability could be damped by synchrotron tune spread via Landau damping. This one could for instance be created by the installation of a harmonic cavity. However, by using a model of synchrotron frequency spread due to fractional filling developed by [14] at the ESRF, it could be shown that the same model can be used to produce enough synchrotron frequency spread in the ALBA ring to provide Landau damping of the HOM. This is inasmuch interesting as the sensitivity of a compact medium energy ring to longitudinal coupled instabilities is 5 times larger than at a larger accelerator as the ESRF. The sensitivity *S* can be expressed in the following way by standard machine parameters (α momentum compaction factor, τ_L longitudinal damping time, *E* energy, *e* elementary charge and Q_s synchrotron tune):

$$S = \frac{\alpha \tau_L}{2(E/e)Q_s} \tag{2}$$

On the other hand, the HOM-threshold at zero synchrotron frequency spread can be expressed in the following, very instructive way (with f_{HOM} as frequency and Z_{HOM} as shunt impedance of the HOM):

$$I_{thres}(\Delta f_s = 0) = \frac{1}{S\, f_{HOM}\, Z_{HOM}} \tag{3}$$

The threshold current is 4.4 times higher than at the ESRF since the value of Z_{HOM} is very small because the ALBA-cavities are (supposed to be) HOM-damped.

The HOM in the DAMPY-cavities is much weaker than corresponding one in the ESRF cavities. Therefore it is also easier to damp it with Landau damping. Therefore although the synchrotron spread due to 2/3 filling in the ALBA-ring is indeed 6 times smaller than the corresponding spread in the ESRF-ring, (because of a smaller value of the R/Q of the fundamental mode of ALBA), this spread is already sufficient to shift the threshold of the HOM from 425mA to 476mA. Figure 5 shows how the threshold current depends on the level of fractional filling for different values of shunt impedance of the HOM whereas figure 6 shows the threshold current as function of synchrotron spread
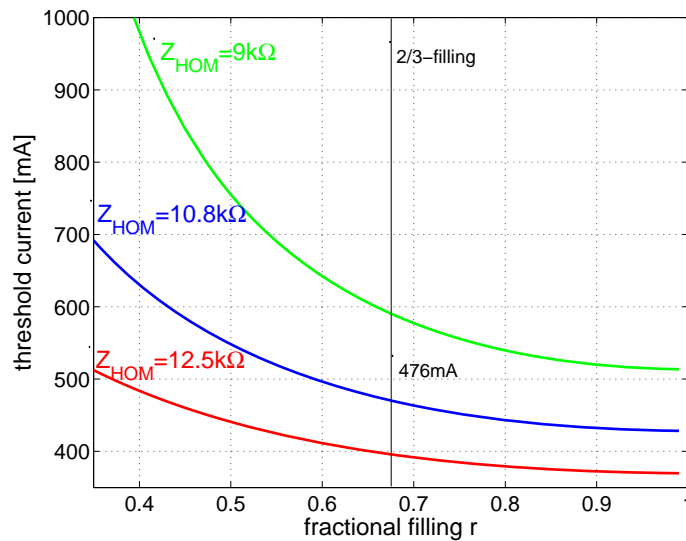
Figure 5: threshold current due to Landau damping as a function of fractional filling r for different values of the HOM shunt impedance Z_{HOM} at ALBA. At r=0.66 and for a shunt impedance of 6·10.8kΩ the threshold reaches a value of 476mA.
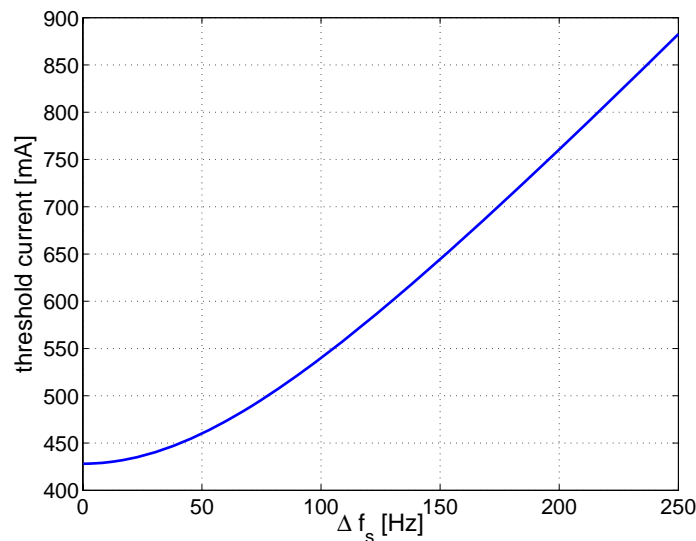
Figure 6: threshold current of the HOM as function of synchrotron tune spread.

4.6.5 Conclusion

The ALBA ring is prone to instabilities driven by impedance due to its compact design and high operation current. The strong resistive wall instability can be cured on the vertical plane by a transverse feedback system. On the horizontal plane it will be checked out if by the provision of some horizontal betatron spread as a function of amplitude the instability can be moved above the operation current.

The unexpected presence of the E011-mode based HOM in the DAMPY cavities can be damped in the initial operation phase by partial filling of the ring and in a more advanced operation phase by the installation of a harmonic cavity. The use of 2/3-filling to cope with the HOM in the DAMPY-cavity seems to be possible in that respect. Even in this filling pattern the microwave instability will probably not be excited. The vacuum chamber elements are supposed to withstand the 50% higher heat load in this filling mode. There is no immediate need for intervention on other instability thresholds because the ALBA ring is not concerned by them. However, this can change in case of a major modification of the vacuum chamber design of the ring. Therefore a detailed follow-up of all vacuum chamber installations is important.

4.6.6 References

1. J. Bordas "The status of the ALBA project", Proceedings of the NATO Advanced Research Workshop on Brilliant Light in Life and Material Sciences, Springer, p. 45-55, 2006, Yerevan (Armenia)
2. M. Muñoz, D. Einfeld, "Lattice and Beam dynamics of the ALBA storage ring", ICFA newsletter 44, p.183-193, (2007)
3. E. Al-Dmour, D. Einfeld, M. Quispe, Ll. Ribó, "The vacuum system for the Spanish synchrotron light source ALBA", EPAC 2006, Edinbourgh, p.3398
4. K. Yokoya, "Resistive Impedance of Beam Pipes of General Cross Section", Part. Acc. 41, (1993), 221
5. W. Bruns, Electromagnetic Field Solver GdfidL, http://www.gdfidl.de
6. V. Smaluk, "Coupling Impedance and Beam Stability Estimation for the ALBA Storage Ring", ALBA internal note, August 2005
7. S.S.Kurennoy, "Coupling impedance of small discontinuities, dependence of beam velocity, arbitrary cross section", Phys. Rev. STAB **9** 054201 (2006)
8. A. Chao, "Physics of collective Beam instabilities in high energy accelerators", J.Wiley & Sons, New York (1993)
9. A. Olmos, T. Günzel, F. Pérez, "BPM design for the ALBA synchrotron", EPAC 2006, Edinbourgh, p. 1190
10. J. Gareyte, J.P. Koutchouk, F. Ruggiero, "Landau Damping, Dynamic Aperture and Octupoles in LHC", LHC Project 91 (revised), CERN, April 1997
11. T.F.Guenzel, "Landau damping of resistive wall modes by octupoles", internal ALBA-report, CELLS, September 2007
12. L.Tosi, V. Smaluk, E. Karantzoulis, "Landau damping via the harmonic sextupole", Phys. Rev. Special Topics Acclerators and Beams, Vol. 6, 054401, (2003)
13. E. Weihrether, private communication, november 2006
14. O. Naumann, J. Jacob, "Fractional Filling induced Landau damping of longitudi-nal instabilities at the ESRF", PAC 1997, 1551, Vancouver

4.7   The Impedance Model of PETRA III

K. Balewski, R. Wanzenberg, O. Zagorodnova
Deutsches Elektronen-Synchrotron, A Research Centre of Helmholtz Association
Notkestr. 85, 22603 Hamburg, Germany
Mail to: rainer.wanzenberg@desy.de

4.7.1   Introduction

The PETRA ring was built in 1976 at DESY as an electron - positron collider and was operated from 1978 to 1986 in this collider mode. From 1988 to 2007 PETRA II was used as a preaccelerator for the HERA lepton hadron collider ring. The PETRA ring is currently being converted into a dedicated 3rd generation synchrotron radiation facility called PETRA III [1]. The planned facility aims for a very high brilliance of about 10^{21} photons /sec /0,1%BW /mm^2/ mrad^2 using a low emittance (1 nm rad) electron or positron beam with an energy of 6 GeV. One octant of the PETRA ring is completely redesigned to provide space for 14 insertion devices in nine double bend achromat (DBA) cells. The location of the new hall is shown in Fig. 1. A photo of the new experimental hall is shown in Fig. 2.

Figure 1: Ground Plan of the DESY site with the PETRA ring. The new experimental hall (red) is situated between the PETRA halls North-East and East.

Nearly the entire vacuum system of the existing storage ring PETRA will be replaced during the conversion into a synchrotron radiation facility. This includes the vacuum chamber in the seven "old" octants, where the new chambers in the dipoles and quadrupoles of the FODO lattice have recently been installed, and also the so called "new" octant between the halls North-East and East, where several undulator chambers with a small vertical gap of about 7 mm will be installed. The positron or electron beam will interact with its vacuum chamber surroundings via electromagnetic fields. These wake fields in turn act back on the beam and can lead to instabilities, which limit either the achievable current per bunch or the total current or even both. The total impedance of PETRA III depends on the RF cavities, undulator chambers, bellows, beam position monitors, kickers, pump ports, the finite resistivity of the chamber and many other

objects [2]. In collaboration between DESY, the University of Darmstadt, the Otto-von-Guericke University of Magdeburg, CANDLE (Yerevan University, Armenia), and the Budker Institut, BINP (Novosibirks, Russia) an impedance model of PETRA III has been built which includes more than 25 objects. The impedance due the resistivity of vacuum chambers, the impedance of the wiggler section, of feedback cavities and of the beam position monitors are discussed in the contributions [3,4,5,6] of this Beam Dynamics Newsletter. An overview of the considered objects is provided in section 4.7.3 of this article.

Figure 2: The new experimental hall of PETRA III. The photo shows the construction site from inside the ring. This photo is taken from the webcam: http://petra3.desy.de/webcam .

4.7.1.1 Parameters

The main parameters of PETRA III are summarized in Tab. 1. The standard bunch filling pattern will consist of a large number of equally spaced bunches with a low bunch population. Additionally a special operation mode is required for time-resolved experiments with a higher charge per bunch (2.5 mA per bunch) in 40 equally spaced bunches.

Table 1: PETRA III parameters

Parameter		PETRA III	
Energy	GeV	6	
Circumference	m	2304	
RF Frequency	MHz	500	
RF harmonic number	-	3840	
RF Voltage	MV	25	
Momentum compaction	-	1.22×10^{-3}	
Synchrotron tune		0.049	
Total current	mA	100	
Number of bunches		960	40
Bunch population	10^{10}	0.5	12
Bunch separation	ns	8	192
Emittance (horz. / vert.)	nm	1 / 0.01	
Bunch length	mm	12	
Damping time H/V/L	ms	16 / 16 / 8	

4.7.1.2   Wakefields, Kick and Loss Parameters, Instabilities

The interaction of the beam circulating with its vacuum chamber surroundings via electromagnetic fields can be characterized with a wake potential. The wake potential of a point charge q_1 is defined as [7]:

$$\vec{W}^{\delta}(\vec{r}_2,\vec{r}_1,s) = \frac{1}{q_1}\int dz\ (\vec{E} + c\ \vec{e}_z \times \vec{B})_{t=(z+s)/c}\ , \tag{1}$$

where r_2 is the transverse coordinate of the witness charge q_2. The impedance is the Fourier transform of the point charge wake potential. The wake potential of a bunch is the convolution of the point charge wake potential with the line charge density $\lambda(s)$:

$$\vec{W}(\vec{r}_2,\vec{r}_1,s) = \int d\bar{s}\ \lambda(s-\bar{s})\ \vec{W}^{\delta}(\vec{r}_2,\vec{r}_1,\bar{s})\ . \tag{2}$$

We will express the impedance of PETRA III in terms of the so-called loss and kick parameters, which are defined via the wake potential and the normalized beam line charge density. The loss parameter $k_{\parallel}$, $k_{\parallel}(1)$ and the kick parameter $k_{\perp}$ are defined as:

$$k_{\parallel} = \int ds\ W_{\parallel}(s)\ \lambda(s) \tag{3}$$

$$k_{\parallel}(1) = \int ds\ W_{\parallel}(s)\ \frac{d}{ds}\lambda(s) = -\int ds\ \lambda(s)\ \frac{d}{ds}W_{\parallel}(s) \tag{4}$$

$$k_{\perp} = \int ds \ W_{\perp}(s) \ \lambda(s). \tag{5}$$

A transverse instability has been observed in PETRA when the storage ring was operated in the collider mode [8]. Single bunch currents of 10 mA could be stored in PETRA II without any evidence of transverse or longitudinal instabilities. The instability threshold for mode coupling instabilities can be estimated from the tune shifts of the lowest order modes in the longitudinal and transverse planes [2, 9] using the loss and kick parameters:

$$\Delta Q_S = Q_S \frac{I_B R T_0}{2 h V_{rf}} k_{\parallel}(1), \qquad \Delta Q_{\beta} = \frac{I_B T_0}{4 \pi E / e} \langle \beta \rangle k_{\perp}, \tag{6}$$

where I_B is the single bunch current, R = 367 m is the mean machine radius, T_0 = 7.685 μs is the revolution time, h = 3840 is the harmonic number, V_{rf} is the total acceleration voltage, E = 6 GeV the energy and $\langle \beta \rangle$ is the average beta-function. Instead of the kick parameter $k_{\perp}$ often an effective transverse impedance $Z_{\perp}^{eff}$ is used [10, 11]. They are related in the following way:

$$k_{\perp} = \frac{1}{2\pi} \ \frac{\sqrt{\pi}}{\sigma_z / c} \ Z_{\perp}^{eff} = 7.05 \frac{V}{pC \ m} \ \frac{Z_{\perp}^{eff}}{k\Omega / m}, \tag{7}$$

where σ_z = 12 mm is the rms bunch length.

4.7.2   The Impedance Model of PETRA III

The impedance model of PETRA III is based on numerical calculations, analytical estimates of the wakefields and on measurements of instability growth rates at PETRA II. Many objects, including the RF cavities, undulator chambers, bellows, beam position monitors (BPMs), kickers, and pumping ports, have been studied in detail. At DESY mainly the code MAFIA [12, 13] has been used to obtain the loss and kick parameters. Furthermore the codes ECHO [14] and GdfidL [15, 16], mainly for the wiggler section, and PBCI [3, 17] have been used. All objects can be categorized into four different sections of PETRA III, which are summarized in Table 2. All insertion devices will be installed in the new experimental hall, which is located between the hall North-East and East. The damping wigglers will be installed in the (long) straight section West and North, while the RF-cavities are being reinstalled in the straight section South. Fig. 3 shows the location of the different sections around the PETRA ring. There are four long straight sections (108 m long) and four short straight sections (64.8 m long). Each "old" arc consists of 14 FODO cells, while the "new" octant consists of 9 DBA cells.

Table 2: PETRA III Sections

Section	Objects
RF-Section	12 rf-cavities, 8 feedback cavities
Damping Wigglers	20 wigglers, several absorbers
Insertion Devices	14 undulators, tapered transitions, absorbers
Arcs, "Old Octants"	196 dipole chambers, 203 quad chambers, 105 BPM's
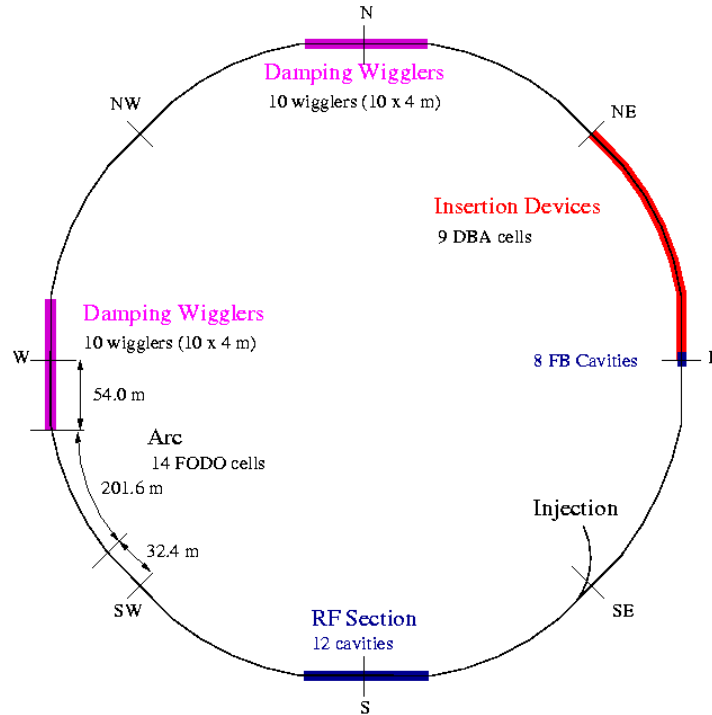
Figure 3: The PETRA III ring. The location of the Insertion Devices, the Wiggler section, and the RF-Sections are shown.

4.7.2.1   Coupled Bunch Instabilities

The long range wake field is dominated by higher order modes (HOMs) in the 7 cell 500 MHz cavities. In PETRA II sixteen cavities were installed. The effective shunt impedance could be determined from measurements of threshold currents and instability growth rates at PETRA II. The results are summarised in Table 3.

Table 3: Measurements at PETRA II related to coupled bunch instabilities

Effective Impedance	Petra II (total) 16 x 7 cell cavities
$Z_{\parallel eff}$ (MΩ)	3.6
$Z_{\perp eff}$ (MΩ/m)	50

The growth rates for longitudinal and transverse coupled bunch instabilities for PETRA III can be estimated from the measured effective impedance of PETRA II according to:

$$\frac{1}{\tau_{\parallel}} = \frac{2\pi Q_S}{T_0} \frac{I_{tot} Z_{\parallel eff}}{2 V_{rf}}, \qquad \frac{1}{\tau_{\perp}} = \frac{2\pi}{T_0} \frac{I_{tot} \beta_{cav} Z_{\perp eff}}{4\pi E/e}, \tag{8}$$

The longitudinal growth rate of 360 Hz and the transverse growth rate of about 1100 Hz is significantly larger than the radiation damping rates of 125 Hz (longitudinal) and 62.5 Hz (transverse). Therefore a powerful feedback system is required to provide additional damping. The longitudinal feedback system is based on eight one cell cavities with a total voltage of 12 kV. The cavity design is based on the DAFNE feedback cavity [18] and has been adopted from the SLS [19]. The transverse feedback system will utilize in total four 1 m long strip-line kickers to damp the transverse coupled bunch instabilities. The required damping is $1/\tau = 800$ Hz for the longitudinal and $1/\tau = 1400$ Hz in the transverse plain (see Table 4) and the required bandwidth is 62.5 MHz for a bunch to bunch spacing of 8 ns.

Table 4: The PETRA III multi-bunch feedback system.

Feedback	Required Damping	Devices
Longitudinal	800 Hz	8 cavities (12 kV)
Horizontal	1400 Hz	2 kickers (1 m)
Vertical	1400 Hz	2 kickers (1 m)

4.7.2.2   Mode Coupling Instabilities – Impedance Budget

The impedance budget for longitudinal and transverse mode coupling instabilities is determined from the formula (6) for tune shifts of the lowest order modes. Assuming that a total tune shift of $\Delta Q_s / Q_s = 0.5$ and $\Delta Q_\beta / Q_s = 0.5$ is acceptable, one obtains limits for the parameters $k_{\parallel}(1)$ and $k_\perp$. The results are summarized in table 5 for single bunch beam current of 2.5 mA and a reference beta-function of 20 m.

Table 5: The PETRA III single bunch impedance budget.

	Impedance Budget
Longitudinal	10900 V/pC/m
Transverse	4800 V/pC/m

The total kick parameter of all elements is a weighted sum:

$$k_{\perp\text{total}} = \frac{1}{\langle\beta\rangle} \sum_n \beta_n\, k_{\perp n}\,, \tag{9}$$

where $\langle\beta\rangle = 20$ m is the reference beta-function. The transverse impedance budget as an effective impedance is 681 kOhm/m.

4.7.3   Wakefield Calculations

A list of all components which have been studied via numerical wakefield calculations is given in table 6. The list contains the horizontal and vertical beta functions and the number or total length of the component.

The synchrotron light absorbers in the wiggler section are discussed in more detail in [6]. The element "Wiggler Absorber (9 mm mask)" corresponds to cell type "A" while "Wiggler Absorber (17 mm mask)" corresponds to cell type "B" in reference [6]. A photo of one wiggler cell in the PETRA III ring is shown in Fig. 4.

Figure 4: One wiggler cell in the PETRA III tunnel. The synchrotron light absorbers are installed downstream of the wiggler and in front of the quadrupole magnet (WL 12 QA).

Table 6: Components of PETRA III

Name	Horz. Beta funct. / m	Vert. Beta- funct. / m	Length / m
Undulator (Resitive wall)	20	5	55
Wiggler (Resitive wall)	15	15	80
Arc (Resitive wall)	20	20	1411
Straight Section (resistive wall)	20	20	248
			Number
7 -cell cavity	14	13.5	12
Feedback cavity	10	7	8
Dipole chamber	15	15	196
Quadrupole chamber	15	15	203
Shielded bellow	15	15	203
BPM - Arc	7	25	105
Pumping ports (cylindrical)	20	20	50
Pumping ports (elliptical)	20	20	100
BPM straigth section	18	13	55
Collimator	13	30	2
Injection Kicker	24	12	3
Horz. Feedback Kicker	27	13	2
Vert. Feedback Kicker	13	30	2
Synchroton light absorber	5	30	9
Standard chamber new octant	5	30	9
Undulator Taper	15	6	16
Bellow Undulator (11 mm gap)	15	6	16
Taper 2 mm transition	15	6	16
BPM Undulator	15	6	16
Wiggler Absorber (9 mm mask)	22	6	8
Wiggler Absorber (17 mm mask)	6	19	8
Dipole magnet mask (17 mm gap)	20	20	2

The results for the wakefield calculations of the beam position monitors (BPMs) and the feedback cavities are summarized in the references [4, 20, 21, 22, 23]. The resistive wall wakefields and the wakefields of the injection kicker are discussed in more detail in references [6, 24]

The transition from the standard vacuum chamber of the "New Octant" to the small gap (7 mm) undulator chamber is shown in a schematic way in Fig. 5. Pumping ports are integrated in the long taper. The wakefields of the long taper have been calculated with PBCI and MAFIA, see ref. [3, 25].

Furthermore many other components including the feedback kickers, collimators, shielded pumping ports, synchrotron light absorbers, have been analyzed using the codes MAFIA [13] and ECHO [14].

The loss parameters $k_\parallel$, $k_\parallel(1)$ and the kick parameter $k_\perp$ for these components and other components are summarized in table 7. Using the data from table 6 and 7 we obtained the total vertical and horizontal kick parameter using Eq. (9), and the sum of the parameter $k_\parallel(1)$. The results are summarized in table 8 and are well within the impedance budget (table 5).

Table 7: Loss- and Kick- Parameters of PETRA III

Name	$k_\parallel$ / V/pC	$k_\parallel(1)$ / V/pC/m	Horz. $k_\perp$ / V/pC/m	Vert. $k_\perp$ / V/pC/m
Undulator (Resitive wall), for L = 1 m	-0.00459	0.28	0.10	32.79
Wiggler (Resitive wall), for L = 1 m	-0.00312	0.11	0.02	3.39
Arc (Resitive wall), for L = 1m	-0.00080	0.05	0.01	0.18
Straight Section (resistive wall), for L = 1m	-0.00200	0.05	0.05	0.05
7 -cell cavity	-3.76900	127.60	35.80	35.80
Feedback cavity	-0.47000	17.50	13.20	13.20
Dipole chamber	0.00000	0.00	0.00	0.00
Quadrupole chamber	-0.00001	-0.01	0.00	0.05
Shielded bellow	-0.00054	-0.27	0.14	0.25
BPM - Arc	-0.00035	-0.09	0.00	0.03
Pumping ports (cylindrical)	-0.00002	-0.02	0.00	0.01
Pumping ports (elliptical)	-0.00005	-0.05	0.00	0.05
BPM straigth section	-0.00035	-0.09	0.00	0.03
Collimator	-0.01900	-21.60	11.70	75.40
Injection Kicker	0.00000	0.00	1.60	1.60
Horz. Feedback Kicker	-0.34000	6.13	31.60	1.30
Vert. Feedback Kicker	-0.30800	5.34	31.70	4.10
Synchroton light absorber	-0.00001	-0.01	0.05	0.00
Standard chamber new octant	-0.00001	-0.01	0.10	0.00
Undulator Taper	-0.00520	-4.60	0.00	62.80
Bellow Undulator (11 mm gap)	-0.13700	-0.98	0.10	14.90
Taper 2 mm transition	-0.00440	-0.73	0.00	32.60
BPM Undulator	-0.00016	-0.05	0.00	3.87
Wiggler Absorber (9 mm mask)	-0.01780	-14.10	15.20	80.60
Wiggler Absorber (17 mm mask)	-0.01730	-11.20	7.56	33.50
Dipol magnet mask (17 mm gap)	-0.03250	-13.10	4.10	31.70
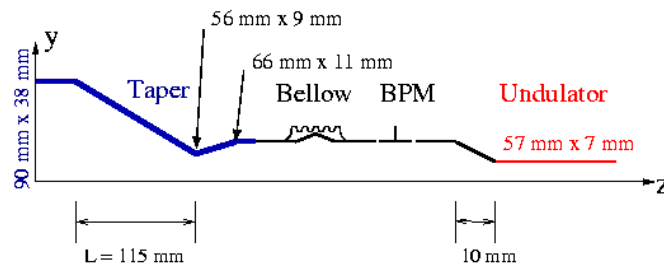
Figure 4: Transition from the standard vacuum chamber (height 38 mm) of the "New Octant" to the small gap (7 mm) undulator chamber.

Table 8: The total loss and kick parameters of PETRA III based on the wakefield calculations of the components of table 5 and 6.

	Parameter	*Impedance Model*
Longitudinal	$k_{\parallel}(1)$	1350 V/pC/m
Horizontal	$k_{\perp \, total}$	750 V/pC/m
Vertical	$k_{\perp \, total}$	2610 V/pC/m

4.7.4 Conclusion

Taking into account the different beta functions at the different vacuum components one obtains a total scaled (vertical) kick parameter of 2610 V/pC/m which is well below the impedance budget of 4800 V/pC/m (20 m beta function). The impedance of the planned X-ray light source PETRA III has been estimated based on measurements for the existing storage ring PETRA II, numerical calculations and analytical results for discontinuities in the beam pipe. Small gap chambers in the insertion devices will contribute significantly to the transverse impedance of PETRA III. But we expect no mode coupling instabilities for the operation mode with 40 bunches which requires a single bunch current of 2.5 mA since tune shifts in units of the synchrotron tune are small. Multi-bunch instabilities are mainly driven by parasitic modes in the RF cavities. The effective impedance has been determined from measurements at PETRA II. The expected growth rate of coupled bunch instabilities in PETRA III is much larger than the radiation damping rate. Therefore a powerful longitudinal and transverse multi-bunch feedback is required to provide the additional damping.

4.7.5 Acknowledgment

We would like to thank Mark Lomperski for carefully reading the manuscript.

4.7.6 References

1. PETRA III: A low Emittance Synchrotron Radiation Source", Technical Design Report, DESY 2004-035
2. K. Balewski, R. Wanzenberg, "Beam Current Limitations in the Synchrotron Light

Source PETRA III", 9th European Particle Accelerator Conference, EPAC04,5 to 9 July, 2004 Lucerne

3. E. Gjonaj, T. Lau, T. Weiland, R. Wanzenberg, "Computation of Short Range Wake Fields with PBCI", this ICFA Beam Dynamics Newsletter, April 2008

4. A.K. Bandyopadhyay, A. Joestingmeier, A.S. Omar, R. Wanzenberg, "Wake Computations for Selected Components of PETRA III", this ICFA Beam Dynamics Newsletter, April 2008

5. M. Ivanyan, E. Laziev, V. Tsakanov, A. Vardanyan, A. Tsakanian, R. Wanzenberg, "PETRA III Storage Ring Resistive Wall Impedance", this ICFA Beam Dynamics Newsletter, April 2008

6. V. Smaluk, R. Wanzenberg, "Geometrical Impedance of the PETRA III Damping Wiggler Section", this ICFA Beam Dynamics Newsletter, April 2008

7. T. Weiland, R. Wanzenberg: "Wakefields and Impedances", in M. Dienes, M. Month, S. Turner (Eds.) Proceedings US-CERN School, Hilton Head 1990, Springer-Verlag, Berlin , 1992

8. R. D. Kohaupt, "Transverse instability in PETRA", Proc. 11th Int. Conf. in High Energy Acc., CERN (1980) EXS Vol. 40, Birkhauser Verlag, p. 566

9. K. Balewski, "Analyse der transversalen Moden-Kopplungsinstabilitaet fuer lokalisierte HF-Strukturen und ihre Kompensierbarkeit durch Rueckkopplungssystemen", DESY 89-108, Aug. 1989

10. T. F. Günzel, "Transverse coupling impedance of the storage ring at the European Synchrotron Radiation Facility", Phys. Rev. ST Accel. Beams **9**, 114402 (2006)

11. N. S. Sereno, Y.-C. Chae, K. C. Harkay, A. Lumpkin, S. V. Milton, B. X. Yang, A Potpourri of Impedance Measurements at the Advanced Photon Source Storage Ring, Particle Accelerator Conference, PAC 97, Vancouver, 12-16 May 1997

12. T. Weiland, "On the Numerical Solution of Maxwell's Equations and Applications in the Field of Accelerator Physics", Part. Acc. 15 (1984)

13. MAFIA Version 4.106, CST GmbH, Büdingerstr. 2a, D-64289 Darmstadt, Germany (2002).

14. I. Zagorodnov and T. Weiland, "TE/TM field solver for particle beam simulations without numerical Cherenkov radiation", Phys. Rev. ST Accel. Beams 8, 042001 (2005).

15. W. Bruns, "Improved GdfidL with Generalized Diagonal Fillings and Reduced Memory and CPU Requirements", International Computational Accelerator Physics Conference, ICAP 98, Monterey, Sep. 14-18, 1998.

16. W. Bruns, "The GdfidL Electromagnetic Field simulator", http://www.gdfidl.de

17. E. Gjonaj, X. Dong, R. Hampel, M. Kärkkäinen, T. Lau, W. F.O. Müller, T. Weiland, "Large Scale Parallel Wake Field Computations for 3D-Accelerator Structures with the PBCI Code", International Computational Accelerator Physics Conference, ICAP 06, Chamonix, France, Oct 2-6, 2006

18. R. Boni, A. Gallo, A. Ghigo, F. Marcellini, M. Serio, M. Zobov, "A waveguide overloaded cavity as longitudinal kicker for the DAFNE bunch-by-bunch feedback system," Particle Accelerators, Vol. 52, pp. 95–113, 1996.

19. M. Dehler, "Kicker design for the ELETTRA/SLS longitudinal multi-bunch feedback," in 8th European Particle Accelerator Conference (EPAC 02), Paris, France, pp. 2070–2072, 2002.

20. A.K. Bandyopadhyay, A. Joestingmeier, A.S. Omar, K. Balewski, R. Wanzenberg , "Wake Computations for the Beam Positioning Monitors of PETRA III", Proceedings of European Particle Accelerator Conference, EPAC 06, Edinburgh, Scotland, 26-30 Jun 2006

21. A.K. Bandyopadhyay, A. Jostingmeier, A.S. Omar, R. Wanzenberg, "Computations of Wakefields for Beam Position Monitors of PETRA III", Internal Report DESY-M-06-02, Jul 2006

22. A.K. Bandyopadhyay, A. Joestingmeier, A.S. Omar, K. Balewski, R. Wanzenberg, "Computation of Wakefields and Impedances for the PETRA III Longitudinal Feedback Cavity", Asian Particle Accelerator Conference, APAC 07, Indore, India, Jan 29-Feb 02, 2007

23. A.K. Bandyopadhyay, A. Joestingmeier, A.S. Omar, R. Wanzenberg, "Wakes and Impedance Computations for the PETRA III Longitudinal Feedback Cavity", Internal Report, DESY-M-07-02, Nov 2007

24. M. Ivanyan, E. Laziev, V. Tsakanov, A. Vardanyan, A. Tsakanian, R. Wanzenberg, "Investigation of the PETRA III Resistive Wall Impedance, Intermediate Report of the PETRA III - CANDLE COLLABORATION", Internal Report, DESY-M-07-01, Sep 2007

25. K. Balewski, E. Gjonaj, T. Weiland, , R. Wanzenberg, "Wake Computations for Undulator Vacuum Chambers of PETRA III", Particle Accelerator Conference, PAC07, Albuquerque, New Mexico, 25 to 29 June, 2007

4.8 PETRA III Storage Ring Resistive Wall Impedance

M. Ivanyan, E. Laziev, V. Tsakanov, A. Vardanyan
CANDLE, Acharyan 31, 375040 Yerevan, Armenia
Mail to: ivanian@asls.candle.am
A. Tsakanian, Hamburg University, Hamburg, Germany
Mail to: tsakania@mail.desy.de
R. Wanzenberg, DESY, Notkestr. 85, Hamburg, Germany
Mail to: rainer.wanzenberg@desy.de

4.8.1 Introduction

The article presents the results of the resistive wall impedance study for the PETRA III storage ring [1] vacuum chamber that consists of different parts with various geometrical (circular and elliptical cross sections) and structural (single layer and laminated) configurations conditioned by the technical solutions for high brightness synchrotron light sources.

The study is based on the impedance calculation for a laminated vacuum chamber with circular-cylindrical geometry using the field matching technique [2,3]. The field transformation matrix concept is introduced to evaluate analytically the longitudinal and transverse impedances for a layered vacuum chamber with arbitrary materials and thicknesses [4,5]. The results are applied to calculate the impedances for various parts of the vacuum chamber listed in Table 1: the finite thickness standard vacuum chamber, the metallic wiggler chamber with NEG coating and the injection kicker ceramic – metallic vacuum chamber. Impedances are evaluated for chambers with circular and elliptical cross sections. Horizontal and vertical geometrical correction factors [6] are used for the impedances calculations of vacuum chambers with elliptical cross section. The kick factor and the integrated gradient of the longitudinal wake potential are also given.

Table 1: The main parameters of PETRA III vacuum chambers.

Vacuum Chamber	Material	Cross-section	Aperture (mm)	Wall thickness (mm)	Conductivity 10^6 $(\Omega m)^{-1}$
Standard straight section	Stainless Steel	Circular	47	2	1.5
Standard arc	Aluminium	Elliptical	40×20	4	36.6
Undulators	Aluminium	Elliptical	28.5×3.5	1	36.6
Wigglers	Aluminium + NEG	Elliptical	48×8.95	2.8	36.6 0.31
Injection Kicker	Ceramic + TSHGS	Circular	90	10	- 2.084

4.8.2 Resistive Impedance of Multi-Layer Vacuum Chamber

The longitudinal $Z_\parallel(\omega,r,\theta)$ and transverse $\vec{Z}_\perp(\omega,r,\theta)$ coupling impedances per unit length are defined as a Fourier transformation of the normalized longitudinal and transverse components of the integrated Lorentz force of the electromagnetic fields, induced by the point charge q moving with constant velocity v along the tube axis z. The m- pole azimuthal components of the impedances in ultra-relativistic approximation are given by [2,3]

$$Z_\parallel^{(m)}(\omega,r,\theta) = \widetilde{Z}_\parallel^{(m)}(k)\left(\frac{r}{a_1}\right)^m\left(\frac{r_q}{a_1}\right)^m \cos m\theta$$

$$\left.\begin{array}{c}Z_r^{(m)}\\Z_\theta^{(m)}\end{array}\right\}(\omega,r,\theta) = \widetilde{Z}_T^{(m)}(k)\left(\frac{r}{a_1}\right)^{m-1}\left(\frac{r_q}{a_1}\right)^m\left\{\begin{array}{c}\cos m\theta\\-\sin m\theta\end{array}\right.$$

(1)

where ω is the frequency, (r,θ) are the polar coordinates, $k = \omega/v$ is the wave number, a_1 is the internal radius of the chamber with circular cross section. The frequency dependent part of impedances $\widetilde{Z}_\parallel^{(m)}(k)$, $\widetilde{Z}_T^{(m)}(k)$ are coupled by Panowsky-Wenzel theorem as $\widetilde{Z}_T^{(m)} = m\widetilde{Z}_\parallel^{(m)}/(ka_1)$ [2]. The dimensions of the longitudinal and transverse impedances per unit length are Ohm/m. For the multi-layered vacuum chamber the impedances can be evaluated using the field matching technique [2], i.e. the continuity of tangential components of electric and magnetic fields on the layers boarders, and introducing the field transformation matrix $\hat{Q}$ for tangential components of the fields [4,5]. The longitudinal impedance can be then expressed via the elements Q_{ij} of field transformation matrix $\hat{Q}$ (dim 4×4) as

$$
\widetilde{Z}_{\parallel}^{(m)}(k) = \begin{cases} j\dfrac{Z_0}{\pi k a_1^2}\left(1-\dfrac{2}{ka_1}\dfrac{Q_{33}}{Q_{23}}\right)^{-1} & for \quad m=0 \\[4mm] j\dfrac{Z_0}{\pi}k\left(\dfrac{k^2a_1^2}{m+1}-m+\dfrac{ka_1V_m^+}{V_m^-}\right)^{-1} & for \quad m>0 \end{cases}
\tag{2}
$$

The field transformation matrix $\hat{Q}$ couples the tangential components of the electric and magnetic fields at the inner ($r=a_1$) and outer ($r=a_{N+1}$) surfaces of the pipe and for N layer tube is calculated as

$$
\hat{Q}=\hat{Q}^{(1)}\hat{Q}^{(2)}\cdots\hat{Q}^{(N)},
\tag{3}
$$

where $\hat{Q}^{(i)}$ is the field transformation matrix through the i-th layer ($i=1,2,3...N$)

$$
\hat{Q}^{(i)}=\begin{pmatrix} q_{11} & q_{12} & -\alpha_0 q_{31} & \alpha_0 q_{32} \\ 0 & q_{22} & -\alpha_0 q_{41} & \alpha_0 q_{42} \\ q_{31} & q_{32} & q_{11} & -q_{12} \\ q_{41} & q_{42} & 0 & q_{22} \end{pmatrix}
\tag{4}
$$

with $\alpha_0 = \varepsilon'_i/\mu'_i$, $\varepsilon'_i = \varepsilon_i/\varepsilon_0$, $\mu'_i = \mu_i/\mu_0$, the relative dielectric and magnetic permeabilities of each layer with respect to the vacuum constants ε_0, μ_0. The seven independent elements of the field transformation matrix $\hat{Q}^{(i)}$ are determined by corresponding geometrical and electromagnetic layer parameters and are:

$$
\begin{aligned}
& q_{11}=-a_{i+1}\chi_i U_3^{(i)}, \quad q_{22}=a_{i+1}\chi_i U_2^{(i)}, \\
& q_{12}=\frac{jkm}{a_i\chi_i^2}\left(\frac{a_i}{a_{i+1}}q_{11}-q_{22}\right), \quad q_{31}=\frac{ja_{i+1}}{\mu'_i a_i}mU_1^{(i)}, \\
& q_{32}=k\left(\beta^2\varepsilon'_i a_{i+1}U_4^{(i)}+\frac{m^2 U_1^{(i)}}{\mu'_i a_i\chi_i^2}\right), \\
& q_{41}=-\frac{a_{i+1}\chi_i^2}{k\mu'_i}U_1^{(i)}, \quad q_{42}=\frac{a_{i+1}}{a_i}q_{31},
\end{aligned}
\tag{5}
$$

where $\chi_i = \sqrt{k^2-\mu_i\varepsilon_i\omega^2}$ ($Re(\chi_i)>0$) are the radial propagation constants. The functions $U_k^{(i)}(k=1,2,3,4)$ are the combinations of modified Bessel functions of both kinds. In the frequency range, the functions $U_k^{(i)}$ can be approximated by hyperbolic functions if the skin depth of a layer is much smaller than the inner radius of the tube, i.e. for all practically important cases:

$$U_1^{(i)} = K_m(\chi_i a_i)I_m(\chi_i a_{i+1}) - I_m(\chi_i a_i)K_m(\chi_i a_{i+1}) \approx Sinh(\chi_i d_i)/\chi_i\sqrt{a_{i+1}a_i},$$

$$U_2^{(i)} = K_m(\chi_i a_i)I_m'(\chi_i a_{i+1}) - I_m(\chi_i a_i)K_m'(\chi_i a_{i+1}) \approx Cosh(\chi_i d_i)/\chi_i\sqrt{a_{i+1}a_i},$$

$$U_3^{(i)} = K_m'(\chi_i a_i)I_m(\chi_i a_{i+1}) - I_m'(\chi_i a_i)K_m(\chi_i a_{i+1}) \approx -Cosh(\chi_i d_i)/\chi_i\sqrt{a_{i+1}a_i},$$ (6)

$$U_4^{(i)} = K_m'(\chi_i a_i)I_m'(\chi_i a_{i+1}) - I_m'(\chi_i a_i)K_m'(\chi_i a_{i+1}) \approx -Sinh(\chi_i d_i)/\chi_i\sqrt{a_{i+1}a_i}.$$

In (6) $d_i = a_{i+1} - a_i$ is the thickness of the i-th layer. All elements of the matrix $\hat{Q}^{(i)}$ (4) are dimensionless and the determinant of the matrix is equal to a_{i+1}^2/a_i^2 . As is seen from (5), for the monopole term $m = 0$ the following elements of field transformation matrix $q_{12} = q_{13} = q_{21} = q_{24} = q_{31} = q_{34} = q_{42} = q_{43} \equiv 0$ are vanishing.

The other coefficients in (2) are determined as

$$V_m^\pm = ka_{N+1}A^\pm + (1 + 2k^2 a_{N+1}^2 P_0)B^\pm \qquad for \quad m = 1,$$

$$V_m^\pm = (m-1)ka_{N+1}A^\pm + [m(m-1) - k^2 a_{N+1}^2]B^\pm, \qquad for \quad m > 1,$$ (7)

with $P_0 = ln(ka_{N+1}/2\gamma) + C_E$, $C_E = 0.577216$ the Euler constant, γ the particle Lorentz factor . Coefficients $A^\pm, B^\pm$ are defined via the elements of field transformation matrix

$$A^+ = Det[\hat{h}_{11;\,22} + \hat{h}_{33;\,44} + j(\hat{h}_{13;\,24} - \hat{h}_{31;\,42})],$$

$$A_m^- = Det[\hat{h}_{21;\,42} + j\hat{h}_{23;\,44}],$$

$$B^+ = Det[\hat{h}_{11;\,23} - j\hat{h}_{31;\,43}],$$ (10)

$$B_m^- = Det[\hat{h}_{21;\,43}],$$

where the matrix $\hat{h}_{pi;qj}$ is composed as

$$\hat{h}_{pi;\,qj} = \begin{Bmatrix} Q_{pi} & Q_{pj} \\ Q_{qi} & Q_{qj} \end{Bmatrix},$$ (11)

Note that in ultra-relativistic limit $(ln\gamma \to \infty)$ for dipole mode $(m = 1)$, $U^+/U^- = B^+/B^-$.

4.8.3   Impedance of Vacuum Chamber with Elliptical Cross Section

In the case of a elliptical vacuum chamber the impedance significantly depends on the transverse position of the beam. We consider the practically important case when the beam has a horizontal or a vertical offset with respect to ellipse center. We will evaluate the impedances for an elliptical vacuum chamber following the approach developed in Ref. [6] that generalize the round chamber impedances for elliptical cross section by introducing longitudinal and transverse geometrical correction factors. For the elliptical geometry with major a and minor b radii the longitudinal and transverse impedances may be expressed then via the round chamber impedances with radius b

(ellipse minor radius) multiplied by the longitudinal $G_\parallel$ or transverse G_v (vertical), G_h (horizontal) geometrical factors:

$$Z_\parallel(\omega) = Z_s^0(\omega)\, G_s, \qquad Z_{v,h}(\omega) = Z_t^0(\omega)\, G_{v,h} \qquad (12)$$

The geometrical factors depend on the ellipse aspect ratio a/b and are defined as

$$G_s(\omega) = \frac{1}{2\pi} \int_0^{2\pi} \frac{f_c^2(\xi)}{g(\xi)}\, d\xi$$

$$G_{v,h}(\omega) = \frac{1}{2\pi(a^2/b^2 - 1)} \int_0^{2\pi} \frac{f_c(\xi) f_t(\xi) + 2 f_{v,h}^2(\xi)}{g(\xi)}\, d\xi \qquad (13)$$

where

$$f_c(\xi) = 1 + 2\sum_{m=1}^{\infty} \frac{\cos m\xi}{ch\,\eta_0} \cos\frac{m\pi}{2}, \quad f_t(\xi) = \sum_{m=1}^{\infty} m^2 \frac{\cos m\xi}{ch\,\eta_0} \cos\frac{m\pi}{2},$$

$$f_v(\xi) = \sum_{m=1}^{\infty} m \frac{\sin m\xi}{\sinh m\eta_0} \sin\frac{m\pi}{2}, \quad f_h(\xi) = -\sum_{m=1}^{\infty} m \frac{\cos m\xi}{\cosh m\eta_0} \sin\frac{m\pi}{2}, \qquad (14)$$

$$g(\xi) = \sqrt{1 + \sin^2\xi/\sinh^2\eta_0}, \quad \eta_0 = \frac{1}{2}\ln\frac{1 + b/a}{1 - b/a},$$

with (ξ, η) the elliptical coordinates.

The geometrical factor for the longitudinal impedance is equal to unity $(G_s = 1)$ for a round tube $(a/b = 1)$ and closed to unity for large values of a/b: $G_s \to 1$ for $a/b \to \infty$, i.e. the longitudinal impedance of the round tube of radius b coincides with the impedance of a flat chamber with a distance of $2b$ between plates [7]. For the transverse impedance: for a large aspect ratio a/b the horizontal geometrical factor drops while the vertical geometrical factor approaches to $\pi^2/8 \approx 1.23$.
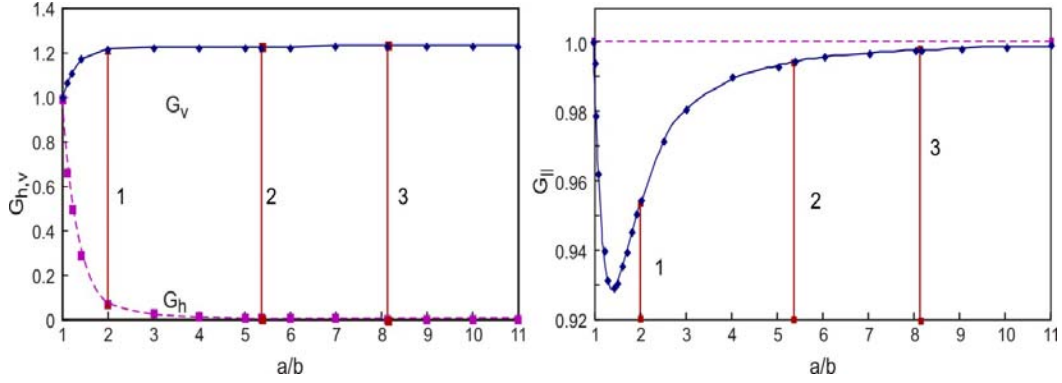
Figure 1: The longitudinal (left) and transverse (right) geometrical factors vs aspect ratio a/b. Standard arc (1), wiggler (2) and undulator (3) chambers.

Table 2 shows the correction factors for the PETRA III vacuum chambers with elliptical cross section. As is seen, the transverse impedance for elliptical vacuum chambers is actually dominated by the vertical impedance.

Table 2: Geometrical factors for PETRA III elliptical vacuum chambers.

	Standard Arc	Wiggler	Undulator
Aspect ratio a/b	2	5.36313	8.14286
Longitudinal $G_\parallel$	0.9531	0.9941	0.9975
Vertical G_v	1.2213	1.2322	1.2330
Horizontal G_h	0.0764	0.0088	0.0038

In the current paper the impedances in all the figures are evaluated for the round chamber geometry. For the vacuum chambers with elliptical cross-section, the transverse vertical impedance should be multiplied by the geometrical factor of $\pi^2/8$.

4.8.4 Impedance of Finite Thickness Single -Layer Vacuum Chamber

For the single layer vacuum chamber of internal radius a and finite wall thickness d the monopole ($m=0$) and dipole ($m=1$) modes of the impedance in ultrarelativistic limit for non-magnetic wall $\left(\mu_1 = \mu_0\right)$ can be presented in explicit form as

$$
\widetilde{Z}_\parallel^{(m)}(k) = \begin{cases} j\dfrac{Z_0}{\pi k a^2}\left(1 + \dfrac{2}{a\chi\varepsilon'}\dfrac{U_3}{U_1}\right)^{-1} & for \quad m=0 \\[4mm] j\dfrac{Z_0 k}{\pi}\left[\dfrac{k^2 a^2}{2} - \dfrac{\varepsilon'+1}{\varepsilon'-1}\left(1 - a\chi\dfrac{U_3}{U_1}\right)\right]^{-1} & for \quad m=1 \end{cases} \tag{15}
$$

If the skin depth of the layer is much smaller than the inner radius of the tube the functions U_1, U_3 are approximated by hyperbolic functions according to (6) and $U_3/U_1 \approx cth(\chi d)$ with d the wall thickness. For the infinite wall thickness $\left(d \to \infty\right)$

and commonly used approximation ($\omega << \sigma/\varepsilon_0$, σ - conductivity) formula (15) is converted to well-known presentation of the impedance [1,2]:

$$\widetilde{Z}_{\parallel}^{(0,1)} = h_{0,1}\frac{Z_0 s_0}{2\pi a^2}\left(\frac{1+j}{\sqrt{k_0}} - \frac{jk_0}{2}\right)^{-1},$$

(16)

where $h_0 = 1$ for the monopole term, $h_1 = 2$ for the dipole term, $s_0 = \left(2a^2/Z_0\sigma\right)^{1/3}$ is the characteristic distance and $k_0 = ks_0$ is the dimensionless wave-number.

4.8.4.1   Standard Straight Section

Figures 2 and 3 present the longitudinal and transverse multipole impedances for the PETRA III standard straight section vacuum chamber with circular cross section (see Table 1) based on the exact solution given by (2).
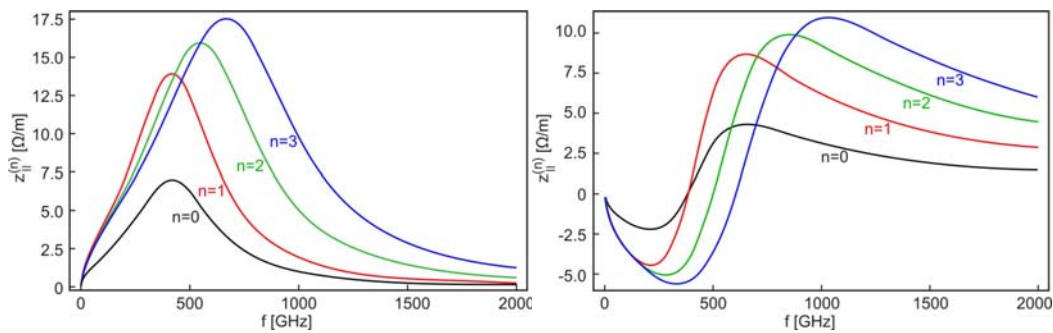
Figure 2: Real (left) and imaginary (right) parts of the longitudinal impedance for a standard straight section. Tube material- stainless steel, inner radius - 47mm, wall thickness - 2mm.
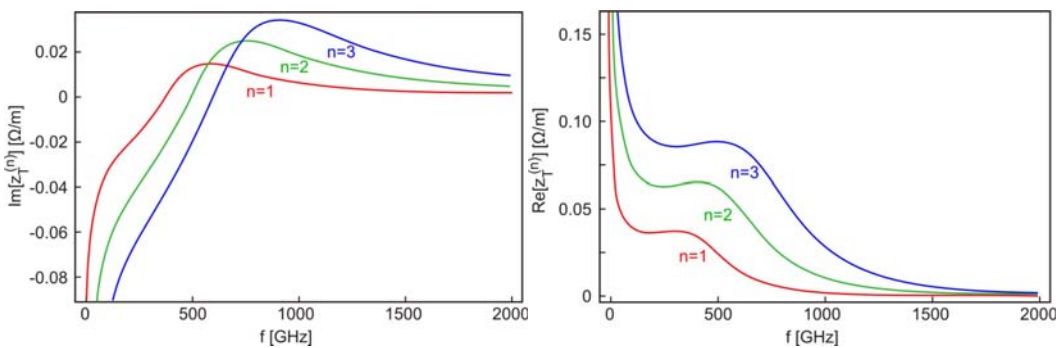
Figure 3: Real (left) and imaginary (right) parts of the transverse impedance for a standard straight section. Tube material- stainless steel, inner radius - 47mm, wall thickness - 2mm.

For a wall thickness of 2 mm the skin depth is equal to the wall thickness when the frequency is equal to $f_0 \sim 42kHz$. For frequencies $f >> f_0$ the results are well described by the general approximation (16) for infinite wall thickness.

The difference arises for the frequencies $f \leq f_0$. Figures 4 and 5 show the real and imaginary parts of the longitudinal monopole and transverse dipole impedances in kHz-frequency region for the exact solution and the approximation (16).
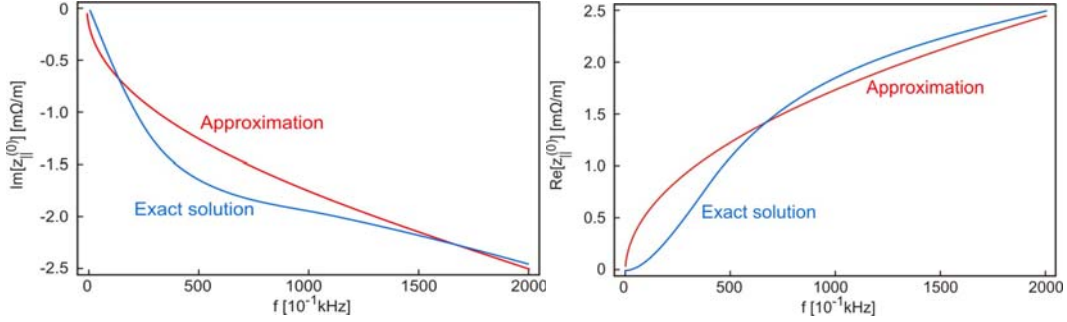
Figure 4: Real and imaginary parts of the longitudinal monopole impedance for the exact solution and the infinite thickness approximation in the kHz-frequency region.
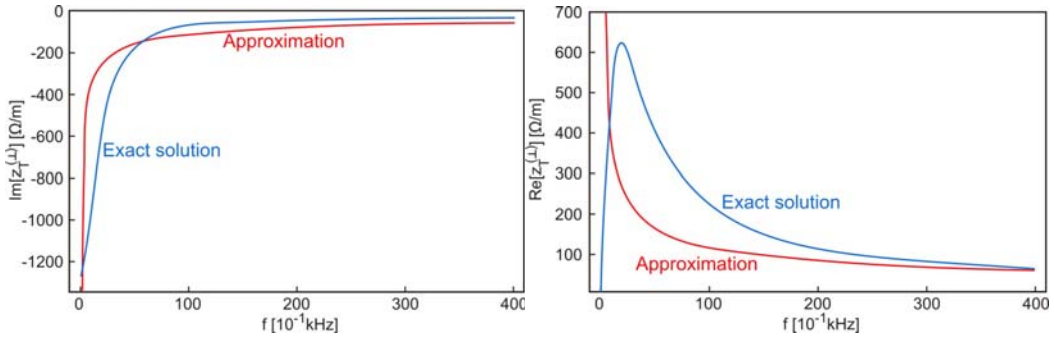
Figure 5: Real and imaginary parts of the transverse dipole impedance for the exact solution and the infinite thickness approximation in the kHz-frequency region.

As one can see from Figure 5, the transverse impedance given by the approximation (16) diverges at $\omega = 0$, while the exact solution gives $Z_T^{(m)}(\omega = 0) = -jZ_0/2\pi a$ for all multipoles and does not depend on the the material and the thickness of the chamber wall.

4.8.4.2   *Frequency-Dependent Conductivity.*

The frequency dependent conductivity of the metal is given by

$$\sigma(\omega) = \sigma_{st}(1 - j\omega\tau)^{-1}, \qquad (17)$$

where σ_{st} is the static conductivity and τ is the relaxation time. A comparison of the longitudinal monopole impedance of the stainless steel tube with a frequency dependent (AC) and a frequency independent (DC) conductivity is presented in Fig. 6. The relaxation time is taken to be $\tau = 3.2 \cdot 10^{-14}$ sec, which corresponds to the relaxation time of iron at a temperature of $T = 77$ K.

The transverse dipole impedance for the same vacuum chamber with AC and DC conductivity is presented in Figure 7. As is seen from the results the impedances actually coincide for the given relaxation time.
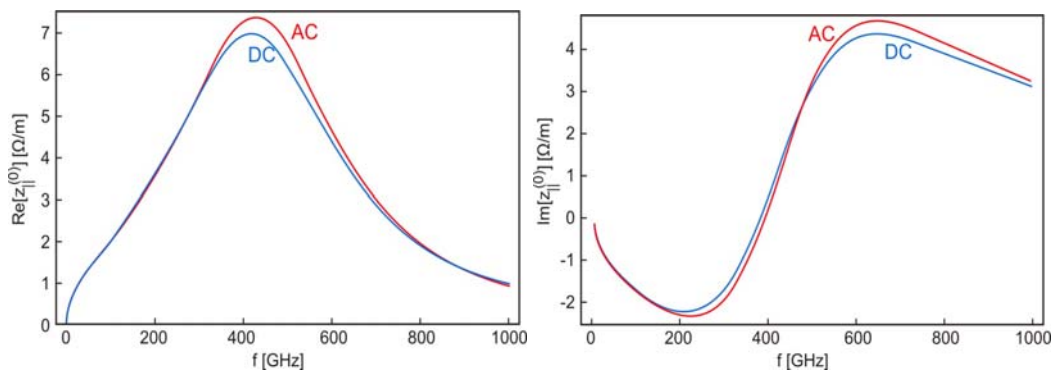
Figure 6: Longitudinal monopole impedance of a standard vacuum chamber for DC and AC conductivities.
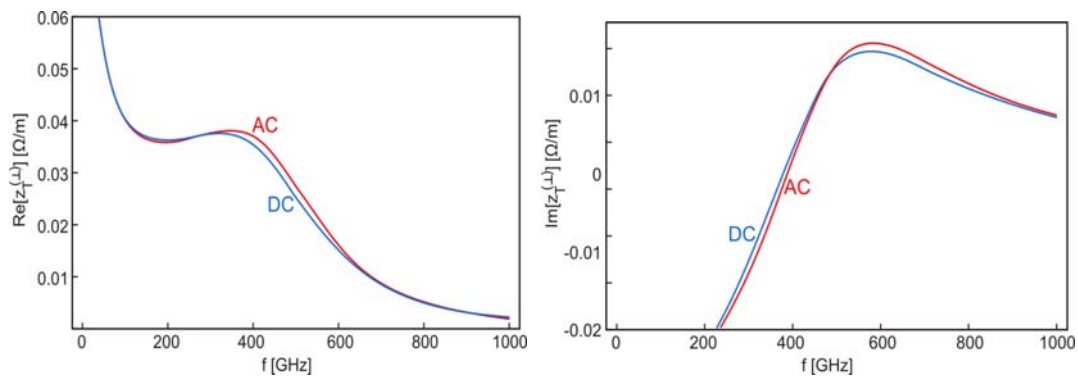
Figure 7: Transverse dipole impedance of a standard vacuum chamber for DC and AC conductivities.

4.8.4.3   *Undulator Vacuum Chamber*

The vacuum chamber of the undulator is an aluminium chamber with elliptical cross section and a wall thickness of 1mm. Figure 8 presents the real and imaginary parts of the transverse dipole impedance.
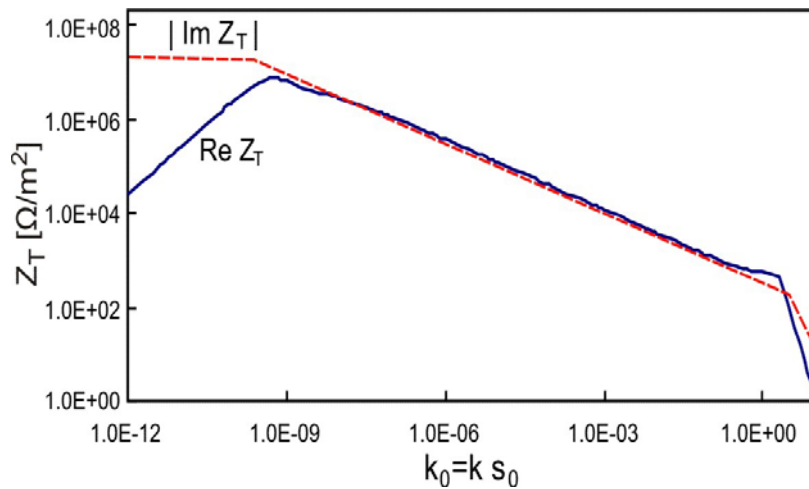
Figure 8: Transverse impedance of undulator vacuum chamber.

4.8.5 Impedance of Two-Layer Vacuum Chamber

The technical solutions for the vacuum chambers of the wiggler magnets and injection kickers in the PETRA III storage ring imply the usage of laminated chamber configurations. The wiggler magnet chamber is an aluminum chamber of elliptical cross section with NEG (Non-Evaporable Getter) coating on the inner side of the wall. The injection kicker vacuum chamber is a ceramic chamber of circular cross section covered with Titanium-Stabilized High Gradient Steel (TSHGS), a special metal alloy.

4.8.5.1 Wiggler Vacuum Chamber

Fig. 9 presents the real and imaginary parts of the transverse dipole impedance for a wiggler aluminum vacuum chamber coated with NEG material of 0.5 μm and 1 μm thickness. For a NEG thickness of 1 μm, the frequency that corresponds to the skin depth equal to cover thickness is in the order of $f_0 \sim 820\,\text{GHz}$. For this case, as it can be seen from Fig. 9, the impact of the NEG-coating is visible for frequencies $f \geq 5 - 10\,GHz$.
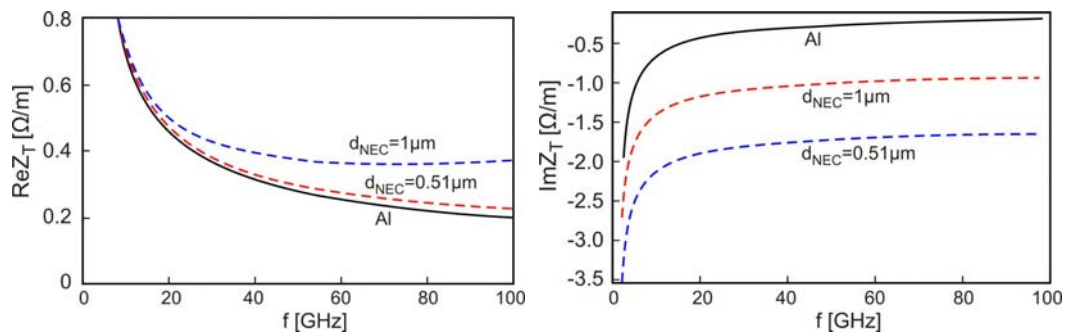
Figure 9: Real and imaginary parts of the transverse dipole impedance for the PETRA III wiggler vacuum chamber coated with NEG material.

Figure 10 presents the dependence of the kick factor k_T and integrated gradient of longitudinal wake $k_{II}(1)$ produced by the wiggler vacuum chamber versus the NEG thickness.
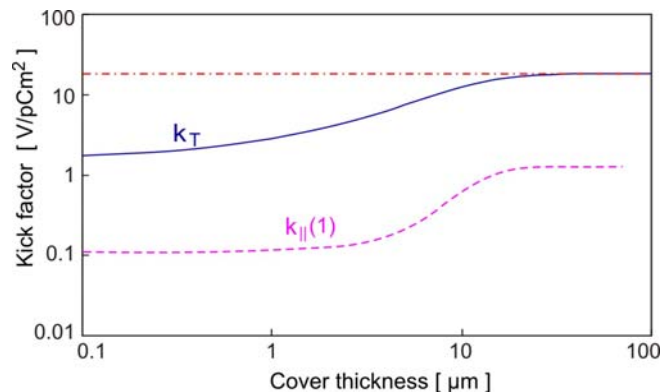
Figure 10: Kick factor (solid) and integral gradient of the longitudinal wake (dashed) versus cover thickness. The long-range approximation is plotted as well.

4.8.5.2   Injection Kicker

The vacuum chamber of the PETRA III injection kicker is a round ceramic tube with thickness $1 cm$, which is covered at the inner side with Titanium-Stabilized High Gradient Steel (TSHGS), a special metal alloy. The layer thickness of the TSHGS is equal to $0.7 \mu m$. The relative electrical permitivity of the ceramic material is taken as $\varepsilon_r = 9.1$ with a loss tangent of $\tan \delta \sim 10^{-4}$, so that the absolute electrical permitivity is equal to $\varepsilon_{cer} = \varepsilon_r \varepsilon_0 (1 - j \tan \delta) \, As/Vm$. The cover conductivity is in the order of $\sigma_{cover} = 2.0841 \cdot 10^6 \, \Omega^{-1} m^{-1}$.

Figure 11 presents the transverse dipole impedance for the injection kicker vacuum chamber which is compared with the impedance of ceramic tube and the impedance of a pure TSHGS vacuum chamber. As seen from Figure 11, the ceramic tube impedance in the low frequency region has a constant value and is characterized by the narrow-meshed periodical oscillations. It should be noted that the oscillations amplitude decreases with the increasing of the wall thickness. The fine structure of ceramic tube impedance is characterized by narrow-band resonances (Fig. 12, left).
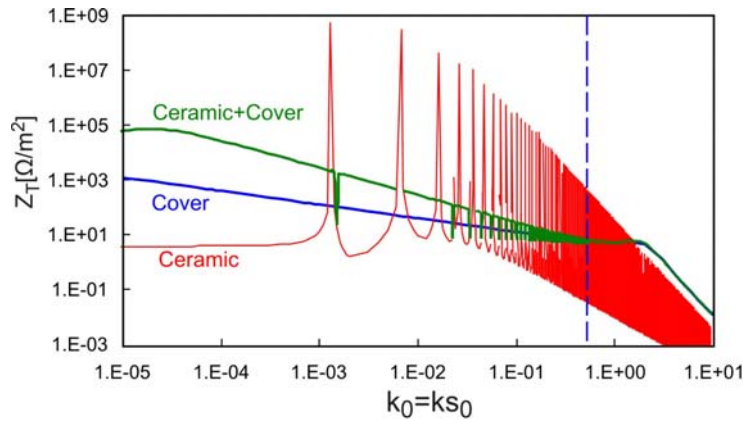
Figure 11: Injection kicker transverse impedance (real part).
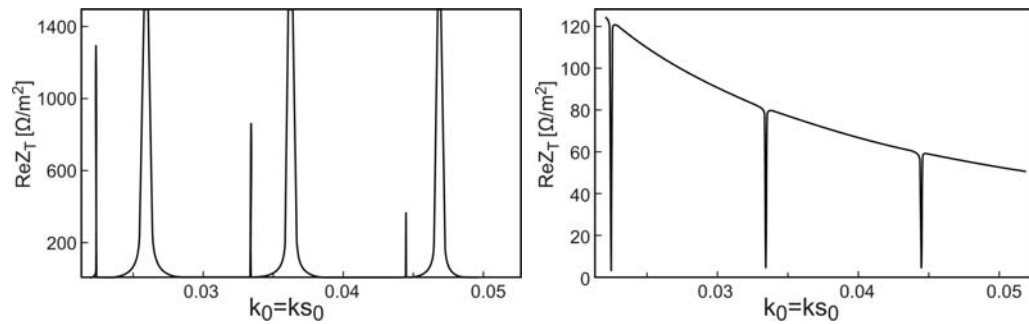
Figure 12: Fine structure of the transverse impedance for a ceramic (left) and a ceramic + TSHGS (right) vacuum chamber.

The impedance of a covered ceramic tube can be interpreted as a smooth curve: the high-level resonances disappear and the low-level notches appear instead of narrow-band low-level resonances of ceramic tube impedance (Fig. 12, right). In the high frequency region, then the skin depth of the cover material surpasses the thickness of the cover layer $(k_0 > 0.52)$ and the impedance of the ceramic-metal tube is fully determined by metallic layer material.

The kick factor of the injector kicker depends weakly on thickness of the ceramic layer if the layer is larger than 2.5 cm, as shown in Fig. 13.
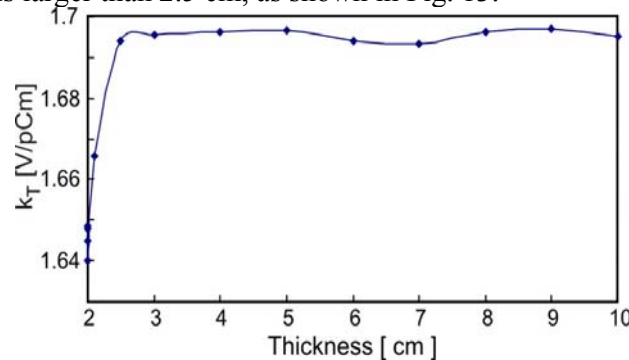
Figure 13: Kick parameter versus ceramic wall thickness.

4.8.6 Transverse Kick Factor and Integral Gradient

The instability threshold for mode coupling instabilities can be estimated from the tune shifts ΔQ_s, ΔQ_β of the lowest order modes in the longitudinal and transverse planes [8]:

$$\Delta Q_\beta = \frac{I_B \langle \beta \rangle T_0}{4\pi E/e} k_\perp,$$

$$\Delta Q_s = Q_s \frac{I_B R T_0}{2hV_{rf}} k_\parallel(1),$$

(18)

where $k_\perp$ is the transverse kick factor, $k_\parallel(1)$ is the integral gradient of longitudinal wake, I_B is the single bunch current, $R = 367m$ is the storage ring mean radius, $\langle \beta \rangle$ is the average beta function, E is the particle energy, T_0 is the revolution period, V_{rf} is RF gap voltage and h is the harmonic number. The following tolerable tune shifts are assumed

$$\frac{\Delta Q_\beta}{Q_s} = 0.5, \quad \frac{\Delta Q_s}{Q_s} = 0.5$$

(19)

That determines the maximal acceptable values for total integrated gradient $k_\parallel(1)$ and kick factor $k_\perp$ in the ring. The integral gradient $k_\parallel(1)$ and kick factor $k_\perp$ of the Gaussian bunch with rms length σ_z are defined by the monopole and dipole impedances as

$$k_\parallel(1) = \left| \frac{1}{\pi} \int_0^\infty d\omega k \, \mathrm{Im}\left[Z_\parallel^{(0)}(\omega) \right] \exp(-k^2 \sigma_z^2) \right|$$

$$k_T = \frac{1}{\pi a} \int_0^\infty d\omega \, \mathrm{Im}\left[\tilde{Z}_T^{(1)}(\omega) \right] \exp(-k^2 \sigma_z^2/).$$

(20)

The total integral gradient of the longitudinal wake and the kick factor of the ring are the sum of the contributions from all vacuum chamber components (wigglers, undulators, standard sections)

$$k_\parallel(1)_{total} = \sum_i k_\parallel(1)_i L_i, \qquad k_{\perp total} = \frac{1}{\langle \beta \rangle} \sum_i \beta_i k_{\perp i} L_i$$

(21)

where β_i is the local beta function ($\beta_y = 5$ m for undulator section, $\beta_y = 15$ m for wiggler section and $\beta_y = 20$ m for the standard arc), $\langle \beta \rangle$ is the average beta function ($\langle \beta \rangle = 20m$), L_i is the length of the corresponding vacuum chamber path.

Table 3: The integrated gradient and kick factor.

Device	β_y (m)	Length (m)	$k_{\parallel}$ (1) (V/pC/m)	$k_{\perp}$ (V/pC/m)
Undulator	5	55	15.57	450.8
Wiggler	15	80	8.45	203.4
Arc	20	1411	68.12	247.6
Total	-	1546	91.14	901.8

Table 3 presents the resistive wall contributions to the longitudinal and transverse impedance budget of PETRA III (in terms of $k_{\parallel}(1)$ and $k_{\perp}$) for a bunch length of $\sigma_z = 12$ mm. The total integral gradient of longitudinal wake is estimated to be $k(1)_{\parallel\,total} = 91.14\,V/pC\,m$ and the total kick factor as $k_{\perp\,total} = 902V/pC/m$. Thus the longitudinal and transverse resistive wall contributions to the total tolerable impedance budget are 0.87% and 15.3% respectively.

4.8.7 Conclusion

In the present paper the longitudinal and transverse resistive impedances for different parts of PETRA III storage ring are evaluated. The impedances for single layer finite thickness and two-layer vacuum chambers are evaluated for both circular and elliptical geometry of the chamber. The contribution of the resistive wall impedance in terms of the kick factor and the integral gradient of the longitudinal wake to the total impedance budget have been estimated.

4.8.8 Acknowledgment

4.8.9 References

1. "PETRA III: A low Emittance Synchrotron Radiation Source", Technical Design Report, DESY 2004-035; http://petra3.desy.de/project_description
2. B.W.Zotter and S. A. Kheifetz, Impedances and Wakes in High-Energy Particle Accelerators, World Scientific, Singapore, 1997.
3. A.W. Chao, Physics of Collective Beam Instabilities in High Energy Accelerators (Wiley, New York, 1993).
4. M. Ivanyan et al, Investigation of the PETRA III Resistive Wall Impedance, DESY M 07-01, September 2007.
5. M. Ivanyan et al, Phys. Rev. ST-AB (to be published).
6. A. Piwinski, Report No. DESY HERA 92-11, 1992, p. 19.
7. H. Henke, O. Napoly, In Proc. of the 2nd European Particle Accelerator Conference, Nice, France, pp. 1046-1048, 1990.
8. K. Balewski and R. Wanzenberg, Proceedings of 2005 Patricle Accelerator Conference, Knoxwill, Tennessee, USA, pp. 1751-1753, 2005.

4.9 Geometrical Impedance of the PETRA III Damping Wiggler Section

Victor Smaluk, Budker Institute of Nuclear Physics, Novosibirsk, Russia
Rainer Wanzenberg, DESY, Notkestr. 85, Hamburg, Germany
Mail to: smaluk@inp.nsk.su

4.9.1 Introduction

For the PETRA III synchrotron radiation source [1], a damping wiggler section has been designed in the Budker Institute of Nuclear Physics. Two such sections will be installed to decrease the PETRA III beam emittance. The wiggler section vacuum chamber includes a set of synchrotron radiation absorbers intended to accept more than 200 kW of radiation power during the machine routine operation. An irregular cross-section of the vacuum chamber results in a quite large coupling impedance. To estimate the contribution of the wiggler section to the total PETRA III broad-band impedance, three-dimensional computer simulations of the wake fields have been performed using GdfidL code [2], in comparison with analytical formulae.

4.9.2 Collective Effects and Coupling Impedance

Particle dynamics of an intensive beam moving in a vacuum chamber differs from a single-particle dynamics. The beam induces quite strong electromagnetic fields (wake fields) affecting the beam itself. The most significant results of the collective effects are various instabilities of beam motion, which can lead to beam losses or beam quality deterioration.

In the time domain, beam-environment interaction is characterized by the wake potential defined as the wake force integrated along the beam trajectory over the interaction length [3]. In the frequency domain, each part of a vacuum chamber can be represented as frequency-dependent coupling impedance, which is the Fourier transform of the wake function. The real (resistive) part of the impedance leads to a particle energy loss, the imaginary (reactive) one leads to a shift of particle oscillation phase. Total impedance of a vacuum chamber is a sum of impedances of all its components.

For almost all practical cases, coupling impedance of a vacuum chamber component can be approximated by a resonant circuit for each oscillation mode:

$$Z_\parallel(\omega) = \frac{R_s}{1+iQ\left(\dfrac{\omega}{\omega_r}-\dfrac{\omega_r}{\omega}\right)} \ , \qquad Z_\perp(\omega) = \frac{\omega_r}{\omega}\frac{R_s}{1+iQ\left(\dfrac{\omega}{\omega_r}-\dfrac{\omega_r}{\omega}\right)} \ , \qquad (1)$$

where R_s is the shunt resistance of the longitudinal (Ω) or dipole transverse (Ω/m) mode, ω_r is the resonance frequency, and Q is the quality factor.

Because a damping (rising) time of an oscillation mode is $\tau = 2Q/\omega_r$, a high-Q (narrow-band) mode is more long-living than a low-Q (broad-band) one. Thus, for a whole vacuum chamber or any its component, the narrow-band impedance and the broad-band one can be separated (see Figure 1). However, this separation is not rigorous because we should take into account the beam oscillation bandwidth. It is more

realistic to consider the narrow-band or the broad-band impedance as a contribution to the beam-environment interaction within the impedance bandwidth rather than as the pure electromagnetic characteristics of the vacuum chamber component itself. Anyway we can assert that the narrow-band impedance leads to the bunch-by-bunch interaction and can result in multi-bunch instabilities, whereas the broad-band impedance leads to the intra-bunch particle interaction and can cause single-bunch instabilities.
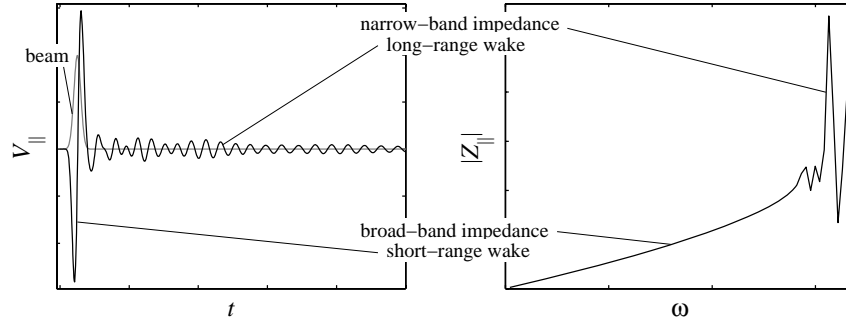
Figure 1: Broad-band and narrow-band impedance.

Broad-band impedance of the vacuum chamber as a whole is a sum of broad-band impedances of all its components. This impedance is generally used as a global criterion of single-bunch beam stability. Since for almost all components of a vacuum chamber, the longitudinal broad-band impedance $Z_\parallel$ is inductive at low frequencies (see Figure 1), it is useful to characterize it in terms of $Z_\parallel$ normalized by the revolution frequency harmonic number $n = \omega/\omega_0$. For a fixed-diameter vacuum chamber with uniformly distributed impedance, there is a relationship between the normalized longitudinal $Z_\parallel/n$ and the transverse dipole $Z_\perp$ impedance:

$$\left| Z_\perp \right| = \frac{2\,c}{\omega_0 b^2} \left| \frac{Z_\parallel}{n} \right| \ , \tag{2}$$

where b is the vacuum chamber radius, c is the light speed. If space charge effects are negligible, this formula can be also used as a reference for a non-round vacuum chamber cross-section, in this case b is the average half-size of the chamber.

Impedance of a perfectly conducting chamber results from its cross-section irregularity. For a cylindrical vacuum chamber, there are formulae to estimate low-frequency impedance of an untapered cross-section step from the radius b up to d [4]:

$$\frac{Z_\parallel}{n} = i\frac{\omega_0 Z_0}{2\pi c}(d-b)\ln\frac{d}{b} \ , \qquad Z_\perp = i\frac{Z_0}{\pi b^2}(d-b)\frac{d^2-b^2}{d^2+b^2} \ , \tag{3}$$

where $Z_0 \approx 377\ \Omega$ is the free space impedance. These formulae multiplied by factor of 2 can be used for a pill-box cavity with $2(d-b)$ replaced by the cavity length. Tapering with a slope of $\tan\theta$ reduces the impedance roughly by factor of $\sin\theta$.

For a small-angle circular tapered transition of the length l, with the longitudinal shape $r(z)$, there are formulae [5,6] valid at frequencies much less than $\dfrac{c\,l}{2\pi\,b^2}$:

$$\frac{Z_\parallel}{n} = i\frac{Z_0\omega_0}{4\pi\,c}\int\left(\frac{dr}{dz}\right)^2 dz \ , \qquad Z_\perp = -i\frac{Z_0}{2\pi}\int\left(\frac{1}{r}\frac{dr}{dz}\right)^2 dz \ . \tag{4}$$

If the taper is linear, $dr/dz = \tan\theta$, the integrals (4) are standard and the impedance is

$$\frac{Z_\parallel}{n} = i\frac{Z_0\omega_0\tan\theta}{4\pi\,c}(d-b) \ , \qquad Z_\perp = i\frac{Z_0\tan\theta}{2\pi}\left(\frac{1}{b}-\frac{1}{d}\right) . \tag{5}$$

The impedance of a rectangular taper with the horizontal half-size h and the vertical half-size b ($h \gg b$) is one half of the impedance of a flat tapered collimator [7]:

$$\left(\frac{Z_\parallel}{n}\right)_{\mathrm{rect}} \sim \frac{h}{b}\left(\frac{Z_\parallel}{n}\right)_{\mathrm{circ}} \ , \qquad Z_\perp = -i\frac{Z_0 h}{4}\int\frac{1}{r^3}\left(\frac{dr}{dz}\right)^2 dz \ . \tag{6}$$

For the linear taper, the impedance is:

$$Z_\perp = i\frac{Z_0 h\tan\theta}{8}\left(\frac{1}{b^2}-\frac{1}{d^2}\right) . \tag{7}$$

For a beam stability analysis, there are useful integral factors: the energy loss factor $k_\parallel(0)$, the longitudinal wake gradient $k_\parallel(1)$, and the transverse kick factor $k_\perp$. These factors are defined as:

$$k_\parallel(0) = \int_{-\infty}^{\infty} W_\parallel(s)\lambda(s)ds \qquad k_\parallel(1) = -\int_{-\infty}^{\infty}\frac{dW_\parallel(s)}{ds}\lambda(s)ds \qquad k_\perp = \int_{-\infty}^{\infty} W_\perp(s)\lambda(s)ds \ , \tag{8}$$

where $W_\parallel(s)$ and $W_\perp(s)$ are the longitudinal and transverse dipole wake potentials correspondingly, $\lambda(s)$ is the longitudinal beam charge distribution.

4.9.3   Cross-section of the Vacuum Chamber

The vacuum chamber of the damping wiggler section is composed of regular cells with exception of two end cells without absorbers. There are 8 regular cells in one wiggler section, 4 of them have minimal vertical aperture of 9 mm (type "A") and other 4 have this size of 17 mm (type "B"). Coupling impedance of the cells is mainly formed by cross-section transitions between the vacuum chamber fragments. To decrease the impedance, all the fragments are connected by long tapered transitions. Each 6131 mm long regular cell consists of fragments having one of eight different cross-section shapes (see Figure 2). A summary of all the regular cell cross-sections is given in Table 1.
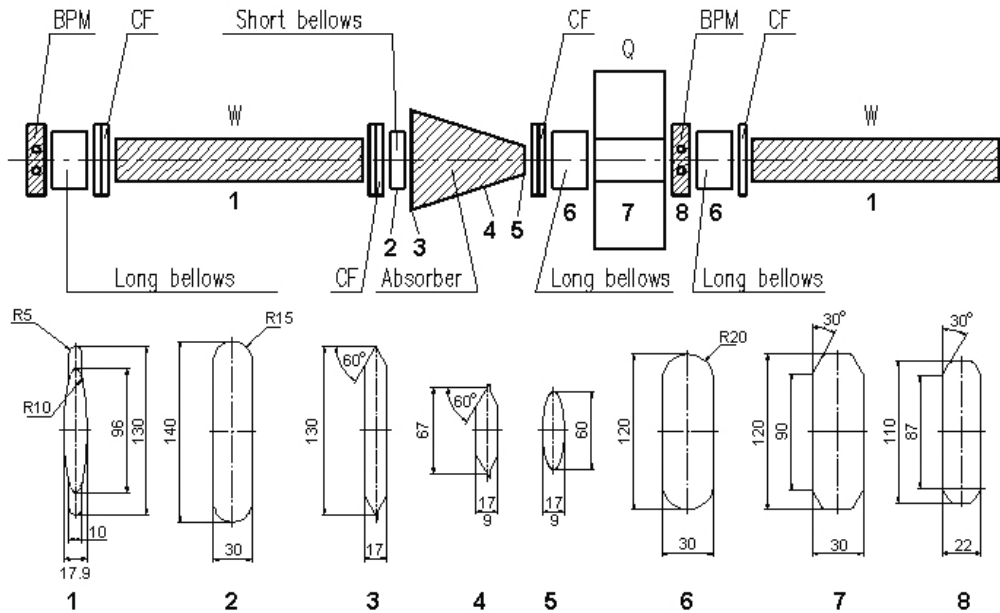
Figure 2: Regular cell of the damping wiggler section.

Table 1: Vacuum chamber cross-sections of the regular cell.

Distance, mm	Cross-section	Aperture, hor×ver, mm²	Length, mm
0	1 (wiggler chamber)	130×17.9	2082
2082	1-2 transition		19.8
2101.8	2 (short bellow)	140×30	84.2
2186	2-3 transition		19
2205	3 (beginning of the absorber)	130×17	0
2205	3-4 transition		500
2705	4 (end of the absorber)	67÷100×9 (A) or 67÷100×17 (B)	0
2705	4-5 transition		160
2865	5 (absorber mask)	60÷96×9 (A) or 60÷96×17 (B)	5
2870	5-6 transition		51.8
2921.8	6 (long bellow)	120×30	118.2
3040	6-7 transition		16
3056	7 (quadrupole)	120×30	740
3796	7-8 transition		20.75
3816.75	8 (BPM mask)	110×20	18.5
3835.25	8-6 transition		20.75
3856	6 (long bellow)	120×30	200
4056	6-1 transition		35
4091	1 (wiggler chamber)	130×17.9	2040

4.9.4   Impedance Budget

To prove reliability of the computer simulations performed using the GdfidL, a cross-check of the GdfidL and MAFIA [8] codes has been carried out. Figure 3 shows an example of the longitudinal (a) and transverse vertical (b) wake potentials calculated using both MAFIA and GdfidL codes for the same cross-section transition 5-6A (see Figure 2 and Table 1). The transition 5-6A is a 51.8 mm-long taper connecting the absorber output with the vertical size of 9 mm and the long bellow with this size of 30 mm. Maximal difference of the MAFIA and GdfidL data is about 0.03 V/pC for the longitudinal wake and 0.05 V/pC for the transverse one, whereas the root-mean-square deviation values are about 0.01 V/pC and 0.02 V/pC correspondingly. Comparative analysis of the GdfidL and MAFIA data allows us to conclude that the GdfidL simulations with the mesh size of 0.5 mm give enough reliable results.
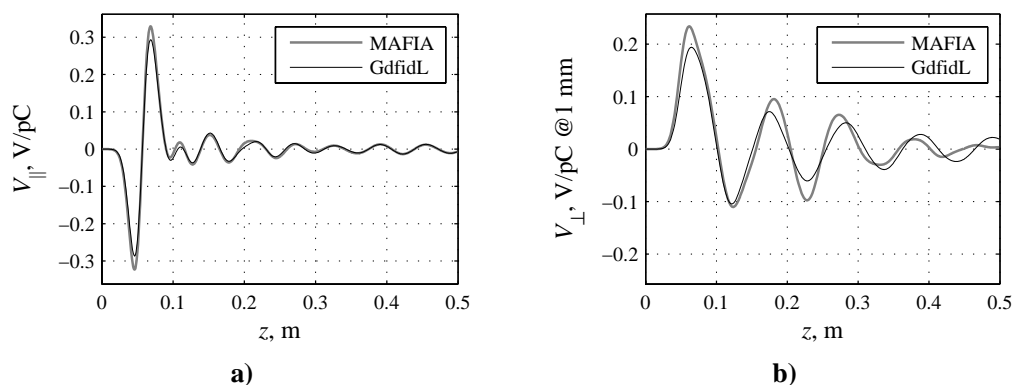
Figure 3: Cross-check of the GdfidL and MAFIA codes.

For all the cross-section transitions of the regular cells, the longitudinal normalized impedance $Z_\parallel/n$, the transverse dipole impedance $Z_\perp$ (both horizontal and vertical), and all the integral factors (8) have been calculated using the GdfidL code [2] in comparison with analytical formulae (3)-(7) as a reference.
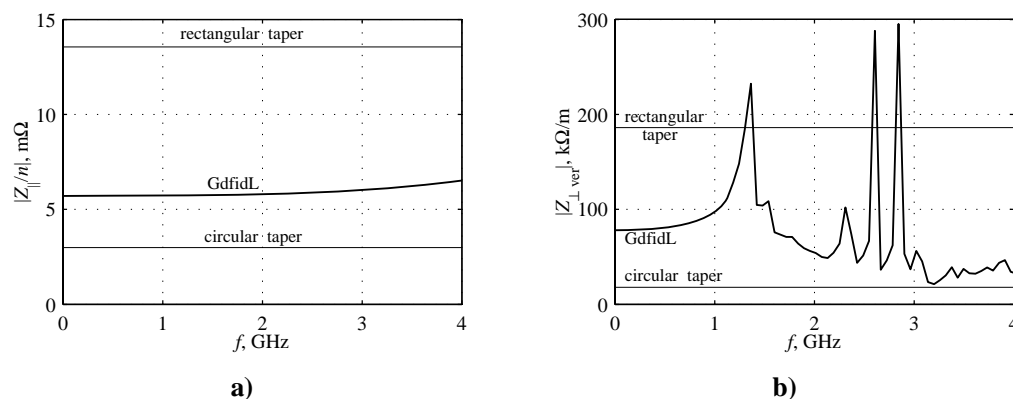
Figure 4: Longitudinal (a) and transverse vertical (b) impedances of one wiggler section.

Total longitudinal and transverse vertical impedances of one wiggler section, calculated as a sum of impedances of all the cross-section transitions, are presented in Figure 4. There are both the results of the GdfidL simulations performed with the real

geometry, and the rough estimation values calculated using the formulae (4)-(5) for a circular taper, and (6)-(7) for a rectangular one. The energy loss factor $k_\parallel(0)$ calculated using GdfidL is about 140 mV/pC, whereas the circular taper formula gives about 70 mV/pC and the rectangular taper formula gives about 330 mV/pC. For the vertical kick factor $k_{\perp\,\text{ver}}$, these values are 456 V/pC/m, 100 V/pC/m and 1000 V/pC/m correspondingly. One can see that the circular taper approximation gives an underestimate result, whereas the rectangular approximation gives an overestimated one. For short round and rectangular tapers (10 mm long), MAFIA simulations give a quite large difference with the (4)-(7) formulae. The tapers in the wiggler section are probably too short to be treated with the analytic formula. Nevertheless, in many cases the formula (4) multiplied by factor of 3 is a good approximation for the PETRA III tapers.

For all the cross-section transitions, the low-frequency broad-band impedance, loss factor and kick factors are summarized in Table 2. The GdfidL data is used, the low-frequency broad-band impedance is defined as a mean value of the impedance in the 0÷1 GHz frequency band, the kick factors are calculated by numerical integration of the expressions (8). The last three rows of the table show the values related to one cell "A", one cell "B", and one wiggler section including 4 cells "A" and 4 cells "B".

Table 2: Broad-band impedance, loss factor and kick factors summary.

| *Taper*	*Aperture* hor×ver, mm²	$\left\|Z_\parallel/n\right\|$ mΩ	$\left\|Z_{\perp\,\text{hor}}\right\|$ kΩ/m	$\left\|Z_{\perp\,\text{ver}}\right\|$ kΩ/m	$k_\parallel(0)$ mV/pC	$k_\parallel(1)$ V/pC/m	$k_{\perp\,\text{hor}}$ V/pC/m	$k_{\perp\,\text{ver}}$ V/pC/m
1-2	130×17.9→140×30	0.151	0.203	1.610	3.406	2.497	1.795	7.455
2-3	140×30→130×17	0.180	0.241	2.334	4.998	3.108	2.139	10.02
3-4A	130×17→80.6×9	0.071	0.407	1.981	0.209	1.287	3.627	17.27
4-5A	80.6×9→60×9	0.000	0.001	0.000	0.000	0.000	0.005	0.001
5-6A	60×9→120×20	0.122	0.534	5.042	0.408	2.040	4.620	31.56
3-4B	130×17→80.6×17	0.000	0.000	0.000	0.000	0.000	0.000	0.000
4-5B	80.6×17→60×17	0.001	0.008	0.001	0.002	0.009	0.071	0.010
5-6B	60×17→120×20	0.021	0.060	0.252	0.080	0.355	0.525	1.714
6-7	120×20→120×30	0.020	0.000	0.188	0.457	0.493	0.000	1.486
7-8	120×30→110×22	0.076	0.089	0.637	3.445	1.401	0.802	3.207
8-6	110×22→120×30	0.075	0.090	0.631	3.446	1.401	0.802	3.199
6-1	120×30→130×17.9	0.106	0.163	1.297	1.426	1.907	1.421	6.393
$\Sigma_{\text{1 cell A}}$		**0.80**	**1.73**	**13.7**	**17.8**	**14.1**	**15.2**	**80.6**
$\Sigma_{\text{1 cell B}}$		**0.63**	**0.85**	**6.95**	**17.3**	**11.2**	**7.56**	**33.5**
$\Sigma_{\text{1 section}}$		**5.7**	**10.3**	**82.7**	**140.2**	**101.2**	**91.1**	**456.3**

Figure 5 shows fractional contributions of the vacuum chamber fragments to the total low-frequency broad-band impedance of one wiggler section. As it was concluded from the simulations, two wiggler sections make a quite big contribution to the total PETRA III vertical kick factor. Main contribution of the wiggler section kick factor comes from the absorber mask taper situated before the quadrupole section. Reducing of the quadrupole vacuum chamber height decreases contribution of the 5-6 taper

(absorber mask), but, unfortunately, contributions of the 7-8 and 8-6 tapers (BPM mask) increase considerably, so a trade-off solution should be found. Last modification of the vacuum chamber geometry allows us to decrease the vertical kick factor of one wiggler section down to 456 V/pC/m. Thus the kick factor of two wiggler sections is 912 V/pC/m, which is about 20% of the total PETRA III design value.
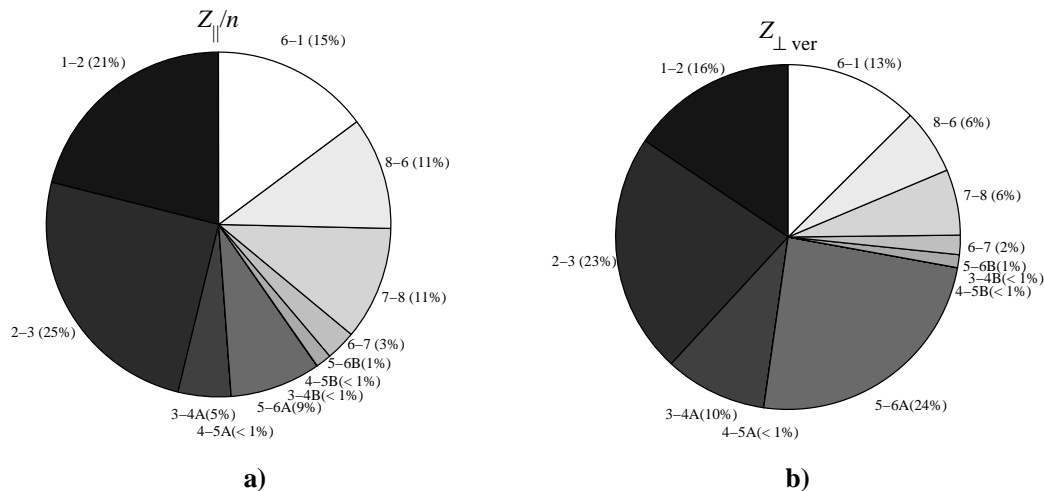
Figure 5: Impedance contributions: longitudinal (a) and transverse vertical (b).

To protect the PETRA III dipole magnets from synchrotron radiation coming out of the damping wiggler section, an additional mask has been designed to place at the end of the section, between the last quadrupole and the dipole magnet. Coupling impedance of this mask has been estimated using the GdfidL code, to optimize the vertical aperture. A rectangular taper has been taken as the model geometry. The horizontal size of the model is constant of 120 mm, the vertical one decreases from 58 mm (quadrupole) down to the minimum, then it increases up to 38 mm (dipole). The calculations have been done for a set of the minimal aperture values in the 9-22 mm range, the low-frequency broad-band impedance, loss factor and kick factors are presented in Table 3.

Table 3: Broad-band impedance, loss factor and kick factors of the dipole magnet mask.

$2b$ mm	$\left\vert Z_\parallel/n \right\vert$ mΩ	$\left\vert Z_{\perp\,\mathrm{hor}} \right\vert$ kΩ/m	$\left\vert Z_{\perp\,\mathrm{ver}} \right\vert$ kΩ/m	$k_\parallel(0)$ mV/pC	$k_\parallel(1)$ V/pC/m	$k_{\perp\,\mathrm{hor}}$ V/pC/m	$k_{\perp\,\mathrm{ver}}$ V/pC/m
9	1.45	1.49	30.0	47.1	19.3	12.4	127.3
10	1.41	1.23	25.3	46.2	18.6	11.1	108.9
12	1.09	0.85	15.0	40.9	16.4	7.13	63.0
14	0.95	0.68	11.7	37.2	15.1	5.85	49.2
17	0.71	0.46	7.41	32.5	13.1	4.10	31.7
20	0.70	0.30	4.47	29.5	10.8	2.73	19.5
22	0.54	0.24	3.26	27.0	9.41	2.10	14.3

Figure 6 shows the broad-band longitudinal normalized impedance $\left\vert Z_\parallel/n \right\vert$ (a) and the transverse vertical impedance $\left\vert Z_{\perp\,\mathrm{ver}} \right\vert$ (b) in dependence of the mask vertical

aperture $2b$. The low-frequency broad-band impedance is the impedance calculated by the GdfidL code averaged over the 0÷1 GHz frequency band. The simulation results are presented by the dots, the dashed curves are fits, the solid curves result from analytical impedance estimation using the formulae (6)-(7).
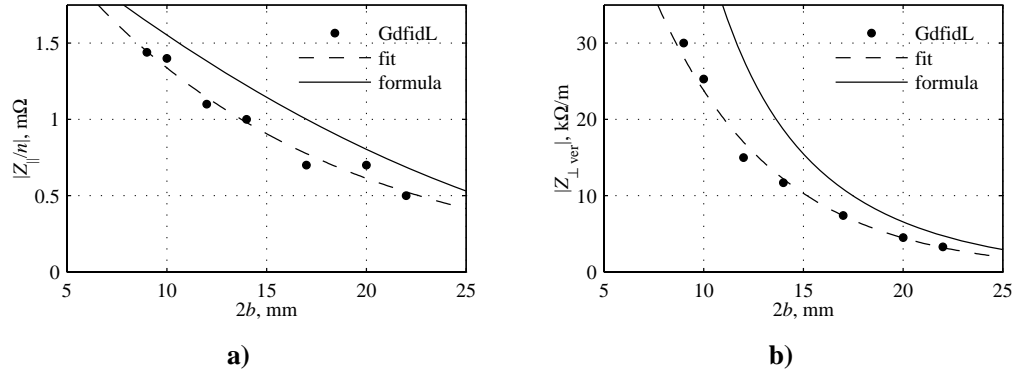
Figure 6: Longitudinal (a) and transverse vertical (b) impedance vs. vertical aperture.

These simulations show that the mask with 9 mm vertical aperture adds about 33% to the energy loss factor and about 27% to the vertical kick factor of the wiggler section, the 22-mm mask adds about 19% and 3% correspondingly. The mask with a vertical aperture of 17 mm has been chosen to be built.

4.9.5   References

1. K.Balewski, W.Brefeld, W.Decking, H.Franz, R.Rohlsberger, E.Weckert, "PETRA III: A Low Emittance Synchrotron Radiation Source", Technical Design Report, DESY, Hamburg (2004).
2. W.Bruns, The GdfidL Electromagnetic Field Simulator, http://www.gdfidl.de/
3. A.Chao, Physics of Collective Beam Instabilities, Wiley, New York, 1993.
4. A.W.Chao, M.Tigner, Handbook of Accelerator Physics and Engineering, World Scientific, 1998.
5. K.Yokoya, Impedance of Slowly Tapered Structures, CERN SL/90-88 (AP), Geneva, Switzerland, 1990.
6. F.Zimmermann, Collection of Wake-Field Formulae, CERN, Geneva, Switzerland, 2000.
7. G.V.Stupakov, Geometrical Wake of a Smooth Flat Collimator, SLAC-PUB-7167, SLAC, Stanford, USA, 1996.
8. http://www.cst.com/Content/Products/MAFIA/Overview.aspx

4.10 Wake Computations for Selected Components of PETRA III

A.K. Bandyopadhyay, A. Joestingmeier and A.S. Omar
Microwave and Communication Engineering, FEIT IESK
Otto-von-Guericke University, Magdeburg, Germany
R. Wanzenberg , DESY, Notkestr. 85, Hamburg, Germany
Mail to: ayan.bandyopadhyay@gmail.com

4.10.1 Introduction

At DESY construction is underway to convert the existing PETRA II storage ring into the 3rd generation synchrotron radiation source PETRA III. The design goal for the maximum beam current is 100 mA. To meet this goal it is essential to estimate the overall machine impedance, hence that of the individual machine components. In this contribution, we summarize the wake and impedance computation results for selected components of PETRA III. The analysed components are the button type Beam Position Monitors (BPM) (in the normal arc and in the narrow beam pipe near the insertion devices) and the longitudinal feedback cavity. The wake and impedance computations are supplemented by modal analysis and shunt impedance computations (for the feedback cavity) which are briefly presented here.

4.10.2 PETRA III

The main design parameters for PETRA III are shown in Table 1. The facility aims at a high brilliance of about 10^{21} photons /sec /0.1%BW /mm^2 /mrad^2 using a low emittance (1 nm rad) beam. More than 100 BPMs are needed to measure the beam orbit around the ring with high precision (10 μm in the arcs and about 0.5 μm in front of the insertion devices). Hence it is important to estimate the contribution of the BPMs to the overall machine impedance and to check if undesired modes can be excited in the vicinity of the BPM which can distort the beam operation.

Table 1: The main design parameters of PETRA III.

Parameter	Unit	Value	
energy	GeV	6	
circumference	m	2304	
RF frequency	MHz	500	
total current	mA	100	
number of bunches	-	960	40
bunch population	10^{10}	0.5	12
bunch seperation	ns	8	192

To ensure the multibunch mode functionality of PETRA III, it has been planned to use powerful feedback systems. The feedback systems should prevent various multibunch instabilities, which are otherwise inevitable in multibunch operations. Eight single cell cavities (adopted from the SLS and DAFNE overdamped feedback cavity design [2,3]) have been foreseen to provide the required damping of $1/\tau = 800$ Hz.

Although these cavities are needed to prevent coupled bunch instabilities, they also contribute to the overall machine impedance. Hence it is important to calculate the wakes and impedances due to these cavities. Another very important parameter is the shunt impedance of these cavities, which basically shows the efficiency of the cavity to transmit the correction signal to the beam.

In this contribution, we report the wake computation results and related analysis for the beam position monitors of PETRA III, mounted at two different positions of the beam pipe. The wakes and impedance computation results due to the longitudinal feedback cavity adopted for PETRA III are also presented. The forward and backward wave shunt impedances of the feedback cavity is also presented. For the computations, the well-known software packages for three-dimensional electromagnetic simulations, namely MAFIA and Microwave Studio [4,5], has been used.

4.10.3 Wakes and Impedances

In a particle accelerator, charged particle beams travel inside a conducting pipe (beam pipe) maintained at high vacuum. The beam encounters different cross sections of the beam pipe and interacts with these discontinuities many times while circulating along the beam pipe. The interactions of the beam with its surroundings are described in the time domain by the wakefields (or wakes) and they are described in the frequency domain by the impedances [6, 7]. From the wakes several quantities, including the loss and kick parameters, can be calculated [1,6]. These loss and kick parameters represent integral measures of the interaction of the beam with the considered part of the accelerator.

4.10.4 Computation Results

4.10.4.1 Computations for the BPMs

The considered geometries of the BPMs at two different positions are shown in Figs. 1 and 2. Fig. 1 shows the modeled BPM at the normal beam pipe, whereas Fig. 2 shows the same at the narrow beam pipe near the insertion devices.
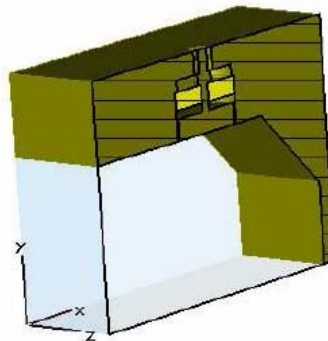

Figure 1: Cross-section of the BPM at the normal beam pipe.

The semi major and semi minor axes of the normal arc beam pipe are 40 mm and 20 mm and those for the narrow beam pipe near an undulator chamber are 45 mm and 3.5

mm respectively. The gap between the BPM button and the beam pipe is considered to be 0.4 mm.
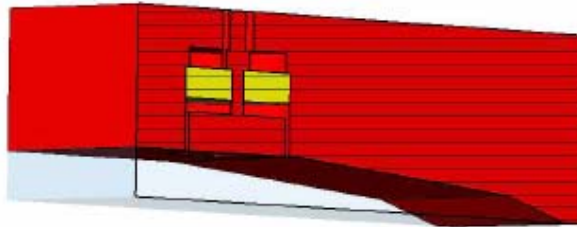

Figure 2: Cross-section of the BPM at the narrow beam pipe near the insertion devices.

4.10.4.1.1 Modal Analysis

The eigenmode solvers have been used to find trapped modes in the vicinity of the BPM buttons. All the eigenmodes up to 10 GHz have been computed and it turns out that three among these are concentrated near the BPM buttons. The resonant frequencies of these three modes computed with Microwave Studio are 1.927 GHz, 9.035 GHz and 9.038 GHz. The field distribution of these modes does not change significantly with different boundary conditions at the boundaries. The field distributions of the modes near 9 GHz indicate that these two modes are almost degenerate dipole modes trapped in the vicinity of the BPM button. The same modes have been found to be concentrated near the BPM button in the narrow beam pipe. To check if these modes can be excited by a particle beam, a time domain computation with a particle beam excitation has been performed. The electric field has been recorded at the gap between the BPM button and the beam pipe (for both the geometries at normal arc and at narrow beam pipe). From the recorded fields, the frequency comes out to be very near to the dipole mode. But as the computed modal loss parameters and quality factors due to these modes are small, it can be concluded that existence of these modes will not noticeably affect the functioning of the BPMs.

4.10.4.1.2 Time Domain Analysis

For the wake computations in the time domain, the three-dimensional simulation tool MAFIA has been used. A beam with Gaussian charge distribution (rms bunch length 10 mm, total charge 1 C) has been used as the excitation source. The uniform mesh step along the longitudinal direction has been taken as 0.12 mm. In order to compute the loss and kick parameters, both cases with on- and off-axis excitations have been considered.

The longitudinal wakes normalized to the bunch charge for the BPMs mounted at the normal beam pipe and at the narrow beam pipe are shown in Figs. 3 and 4 respectively. For the wake computations, the coaxial output ports from the BPMs have been terminated with the corresponding matched terminations. From the wakes, the loss parameter, the k(1) parameter and the kick parameters can be computed [1,6]. The loss and kick parameters computed for the BPMs are tabulated in Table 2. From Table 2 it can be seen that the transverse kick parameters computed for the BPMs at the narrow beam pipe are two orders of magnitude higher than those computed for the BPMs at the

normal beam pipe. It may be noted that the estimated impedance and the loss and kick parameters due to the BPMs are well inside the impedance budget.
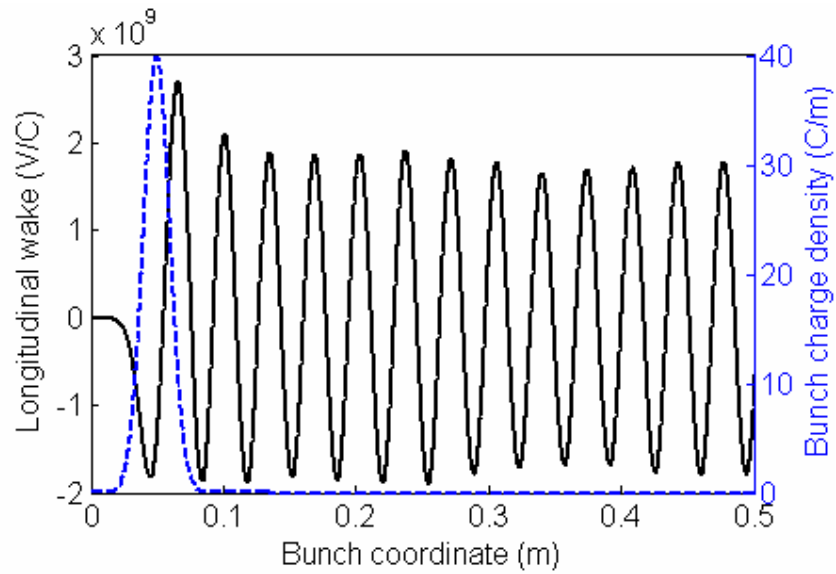

Figure 3: The longitudinal wake and bunch charge density (dashed line) vs the bunch coordinate for the BPMs in the normal beam pipe.
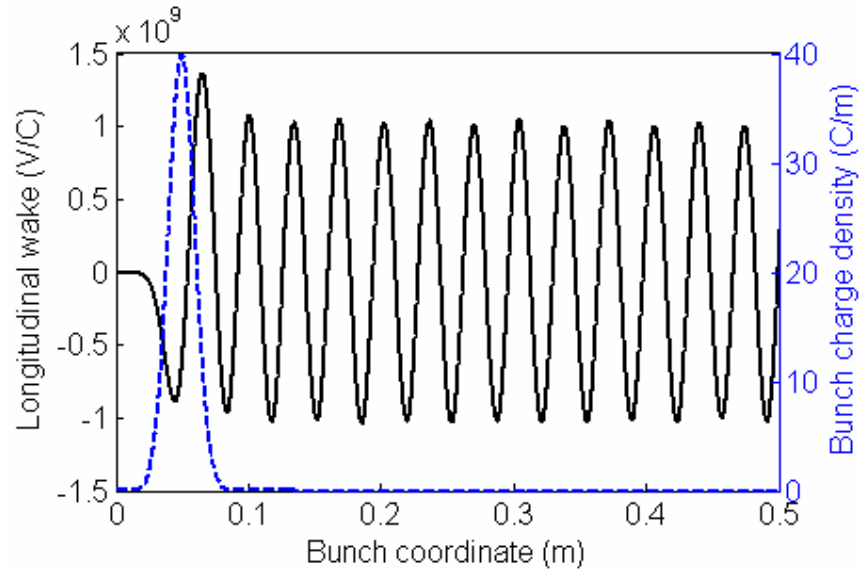

Figure 4: The longitudinal wake and bunch charge density (dashed line) vs the bunch coordinates for the BPMs in the narrow beam pipe.

Table 2: The loss and kick parameters for the button type BPMs of PETRA III in the normal and narrow beam pipes.

BPM mounted at	Longitudinal loss parameter (V/C)	k(1) parameter [V/(C m)]	Transverse kick parameter [V/(C m)]
Normal beam pipe	-3.5276×10^8	-9.0985×10^{10}	n.a.
	-3.3527×10^8 (Offset 5.0 mm)	-8.6656×10^{10}	-2.5256×10^{10}
Narrow beam pipe	-1.6211×10^8	-5.2732×10^{10}	n.a.
	-7.0962×10^7 (Offset 2.0 mm)	-2.3176×10^{10}	-3.8739×10^{12}

4.10.4.2   Computations for Longitudinal Feedback Cavity
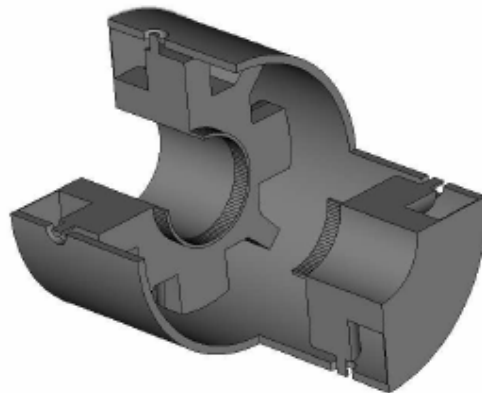
Figure 5: Cut view of the PETRA III longitudinal feedback cavity (adopted from SLS/ DAFNE design).

The longitudinal feedback cavity of PETRA III is basically a heavily loaded pillbox cavity. It has eight coaxial ports to connect the driving amplifiers (input ports) and the dummy loads (output ports). A cut view of the longitudinal feedback cavity is shown in Fig. 5. In order to damp all coupled bunch instabilities, the required maximum bandwidth is (f_{RF} /2), if all rf-buckets are filled. For PETRA III, the maximum required bandwidth is 62.5 MHz, corresponding to a bunch spacing of 8 ns [1]. The high bandwidth is achieved by strongly loading the cavity with specially ridged waveguides, which can be connected to the external loads.

4.10.4.2.1 Modal Analysis

The resonant frequency of the TM_{010} like mode, which is to be used for the beam correction, is 1.3020 GHz with a quality factor of 10579. The resonant frequency of the operating mode without the nose cones is 1.392 GHz. It may be noted that Microwave Studio has been used for the eigenmode computations. The resonant frequencies of the operating modes with and without the nose cones computed with MAFIA are found to be 1.3079 GHz and 1.398 GHz respectively. The slight difference in the resonant frequencies computed with the two software packages is due to the difference in

meshing schemes between Microwave Studio and MAFIA. Fig. 6 shows the electric field distribution of the operating mode for the PETRA III longitudinal feedback cavity with nose cones. From the field distributions this mode can clearly be identified as the TM_{010} mode, which is the operating mode.
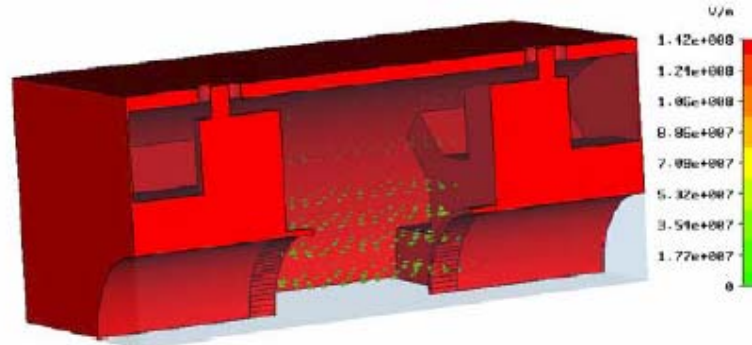
Figure 6: Electric field distribution of the operating TM_{010} like mode at 1.3079 GHz

4.10.4.2.2 Wake Computations

For the wake computations, a uniform mesh step size of 0.77 mm in the longitudinal direction has been used. This is a compromise between the available computer memory and the necessity to model the small details of the cavity geometry. The properties of the exciting beam are the same as those used for the wake computation of the BPMs.
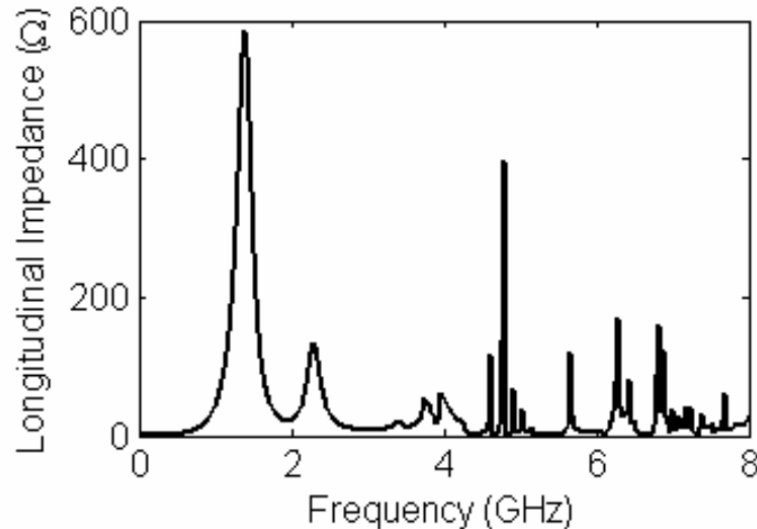
Figure 7: Longitudinal impedance of the feedback cavity

Fig. 7 shows the impedance spectra of the PETRA III longitudinal feedback cavity, normalized to the bunch spectrum. Under the cutoff frequency of the beam pipe (3.829 GHz, for TM mode) some impedance peaks are visible due to the resonant modes of the cavity. From the plot, it can be seen that the frequency of the first peak (corresponding to the operating mode of the cavity) is 1.379 GHz. This is a bit higher than the computed resonant frequency (1.3079 GHz) of the cavity fundamental mode. The reason for the difference is that for the eigenmode computations the coaxial ports of the cavity have been treated as short-circuited. On the other hand, for the time domain

wake computations the ports have been terminated with corresponding matched termination. In addition to the peak due to the fundamental cavity mode, the presence of another impedance peak at 2.278 GHz can be noticed. A similar computation with short-circuited coaxial ports shows the impedance peak corresponding to the fundamental mode at 1.39 GHz. In this case additional impedance peaks appears with much larger values.

For the transverse impedance computations one quarter of the cavity have been considered, with different boundary conditions at the horizontal plane. Combining the wake computation results with different boundary conditions, the wakes due to an offset beam can be obtained [8]. It may be noted here that for the wake computations, the coaxial ports of the cavity have all been terminated with matched loads. Table 3 summarizes the different loss and kick parameters due to the feedback cavity.

Table 3: The loss and kick parameters for the PETRA III longitudinal feedback cavity.

Longitudinal loss parameter (V/C)	$k(1)$ parameter [V/(C m)]	Transverse kick parameter [V/(C m)]
-4.6997×10^{11}	1.7489×10^{13}	n.a.
-4.7400×10^{11} (Offset 2.0 mm)	1.7195×10^{13}	1.3150×10^{13}

4.10.4.2.3 Shunt Impedance Computations

For the shunt impedance computations, the MAFIA T3 module has been used. The excitation signal to the cavity has been provided through one of the coaxial ports. A wakefield monitor along the path of the beam has been used to compute the accelerating voltage due to the excitation through the coaxial port [8]. Two sets of computation runs have been done - one for the forward wave case and the other for the backward wave case. For the forward wave case, the excitation signal is fed through one of the upstream coaxial ports, while keeping all the other ports matched. As the beam pipe is circular, it is sufficient to use one coaxial port for the excitation. Fig. 8 shows the variation of the forward and backward wave shunt impedances with frequency. From the plot, it can be noticed that the peaks of the shunt impedances occur around 1.38 GHz with the maximum values 1282 Ω (forward wave) and 1058 Ω (backward wave). The shunt impedances have also been computed for the feedback cavity without the nose cones. The computed shunt impedances without the nose cones are 13 % lower than those with the nose cones.
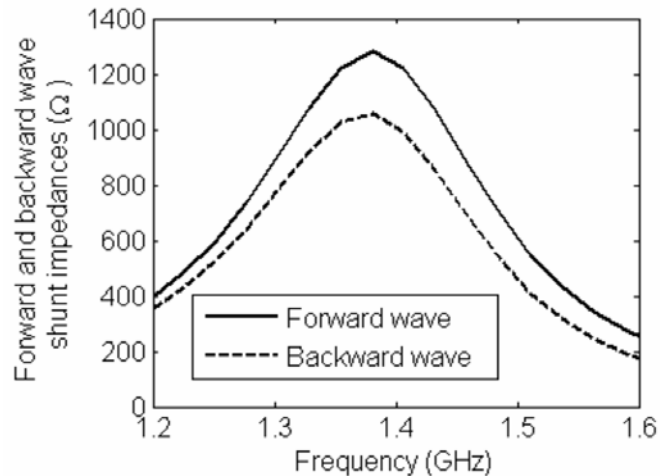
Figure 8: Forward and backward wave shunt impedances for the feedback cavity (with nose cones)

4.10.5 Summary

Wake computation results for the button type BPMs mounted at the normal and the narrow beam pipe have been presented. The loss and kick parameters for both cases have also been calculated. Modal analysis has been done to investigate the trapped modes in the vicinity of the BPM. The wakes and impedances computation results for the PETRA III longitudinal feedback cavity have been presented. The corresponding loss and kick parameters have been calculated. The forward and backward wave shunt impedances have also been presented.

4.10.6 Acknowledgment

We would like to thank Mark Lomperski for carefully reading the manuscript.

4.10.7 References

1. K. Balewski et. al. (ed.), "PETRA III Technical Design Report", DESY 2004-035, Hamburg, 2004.
2. M. Dehler, "Kicker Design for the ELETTRA/SLS Longitudianl Multibunch Feedback", proceedings of the 8th European Particle Accelerator Conference (EPAC), Paris, France, 2002.
3. R. Boni, A. Gallo, A. Ghigo, F. Marcellini, M. Serio, and M. Zobov, "A Waveguide Overloaded Cavity as Longitudinal Kicker for the DAFNE Bunch-by-bunch Feedback System," Particle Accelerators, vol. 52, pp. 95–113, 1996.
4. "MAFIA." Release 4, Nov 2004, CST GmbH.
5. "CST Microwave Studio." Version 5, March 2005, CST GmbH.
6. T. Weiland and R. Wanzenberg, "Wakefields and impedances." Joint US-CERN particle accelerator school, Hilton Head Island, SC, USA, November 1990.
7. A. Chao, "Physics of Collective Beam Instabilities in High Energy Accelerators," John Wiley and Sons, New York, 1993.
8. A.K. Bandyopadhyay, A. Jöstingmeier, A.S. Omar, and R. Wanzenberg, "Wakes and Impedance Computations for The PETRA III Longitudinal Feedback Cavity", Internal Report, DESY M 07-02, November 2007.

5 Workshop and Conference Reports

5.1 Summary of Wake Fest 07

Karl Bane, SLAC, 2575 Sand Hill Rd., Menlo Park, CA 94025
Mail to: kbane@slac.stanford.edu

5.1.1 Introduction

The ILC mini-workshop, Wake Fest 07, was held at SLAC on 11-13 December 2007, simultaneously with the LET Beam Dynamics Workshop; on the last day the two workshops were held as a joint meeting. Participants at Wake Fest came from Fermilab, U. of Manchester, TU Darmstadt, as well as from SLAC. There were a total of 22 talks in Wake Fest 07 itself. Talks for the two workshops can be found at [1], [2].

Two of the main goals of Wake Fest 07 were to answer questions pertaining to the ILC main linac RF cavities: (1) What is the wakefield effect of the RF and HOM couplers? (2) What is the RF kick due to the couplers?

5.1.2 Coupler Wakes

Each RF cavity comprises nine cells and contains one higher mode (HM) coupler in the upstream end and one HM coupler plus one fundamental mode coupler (FM) in the downstream end (see Fig. 1). The couplers intrude within the 35 mm iris radii and break the cylindrical-symmetry of the cavities, resulting in non-zero transverse wakefields and RF kicks experienced by a beam even on the cavity axis. At an ILC workshop at DESY in May 2007, I. Zagorodnov and M. Dohlus presented initial calculations that found the on-axis transverse wake due to the couplers to be similar in size to that induced by a beam offset by 3 mm in a cavity without couplers—i.e. the effect appeared to be large and warranted further investigation [3].

At Wake Fest, talks on the coupler wake kicks were given by me, V. Yakovlev of Fermilab, and S. Schnepp of TU Darmstadt. I presented results of I. Zagorodnov, obtained by his program ECHO3D, that gave the on-axis wakes of the couplers in their beam pipes (same result as in May 2007), of a 9-cell cavity with its couplers, and of 2 and 3 cavities with their couplers. The on-axis transverse wake, averaged over a 1 mm rms bunch, were $<W>$= 20 V/nC/m (one set of couplers in beam pipe), 10.5 V/nC/m (one cavity with couplers), and 7 V/nC/m (steady-state, per cavity result). (The kick in x was about the same as the kick in y.) V. Yakovlev, presenting work performed together with I. Gonin, A. Lunin, and N. Solyak, and using the program GdfidL, obtained similar results. S. Schnepp of TU Darmstadt, using the MAFIA/Microwave Studio programs, presented only very preliminary results at the meeting.

I showed that the first results (couplers in beam pipe) could be reproduced fairly accurately using the analytical Optical Model of Impedance [4], both in the form of the wake and in amplitude. The reduction in effect that occurs in the case of one cavity with couplers can be understood as due to shadowing of the cavity irises (the radius of the coupler beam pipe is 39 mm, that of the irises is 35 mm, and the couplers themselves extend down to 30 mm from the axis). The further reduction that occurs for the

periodic solution seems to be the same kind that occurs for the transverse wake of short bunches in cylindrically-symmetric periodic structures. Because of computer resource limitations (even though the GdfidL and MAFIA runs were performed in parallel on computer farms) all results were limited to an rms bunch length of 1 mm (instead of the 0.3 mm bunch length in the ILC). V. Yakovlev showed that, as function of bunch length, his periodic solution was decreasing approximately linearly, and the extrapolation to 0.3 mm gives $<W> \sim 2$ V/nC/m. Note that the transverse wake kick going to zero as bunch length approaches zero is in accord with what one would expect from physical principles alone. The Fermilab and Darmstadt groups will continue to pursue the numerical calculation of the steady-state kick for a 0.3 mm bunch, to try to verify V. Yakovlev's extrapolation.
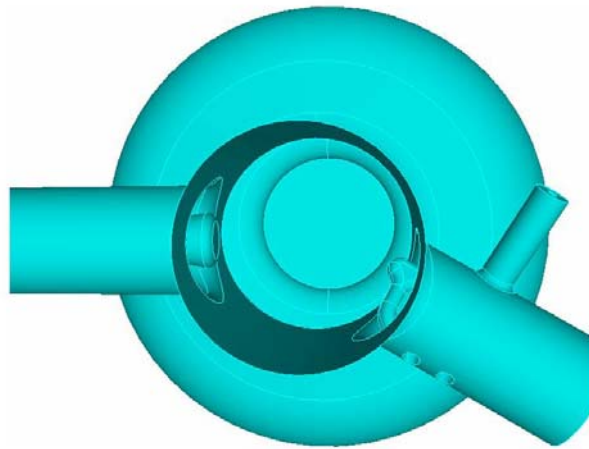
Figure 1: Detailed view of the downstream end of an ILC cavity, showing the fundamental mode (FM; the one on the negative x axis) and one higher mode (HM) coupler.

A next order term in transverse wake of the couplers depends linearly on offset from the structure axis, like the normal wake—due to the irises—of the accelerating cavity (without couplers). I. Zagorodnov's calculations show that this component of coupler wake is an order of magnitude weaker than the wake due to the irises, and can thus be ignored.

What is the effect of the on-axis coupler wake on beam emittance? I showed that a wake kick that is independent of transverse offset has a very different effect than the normal transverse wake in a cylindrically-symmetric structure. The former type of wake generates a kind of dispersion that depends on longitudinal position within the bunch. Bunch particles will perform free betatron oscillation about different centers, depending on their longitudinal position. The projected emittance will oscillate and somewhat damp (due to adiabatic damping). At the same time the average emittance will grow gradually due to energy spread (filamentation), and because the oscillations drive the normal cavity wake. An analytical estimate yields an emittance growth maximum of 200% (occuring near the beginning of the linac) when the average wake kick $<W>= 20$ V/nC/m, which reduces to 4% when $<W>= 2$ V/nC/m. (Note that D. Krueker—at the LET meeting—presented Merlin numerical simulations applied to the former case; his

results were in reasonable agreement with this estimate [2].) We see that if the latter wake is correct—$<W>$= 2 V/nC/m—then the wake effect of the coupler asymmetry is small and can be ignored.

To ameliorate the wake kicks, in their May 2007 talk M. Dohlus and I. Zagorodnov suggested rotating each HM coupler by 90°; according to their calculation (for one set of couplers in a beam pipe) the wake kick becomes more than an order of magnitude smaller in both directions. Recently Z. Li proposed rotating only the HM coupler on the non-FM coupler cavity end by 180°; the Optical Model approximation finds a similar-sized reduction in wake with this modification. For the case of many cavities with their couplers, both modified configurations are expected to give steady-state wakes that are significantly smaller than in the original (unmodified) case, though no numerical calculations have yet been performed to confirm this.

5.1.3   Coupler RF Kicks

Due to the coupler asymmetry, in addition to the transverse wake kicks, on-axis RF kicks in the fundamental mode will also be generated. V. Yakovlev and Z. Li presented independent calculations of these kicks for the ILC structure, which agree reasonably well. In Table 1, Z. Li's per cavity results, assuming an accelerating gradient V_{acc}= 31.5 MeV/m and a Gaussian bunch with rms bunch length of 0.3 mm, are shown. Listed are the average kick $<k>$ and rms kick k_{rms}, in x and y, for both the original and Z. Li's modified configurations. For emittance growth in the ILC linac, k_{rms} in y is most important and we see that the result for both configurations is ~2 V/cavity, which is small (for ILC parameters). V. Yakovlev also showed that the RF kicks of the linac cavities were acceptable; the RF kicks in the compressor cavities, however, resulted in large emittance growth. In his talk he further considered completely different coupler designs that significantly reduce the RF kicks.

Table 1: Coupler RF kicks per cavity assuming V_{acc}= 31.5 MeV/m and an rms bunch length of 0.3 mm, as obtained by Z. Li. Given are the average and the rms of the kick in x and y, in the cavity as-is and after following Z. Li's rotation of the upstream HM coupler by 180°.

Case	$<k>$ [V]	k_{rms} [V]
x	-2100	18.
y	-780	1.9
ZLi_x	760	13.
ZLi_y	2620	2.2

5.1.4   Other Talks

There were talks on calculating the dipole wakefields in the ILC structure by L. Xiao, P. Stolz, I. Shinton, C. Ng, and R.M. Jones. A. Kabel talked on the effect of x-y coupling in wakefields on beam dynamics. O. Nezhevenko and L. Xiao presented simulations of ILC cavities with higher order mode (HOM) absorbers, and the effectiveness of mode absorption. S. Molloy reviewed HOM measurements and SVD analysis at FLASH, and S. Pei presented a new analysis of such data. Multipacting simulations were presented in talks by I. Gonin and N. Solyak, L. Ge, and F. Wang. Finally, S. Molloy described collimator wake experiments and their results at SLAC.

5.1.5 References

1. Wake Fest 07 at:
   http://ilcagenda.linearcollider.org/conferenceDisplay.py? confId=2378.
2. LET Beam Dynamics Workshop:
   http://ilcagenda.linearcollider.org/conference Display.py?confId=2364.
3. I. Zagorodnov and M. Dohlus, "Coupler Kick" at http://ilcagenda.linearcollider.org/getFile.py/access?contribId=89&sessionId=56&resId=0&materialId=slides&confId=1296.
4. G. Stupakov, K. Bane, I. Zagorodnov, "Optical Approximation in the Theory of Geometric Impendance," PRST-AB **10**:054401, 2007.

6   Recent Doctorial Theses

6.1   Quantum Aspects of the Free Electron Laser

Roberto Gaiba
University of Hamburg, Hamburg, Germany

Abstract:

We study the role of Quantum Mechanics in the physics of Free Electron Lasers. While the Free Electron Laser (FEL) is usually treated as a classical device; we review the advantages of a quantum formulation of the FEL. We then show the existence of a regime of operation of the FEL that can only be described using Quantum Mechanics: if the dimensionless quantum parameter $\bar{\rho}$ is smaller than 1, then in the 1-dimensional approximation the Hamiltonian that describes the FEL becomes equivalent to the Hamiltonian of a two-level system coupled to a radiation field. We give analytical and numerical solutions for the photon statistics of a Free Electron Laser operating in the quantum regime under various approximations. Since in the quantum regime the momentum of the electrons is discrete, we give a description of the electrons in phase space by introducing the Discrete Wigner Function.

We then drop the assumption of a mono-energetic electron beam and describe the general case of a initial electron energy spread $G(\gamma)$. Numerical analysis shows that the FEL quantum regime is observed only when the width of the initial momentum distribution is smaller than the momentum of the emitted photons. Both the analytical results in the linear approximation and the numerical simulations show that only the electrons close to a certain resonant energy start to emit photons. This generates the so-called Hole-burning effect in the electrons energy distribution, as it can be seen in the simulations we provide.

Finally, we present a brief discussion about a fundamental uncertainty relation that ties the electron energy spread and the electron bunching.

The full text can be accessed via the web page:
    http://www-library.desy.de/cgi-bin/showprep.pl?desy-thesis-07-004

6.2 Measurement and Analysis of Coherent Synchrotron Radiation Effects at FLASH

Bolko Beutner
University of Hamburg, Hamburg, Germany

Abstract:

The vacuum-ultra-violet Free Electron Laser in Hamburg (FLASH) is a linac driven SASE-FEL. High peak currents are produced using magnetic bunch compression chicanes. In these magnetic chicanes, the energy distribution along an electron bunch is changed by effects of Coherent Synchrotron Radiation (CSR). Energy changes in dispersive bunch compressor chicanes lead to transverse displacements along the bunch. These CSR induced displacements are studied using a transverse deflecting RF-structure.

Experiments and simulations concerning the charge dependence of such transverse displacements are presented and analyzed. In these experiments an over-compression scheme is used which reduces the peak current downstream the bunch compressor chicanes. Therefore other self interactions like space charge forces which might complicate the measurements are suppressed.

Numerical simulations are used to analyze the beam dynamics under the influence of CSR forces. The results of these numerical simulations are compared with the data obtained in the over-compression experiments at FLASH.

The full text can be accessed via the web page:
http://www-library.desy.de/cgi-bin/showprep.pl?desy-thesis-07-040

7 Forthcoming Beam Dynamics Events

7.1 The 11th European Particle Accelerator Conference, EPAC'08

Caterina Biscari, EPAC'08 chair
Mail to: caterina.biscari@lnf.infn.it

Oliver Bruning, EPAC'08 SPC Chair
Mail to: oliver.bruning@cern.ch

Paolo Pierini, EPAC'08 LOC Chair
Mail to: paolo.pierini@mi.infn.it

On behalf of the European Physical Society Accelerator Group (EPS-AG), which forms the core of the Organizing Committee (OC) of the EPAC series of conferences, we are pleased to announce the 11th biennial European Particle Accelerator Conference, EPAC'08, to be held in Genoa, Italy, from 23 to 27 June 2008, in the Magazzini del Cotone Venue. Details on the conference organization can be found in www.wpac08.org.

Genoa overlooks the Mediterranean Sea. Its history has been molded by the sea presence, giving birth to navigators, discoverers, artists. The Conference poster reflects Genoa international vocation: Cristoforo Colombo, from whose voyage Europe became aware of America's existence, was born in Genoa. Marco Polo, who opened the European roads to Asian countries, wrote his travel book, Il Milione, in his forced Genoa sojourn.

The Genoa conference will be the last EPAC, held twenty years after the first EPAC'88 in Rome. The European series of accelerator conferences will move to a three-year cycle of conferences, alternating around the world with conferences organized by Asian and North American colleagues. The first international conference on particle accelerators will thus be held in Kyoto, Japan in 2010, followed by Valencia, Spain in 2011 and New Orleans in the United States of America in 2012.

The EPAC'08 scientific conference programme represents the status, progress, and new ideas in the accelerator physics fields. More than 1500 abstracts have been submitted to be presented in the poster sessions, which we expect to be vividly attended (http://www.epac08.org/index.php?n=Main.Programme#).

Almost ninety industrial exhibitors will be showing their products, their presence confirming the spin-off relevance in our community and the close collaboration between the laboratories and the industry.

A rich student grant programme sponsored by the major European Laboratories and Universities will allow more than 60 young students to attend the conference and to serve as scientific secretaries.

The EPS-AG 2008 prizes will be granted during a prize ceremony to Alex Chao, Norbert Holtkamp and Viatcheslav Danilov.
(http://www.epac08.org/index.php?n=Main.2008AcceleratorPrizeWinners)

We hope that all conference attendants will enjoy the scientific programme, the environment, and the possibility of contacting a large number of members of the accelerator community worldwide.

7.2 Announcement for the "2nd Collaboration Meeting on X-Band Accelerator Structure Design and Test Programs"

S. Tantawi, SLAC, USA
Mail to: tantawi@slac.stanford.edu

The meeting will be held at KEK, Tsukuba, Japan from May 13 to May 15, 2008

Organizers:
Toshiyasu Higo, KEK, Japan
Walter Wuensch, CERN, Switzerland
Sami Tantawi, SLAC, USA

The collaboration meeting on X-Band Accelerator Structure Design and Test Programs is an annual meeting to discuss aspects of design, manufacturing, and testing of high-gradient microwave linear accelerators based on room-temperature accelerator structures.

The primary goal of this effort is to push forward the relevant technologies to a level that is readily applicable to highly reliable, higher-gradient accelerators of various scales, such as those needed for future linear colliders.

The main topics of this meeting are structure design and associated test programs. The discussions aim to establish a better understanding of the frequency scaling of the limiting gradient, as well as its dependence on material, surface preparation, pulsed heating, etc. To this end, the meeting will allot a reasonable share of time for discussions on the RF breakdown phenomenon from both theoretical and experimental standpoints. Test facilities and the collaborative development of such facilities around the world will be discussed. We will also attempt at this meeting to gain perspective on the ultimate gradient reach.

Recent developments will be discussed with the goal of firmly establishing the gradient reach of these technologies and furthering their practical application to specific accelerator designs.

For further information please see:

http://indico.cern.ch/conferenceDisplay.py?confId=30911

7.3 15th International Workshop on Beam Dynamics and Optimization, July 10-13, 2008, St. Petersburg, Florida

Pavel Snopok, University of California, Riverside, California, U.S.A.
Mail to: bdo08@bt.pa.msu.edu

7.3.1 Introduction

Traditionally, the objective of the Workshop is to bring together physicists, engineers, and mathematicians to present and discuss recent developments in the area of mathematical control methods, modeling and optimization and theory and design of charged particle beams, space charge effects, and plasma, including tools based on parallel and distributed computing in accelerator physics.

7.3.2 Historical Overview

The series of workshops on Beam Dynamics and Optimization started in 1994. Since then, 14 workshops were held in Russia: in St. Petersburg, Saratov, and in Dubna. In the years 2004 and 2005, the BDO workshops were included as separate sections into the 8th International Computational Accelerator Physics Conference (ICAP 2004), and the International Conference "Stability and Control Processes" (SCP 2005), respectively. This year is the first time the workshop is held outside the borders of Russia, although the name of the location will be instantly familiar to earlier participants: BDO 2008 will take place in St. Petersburg, but this time it is St. Petersburg, Florida, USA.

7.3.3 Dates and Venue

The workshop will be held from July 10-13, 2008 in St. Petersburg, Florida, USA at the Hampton Inn & Suites in downtown St. Petersburg, Florida (80 Beach Drive NE, St. Petersburg, Florida 33701, phone: +1-727-892-9900, fax: +1-727-892-9205).

Web site: http://www.stpetehamptonsuites.com

7.3.4 Organizing Committees

7.3.4.1   *The workshop is organized by*

- Department of Applied Mathematics and Control Processes
  St. Petersburg State University, Russia
- Department of Physics and Astronomy
  Michigan State University, Michigan, USA
- Department of Physics and Astronomy
  University of California, Riverside, USA

7.3.4.2   *Chairs*

Dmitri A Ovsyannikov (Russia)
Martin Berz (USA)
Pavel Snopok (USA/Russia)

7.3.4.3   *Organizing Committee*

S.N.Andrianov (Russia)	G.Hanson (USA)	Yu.Senichev (Germany)
Yu.A.Budanov (Russia)	R.Jameson (USA)	M.F.Vorogushin (Russia)
A.N.Dovbnya (Ukraine)	C.Johnstone (USA)	I.P.Yudin (Russia)
N.V.Egorov (Russia)	A.B.Kurzhanskiy (Russia)	D.V.Zhukov (Russia)
V.P.Gorbachev (Russia)	A.Poklonskiy (Russia)	

7.3.4.4   *Scientific Committee*

S.Kawata (Japan)	D.Neuffer (USA)	E.I.Veremey (Russia)
E.D.Kotina (Russia)	A.D.Ovsyannikov (Russia)	W.Wan (USA)
E.S.Masunov (Russia)	R.Ryne (USA)	A.P.Zhabko (Russia)
K.Makino (USA)	Yu.A.Svistunov (Russia)	
F.Meot (France)	A.Todd (USA)	

7.3.5 Technical Program

- Beam Dynamics
- Optimal Control Theory and Methods of Optimization
- Mathematical Modeling of Electromagnetic Fields
- Charged Particle Beam Generation
- Plasma Control and Optimization
- Applications of Accelerators
- Code Development

We will consider other topic proposals related to beam dynamics if there are a significant number of talks.

For further information please visit the Workshop website: http://bdo08.org or http://bt.pa.msu.edu/bdo08.

The PDF version of the First Announcement can be found at http://bt.pa.msu.edu/bdo08/data/announcements/bdo08_first_announcement.pdf.

7.4   Workshop on High-Intensity High-Brightness Hadron Beams

Stuart Henderson
Spallation Neutron Source, Oak Ridge National Laboratory
P.O. Box 2008, Oak Ridge, TN 37831
Mail to: shenderson@ornl.gov

The fourth in the series of High-Intensity High-Brightness Hadron Beams Workshops, HB2008 will be hosted by Oak Ridge National Laboratory, and will be held August 25-29, 2008 in Nashville TN, USA. HB2008 continues the tradition of successful workshops held in Batavia (2002), Bensheim (2004), and Tsukuba (2006).

It is an exciting time for the field with a large number of high-intensity proton facilities in all phases of the "life cycle"; from those that are imagined, to those in the design phase, to those nearing completion of construction, to those in the early operations phase, to those in full mature operation.

The workshop has become an important venue for detailed discussion, close interaction amongst experts, and collaboration in the field of high-intensity hadron beams. The program is expected to cover experimental and theoretical developments in high-intensity, high-brightness hadron beams, in the context of a traditional workshop setting. Further information is available at the conference website:

http://neutrons.ornl.gov/workshops/hb2008/index.shtml

8   Announcements of the Beam Dynamics Panel

8.1   ICFA Beam Dynamics Newsletter

8.1.1   Aim of the Newsletter

The ICFA Beam Dynamics Newsletter is intended as a channel for describing unsolved problems and highlighting important ongoing works, and not as a substitute for journal articles and conference proceedings that usually describe completed work. It is published by the ICFA Beam Dynamics Panel, one of whose missions is to encourage international collaboration in beam dynamics.

Normally it is published every April, August and December. The deadlines are 15 March, 15 July and 15 November, respectively.

8.1.2 Categories of Articles

The categories of articles in the newsletter are the following:

1. Announcements from the panel.

2. Reports of beam dynamics activity of a group.

3. Reports on workshops, meetings and other events related to beam dynamics.

4. Announcements of future beam dynamics-related international workshops and meetings.

5. Those who want to use newsletter to announce their workshops are welcome to do so. Articles should typically fit within half a page and include descriptions of the subject, date, place, Web site and other contact information.

6. Review of beam dynamics problems: This is a place to bring attention to unsolved problems and should not be used to report completed work. Clear and short highlights on the problem are encouraged.

7. Letters to the editor: a forum open to everyone. Anybody can express his/her opinion on the beam dynamics and related activities, by sending it to one of the editors. The editors reserve the right to reject contributions they judge to be inappropriate, although they have rarely had cause to do so.

The editors may request an article following a recommendation by panel members. However anyone who wishes to submit an article is strongly encouraged to contact any Beam Dynamics Panel member before starting to write.

8.1.3 How to Prepare a Manuscript

Before starting to write, authors should download the template in Microsoft Word format from the Beam Dynamics Panel web site:

http://www-bd.fnal.gov/icfabd/news.html

It will be much easier to guarantee acceptance of the article if the template is used and the instructions included in it are respected. The template and instructions are expected to evolve with time so please make sure always to use the latest versions.

The final Microsoft Word file should be sent to one of the editors, preferably the issue editor, by email.

The editors regret that LaTeX files can no longer be accepted: a majority of contributors now prefer Word and we simply do not have the resources to make the conversions that would be needed. Contributions received in LaTeX will now be returned to the authors for re-formatting.

In cases where an article is composed entirely of straightforward prose (no equations, figures, tables, special symbols, etc.) contributions received in the form of plain text files may be accepted at the discretion of the issue editor.

Each article should include the title, authors' names, affiliations and e-mail addresses.

8.1.4   Distribution

A complete archive of issues of this newsletter from 1995 to the latest issue is available at

http://icfa-usa.jlab.org/archive/newsletter.shtml.

This is now intended as the primary method of distribution of the newsletter.

Readers are encouraged to sign-up for electronic mailing list to ensure that they will hear immediately when a new issue is published.

The Panel's Web site provides access to the Newsletters, information about future and past workshops, and other information useful to accelerator physicists. There are links to pages of information of local interest for each of the three ICFA areas.

Printed copies of the ICFA Beam Dynamics Newsletters are also distributed (generally some time after the Web edition appears) through the following distributors:

Weiren Chou	chou@fnal.gov	North and South Americas
Rainer Wanzenberg	rainer.wanzenberg@desy.de	Europe^{++} and Africa
Susumu Kamada	susumu.kamada@kek.jp	Asia** and Pacific

++   Including former Soviet Union.
**   For Mainland China, Jiu-Qing Wang (wangjq@mail.ihep.ac.cn) takes care of the distribution with Ms. Su Ping, Secretariat of PASC, P.O. Box 918, Beijing 100039, China.

To keep costs down (remember that the Panel has no budget of its own) readers are encouraged to use the Web as much as possible. In particular, if you receive a paper copy that you no longer require, please inform the appropriate distributor.

8.1.5   Regular Correspondents

The Beam Dynamics Newsletter particularly encourages contributions from smaller institutions and countries where the accelerator physics community is small. Since it is impossible for the editors and panel members to survey all beam dynamics activity worldwide, we have some Regular Correspondents. They are expected to find interesting activities and appropriate persons to report them and/or report them by themselves. We hope that we will have a "compact and complete" list covering all over the world eventually. The present Regular Correspondents are as follows:

Liu Lin	Liu@ns.lnls.br	LNLS Brazil
Sameen Ahmed Khan	Rohelakan@yahoo.com	SCOT, Middle East and Africs

We are calling for more volunteers as Regular Correspondents.

8.2   ICFA Beam Dynamics Panel Members

Name	eMail	Institution
Marica Biagini	marica.biagini@lnf.infn.it	LNF-INFN, Via E. Fermi 40, Frascati 00044, Italy
Yunhai Cai	yunhai@slac.stanford.edu	SLAC, 2575 Sand Hill Road, MS 26 Menlo Park, CA 94025, U.S.A.
Swapan Chattopadhyay	swapan@dl.ac.uk	The Cockcroft Institute, Daresbury Laboratory, Daresbury, Warrington WA4 4AD, U.K.
Weiren Chou (Chair)	chou@fnal.gov	Fermilab, MS 220, P.O. Box 500, Batavia, IL 60510, U.S.A.
Yoshihiro Funakoshi	yoshihiro.funakoshi@kek.jp	KEK, 1-1 Oho, Tsukuba-shi, Ibaraki-ken, 305-0801, Japan
Miguel Furman	mafurman@lbl.gov	Center for Beam Physics, LBL, Building 71, R0259, 1 Cyclotron Road, Berkeley, CA 94720-8211, U.S.A.
Jie Gao	gaoj@ihep.ac.cn	Institute for High Energy Physics, P.O. Box 918, Beijing 100039, China
Ajay Ghodke	ghodke@cat.ernet.in	RRCAT, ADL Bldg. Indore, Madhya Pradesh, India 452 013
Ingo Hofmann	i.hofmann@gsi.de	High Current Beam Physics, GSI Darmstadt, Planckstr. 1, 64291 Darmstadt, Germany
Sergei Ivanov	ivanov_s@mx.ihep.su	Institute for High Energy Physics, Protvino, Moscow Region, 142281 Russia
Kwang-Je Kim	kwangje@aps.anl.gov	Argonne Nat'l Lab, Advanced Photon Source, 9700 S. Cass Avenue, Bldg 401/C4265, Argonne, IL 60439, U.S.A.
In Soo Ko	isko@postech.ac.kr	Pohang Accelerator Lab, San 31, Hyoja-Dong, Pohang 790-784, South Korea
Alessandra Lombardi	Alessandra.Lombardi@cern.ch	CERN, CH-1211, Geneva 23, Switzerland
Yoshiharu Mori	mori@kl.rri.kyoto-u.ac.jp	Research Reactor Inst., Kyoto Univ. Kumatori, Osaka, 590-0494, Japan
Chris Prior	c.r.prior@rl.ac.uk	ASTeC Intense Beams Group, STFC RAL, Chilton, Didcot, Oxon OX11 0QX, U.K.
David Rice	dhr1@cornell.edu	Cornell Univ., 271 Wilson Laboratory, Ithaca, NY 14853-8001, U.S.A.
Yuri Shatunov	Yu.M.Shatunov@inp.nsk.su	Acad. Lavrentiev, prospect 11, 630090 Novosibirsk, Russia
Junji Urakawa	junji.urakawa@kek.jp	KEK, 1-1 Oho, Tsukuba-shi, Ibaraki-ken, 305-0801, Japan
Jiu-Qing Wang	wangjq@mail.ihep.av.cn	Institute for High Energy Physics, P.O. Box 918, 9-1, Beijing 100039, China
Rainer Wanzenberg	rainer.wanzenberg@desy.de	DESY, Notkestrasse 85, 22603 Hamburg, Germany
Jie Wei	wei1@bnl.gov	Institute for High Energy Physics, P.O. Box 918, 9-1, Beijing 100039, China

The views expressed in this newsletter do not necessarily coincide with those of the editors.
The individual authors are responsible for their text.